List of Contributors

Melinda J. Duer, *Department of Chemistry, University of Cambridge, Lensfield Road, Cambridge CB2 1EW, UK*

John Higinbotham, *School of Applied Mathematical and Physical Sciences, Napier University, 10 Colinton Road, Edinburgh EH10 5DT, UK*

Ian Marshall, *Department of Medical Physics and Medical Engineering, The University of Edinburgh, Western General Hospital, Crewe Road, Edinburgh EH4 2XU, UK*

Mark E. Smith, *Department of Physics, University of Warwick, Coventry CV4 7AL, UK*

Preface

It is a pleasure for me to introduce Volume 43 of *Annual Reports on NMR Spectroscopy* and to express my thanks to the reporters for their pellucid and refulgent accounts of NMR activities in a number of areas of molecular science. The volume commences with a report on Solid-State NMR Studies of Molecular Motion by M. J. Duer; this is followed by a contribution from J. Higinbotham and I. Marshall on NMR Lineshapes and Lineshape Fitting Procedures; the final chapter is on Recent Progress in Solid-State NMR of Low-γ Nuclei by M. E. Smith. My gratitude to the production staff at Academic Press (London) for their meticulous efforts in the realization of this, and other volumes in the series, is hereby recorded.

Department of Chemistry
University of Surrey
Guildford
Surrey, UK

G. A. WEBB
May 2000

Solid-State NMR Studies of Molecular Motion

MELINDA J. DUER

Department of Chemistry, University of Cambridge, Lensfield Road, Cambridge, CB2 1EW, UK

1. Introduction 1
2. Powder lineshape analysis 3
   2.1. Basics 3
   2.2. Chemical shift anisotropy lineshapes 9
   2.3. Dipolar coupling lineshapes 16
   2.4. Quadrupolar lineshape analysis – ^{2}H NMR 20
3. Relaxation time measurements 25
4. Exchange experiments 32
   4.1. Basics 32
   4.2. Higher-dimensional exchange spectra 36
   4.3. Improving resolution in exchange experiments 40
5. Polymers 45
6. Biological materials 47
7. Host–guest compounds 51
8. Organometallic compounds 53
   References 55

1. INTRODUCTION

Ever since NMR was first used by chemists, there have been reports of its use to study molecular motion in solid materials. In the last ten years or so, the interest in this area has increased hugely, and it is now surely one of the principal applications of solid-state NMR.

This review surveys the studies of molecular motion, dynamics and exchange in solids using NMR that have appeared in the literature in the period 1994–1999. It is not intended to be exhaustive, but rather to provide a critical account of work in the main areas of interest during this time and to highlight any new advances.

NMR is an excellent method for studying dynamics of molecules in solids; all nuclear spin interactions are in general anisotropic, i.e. they depend on the

ANNUAL REPORTS ON NMR SPECTROSCOPY
VOLUME 43 ISBN 0-12-505343-6

molecular orientation within the applied magnetic field of the NMR experiment. Thus a change of molecular orientation is accompanied by a change in strength of the chemical shielding, any dipole–dipole coupling and, for $I > \frac{1}{2}$, the quadrupole coupling.

Very slow motions ($<10^3$ Hz) may be studied via two-dimensional (or higher-dimensional) exchange methods. In such techniques, the strength of a particular nuclear spin interaction is monitored during the t_1 period of the experiment. A mixing period then follows, during which molecular reorientation may occur. Finally, the new strength of the nuclear spin interaction, resulting from the change of molecular orientation/chemical site is recorded in t_2. The final two-dimensional spectrum then correlates the strengths of the interaction during t_1 and t_2 and, from this, the angular reorientation involved in the motion can be inferred. Repeating the experiment for different mixing times allows the correlation time for the motion to be determined.

Motions with rates of the order of the nuclear spin interaction anisotropy can be assessed via lineshape analysis. These are generally motions of intermediate rates, a few kHz to tens of kHz for chemical shift and dipolar interactions, higher for quadrupolar interactions.

Finally, higher-rate motions (10^6–10^9 Hz) can be examined by spin–lattice relaxation time studies. Spin–lattice relaxation (as other relaxation processes) relies on fluctuations in nuclear spin interactions induced by molecular motion. Thus, in cases where relaxation is dominated by one particular nuclear spin interaction, the spin–lattice relaxation times can be calculated for different motions and compared with experimentally derived values.

These methods for studying molecular motion in solids are well understood and have been well documented in the literature prior to the review period. Therefore, it is not the intention of this review to discuss the underlying principles of these experiments in detail. However, there have been experimental and theoretical advances in all of these areas and these are discussed in Sections 2–4.

The interest in molecular motions in solids has developed in part because of the realization that many bulk material properties are dependent on the flexibility and degrees of freedom of the underlying molecules. For instance, the flexibility of a bulk polymer ultimately rests with the flexibility of the constituent molecules. The ability of a material to withstand stress depends upon the molecular degrees of freedom that can absorb the energy of the stress imposed on the material. Most solid–solid phase transformations, including glass transitions of polymers, are accompanied by the onset (or quenching) of some molecular motion, and understanding how these motions arise leads to an understanding of the occurrence of the phase transition itself. For these reasons, studies of molecular dynamics in solid polymers continues apace. This area is discussed in detail in Section 5.

An area that has truly blossomed in the last five years is that surrounding biological materials, and in particular biological membranes. The transport of

molecules across membranes is clearly a very important area and it could well be that such transport is dependent on the dynamics of at least some components in the membrane. The study of molecular dynamics in solid biological materials is discussed in Section 6.

A more general reason for studying molecular motion in solids is that any observed motion is governed by the intermolecular potential that operates in the solid. Thus, by studying the nature and rate of the motions that occur as a function of temperature, for instance, we can gain information on the intermolecular potential. This is crucial if we are to understand the structure and properties of any material. It is this reasoning that probably underlies many of the studies of the dynamics of molecules adsorbed in porous solids or on surfaces (Section 7) and of ligand dynamics in organometallic compounds, for instance (Section 8).

2. POWDER LINESHAPE ANALYSIS

2.1. Basics

By 'powder', is meant samples that consist of many crystallites with random orientation, such that all molecular orientations are present simultaneously with a statistical distribution. The orientation dependence of each nuclear spin interaction means that, for powder samples, the NMR spectrum consists of a broad *powder pattern* for each distinct chemical site. The powder pattern can be considered as being made up of an infinite number of sharp lines, one from each different molecular orientation, the frequency of each line being determined by the molecular orientation itself. The lines from different orientations all overlap and result in the observed broad (but not featureless) line. The intensity at any point in the powder pattern reflects the population of the corresponding molecular orientation. Any molecular motion that changes molecular orientation within a crystallite in the sample changes the spectral frequency associated with the crystallite; the resonance line for that crystallite now moves to some other part of the powder pattern. If the motion is at a rate similar to the width of the powder pattern, then coalesence occurs between the lines corresponding to the different molecular orientations that arise during the course of the motion. This in turn causes distinctive distortions of the powder patterns, the distortions being dependent on both the rate and geometry of the molecular motion. Powder pattern lineshapes can be simulated for likely models of the molecular motion and compared with experiment to reveal details of the molecular dynamics.

Resolving powder patterns

For simple materials, where there is only one chemical site (or a few), powder patterns can easily be measured on static, i.e. nonspinning, samples in simple

one-dimensional experiments. However, many materials of interest are complex, with many different chemical sites for a given nuclear species. In a static experiment in such cases, powder patterns from different sites overlap and the concomitant lack of resolution prohibits analysis of the lineshapes. Consequently, much effort in recent years has been directed towards resolving powder patterns from different chemical sites, for the purposes of studying molecular motion. One of the simplest methods is to use slow-speed magic-angle spinning.[1,2] Magic-angle spinning (MAS) has the effect of averaging second-rank terms in the nuclear spin Hamiltonian to zero, and so removing the effects of chemical shift anisotropy and so on from the NMR spectrum. This in itself would then remove the useful information on molecular reorientations that is contained in the anisotropic parts of the spectrum. However, under slow-speed spinning (spinning speed less than the powder pattern linewidth), spinning sidebands appear in the spectrum. For inhomogeneous nuclear spin interactions, the sidebands are sharp, and thus sideband patterns from different chemical sites are relatively easily resolved. The important point, however, is that the intensities of spinning sidebands are dependent on the anisotropic parts of the nuclear spin interaction and thus on any motional process in the sample; the linewidth of spinning sidebands is also affected by molecular motion. Thus, simulation of magic-angle spinning sideband patterns for particular models of molecular motion can yield information on molecular motions in much the same way as for static powder patterns. An example of such use in the review period examined the motion of aromatic rings in two hydrogen-bonded carboxylic acid–pyridyl complexes via ^{13}C magic-angle spinning sideband analysis.[3] In one compound, there were seven different aromatic ^{13}C sites; all were resolved and their respective motions were analysed by simulation of their sideband patterns arising from ^{13}C chemical shift anisotropy at different temperatures.

The other general way of resolving powder patterns from different chemical sites is to generate multidimensional NMR spectra in which the desired powder patterns (or magic-angle spinning sideband patterns) are resolved in one dimension, separated according to (for instance) isotropic chemical shift in another dimension. These techniques are discussed below in the relevant section for each type of nuclear spin interaction.

Analysis of lineshapes

Obtaining information from powder pattern lineshapes (or sideband patterns) always involves matching the experimental lineshapes to those obtained from simulation, and the simulations necessarily involve some model for the molecular motion. This model dependency is an inevitable limitation on this general method for studying molecular motion. The vast majority of studies assume some kind of Markov model for the motion,[4] that is, it is assumed that the nucleus/molecule jumps between N discrete sites and that the time taken to

move between sites is very small compared with the time of residence in each site. This leads to a particularly simple form for the free-induction decay (FID). In the absence of motion, the FID is simply given by

$$g(t) = \frac{1}{8\pi^2} \int_0^{2\pi} \int_0^{\pi} M_0(\theta, \phi) \exp(i\omega(\theta, \phi)t + T_2) \sin\theta \, d\theta \, d\phi \qquad (1)$$

where $M_0(\theta, \phi)$ is the magnitude of the magnetization at the start of the FID (which in turn has been determined by the preceding pulse sequence, whatever it may be), θ and ϕ are spherical polar angles describing the orientation of the applied field $\mathbf{B}_0$ in a crystallite-fixed frame of reference, and $\omega(\theta, \phi)$ is the resonance frequency of the spin in crystallite orientation (θ, ϕ). If the experiment is conducted under magic-angle spinning, $\omega(\theta, \phi)$ is also time dependent. T_2 is the transverse relaxation time for the spins (assumed here to be independent of orientation). The integral in Eq. (1) is over all molecular orientations in the powder sample, so that $g(t)$ represents the FID for the whole powder sample. To take account of molecular reorientations using a Markov model, Eq. (1) is simply modified to

$$\mathbf{g}(t) = \frac{1}{8\pi^2} \int_0^{2\pi} \int_0^{\pi} \mathbf{M}_0(\theta, \phi) \exp(i\boldsymbol{\omega}(\theta, \phi)t + \mathbf{T}_2 + \mathbf{A}) \sin\theta \, d\theta \, d\phi \qquad (2)$$

$\mathbf{M}_0$ is now an N-dimensional vector, each component being the complex transverse magnetization from one of the N sites involved in the Markov process. $\boldsymbol{\omega}$ is an $N \times N$ diagonal matrix whose elements are the resonance frequencies associated with the N sites for a crystallite orientation (θ, ϕ). $\mathbf{A}$ is also an $N \times N$ matrix whose elements A_{ij} are given by Ω_{ij}/p_i where Ω_{ij} is the rate of hopping from site j to site i and p_i is the population of site i. The final FID is given in this case by the sum of the elements in the N-dimensional vector $\mathbf{g}(t)$, each element being the FID at time t resulting from each of the N sites.

The Markov approach works well for high ordering potentials, that is for situations where there are high and sharp potential barriers between alternative sites. The approach, however, breaks down for small ordering potentials, where there are barriers of the order of kT for at least part of the motion. The case of continuous rotational diffusion was treated some time ago,[5] but for many cases, the 'truth' probably lies somewhere between this limit and that implied by the Markov model. For instance, we might imagine a case where there are indeed hops between different sites but where there are, in addition, oscillations within the potential wells defining each 'site' (Fig. 1). This situation has only recently received detailed attention[6]. The approach uses the Smoluchowski model, which allows the description of diffusion in an arbitrary ordering potential with an arbitrary diffusion tensor. The model is computationally intensive, and certainly less appealing than the Markov approach as an

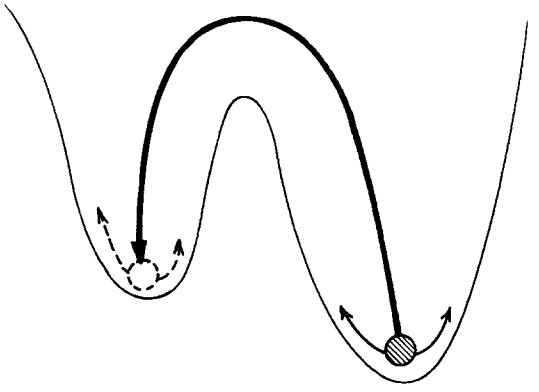

Fig. 1. An illustration of the potential governing molecular motion in a system. The nucleus may hop between different potential wells, and in addition oscillate within a well. The often-used Markov model assumes that nuclei hop between discrete sites and that the length of time taken to hop is very small compared with the residence time in each site. Such a model can only account effectively for hops between the minima of the potential wells in this illustration; diffusion within wells cannot be treated properly.

algorithm. However, the work[6] shows quite conclusively that for ^{2}H powder lineshapes (recorded with the quadrupole echo pulse sequence) and ^{2}H MAS spinning sideband patterns there can be considerable effects on the spectrum arising from local oscillations within potential wells (Fig. 2).

The difference between the Markov model lineshapes and those from the Smoluchowski model is particularly pronounced when the diffusion coefficient is of the order of the quadrupole coupling constant. In the limit of large diffusion coefficients, the two models converge, and in the limit of low diffusion coefficients, the spectra are dominated by small-amplitude oscillations within potential wells, which can be approximately modelled by a suitable Markov model. This work strongly suggests that there could well be cases where analysis of powder pattern lineshapes with a Markov model leads to a fit between experimental and simulated spectra but where the fit model does not necessarily describe the true dynamics in the system.

A further advantage of using the Smoluchowski model is that the fit parameters resulting from an analysis can be directly interpreted at a molecular level, as they describe intra- and intermolecular interactions. The parameters arising from a Markov model – namely the relative angular orientation of the sites involved in the dynamics process, the rate of hopping between sites, and the populations of those sites – are rather less easy to interpret at a molecular level. To be more specific, the site orientation information that arises from a lineshape analysis using a Markov model is the relative angular orientation of the nuclear spin interaction principal axis frame in the N different sites involved in the motion. However, this

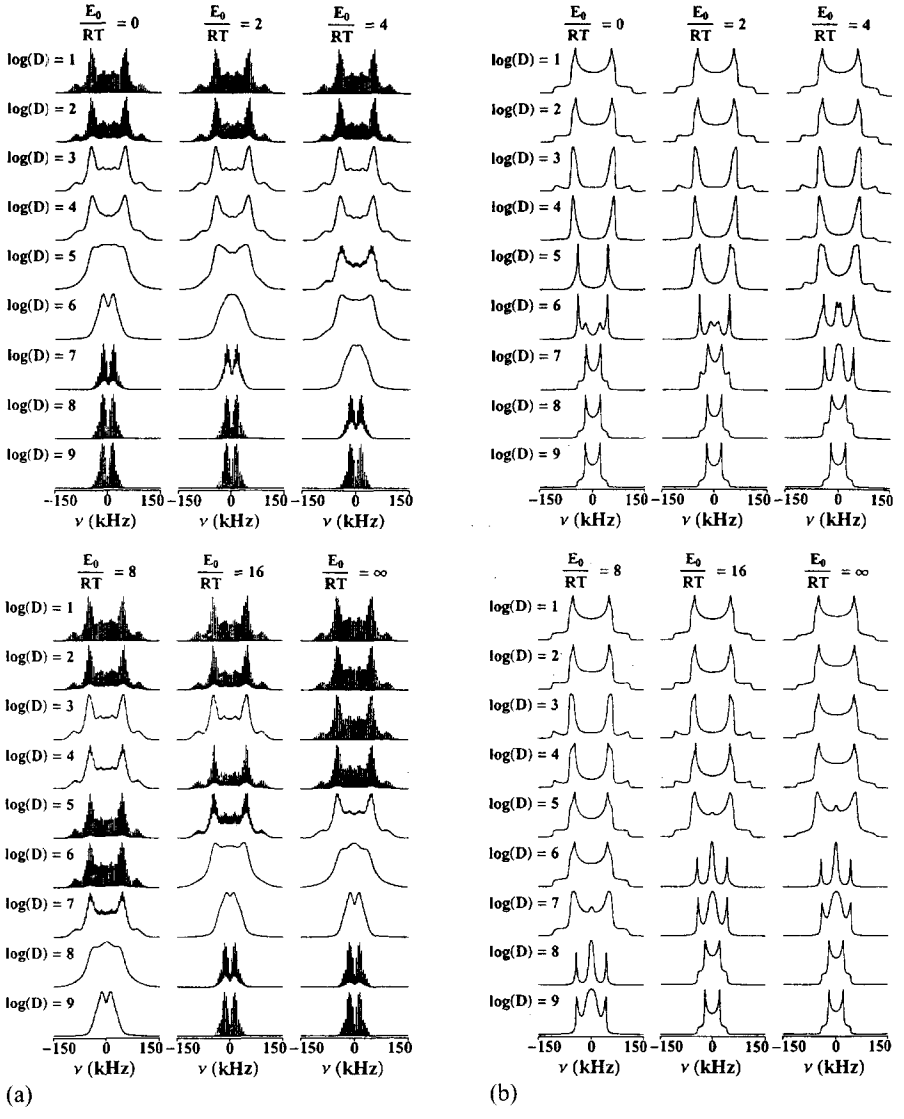

Fig. 2. Calculated ^{2}H NMR spectra for the situation illustrated in Fig. 1, where nuclei can move between potential wells and diffuse under the governing potential within wells. (a) ^{2}H MAS spectra. (b) Static ^{2}H spectra. The spectra are calculated as a function of D, the diffusion coefficient and E_0, the potential barrier between wells. Spectra are taken from reference 6.

information is only useful if the orientation of the principal axis frame is known relative to some molecular frame, as only then can the *molecular* motion (as opposed to the *principal axis frame* motion) be revealed. In the case of the quadrupole interaction for ^2H, this latter information can generally be fairly well predicted, at least for organic compounds, where the ^2H quadrupole coupling tensor is generally axially symmetric (or nearly so), with its unique axis along the C–^2H bond. However, when the nuclear spin interaction in question is a chemical shift anisotropy, the principal axis frame orientation is usually rather less obvious (unless the nucleus is at a site of crystallographic axial symmetry). In such a case, knowing how the chemical shift anisotropy tensor moves as a result of molecular motion may not lead to much insight into how the molecule itself is moving. For instance, a ^{13}C experimental lineshape for an aromatic ring ^{13}C site in a polymer may be fitted by a motional model that involves hopping between two sites in which the principal axis frame z axes are, say, 20° apart. This could mean that the aromatic ring itself is undergoing a librational motion with amplitude 20°, or it could equally well be interpreted as the whole polymer chain moving in such a way as to shift the aromatic ring principal axis frame by 20°. There is nothing in the lineshape analysis process that can remove this ambiguity. An ingenious experiment recently reported goes at least part way to solving this problem.[7] This work reports the use of a one-dimensional dipolar-shift experiment[8] for relating the chemical shift tensor orientation to that of a heteronuclear dipole coupling tensor orientation under the condition of fast molecular motion (i.e. hopping rate much greater than chemical shift anisotropy). In most chemical shift anisotropy lineshape measurements, the effects of heteronuclear dipolar coupling, for instance coupling to ^1H in ^{13}C lineshape measurements, is removed by ^1H decoupling, in order to avoid the massive line broadening that would otherwise result. However, the dipolar coupling can be useful; dipolar coupling between two nuclei, for instance ^{13}C and ^1H, is described by an axial coupling tensor whose unique axis necessarily lies along the internuclear vector. So, if the orientation of the chemical shift tensor can be determined relative to the dipolar coupling tensor, then the orientation of the chemical shift tensor relative to the molecule has been determined. The one-dimensional dipolar-shift experiment[8] applies off-resonance decoupling to the unobserved dipolar-coupled ^1H nucleus, such that the net field felt by this nucleus in the rotating frame is oriented at the magic angle relative to the applied field. This has the effect of largely removing the ^1H–^1H dipolar coupling effects from the ^{13}C spectrum. However, the ^{13}C–^1H dipolar coupling remains, albeit scaled by a factor of 0.58. Now, any ^{13}C powder patterns recorded result from the sum of the chemical shift anisotropy and the ^1H–^{13}C dipolar coupling scaled by 0.58. Consequently, the powder patterns are a sensitive function of the relative orientations of the two interaction tensors. In the slow-speed[8] or fast-speed limiting cases[7] (motional hopping rate much less than or much greater than

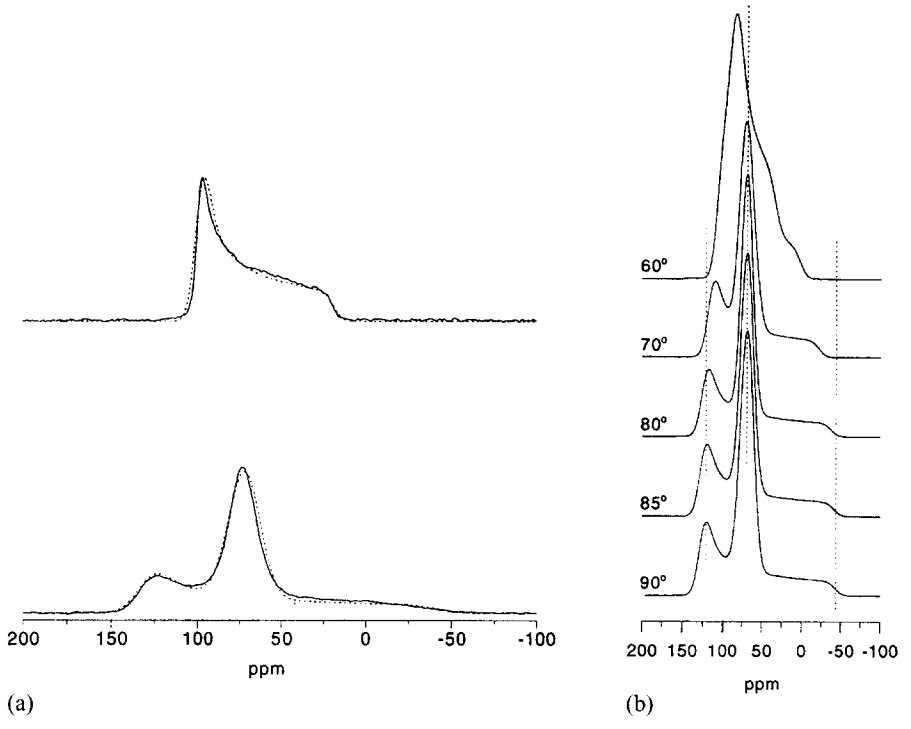

Fig. 3. Example spectra from the one-dimensional dipolar-shift experiment taken from reference 7. (a) (Top) Experimental ^{13}C chemical shift anisotropy powder pattern for $Ru(C_5H_5)_2$ and (below) for comparison, the dipolar shift ^{13}C spectrum for the same compound. (b) Calculated dipolar-shift lineshapes for different angles (indicated) between the $^{1}H-^{13}C$ dipolar and chemical shift anisotropy tensor principal z-axes.

the chemical shift anisotropy), the powder patterns are easily analysed to reveal this vital information (Fig. 3).

The case of intermediate motional rates has not yet been addressed, but should be a fairly simple extension, merely requiring details of the lineshape simulation to be derived for this case.

2.2. Chemical shift anisotropy lineshapes

In the review period there have been many studies of molecular motion using analysis of chemical shift anisotropy lineshapes. One that nicely illustrates what is currently possible concerns the motion of ^{13}CO intercalated in C_{60}.[9] This is a particularly interesting example as both the CO and C_{60} molecules undergo reorientation, with the onset of motion occurring at different temperatures for the two species. Furthermore, the work uses a prior calculation of the potential

energy surface for the intercalated molecule to derive a sensible motional model for use in the analysis. This type of combined approach is likely to see much greater use in the future as computational power becomes cheaper and the materials under investigation become more complex. In pure C_{60}, the molecules reorient rapidly and isotropically on the NMR timescale down to 260 K in a face-centred cubic (fcc) phase. At this temperature there is a phase transition to a simple cubic (sc) phase. Below this, there are rotational jumps of molecules on their crystallographic sites between symmetry-equivalent orientations and, additionally, jumps between symmetry-inequivalent orientations, commonly labelled *h* and *p*; the ratio of *h* to *p* orientations depends upon temperature. A glass transition occurs at 90 K, below which the ratio of *h*:*p* orientations remains constant and exchange between them ceases. Intercalation with ^{13}CO does not alter the crystal symmetry but simply shifts the temperatures of the various phase transitions to 243 K for the fcc–sc transition and 84 K for the glass transition. The work began with calculations of the potential energy surface for CO in its pseudo-octahedral intercalation site.[10] The CO molecule was assumed to sit at a site of S_6 symmetry at the centre of a unit cell, in which static C_{60} molecules are at the vertices (Fig. 4).

Eight potential energy minima were found, each minimum corresponding to the CO molecule lying parallel or antiparallel to one of the four body diagonals of the unit cell. The parallel and antiparallel positions on each body diagonal

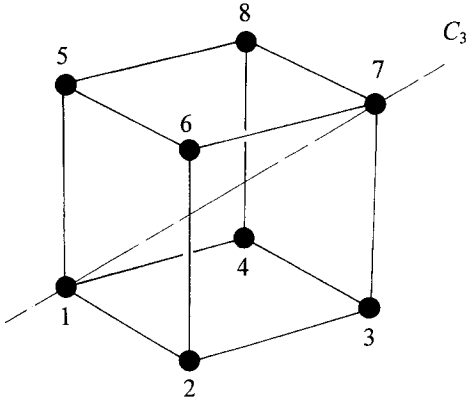

Fig. 4. Schematic illustration of the eight ^{13}C sites assumed in the model of the dynamics of ^{13}CO in C_{60}.[9] The cube represents the C_{60} unit cell; the CO lies at the centre of the unit cell, along one of the four body diagonals of the cell. The numbered vertices of the cell then represent the eight possible orientations of the ^{13}CO molecule, with the ^{13}C pointing towards the particular numbered vertex along the corresponding body diagonal. One of the body diagonals is a C_3 axis of symmetry. The two orientations along this diagonal (1 and 7) are degenerate among themselves but different from the remaining six orientations. The remaining six orientations (2, 3, 4, 5, 6, 8) are all degenerate.

are degenerate with the body diagonal corresponding to the C_3 axis through the unit cell being different from the other three, which are otherwise all degenerate among themselves. If all the C_{60} molecules are in the *h* orientation, it was found that the lowest energy CO orientation is (parallel or antiparallel) along the C_3 body diagonal (6 cm^{-1} lower than the remaining six degenerate sites). However, if the C_{60} molecules are all in the *p* orientation, the six orientations off the C_3 axis are the preferred ones by 48 cm^{-1}. In fact, of course, there will be a random and frozen-in distribution of *h* and *p* orientations in the sample below the glass transition temperature, and so the true potential for a ^{13}CO molecule will be some linear combination of the calculated potentials. However, the CO molecule still lies at a site of S_6 symmetry and so presumably a motional model involving eight potential minima is still appropriate. Above 245 K, the fcc–sc phase transition temperature, the ^{13}C static lineshapes for CO are isotropic, indicating isotropic reorientation of the molecules. An abrupt change occurs with the phase transition at 245 K and a typical tensor powder pattern appears below this temperature, which broadens with decreasing temperature. These powder patterns were all simulated[9] assuming a motional model in which the six degenerate sites off the C_3 axis (sites 2, 3, 4, 5, 6 and 8 in Fig. 4) all exchange amongst themselves at rate k_1. The two degenerate sites on the C_3 axis (sites 1 and 7 in Fig. 4) then exchange with these six at rate k_2. It is worth noting that fast exchange between the parallel and antiparallel CO orientations along any axis corresponds to a 180° rotation of the ^{13}C shielding tensor and so does not alter the ^{13}C powder lineshape. The orientation of the CO ^{13}C shielding tensor was assumed to be the same as for free CO, namely the principal axis frame lying along the molecular axes. The k_1 and k_2 exchange parameters are related by

$$k_2 = k_1 \exp(-\Delta E/RT) \tag{3}$$

where ΔE is the energy difference between the two groups of potential minima, so in fitting values of k_1 and k_2, values for ΔE may be determined. Above 235 K, $\Delta E \sim 0$ cm^{-1}; in other words, all the eight sites for CO are degenerate, and so the CO molecule sits at a site of octahedral symmetry. This is consistent with the fact that the C_{60} molecules undergo *h* to *p* reorientations above this temperature, rendering the effective CO site symmetry O_h when the C_{60} motion is fast enough. Below 235 K, ΔE depends on the ratio of CO : C_{60}, but for the sample studied[9] it was between 31.3 cm^{-1} at 235 K and 39.7 cm^{-1} at 100 K. Below the glass transition at 84 K, the motional model described above was recognized by the authors of the work[9] to be strictly inappropriate. Once the C_{60} molecules are static, there are several different distorted octahedral sites possible for CO, each depending on the ratio of *h* : *p* C_{60} orientations in the specific unit cell and their distribution around the unit cell. Nevertheless, the model is still a reasonable approximation and ^{13}C static lineshapes were fitted

in the temperature range 4–30 K with a (constant) value of 25.3 cm^{-1} for ΔE. At 4 K, all the CO molecules were localized within potential minima, with no exchange between minima on the NMR timescale. One important point made by the authors of this work is that the effect of the k_1 rate parameter is very largely to cause line broadening only. Therefore it is very difficult to extract a unique value for this parameter from that for T_2, the transverse relaxation time, which also, of course, simply causes line broadening. This type of parameter redundancy is common and is likely to become more so as more complex motional models are considered.

Magic-angle spinning with subsequent analysis of the spinning sideband patterns arising from chemical shift anisotropy has also been used to study molecular motion in the review period. In static, i.e. nonspinning samples, the powder pattern lineshape depends on the rate of the molecular motional process relative to the chemical shift anisotropy; in particular, the lineshape is most sensitive to motions with rates of the order of the chemical shift anisotropy. Under magic-angle spinning, however, the dynamic range of the experiment, i.e. the motional frequency range that the sideband pattern is sensitive to, changes,[1,2] and depends additionally on the sample spinning speed. This feature can be very useful, as it offers a method for studying motions that are out of the sensitive frequency range for static techniques. The other advantage of magic-angle spinning is the improved resolution it offers, often allowing the sideband patterns from different sites to be resolved. For rapid motions, the sideband pattern, as with static powder patterns, can be described by an effective chemical shift tensor that is the average over the molecular motion. The effective chemical shift anisotropy and asymmetry can give useful information on the angular reorientation involved in the motion (providing that the orientation of the true chemical shift tensor with respect to the molecule is known), even though the rate of the motion is unobtainable by lineshape analysis in this instance. An example of such an analysis is the reorientation of the fluorine ligands in $(F_3PNPh)_2$ (Fig. 5).[11]

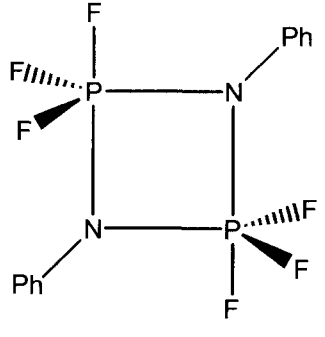

Fig. 5. The molecular structure of $(F_3PNPh)_2$.

In this molecule, the phosphorus is five-coordinate, trigonal bipyramidal, with the ring nitrogens occupying one axial and one equatorial site; the fluorines then occupy the remaining one axial and two equatorial sites. Analysis of both ^{19}F and ^{31}P spinning sideband patterns in the fast-motion limit arising from MAS experiments in which the unobserved nucleus and ^{1}H are decoupled yields effective chemical shift anisotropies and asymmetries that suggest that the fluorine ligands are undergoing rapid axial–equatorial exchange. Scalar couplings are rarely observed in the solid state, but in this work[11] the resolution is extremely good, and $^{31}P-^{19}F$ scalar coupling is clearly seen. In the fast-motion limit, the ^{31}P signal consists of a quartet, showing that the three bonded ^{19}F are all equivalent on the NMR timescale. As the temperature is decreased and the fluorine motion slows, so the two central lines of the quartet broaden, indicating that there are now two different ^{19}F sites.

A novel use of MAS lineshape analysis is in the study of bond rearrangements in the solid state.[12,13] One study[12] examined the reorientation of fluorobullvalene (Fig. 6a) in the solid-state via MAS lineshape analysis. This molecule has a C_3 axis of symmetry and so a threefold jump model was used to simulate the experimental ^{13}C NMR spectra at temperatures between 293 K and 258 K for spinning speeds of 4.7 kHz and 10 kHz. Excellent agreement is obtained between experimental and simulated spectra for all ^{13}C resonances with jump rates in the millisecond range. A second study then examined cyanobullvalene (Fig. 6b) using the same technique.[13] However, here it was found that only some of the ^{13}C resonances in the NMR spectrum were affected by motion; notably, only resonances from ^{13}C in wing A of the molecule (see Fig. 6b) suffered line broadening, the signature of molecular motion. Clearly, such a localized effect cannot be due to complete molecular reorientation as in the case of fluorobullvalene[12]. Instead, the linebroadening is ascribed to a very specific Cope rearrangement. There are several possible rearrangement mechanisms; that actually operating was deduced from two-dimensional MAS ^{13}C exchange spectra, and this was then used as a model to analyse the one-dimensional MAS spectra as a function of temperature to determine the rate of the process. The mechanism determined in this way is shown in Fig. 7; the rate of the process is a few hundred hertz at temperatures between 308 K and 323 K.

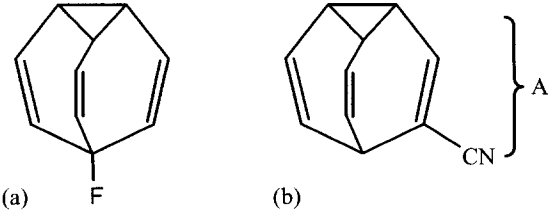

Fig. 6. The molecular structures of (a) fluorobullvalene and (b) cyanobullvalene.

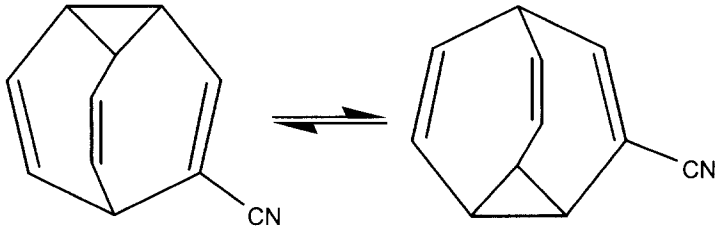

Fig. 7. The mechanism of the Cope rearrangement in cyanobullvalene as deduced from two-dimensional MAS ^{13}C exchange NMR spectra in reference 13.

Another way of dealing with the resolution problem for powder lineshapes is to use multidimensional NMR techniques to separate powder pattern lineshapes (or magic-angle spinning sideband patterns) according to isotropic chemical shift, as mentioned previously.

A great many techniques exist for separating chemical shift anisotropy powder patterns. Three of the most used are the method due to Tycko *et al.*,[14] variable-angle correlation spectroscopy (VACSY)[15] and the magic-angle turning experiment.[16] The first two of these have been adapted for molecular motion studies.[17,18] However, the magic-angle turning experiment generates the isotropic dimension of the two-dimensional experiment by employing very slow-speed spinning (<100 Hz), where it can be assumed that the rotor, and hence the nuclear spins, are effectively stationary for periods of $t_1/3$. Any molecular reorientation during t_1 would invalidate this assumption and lead to a much broadened spectrum in the corresponding f_1 dimension of the final two-dimensional spectrum.

The VACSY experiment[15] is a two-dimensional experiment. FIDs are recorded in successive experiments in which the spinning angle is varied. Subsequent processing of the two-dimensional dataset[15] produces a two-dimensional experiment with an isotropic spectrum in one dimension and chemical shift powder patterns in the other. These powder patterns are able to reflect motional processes in a similar manner to a normal one-dimensional experiment.[17] Interestingly, the motionally averaged lineshapes are different from those expected from a one-dimensional spectrum of a chemical shift anisotropy powder pattern; they can, however, be simulated to reveal the details of the molecular dynamics. Moreover, the dynamic range of the experiment is different from that of the normal one-dimensional chemical shift anisotropy powder pattern measurement; in particular, the VACSY experiment is sensitive to slower motions than is the one-dimensional experiment. To understanding this, it is important to remember that powder patterns are sensitive to motions that have rates of the order of the interaction anisotropy. When spinning the sample about an axis inclined at an angle θ to the applied magnetic field, the chemical shift anisotropy is averaged to an effective value of

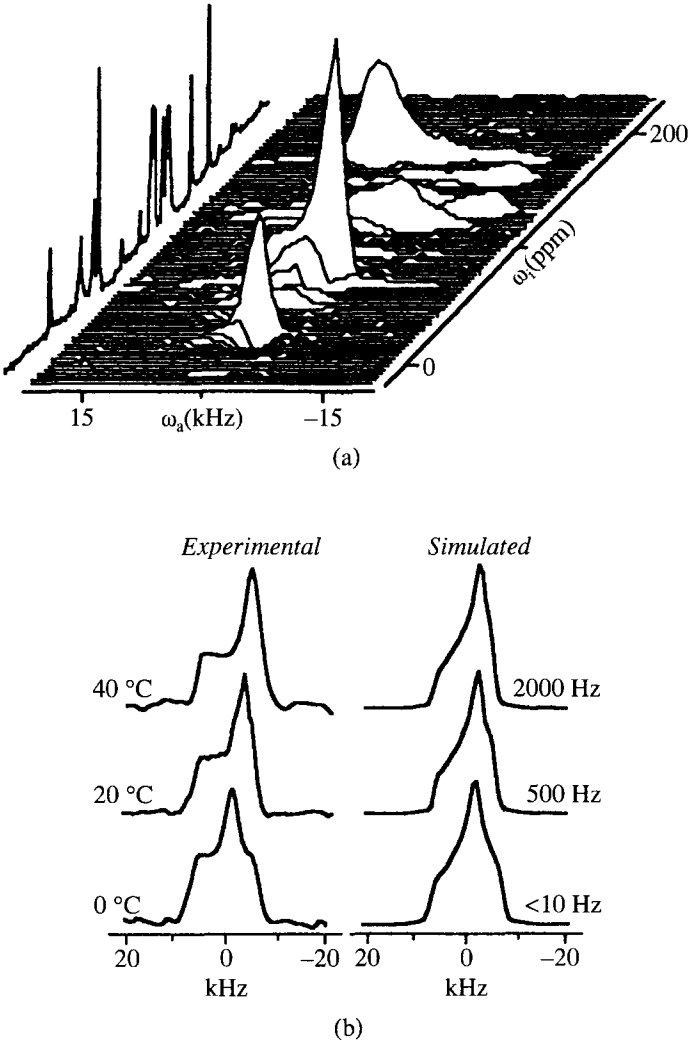

Fig. 8. Results of the ^{13}C VACSY experiment on tyrosine ethyl ester.[17] The experiment separates ^{13}C (or other) chemical shift anisotropy powder patterns according to isotropic chemical shift. Motional details of each ^{13}C site may then be determined by simulation of the relevant chemical shift anisotropy powder pattern. (a) The complete two-dimensional ^{13}C VACSY spectrum. (b) Slices from the ^{13}C VACSY experiment for the tyrosine phenyl ring at different temperatures. The simulations assume the phenyl ring is undergoing 180° flips at the rates indicated. All spectra are taken from reference 17.

$\frac{1}{2}(3\cos^2\theta - 1)$ times the true chemical shift anisotropy; that is, it is averaged to a smaller value in general (zero if θ is the magic angle). In the VACSY experiment, the sample is sequentially spun at different angles, and for every spinning angle (except $\theta = 0$), the effective chemical shift anisotropy is reduced from its true value, so that at all spinning angles, the spectrum recorded is sensitive to motions with slower rates than is the normal one-dimensional powder pattern.[17] The VACSY experiment was first tested on ^{13}C in dimethylsulfone (DMS),[17] whose dynamics in the solid state as a function of temperature are well known. It was then employed to study the ^{13}C dynamics in solid tyrosine ethyl ester as a function of temperature (Fig. 8), where it gave a detailed account of the phenyl ring rotation.[17]

The chemical shift anisotropy recoupling scheme of Tycko *et al.*[14] is particularly useful for studying molecular motions in complex solids, as its dynamic range can be 'tuned'.[18] In Tycko's experiment, the chemical shift anisotropy is removed with magic-angle spinning, but then reintroduced during the t_1 period by series of $2n + 2$, $n = 0, 1, 2, 3, \ldots$ 180°, pulses per rotor period. The effective chemical shift anisotropy that acts during t_1 is scaled from the true chemical shift anisotropy by an amount that depends on the exact timing of the pulses, with scalings of 0.4 to near zero being possible.[18] The scaled chemical shift powder patterns, which appear in the f_1 dimension of the final two-dimensional spectrum, are sensitive to molecular motions with rates of the order of the *scaled* chemical shift anisotropy. Thus the experimenter can choose the dynamic range of this experiment to suit the particular motional processes in their sample at the temperature of interest.[18] This principle was demonstrated on dimethylsulfone by showing the different lineshapes that occurred for a single temperature, for experiments with different chemical shift anisotropy scalings.

2.3. Dipolar coupling lineshapes

Pure dipolar coupling powder patterns are rarely used for studying molecular motion, for the simple reason that dipolar powder patterns that can be usefully analysed rarely occur. Ideally, one would wish to examine powder patterns arising from isolated spin pairs. Having more than two spins leads to complex lineshapes that would be very time consuming to analyse, and more than three or so spins leads to such a degree of line broadening that the lineshape becomes a featureless, approximately Gaussian-shaped line. In most samples, the spin of interest is either an isolated single spin (often the case when low-abundance nuclei are being considered), so that no dipolar coupling is possible, or is surrounded by many other spins. Often the only way to obtain isolated spin pairs is to specifically label the sites of interest; this practice is becoming much more common, particularly in biological areas, where it seems the only hope for obtaining any useful structural as well as dynamical information by solid-state NMR. One example where specific isotope labelling has been used to

great effect is in a study of the α-relaxation process in high-density polyethylene.[19] The α-relaxation process is important for material properties such as creep, annealing and crystallization.[19] The underlying microscopic chain motion is thought to be 180° chain flips, but this has never been determined with certainty because ^{13}C chemical shift anisotropy, geminal ^{1}H–^{1}H dipolar coupling, ^{13}C–^{1}H dipolar coupling and ^{2}H quadrupole coupling are all invariant to 180° flips. As Fig. 9 shows, however, the ^{13}C–^{13}C dipolar coupling does vary with 180° chain flips, and so should monitor such motions in the dipolar coupling powder pattern.

For this reason, the study in question[19] examined a sample of high-density polyethylene that was isotopically labelled with ^{13}C so as to produce isolated ^{13}C spin pairs. Static ^{13}C powder lineshapes were then observed as a function of temperature. Analysis of these by lineshape simulation shows that, indeed, the polyethylene chains do undergo 180° chain flips. The static lineshapes in this case result from the sum of chemical shift anisotropy and dipolar coupling. However, the chemical shift anisotropy is known and, as mentioned previously,

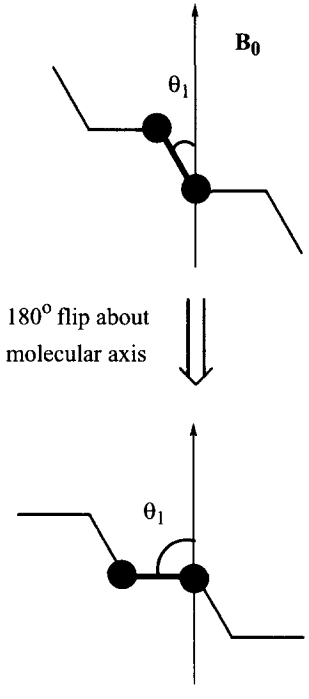

Fig. 9. Schematic illustration of how the strength of ^{13}C–^{13}C dipolar coupling between neighbouring ^{13}C spin pairs in polyethylene changes by virtue of the change in orientation of the ^{13}C–^{13}C vector (described by θ_1 and θ_2) with respect to the applied field, $\mathbf{B}_0$, when the polyethylene chain undergoes a 180° flip about the molecular chain axis.

the chemical shift tensor is unaffected by the chain motion, so only the contribution to the lineshape from dipolar coupling is affected by the motion.

^1H–^1H dipolar coupling lineshapes in organic solids are frequently used as a qualitative monitor of motion in a sample. In a sample with little molecular motion in the tens of kHz frequency range or higher, the ^1H lineshape is simply a broad, Gaussian line; slow-speed magic-angle spinning has little effect on this and very rapid spinning (>30 kHz in general) is needed to produce a high-resolution spectrum.[20] Intermediate spinning rates create sideband patterns consisting of rather broad sideband lines. However, any molecular motion that averages or partially averages the dipolar coupling on the NMR timescale can significantly reduce the ^1H linewidth in static spectra, and produce much sharper sidebands in magic-angle spinning spectra. The problem is that in most organic samples there are several different ^1H sites and, inevitably, the ^1H lines from each overlap. Accordingly, the two-dimensional WISE (wideline spectroscopy) technique[21] has become very popular; in this the ^1H lineshapes are separated according to the isotropic chemical shifts of the ^{13}C they are bonded to. This is achieved by the pulse sequence shown in Fig. 10. By keeping the cross-polarization step in this pulse sequence very short, ^1H magnetization is transferred only to the closest, i.e. the bonded, ^{13}C spins. One slight difficulty with this experiment is the fact that any molecular motion in the sample has the effect of reducing ^1H–^{13}C dipolar coupling, and yet it is this very coupling that mediates the cross-polarization used in the WISE experiment. Accordingly, it is

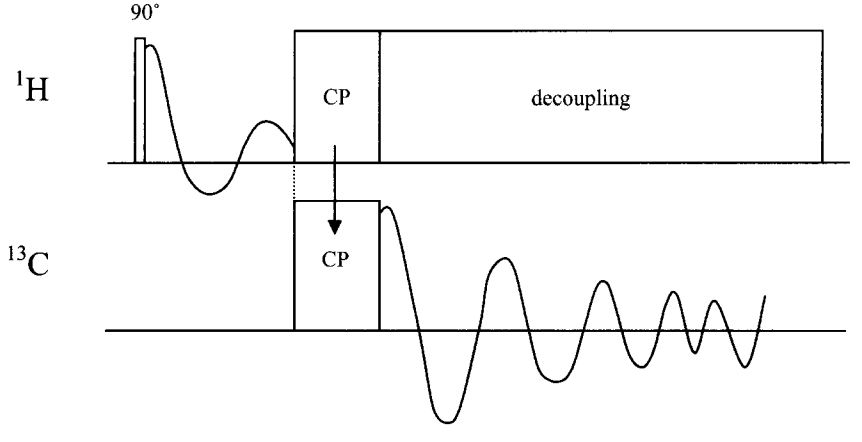

Fig. 10. The pulse sequence for the WISE experiment.[21] This two-dimensional experiment separates ^1H wideline spectra according to the isotropic ^{13}C chemical shift of the ^{13}C each ^1H is bonded to. An initial ^1H 90° pulse creates transverse ^1H magnetization that is allowed to evolve in t_1. A short cross-polarization step then transfers the remaining ^1H magnetization to the nearest ^{13}C spin, i.e. the bonded one. The resulting ^{13}C transverse magnetization is then allowed to evolve in t_2 under magic-angle spinning, where an FID is recorded.

found that the ^1H intensities in a WISE spectrum are not quantitative if there is some motion in part of the sample.[22] Nevertheless, the WISE experiment has been used extensively in studies of dynamics in polymers and biological systems, as is discussed in Sections 5 and 6. A slight variation in the WISE experiment has recently been proposed;[23] instead of separating the ^1H wideline spectra according to the ^{13}C chemical shift of the bonded ^{13}C, they can be separated according to the isotropic ^1H chemical shift.[16] This is done using combined magic-angle spinning and multiple pulse sequences (CRAMPS) in the t_1 dimension of the two-dimensional experiment, so as to produce a high-resolution ^1H spectrum in the corresponding f_1 dimension, while recording the ^1H wideline spectra in t_2 as usual.

A new twist on the dipolar coupling theme is to measure double-quantum spectra for spin-$\frac{1}{2}$ nuclei in a two-dimensional experiment under rapid magic-angle spinning.[24] This is particularly useful in systems where the nucleus of interest is abundant, as the double-quantum excitation necessarily picks out spin *pairs* for study, even though these spins may be part of a much bigger spin system. Very fast magic-angle spinning removes the effect of dipolar coupling in the single-quantum dimension of the two-dimensional experiment.[24] Double-quantum coherence is excited in this experiment using one of various dipolar recoupling pulse sequences, which all have the effect of preventing the averaging of the dipolar coupling by the rapid magic-angle spinning. Double-quantum experiments of this type may be used to measure the dipolar coupling between pairs of spins; this is done by simulation of the spinning sideband patterns that appear in the double-quantum dimension of the spectrum.[25] Rapid molecular motion in a sample reduces the dipolar coupling by a factor that depends on the geometry of the molecular motion relative to the internuclear vector defining the dipolar coupling. Thus, the geometry of rapid molecular reorientations can be determined by first measuring the dipolar coupling under conditions of very slow motion, or no motion, and then re-measuring at higher temperature in the regime of very rapid motion. This technique was used on hexabenzocoronene, which forms a columnar liquid-crystal phase (Fig. 11).[26] The $^1H-^1H$ dipolar coupling between the aromatic ^1H spins indicated in Fig. 11 was measured using double-quantum spectroscopy in the solid state where the molecules are near stationary. The same experiment repeated on the liquid-crystal phase yielded a dipolar coupling constant that was a factor of 0.4 smaller than the solid-state value, indicating that the molecules undergo rapid motion in the molecular plane, plus some additional, unidentified motion.

An interesting use of dipolar coupling to study molecular motion is in the dipolar dephasing, or dipolar filter, experiment.[27] This experiment is used predominantly to examine quaternary ^{13}C in organic samples. After cross-polarization from ^1H to ^{13}C, the ^1H decoupling is interrupted for a period of tens of microseconds before the ^{13}C FID is acquired. During the period of interrupted decoupling, the ^{13}C signals from ^{13}C spins bonded to ^1H spins

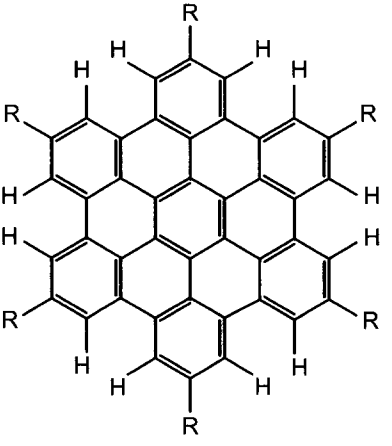

Fig. 11. The molecular structure of hexabenzocoronene.

dephase under the influence of the $^{1}H-^{13}C$ dipolar coupling. Only those ^{13}C spins without bonded ^{1}H then appear in the final ^{13}C spectrum. However, ^{13}C spins with bonded ^{1}H, where the $^{13}C-^{1}H$ internuclear vector is involved in some reorientation process such that the $^{13}C-^{1}H$ dipolar coupling is at least partially averaged away, also appear. One particularly good use of this experiment is in the study of the pyridine molecular reorientation in the tri-*o*-thymotide–pyridine clathrate compound.[28] Here a dipolar dephasing ^{13}C NMR experiment showed only a slight reduction in intensities of the pyridine *ortho* and *meta* ^{13}C signals compared with the normal cross-polarization spectrum, whereas the *para* ^{13}C signal showed a pronounced loss of intensity. Thus, the motion of the pyridine ring affects the $^{1}H-^{13}C$ internuclear vector for the *ortho* and *meta* carbons, but not that for the *para* carbon. Thus, the motion must consist of rotation about the molecular twofold axis. This information was then used as the starting point for a detailed ^{2}H lineshape analysis of fully deuterated pyridine in the clathrate.

2.4. Quadrupolar lineshape analysis – ^{2}H NMR

Although there are many quadrupolar nuclei (some 75% of NMR-active nuclei in fact), very few have been used in molecular motional studies except ^{2}H. In contrast, ^{2}H has been, and will almost certainly continue to be, used extensively in molecular motion studies. This spin-1 nucleus gives rise to quadrupole coupling constants in the range 160–220 kHz in most organic solids. Its static quadrupole-broadened powder patterns are thus sensitive to motions with rates in the range $10^{4}-10^{7}$ Hz, which makes them ideal for studying a large range of motions in solids. ^{2}H quadrupole powder patterns are generally fairly

straightforward to record, a solid or quadrupole echo ($90^\circ_x - \tau - 90^\circ_y - \tau$–FID) normally being used to circumvent receiver dead time problems. In later sections, it will be seen that ^{2}H static lineshape analysis has been applied to polymers, biological macromolecules, adsorbed species in porous solids and organometallics. Magic-angle spinning ^{2}H NMR is also being used nowadays; it has the advantage of giving better signal-to-noise by virtue of concentrating the intensity into sharp spinning sidebands rather than smearing it out over a whole powder pattern. Magic-angle spinning has the added advantage that ^{2}H signals from different sites may be resolved.[29,30] In the past, simulations of MAS spectra were considered prohibitively slow for MAS to be used routinely in motional studies. However, the average desktop computer now has quite sufficient power to run ^{2}H MAS spectral simulations in an acceptable time, so it can be expected that MAS will become the method of choice more often in the future. One particular study investigates the use of ^{2}H MAS NMR spectroscopy to study multiaxial rotations or composite motions.[31] A theoretical formalism is developed to allow the effects of RF pulses to be accounted for, and computationally efficient algorithms are proposed for the necessary time and powder integrations.

An experimental advance for the recording of ^{2}H powder lineshapes is the use of the quadrupolar Carr–Purcell–Meiboom–Gill (QCPMG) pulse sequence.[32,33] This pulse sequence is shown in Fig. 12. It consists of a standard quadrupole echo pulse sequence, after which the echo decay is recorded (step 1). Following this is a series of refocusing 90° pulses, with a complete echo being recorded after each (step 2). Finally, any remaining signal is allowed to decay and is again recorded (step 3). The complete time domain series resulting from the outputs of steps 1, 2 and 3 strung together is then Fourier transformed. This experiment has the effect of splitting the quadrupole echo powder pattern into a manifold of spin-echo sidebands separated by $1/\tau_a$ (see Fig. 12 for definition of τ_a). This in itself generates a sensitivity enhancement of an order of magnitude. Moreover, both the envelope of the spin-echo sidebands and their individual lineshapes contain information on molecular motions. It is once again obtained by simulating the spectrum for particular motional models, but the initial study[32] shows that the dynamic range of the experiment is at least two orders of magnitude larger than the conventional quadrupole echo experiment. The full dynamic range is 10^2–10^8 Hz, that is it is sensitive to motions that are both slower and faster than those that the quadrupole echo experiment can monitor. Sideband shapes tend to monitor the lower end of this range, while the overall sideband envelope is sensitive to higher-frequency motions. Some example spectra recorded using this technique are shown in Fig. 13.

In the review period there have been several papers on ^{2}H lineshape analysis. One of the most important is that discussing the validity of Markov models for modelling molecular dynamics[6] discussed previously. Another important paper discusses the effect of dipolar coupling on ^{2}H lineshapes, with particular emphasis on ND and ND_2 groups.[34] The effect of any dipolar

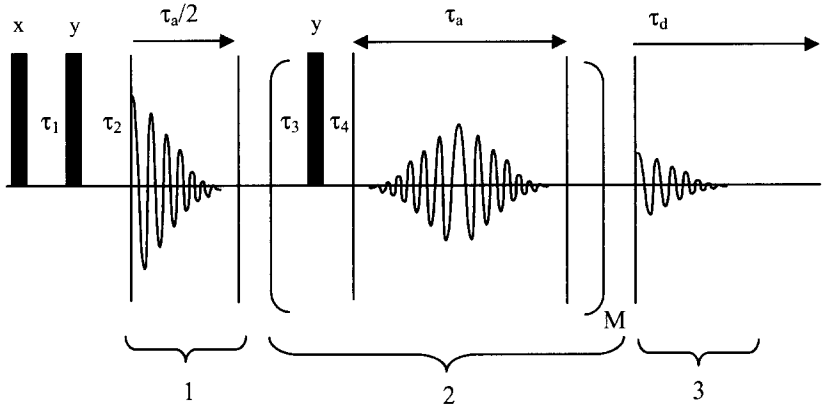

Fig. 12. The quadrupolar Carr–Purcell–Meiboom–Gill (QCMPG) pulse sequence[32,33] for recording ^{2}H NMR spectra. Use of this sequence gives ^{2}H spectra that are sensitive to molecular motions over a much wider frequency range than static or magic-angle spinning ^{2}H spectra. The final FID from the experiment is the results from steps 1, 2 and 3 strung together in a single time domain series; the FIDs are collected between the vertical line in the diagram for periods $\tau_a/2$, τ_a and τ_d, respectively, in steps 1, 2 and 3. All pulses are 90° pulses with the phases given in the diagram. The echo delays τ_1 and τ_2 are approximately equal, with τ_2 being adjusted so that the acquisition in step 1 begins exactly at the echo maximum. Step 2 is repeated M times and consists of M refocusing 90° pulses with collection of the resulting echo FID after each. τ_3 and τ_4 are short delays designed to protect the receiver from the 90° pulses in step 2.

coupling on ^{2}H NMR spectra is usually accounted for in simulations by including a Gaussian line broadening, which is considered to be orientation independent. This approach is sufficient if the dipolar coupling is too small to affect the ^{2}H T_2 anisotropy. However, for ^{2}H spins directly bound to ^{14}N, the dipolar coupling is generally too big for this to be the case. ^{14}N spin–lattice relaxation will then contribute to the ^{2}H T_2 anisotropy, affecting both the quadrupole echo intensity (in a quadrupole echo experiment), *and* the resulting ^{2}H lineshape. The paper[34] uses calculations of the spin density operator for two dipolar-coupled spin-1 nuclei and takes into account ^{14}N spin–lattice relaxation effects to simulate ^{2}H lineshapes and relative echo intensities for the ND_2 group in *p*-nitroaniline-*N*,*N*-d_2. This work clearly shows that for longer echo delays ($2\tau > 80$ μs), the effects of dipolar coupling must be taken into account. This is the first time dipolar relaxation of the second kind (as designated by Abragam[4]) in solids has received a detailed treatment. With the increasing emphasis on isotopically labelled biological samples, where ND_n groups may become common, considerations of this kind are likely to be most important.

The effect of chemical shift anisotropy on ^{2}H powder lineshapes has also been discussed.[35] Another study emphasizes the importance of recording ^{2}H

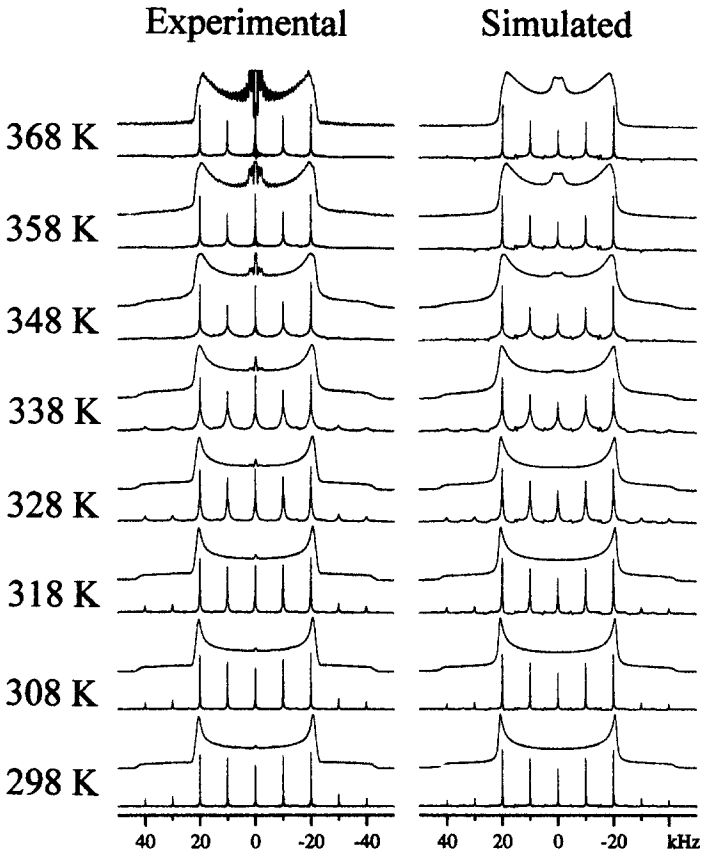

Fig. 13. ^{2}H NMR spectra of DMS recorded with the QCMPG pulse sequence (see Fig. 12) at the temperatures shown, from reference 33. For each temperature, the normal quadrupole echo ^{2}H spectrum is shown above the QCMPG spectrum for comparison. Also shown are simulated quadrupole echo and QCMPG spectra, also taken from reference 33.

quadrupole echo FIDs from the exact echo maximum;[36] mis-setting the start of the FID away from the echo maximum can severely distort the resulting ^{2}H powder pattern, as is now well known. Unfortunately, this work does not suggest a remedy for this problem, though it does show how the distorted powder patterns can be mistakenly simulated with alternative motional models rather than the 'correct' one.

Resolution of ^{2}H powder pattern lineshapes can be a problem in uniformly or multiply labelled samples. In many cases, ^{2}H labelling of specific sites is near impossible, especially in more complex molecules, or in naturally occurring samples. In other cases, it would be excessively time consuming and expensive to specifically label all sites of interest in a molecule, separately in successive

samples. Clearly, some method is needed to resolve ^2H signals from different sites. Magic-angle spinning can be useful, although the chemical shift range of ^2H is very small, so often MAS is not sufficient to resolve different sites. Two possibilities have been proposed for separating ^2H lineshapes in two-dimensional experiments. In the first, ^2H spinning sideband patterns (or static-like powder patterns) are separated according to the double-quantum ^2H chemical shift (Fig. 14).[37] This has the effect of doubling the frequency gap between ^2H signals in the double-quantum dimension over what would occur in a single-quantum spectrum, and so improves the resolution over that in a normal one-dimensional MAS spectrum.

In the second method, static-type ^2H powder patterns are separated according to the ^{13}C chemical shift of the ^{13}C nucleus to which the ^2H is bonded.[38] The pulse sequence is shown in Fig. 15. Initial ^{13}C transverse magnetization is generated by cross-polarization from ^1H. The entire experiment is conducted under magic-angle spinning, which averages the $^{13}C-^2H$ dipolar coupling to zero. It is reintroduced by a series of rotor-synchronized 180° pulses; $2N-2$ 180° pulses are applied in N rotor periods. Thus multiple-quantum coherences involving the ^{13}C and ^2H spins can now be excited, via the agency of the $^{13}C-{}^2H$ dipolar coupling. During the first two rotor periods of the pulse sequence shown in Fig. 15, zero- and double-quantum coherences between ^{13}C and ^2H spins are excited. In the t_1 period, transverse ^2H magnetization is excited and allowed to evolve; in doing so it modulates the

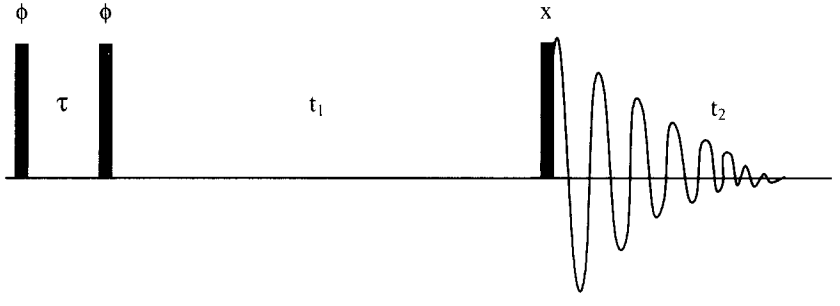

Fig. 14. The pulse sequence for recording the double-quantum ^2H experiment.[37] The entire experiment is conducted under magic-angle spinning. This two-dimensional experiment separates ^2H spinning sideband patterns (or alternatively, static-like ^2H quadrupole powder patterns) according to the ^2H double-quantum chemical shift, so improving the resolution over a single-quantum experiment. In addition, the double-quantum transition frequency has no contribution from quadrupole coupling (to first order) so, the double-quantum spectrum is not complicated by spinning sidebands. Details of molecular motion are then extracted from the separated ^2H spinning sideband patterns by simulation.[37] All pulses in the sequence are 90° pulses with the phases shown (the first two pulses are phase cycled to select double-quantum coherence in t_1). The τ delay is of the order 10 μs. The t_1 period is usually rotor-synchronized.

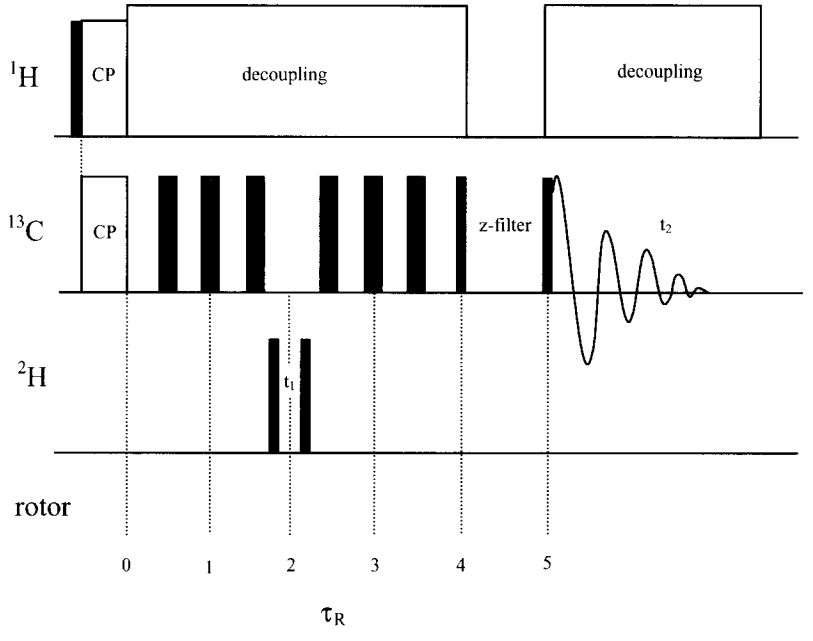

Fig. 15. The pulse sequence for the $^{13}C-^2H$ correlation experiment.[38] This two-dimensional experiment, conducted under magic-angle spinning, separates ^2H lineshapes according to the ^{13}C isotropic chemical shift of nearby ^{13}C spins, i.e. the bonded ^{13}C in practice. The narrow black pulses are 90° pulses; wide ones are 180° pulses. The ^2H pulses are placed symmetrically within the rotor period.

zero- and double-quantum coherences, and this is reflected in the final FID recorded in t_2. During the next two rotor cycles after t_1, the multiple-quantum coherences are reconverted. A z-filter preceding the detection period ensures a purely absorptive spectrum. Only one data set needs to be recorded, as it may be assumed that the f_1 spectrum (^2H dimension) is symmetric about $\omega_1 = 0$, providing of course that ^2H is set on resonance. The whole experiment can be considered as a solid-state HMQC (heteronuclear multiple-quantum correlation) experiment, with added $^{13}C-^2H$ dipolar recoupling during the multiple-quantum excitation and reconversion periods to get over the effects of magic-angle spinning.

3. RELAXATION TIME MEASUREMENTS

Relaxation time measurements have long been used to characterize molecular motions in solids. All nuclear spin relaxation processes are mediated by fluctuating nuclear spin interactions, with the fluctuations (generally) arising

from molecular motion. A very brief description of the theoretical basis for understanding relaxation processes is given here simply to introduce the nomenclature that is used in the rest of this article.

Relaxation is the change in time of the density matrix describing the spin system as the system moves back towards equilibrium from some non-equilibrium state imposed, for instance, by a sequence of radiofrequency pulses.[39] Longitudinal relaxation, for example, restores the populations of the various spin levels to the equilibrium Boltzmann distribution. It thus affects the diagonal elements of the density matrix, which describe the populations of the spin levels.[39] The rate of change of population of any given spin level can be written in terms of the transition rate to that level from all others, and vice versa, in combination with the populations of those spin levels, in the usual manner for any kinetic process. In turn, the transition rate between two levels i and j is given by the golden rule of quantum mechanics:

$$W_{ij} = \frac{1}{\hbar^2} \int_{-\infty}^{+\infty} \langle \mathrm{Tr}\{\tilde{\mathbf{H}}(t+\tau)\}\tilde{\mathbf{H}}(t)\rangle \, \mathrm{d}t \tag{4}$$

where $\tilde{\mathbf{H}}(t)$ is the Hamiltonian matrix in the Zeeman interaction representation, describing the fluctuating nuclear spin interaction acting on the spin system. The time dependence of $\tilde{\mathbf{H}}(t)$ arises from molecular motions and the intrinsic anisotropy (variation with molecular orientation) of the nuclear spin interaction. The Hamiltonian operator in the Zeeman interaction representation is simply

$$\tilde{H} = \exp(-\mathrm{i}H_Z t)H \exp(+\mathrm{i}H_Z t) \tag{5}$$

where H_Z is the Zeeman Hamiltonian and H is the laboratory-frame Hamiltonian describing the nuclear spin interaction. Equation (4) for the transition rate involves the ensemble average over the sample (angle brackets), and the *trace* of the product of Hamiltonian matrices at different times t and $t+\tau$. This latter term is a sum with components of the form $\tilde{H}_{ij}(t+\tau)\tilde{H}_{ji}(t)$, for all i and j, where $\tilde{H}_{ij}$ and $\tilde{H}_{ji}$ are Hamiltonian matrix elements. Many of these terms can be zero. To gain some insight into this sum, we restrict ourselves to consideration to relaxation by dipolar coupling and write the corresponding dipolar Hamiltonian in tensorial form:

$$\tilde{H}(t) = \sum_{M=-2}^{+2} (-1)^M A_{2M}(t)\tilde{T}_{2M} \tag{6}$$

where the $\tilde{T}_{2M}$ are spherical tensor operators and the $A_{2M}(t)$ are components of the nuclear spin interaction tensor expressed in irreducible tensor form,

rather than as a Cartesian tensor and expressed in the laboratory frame.* The time dependence of the Hamiltonian due to molecular motion is expressed through the nuclear spin interaction tensor, which changes as the molecule changes orientation through motion with respect to the applied magnetic field in the NMR experiment. When $\tilde{H}$ is expressed in this form, it is clear that $\tilde{H}$ only has nonzero matrix elements between Zeeman spin levels whose m quantum numbers differ by M, where M is the index in Eq. (6). The nonzero matrix elements of $\tilde{H}$ then depend only on the corresponding A_{2M} and the matrix elements of the $\tilde{T}_{2M}$ operators, which are just numbers. Thus, the integral in Eq. (4) can be rewritten as a sum of integrals[39] labelled $J_M(M\omega_0)$ where

$$J_M(M\omega_0) = \int_0^\infty \exp(-iM\omega_0 t) C_M(t)\, dt \tag{7}$$

in which M is restricted to 0, 1, 2, i.e. $|M|$ and $C_M(t)$ is a correlation function describing the time dependence of the nuclear spin interaction, i.e. the molecular motion. The frequency ω_0 is the Larmor frequency arising from the Zeeman interaction (in the case of longitudinal relaxation). The function $J_M(M\omega)$ is a *spectral density* function. The correlation function $C_M(t)$ is given by

$$C_M(t) = \langle A_{2M}(0) A^*_{2M}(t) \rangle - |\langle A_{2M}(0) \rangle|^2 \tag{8}$$

The spectral density is a measure of the amplitude of the M-quantum component of the nuclear spin interaction oscillating at frequency $M\omega_0$ as a result of molecular motion.

In summary, then, all relaxation processes can ultimately be described as some linear combination of such spectral density functions. We have here only explicitly considered longitudinal relaxation processes in the laboratory frame, but a similar case can be made for transverse relaxation, relaxation processes in the rotating frame and cross-relaxation processes. The spectral densities

* The nuclear spin interaction tensor is most readily expressed in its *principal axis frame* where only the $M = 0, \pm 2$ terms are nonzero (and only the $M = 0$ term is nonzero for axial symmetry). It can then be expressed in the laboratory frame via

$$A_{2M} = \sum_{M' = 0, \pm 2} D^{(2)}_{MM'}(\alpha, \beta, \gamma) \rho_{2M'}$$

where $\rho_{2M'}$ is the interaction tensor in its principal axis frame and α, β, γ are the Euler angles relating the principal axis and laboratory frames; $D^{(2)}_{MM'}(\alpha, \beta, \gamma)$ are Wigner rotation matrix elements.

involved are, in each case, $J_M(M\omega)$ where ω is the frequency of the M-quantum transition involved in the relaxation process, whatever it may be – Larmor frequencies in the case of longitudinal relaxation. In transverse relaxation processes, the transitions involved include zero-quantum transitions, and their respective frequencies then appear in the relevant spectral density. In rotating frame relaxation, the transitions involved are those in the rotating frame, and so the corresponding transition frequencies are the nutation frequencies of the relevant nuclei. Hence, longitudinal relaxation processes are sensitive to molecular motions of the order of the Larmor frequency (generally tens to hundreds of MHz). In contrast, transverse relaxation processes are sensitive to very low-frequency motions, of the order of zero-quantum transition frequencies. Rotating frame relaxation processes fall somewhere between the two, being sensitive to motions in the region of the nutation frequency of the particular nuclear spin under a spin-locking pulse, generally tens to a few hundred kHz. Thus, a very wide range of motional frequencies may be studied by choosing different relaxation processes to monitor the motion.

In analysing relaxation data, the dominant nuclear spin interaction effecting relaxation must be known, and it must exceed other effects by at least an order of magnitude, otherwise the data become extremely complex to interpret. Accordingly, relaxation times studies are often applied to ^{2}H, where the dominant relaxation mechanism is nearly always through quadrupole coupling. In other cases, nuclei with ^{1}H bonded to them often have a dominant mechanism involving dipolar coupling with the ^{1}H (providing that the chemical shift anisotropy associated with that nucleus is small), owing to the particularly large magnetic moment of ^{1}H.

In the review period, ^{2}H relaxation studies received much more attention than previously. In particular, the anisotropy (i.e. dependence on molecular orientation) in the relaxation of Zeeman order (as described by the parameter T_{1Z}) and quadrupolar order (as described by the parameter T_{1Q}) has been used with good effect to study fast molecular motions in solids.[40–42] T_1 anisotropy for ^{2}H has been used before in a two-dimensional experiment[43] where the full T_1 anisotropy is displayed in one dimension of the experiment (T_2 anisotropy was dealt with similarly.[43]) In this early work, the full two-dimensional spectrum was simulated according to given motional models and molecular jump rates and was compared with experiment. However, the fitting of a two-dimensional contour plot or surface plot is notoriously difficult and perhaps it is for this reason that the technique has never been taken up in this form by other spectroscopists. In the recent studies of ^{2}H T_{1Z} and T_{1Q} anisotropy, the approach has been slightly different. The procedure in the analysis of the relaxation rate anisotropy is to calculate the spectral density functions (Eq. (7) above) for given motional models and given molecular jump rates as in the early study.[43,44] From the spectral densities, it is then straightforward to calculate the partially relaxed ^{2}H spectral lineshapes for the particular inversion-recovery delays used in the experiment. A good fit of the partially

relaxed lineshapes then implies that the motional model and jump rate are possible descriptions of the true motion in the sample. In a study of the methyl group rotation in methyl-deuterated bisphenol-A polycarbonate at 30 °C, it was found that while the T_{1Z} anisotropy could be reproduced by several different motional models, the combination of T_{1Z} and T_{1Q} anisotropy could only be reproduced by a single model. This was a three-site jump model, with an activation energy of 19.2 ± 2 kJ mol^{-1} and a jump rate of $(2.9 \pm 0.2) \times 10^8$ Hz at 30 °C.[41] This same work highlights that when the molecular motion is slow enough to affect the ^{2}H powder pattern lineshape, Redfield theory is not valid for calculating relaxation times and the stochastic Liouville equation must be used. In this regime, however, both the lineshapes and the orientation dependence of the relaxation times are sensitive to details of the molecular motion, allowing very accurate determinations. An earlier study[42] used a similar mode of analysis to examine the overall motion of the methyl groups in fully deuterated hexamethylbenzene. This study again concluded that the combined use of T_{1Z} and T_{1Q} anisotropies allowed for unambiguous analysis of the motion in terms of a combined whole-molecule rotation about the molecular hexad axis and methyl group rotation.

Another study[45] used the ^{2}H T_{1Z} anisotropy of CD_3 groups in 6-*s*-*cis*-retinoic acid, in 6-*s*-*trans*-retinoic acid (Fig. 16a) and in the membrane protein bacteriorhodopsin regenerated with CD_3-labelled retinal (Fig. 16b) to examine the motion of the CD_3 groups. It was found that for both forms of retinoic acid, a three-site hopping model fitted the experimental data, but with the difference that the activation energy for the *cis* isomer was 14.5 ± 1 kJ mol^{-1} whereas for the

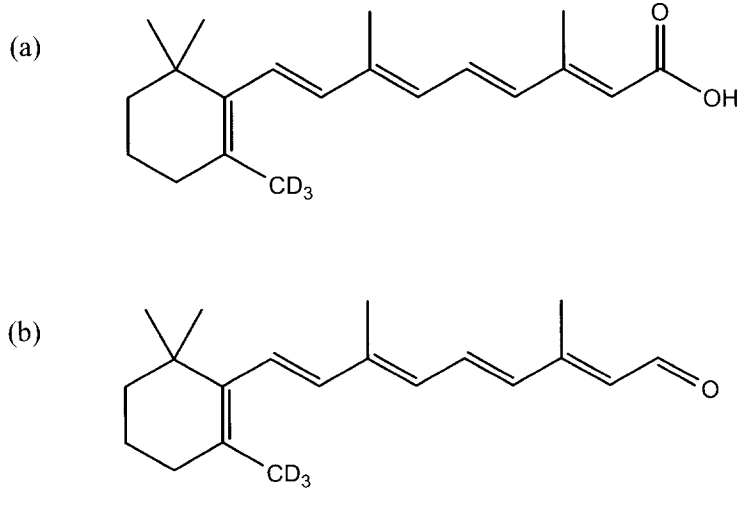

Fig. 16. The molecular structures of (a) 6-*s*-*trans*-retinoic acid and (b) CD_3-labelled retinal.

trans isomer it was only 5 ± 1 kJ mol^{-1}. The question the work aimed to answer was what isomer of the related molecule, retinal, is present in bacteriorhodopsin. Analysis of the T_{1Z} anisotropy for the CD_3-labelled retinal in bacteriorhodopsin produced an activation energy for the methyl group rotation of around 9 kJ mol^{-1}, which suggested that it was the *trans* isomer of retinal that was present. This study therefore solved a structural problem by examining the dynamics of a pertinent functional group, in a rather unique fashion.

Selective inversion recovery experiments i.e. only select frequencies within the powder pattern are excited, have also been performed on ^{2}H for the purposes of studying molecular motion. Initial experiments were performed on deuterated dimethylsulfone (DMS) to demonstrate the utility of the experiment.[46] Selective inversion recovery curves were fitted to a suitable motional model, a two-site jump model in the case of DMS, to yield the motional rates as a function of temperature. A significant feature of this work is that the activation energy for the motion so obtained differs markedly from that obtained from earlier ^{13}C chemical shift anisotropy lineshape studies.

Selective inversion is not straightforward for a powder sample for a spin-1 system suffering quadrupolar broadening. This problem was addressed in a further paper,[47] which proposed the use of double sideband modulated pulses. If only the $\omega_0 + \omega_Q$ or $\omega_0 - \omega_Q$ transition is excited, where ω_0 is the Larmor frequency and ω_Q is the quadrupolar frequency for a given molecular orientation, then both Zeeman and quadrupolar order are created. Subsequent hard detection pulses in the inversion recovery experiment then mix the Zeeman and quadrupolar order, giving an apparent decrease in the selective inversion efficiency by a factor of 4.[47] To avoid this, one must simultaneously irradiate at $\omega_0 \pm \omega_Q$; hence the need for double-sideband modulated pulses. The frequency-selective profile is then improved by shaping the RF pulses.[47] The selection of pulse shape in this case is limited by the short and anisotropic T_2 for ^{2}H and the effects of exchange during the pulse. Consequently, it is most desirable to use pulse shapes with low bandwidth–duration product.

A novel use of relaxation time studies was the examination of ultrafast ^{1}H transfer in polycrystalline dimethyldibenzotetraaza[14]annulene (Fig. 17), using ^{1}H relaxation.[48] The rates of ^{1}H transfers in this and related compounds in the solid state, in the millisecond to nanosecond timescale, were derived by analysis of the spin–lattice relaxation times, T_1, of heteronuclei located in such a way that their interaction with the mobile ^{1}H is modulated by the transfer process. The work includes a theoretical description of the heteronucleus T_1 derived for the cases of static powders, powders under magic-angle spinning and samples where spin–lattice relaxation is isotropically averaged by magnetization transfer. In the example shown in Fig. 17, a ^{15}N cross-polarization, magic-angle spinning T_1 study was used to determine the rate of ^{1}H transfer.

Finally, Spiess and co-workers[49] have shown how the nuclear Overhauser effect (NOE) can be used to study motions in soft solids, such as amorphous polymers. ^{1}H–^{1}H dipolar coupling is already partially removed in such samples

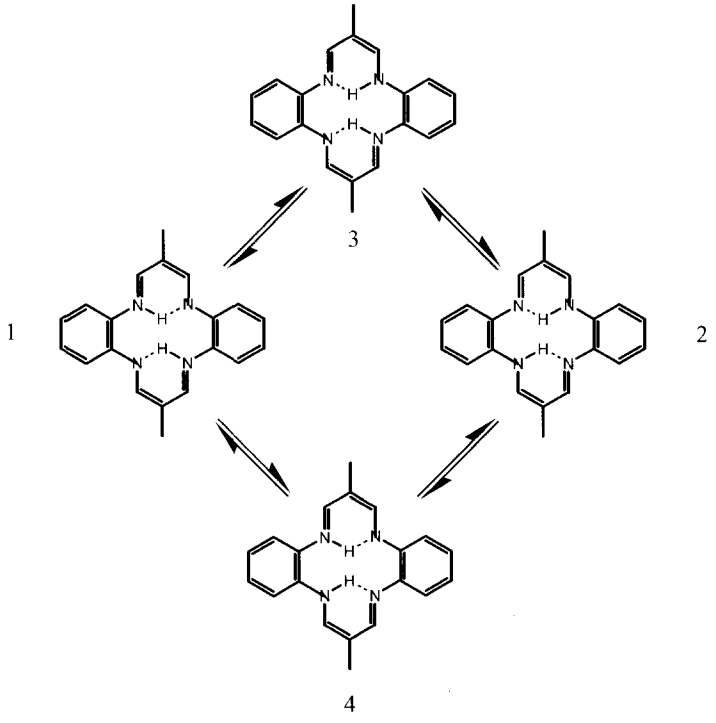

Fig. 17. The molecular structure of dimethyldibenzotetraaza[14]annulene and the proton rearrangement deduced from ^{15}N T_1 relaxation studies.[48]

by the presence of considerable molecular motion; magic-angle spinning at relatively slow rates (<10 kHz) is usually sufficient to remove what residual couplings are left. Then, any cross-peaks that appear in a two-dimensional NOESY experiment, for instance, are due only to cross-relaxation between spins via the dipolar coupling mechanism. If the experiment is performed without magic-angle spinning, then residual dipolar couplings promote a coherent magnetization exchange that dominates the cross-peak intensity for short mixing times, and short mixing times are most desirable in a NOESY experiment, as the resulting data are much easier to analyse quantitatively in this region. The work[49] determines expressions for the rate constants for cross-relaxation between spins in terms of the transition rates between coupled spin levels; of particular note is that zero-quantum transition rates, which always contribute to cross-relaxation rate constants, depend on spectral densities at the sample spinning speed, i.e. on $J_M(M\omega_R)$ where ω_R is the spinning speed. Thus, not surprisingly, the cross-relaxation rate curves derived experimentally from two-dimensional NOESY spectra (see Fig. 18 for the pulse sequence used) for synthetic rubber SBR 1500 (poly(styrene-co-butadiene); 23.5%

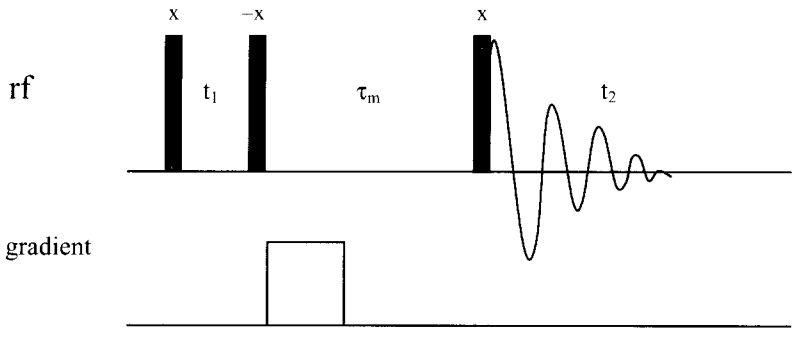

Fig. 18. The pulse sequence used for the two-dimensional NOESY experiment for measuring $^1H-^1H$ cross-relaxation rates in soft polymers. The entire experiment is conducted under magic-angle spinning. Gradient pulses are used to remove unwanted coherences, as this allows for much faster experiments than phase cycling.

styrene, 76.5% butadiene distributed in random sequence) are found to be sensitive to molecular motions with rates of the order of the spinning speed. Three-dimensional NOESY spectroscopy is used to examine two-step cross-relaxation processes.[49] In both the two- and three-dimensional experiments, gradient pulses are used during the mixing times (Fig. 18) to get rid of unwanted coherences, allowing much faster experiments than those with phase cycling.

4. EXCHANGE EXPERIMENTS

4.1. Basics

Exchange experiments are invaluable for studying slow molecular motions (with correlation times of the order of milliseconds or slower) in solids,[20] and accordingly have seen many applications in polymers, for instance, as discussed in Section 5. The essential concept of a two-dimensional exchange experiment is straightforward and is illustrated in Fig. 19.

Transverse magnetization is created by an initial 90° pulse or cross-polarization step and allowed to evolve during the period t_1 under its characteristic frequency ω_1. This characteristic frequency arises from the nuclear spin interaction that operates during t_1. At the end of t_1, the magnetization is stored along z (the direction of applied magnetic field in the NMR experiment) for a period τ_m, the mixing time, during which molecular dynamical processes may occur. Finally, the magnetization is returned to the transverse plane, where it again evolves under its characteristic frequency, this time ω_2, the evolution being recorded as a FID. Appropriate processing[20] of the resulting two-dimensional time domain datasets yields a two-dimensional frequency

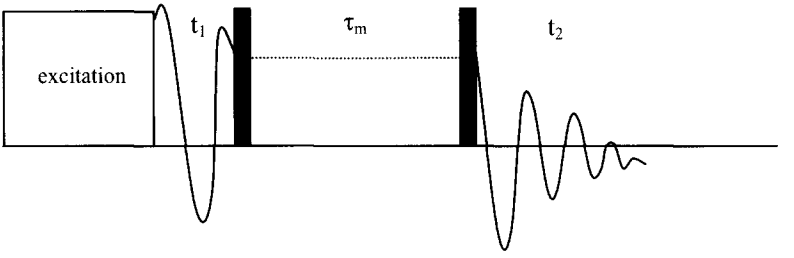

Fig. 19. Schematic diagram of a two-dimensional exchange experiment. It may be conducted under magic-angle spinning or on static samples. An initial excitation period (90° pulse or cross-polarization) creates transverse magnetization on the spin of interest, which then evolves at its characteristic frequency during t_1. A pulse (90° for spin-$\frac{1}{2}$ or 54.7° for spin-1) then stores the magnetization along z (the applied magnetic field direction) for a mixing time τ_m, during which the spin may be involved in some motional/exchange process that changes its resonance frequency. A further pulse (again 90° for spin-$\frac{1}{2}$ or 54.7° for spin-1) at the end of the mixing time then re-creates transverse magnetization, which now precesses at the new resonance frequency in t_2, while an FID is recorded. The correlation time for the motion may be determined by repeating the two-dimensional experiment for different mixing times, τ_m.

correlation spectrum, correlating the characteristic frequency the spin had during t_1 with that it subsequently had in t_2. If molecular reorientation or site exchange has occurred during the mixing time (which happens if the correlation time for the motion, $\tau_c < \tau_m$), the resonance frequency after the mixing time, ω_2 is different from the initial frequency before molecular reorientation/exchange, ω_1, and so the two-dimensional frequency spectrum contains off-diagonal intensity at (ω_1, ω_2). If there is no exchange during the mixing time, $\omega_1 = \omega_2$ ($\tau_c \gg \tau_m$), and spectral intensity appears only along the diagonal of the two-dimensional frequency spectrum. Analysis of the resulting spectrum in terms of molecular motion clearly relies on the resonance frequencies ω_1 and ω_2 being constant during the t_1 and t_2 periods, respectively, that is on there being no molecular motion during these periods. It is for this reason that exchange experiments are only suitable for studying slow molecular motions. By assessing the exchange intensity as a function of mixing time (with $\tau_m \gg t_1, t_2$), the correlation time for the motion can be determined; the pattern of exchange intensity in the two-dimensional frequency spectrum allows the geometry the motion to be determined. A key feature here is that motional models are *not* required to extract this latter information, in contrast with lineshape analyses and relaxation time studies.

For the most part, exchange experiments in the solid state use either chemical shift anisotropy (for spin-$\frac{1}{2}$) or quadrupole coupling (for spin $> \frac{1}{2}$) under static conditions, i.e. no sample spinning, to generate frequencies ω_1 and ω_2 that depend on molecular orientation. The projections onto the two spectral frequency axes are then the corresponding powder patterns resulting from the

particular anisotropic spin interaction. The resulting two-dimensional spectrum is, in effect, a correlation map between the molecular orientations in t_1 and t_2. Although chemical shift anisotropy and quadrupole coupling are most commonly used in exchange experiments, any anisotropic nuclear spin interaction can be employed. In one example, Schmidt-Rohr *et al.* used the dipolar coupling between isolated pairs of ^{13}C spins in high-density polyethylene to label the frequencies in t_1 and t_2.[19] The experiment used static conditions and refocused the ^{13}C chemical shift anisotropy, so that the two-dimensional exchange spectrum relied exclusively on the $^{13}C-^{13}C$ dipolar coupling. This work also included analysis of the experiment in terms of the time-evolution of a density operator expanded as Cartesian operators.

High-resolution two-dimensional exchange experiments can be performed in the solid state in analogous fashion to solution-state exchange experiments by conducting the experiments (for spin-$\frac{1}{2}$) under rapid magic-angle spinning. These experiments monitor only chemical exchange, where the site exchange is accompanied by a change of isotropic chemical shift. Such experiments are generally much simpler to perform and to analyse than the static experiments, but obviously their field of application is much smaller, and consequently there are fewer studies of this type. One useful example in the review period concerns the dynamics of $E(SiMe_3)_4$, E = C, Si, in their low-temperature phases.[50] In these phases, both molecules crystallize in the $P2_13$ space group with the molecules centred at sites of C_3 symmetry. There are two possible dynamical processes available to the molecules in this phase: (i) internal reorientation of the $Si(Me)_3$ groups around the E–Si bonds and (ii) whole-molecule jumps about molecular axes that coincide with the E–Si bonds. The molecular symmetry means that there are two different ^{29}Si sites, in ratio 1 : 3 (see Fig. 20) and four different ^{13}C sites (labelled 1–4 in Fig. 20) with equal populations. These different sites are easily resolved via their isotropic chemical shifts in their respective NMR spectra. Two-dimensional MAS exchange ^{29}Si and ^{13}C spectra were obtained for each compound at low temperature. The ^{29}Si spectra necessarily report only on whole molecule rotations, as local rotations of the $Si(Me)_3$ groups do not affect the ^{29}Si isotropic chemical shift, and so cannot produce any exchange intensity. At slightly raised temperatures, for long mixing times, both compounds show ^{29}Si exchange intensities that correspond to complete four-site exchange (i.e. whole-molecule jumps about all E–Si axes), namely diagonal intensities for the two ^{29}Si resonances in the ratio 1 : 9, and off-diagonal intensity of relative intensity 3. The ^{13}C two-dimensional MAS exchange spectrum can be affected by both whole-molecule jumps and local rotations about the E–Si bonds. At the lowest temperature of observation, the E = Si compound shows ^{13}C exchange only between methyl groups 1, 2 and 3 (see Fig. 20 for methyl group labelling), which corresponds to local rotations about the E–Si bonds interchanging these methyl groups. Only as the temperature is raised is exchange between all four methyl sites observed. In the E = C compound, however, exchange between all four methyl groups

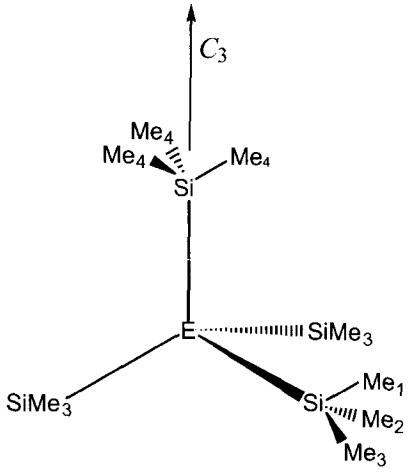

Fig. 20. The molecular structure of $E(SiMe_3)_4$, where E = Si, C. The molecule has a threefold axis of symmetry as indicated, giving two different $^{29}SiMe_3$ sites, and four different $^{13}CH_3$ sites in the absence of any molecular motion.[50]

(whole-molecule jumps) is observed at all temperatures of observation. The combination of ^{29}Si and ^{13}C exchange NMR thus serves to separate the two possible molecular motions so that each may be analysed.

In static exchange experiments, powder pattern lineshapes are recorded indirectly in t_1 and directly in t_2. The simple three-pulse exchange experiment (Fig. 19) can lead to rather distorted two-dimensional spectra as a result of truncation of the t_1 and t_2 signals, through dead-time problems (t_2) or finite pulse lengths (t_1), preventing spectra with t_1 and t_2 truly equal to zero from being recorded. These truncations lead to frequency-dependent phase distortions in the respective spectral dimensions. In principle, these could be corrected by first-order phase corrections, *providing that the loss of information arising from the truncation is not too great.* In practice, for the wider powder lineshapes arising from ^2H quadrupole coupling, for instance, such corrections are not effective. Instead, datasets from t_1, $t_2 = 0$ are produced by interpolating the experimentally obtained signal and extrapolating back to zero.[20] This is not a simple procedure, however, and requires some experience if undistorted spectra are to be obtained. More recently, a five-pulse sequence has been introduced for ^2H exchange experiments[51] to avoid the truncations in the first place, so greatly simplifying the data processing. The five-pulse sequence (Fig. 21) differs from the simple three-pulse sequence by the addition of two $\tau - 90° - \tau$ echo sequences, one prior to t_1 and the other prior to t_2, to circumvent dead-time and finite pulse width problems. Then, the acquisition of the FID can be set to begin exactly at $t_2 = 0$, and likewise the pulse that defines the beginning of the mixing period can be set exactly on top of the first echo to

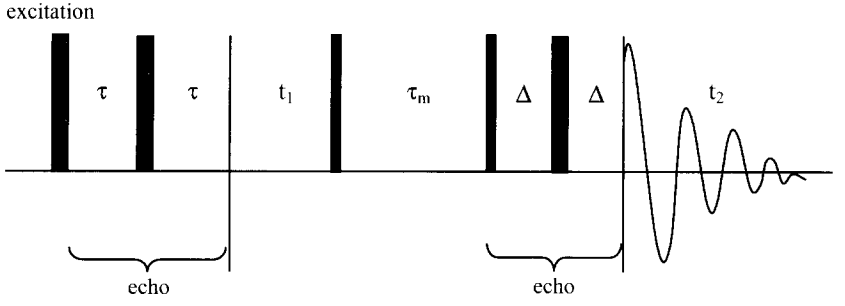

Fig. 21. The new five-pulse sequence for recording static ^{2}H exchange spectra.[51] The experiment differs from the simple three pulse sequence in Fig. 19 in the addition of $\tau - 90° - \tau$ (or $\Delta - 90° - \Delta$) echo sequences before the t_1 and t_2 periods to avoid spectral distortions caused by receiver deadtime and finite pulse width problems. The broader pulses are 90° pulses; the narrower ones 54.7° pulses.

acquire a $t_1 = 0$ spectrum. The necessary minimum phase cycling for the new five-pulse experiment is also deduced in this work.[51]

4.2. Higher-dimensional exchange spectra

Three-dimensional and higher dimensional exchange spectra can be recorded by simple extensions of the basic two-dimensional pulse sequence[20] (Fig. 22). The resulting multidimensional frequency spectra then correlate the molecular orientation at three (or more for higher-dimensional spectra) points in time.

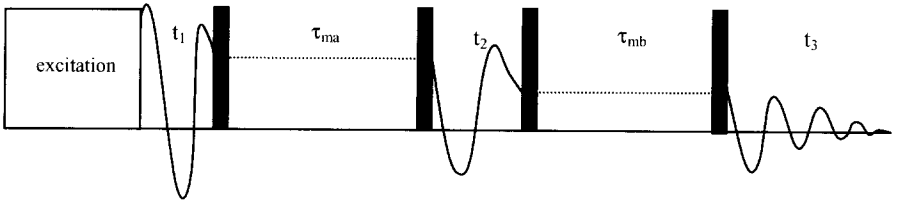

Fig. 22. The basic form of a three-dimensional exchange pulse sequence. This has the same form as the two-dimensional sequence in Fig. 19, but with the addition of a further mixing time τ_{mb} and evolution period, t_3. The resulting three-dimensional spectrum then correlates the spin's resonance frequency (and through this, its position) at three different points in time, t_1, t_2 and t_3, with motion potentially occurring during the (much longer) intervening mixing times, τ_{ma} and τ_{mb}. The pulses after the excitation sequence move the magnetization to and from the z axis (applied magnetic field direction) as appropriate through the pulse sequence; thus they are 90° pulses for spin-$\frac{1}{2}$ systems and 54.7° pulses for spin-1.

This allows assessment of the degree to which different motions or molecular jumps are correlated in time. An eight-pulse experiment has been proposed[51] for three-dimensional ^2H exchange experiments, incorporating echo steps in analogous fashion to the five-pulse sequence for two-dimensional exchange. The generation of pure absorption mode three-dimensional ^2H exchange spectra is also discussed; here it is most important that spectral distortions arising from truncation of the time domain data are avoided.[51]

Three-dimensional exchange spectroscopy is very useful in heterogeneous systems, such as glasses, where there is a broad distribution of molecular motions present. In such systems, there are often small-angle and large-angle jump motions present simultaneously, and it is important when understanding the material properties of the systems to know how these motions are correlated. A two-dimensional exchange spectrum can reveal that both types of motion are present in the system but can give no information on how they occur over a sequence of time. In other words, it cannot answer the question whether some parts of the system undergo small-angle jumps exclusively and others large angle-jumps, or whether those parts that undergo a certain small-angle jump are then likely to undergo a large-angle jump. A three-dimensional exchange spectrum, however, by revealing the molecular reorientation that occurs in two separate time periods, can give the required information. The only problem is that a three-dimensional exchange spectrum can take days to record! Accordingly, a new reduced three-dimensional exchange experiment has been invented that yields much of the same information as a full three-dimensional experiment.[52]

Three-dimensional difference correlation (3D-DICO) spectroscopy[52] is a two-dimensional experiment that produces a projection of the full three-dimensional spectrum onto the diagonal plane shown in Fig. 23. This is done in practice with the three-dimensional pulse sequence of Fig. 22, but with $t_1 = t_2$ throughout the experiment, i.e. t_1 and t_2 are increased in concert. As usual with two-dimensional exchange spectroscopy, two time domain datasets are recorded[20] and, after appropriate processing in this case, a two-dimensional spectrum results with frequency coordinates ω_d $(=\omega_2 - \omega_1)$ and ω_3, where ω_1, ω_2 and ω_3 refer to the frequency coordinates corresponding to the t_1, t_2 and t_3 time domain variables. ω_d represents the degree of reorientation during the first mixing period, τ_{ma}; it is zero if there is no reorientation, but the larger it is, the larger the angle of reorientation during τ_{ma}. If the signal intensity at (ω_d, ω_3) is equal to that at $(-\omega_d, \omega_3)$, then the motion occurring in the second mixing period is uncorrelated with that in the first mixing period of the experiment, i.e. the reorientation that gives rise to the spectral frequency ω_3 during t_3 does not depend on the reorientation in the first mixing period. The method is demonstrated on both ^{13}C in dimethylsulfone (DMS) and ^2H in deuterated polystyrene.[52]

Four-dimensional exchange NMR was introduced some time ago for examining the correlations between different molecular motions.[53] The

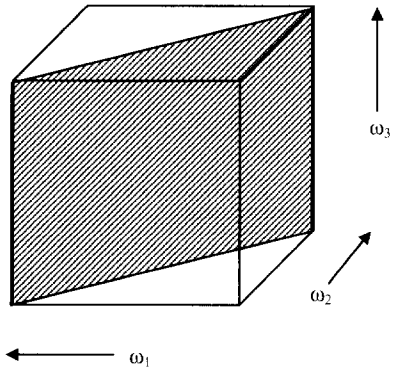

Fig. 23. The form of the reduced three-dimensional DICO experiment.[52] The experiment produces a two-dimensional experiment that is in effect, the projection of the full three-dimensional exchange spectrum onto the diagonal plane shown. This spectrum is then sufficient to determine whether two different motional processes revealed by the experiment are correlated.

principal application of such experiments has been in examining polymer dynamics near the glass transition. Near the glass transitions, the α (structural) relaxation process is known to be highly nonexponential. Two-dimensional exchange spectra in this regime can be fitted with a distribution of correlation times, but the question that remains is the following: Is this dynamic heterogeneity due to a spatial heterogeneity with different motional correlation times in different spatial regions, or does each polymer segment suffer motions with correlation times that themselves vary with time? The reduced four-dimensional exchange experiment goes part way to providing information to answer this question.[53] The basic scheme of the experiment is shown in Fig. 24.

The initial part of the experiment (labelled A in Fig. 24) is simply a two-dimensional exchange experiment, except that t_1 is set equal to t_2. Thus, at the end of t_2, there will be a stimulated echo arising from all those polymer segments that did *not* reorientate during the first mixing time τ_{ma}, or at least reoriented only through small angles. Providing that t_1 $(=t_2)$ is long enough, signal from polymer segments that have reoriented significantly during τ_{ma} will have dephased at the end of t_2, so that the only signal that goes on to the rest of the pulse sequence is that from polymer segments that are immobile during τ_{ma}. In other words, part A of the pulse sequence simply acts as a filter, filtering out signal from segments that have moved by more than small angles during τ_{ma} and leaving only signal from segments with small-angle reorientations and long motional correlation times $\tau_c \gg \tau_{ma}$. There then follows another mixing time τ_{mb}, which is to allow the timescale of the motional process for the selected polymer segments to change, if it can. Finally, another two-dimensional

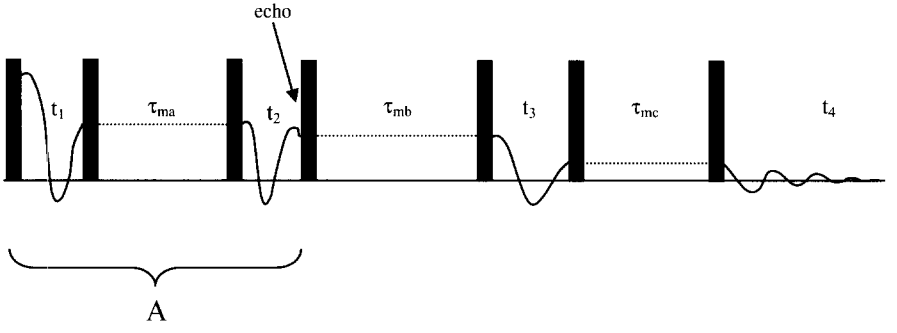

Fig. 24. The basic scheme of the reduced four-dimensional exchange experiment as performed on ^{13}C.[53] All pulses are 90° pulses. Part A of the experiment is simply a two-dimensional exchange experiment with t_1 set equal to t_2. The effect of this part of the pulse sequence is to select out only those spins that did not reorientate significantly during the mixing period of part A, τ_{ma}. The remainder of the experiment then serves to examine whether the motional timescale of these selected components subsequently changes during the second mixing time, τ_{mb}. The experiment thus probes the timescale of motional heterogeneity.

exchange filter follows, with a mixing time τ_{mc} set equal to the first mixing time, τ_{ma}. The final result from the experiment is a two-dimensional exchange frequency spectrum that is a function of the intermediate mixing time τ_{mb}, with frequency axes corresponding to the t_3 and t_4 time domain variables in the pulse sequence (Fig. 24). If the polymer segments selected in part A of the pulse sequence continue to undergo only small-angle reorientations during the second mixing time τ_{mb}, the final two-dimensional exchange spectrum will look the same as a normal two-dimensional exchange spectrum with mixing time τ_{mc}, and will consist entirely of diagonal (or near diagonal) intensity. However, if the reorientational motion changes during τ_{mb} to include large-angle reorientations with short correlation times, the two-dimensional exchange spectrum will contain significant off-diagonal intensity. Analysis of the two-dimensional exchange spectra as a function of τ_{mb} allows the heterogeneity in the motional timescales to be assessed.

A new experiment based on much the same principles as the reduced four-dimensional experiment just discussed now allows the *spatial* heterogeneity of the polymer dynamics to be assessed also.[54,55] The pulse sequence for this experiment is shown in Fig. 25. It produces two-dimensional ^{13}C exchange spectra, the initial ^{13}C transverse magnetization being derived from cross-polarization from ^{1}H. It differs from the previously described reduced four-dimensional experiment only in that, prior to the τ_{mb} mixing time, the ^{13}C magnetization is transferred back to ^{1}H by cross-polarization, and the resulting ^{1}H magnetization stored along z for the τ_{mb} mixing time. At the end of the mixing time, the ^{1}H is transferred back to ^{13}C in another cross-polarization

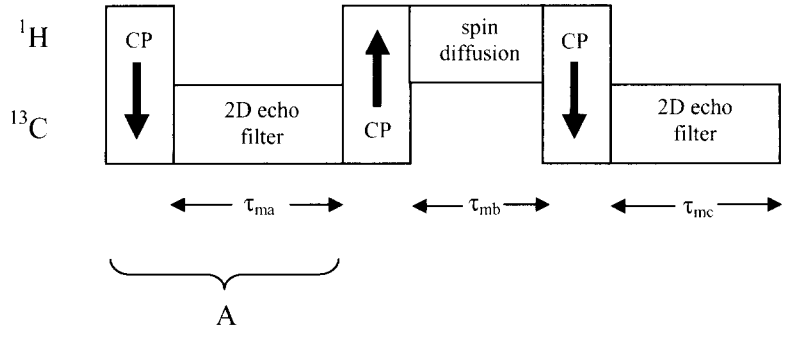

Fig. 25. Schematic pulse sequence for the reduced four-dimensional experiment to probe the spatial heterogeneity of molecular motions.[54,55] As for the experiment in Fig. 24, part A of the sequence selects out only signal from any slow components in the system. This experiment differs from that in Fig. 24 only in that the central mixing time, τ_{mb}, provided to allow the motional timescale to change if it can, now allows ^{1}H–^{1}H spin diffusion instead, so that the size of the region with slow molecular motions may be estimated. The two other mixing times τ_{ma} and τ_{mc} are equal.

step, and the experiment proceeds as for the previous reduced four-dimensional experiment. During the τ_{mb} mixing time in this new experiment, ^{1}H spin diffusion can occur, allowing spatial redistribution of the slow segment magnetization to spatial regions with faster motional processes. If such redistribution occurs, the final two-dimensional exchange spectrum has significant off-diagonal intensity. Following the height of the final stimulated echo at $t_4 = t_3$ as a function of the mixing time τ_{mb} allows the length scale of the dynamic heterogeneity to be assessed. If the magnetization remains in motionally slow segments, the echo height approaches its theoretical maximum, but as the magnetization is transferred to other motional regions, the degree to which the ^{13}C magnetization is refocused by the final two-dimensional exchange filter decreases, so the echo height reduces. The experiment was carried out[55] on poly(vinyl acetate) with 40% ^{13}C enrichment at the carbonyl position, where it was found that the length scale of the dynamic heterogeneity was 3 nm $\pm$ 1 nm.

4.3. Improving resolution in exchange experiments

Static exchange experiments can give immense amounts of information on dynamical processes, but they suffer from an inherent lack of resolution. Clearly, this is not important if there is only one chemical site for the observed nucleus, but it is critical if there is more than one site. Various experiments have been suggested in the review period to deal with this problem.

Perhaps the most comprehensive solution is the three-dimensional variable-angle correlation spectroscopy (VACSY) exchange experiment.[56] A three-dimensional VACSY exchange experiment has been implemented before that relies on a change of spinning angle during a two-dimensional exchange experiment. This is technically difficult, and it limits the samples that can be studied, as the change of spinning angle takes a finite length of time and samples that have short spin–lattice relaxation times lose significant amounts of magnetization during this period. The new experiment[56] is much simpler to implement in that the change of spinning angle occurs only between successive two-dimensional exchange experiments, that is the experiment consists of recording two-dimensional exchange spectra at several different spinning angles.

It can be seen from the following discussion that this can lead to a three-dimensional spectrum in which two-dimensional anisotropic exchange spectra for the different chemical sites are separated according to the isotropic chemical shifts associated with the different sites. Consider first a two-dimensional VACSY experiment (Fig. 26), in which a simple FID is collected under sample spinning at different spinning angles. The signal acquired has the form

$$F(t) = \exp([\omega_i + \omega_a(\theta, \phi)P_2(\cos\beta)]t) \tag{9}$$

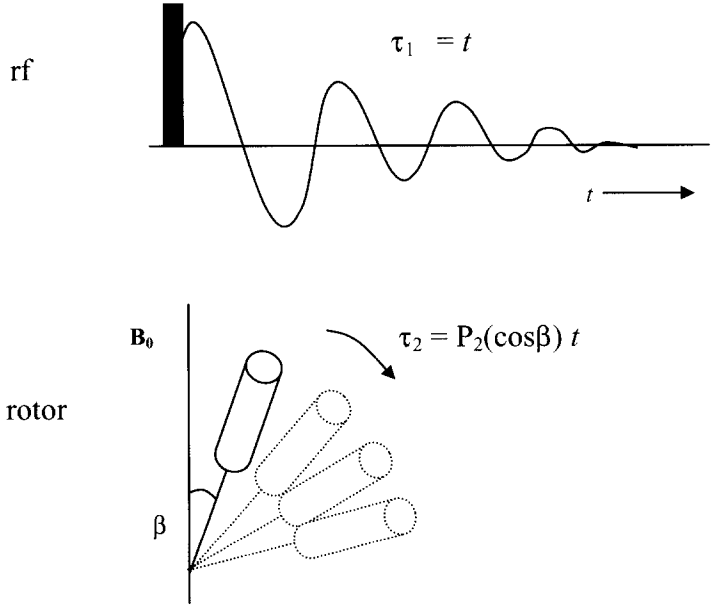

Fig. 26. A schematic diagram of the normal two-dimensional VACSY experiment. FIDs (spin-$\frac{1}{2}$) are collected for different sample spinning angles, β. After appropriate processing, a two-dimensional frequency spectrum is produced in which the chemical shift anisotropy powder patterns are separated according to the isotropic chemical shift.

where ω_i is the isotropic chemical shift, ω_a is the anisotropic chemical shift, dependent on the spherical polar angles θ and ϕ relating the chemical shift tensor principal axis frame to the applied field $\mathbf{B}_0$, β is the spinning angle (with respect to the applied magnetic field) and $P_2(\cos\beta)$ is a Legendre polynomial that describes the scaling of the chemical shift anisotropy by the sample spinning at angle β. Equation (9) can be rewritten as

$$F(t) = F(\tau_1, \tau_2) = \exp(\omega_i \tau_1) \exp(\omega_a(\theta, \phi)\tau_2) \tag{10}$$

where $\tau_1 = t$ and $\tau_2 = P_2(\cos\beta)t$. Equation (10) has the form of the signal from a two-dimensional experiment. Collecting a two-dimensional dataset for many values of τ_1, i.e. t, the time variable in the FID of the experiment, and of τ_2, i.e. different $P_2(\cos\beta)t$ obtained by collecting FIDs for different values of the spinning angle, β, and subsequent processing gives a frequency spectrum with spectral coordinates ω_1 and ω_2 corresponding to the time domain dimensions τ_1 and τ_2. From Eq. (10), the frequency dimension ω_1 contains resonances at ω_i, the isotropic chemical shift, and ω_2 contains frequencies $\omega_a(\theta, \phi)$, i.e. powder patterns associated with the anisotropic chemical shift. Now consider a two-dimensional exchange experiment conducted at spinning angle β (refer to Fig. 19 for definitions of the frequency and time variables). The resonance frequency for a given crystallite during t_1 is

$$\omega_1 = \omega_i p + \omega_{1a}(\theta, \phi)P_2(\cos\beta)p \tag{11}$$

where p is the coherence order during t_1 and can take values of ± 1. Similarly, the resonance frequency during t_2 is

$$\omega_2 = \omega_i + \omega_{2a}(\theta, \phi)P_2(\cos\beta) \tag{12}$$

where only coherence order -1 is observed. Thus, the final signal observed is

$$F(t_1, t_2) = \exp([\omega_i p + \omega_{1a}(\theta, \phi)P_2(\cos\beta)p]t_1) \exp([\omega_i + \omega_{2a}(\theta, \phi)P_2(\cos\beta)t_2) \tag{13}$$

This equation can be rewritten in a similar manner to Eq. (9) as

$$F(t_1, t_2) = F(\tau_1, \tau_2, \tau_3) = \exp(\omega_{1a}(\theta, \phi)\tau_1) \exp(\omega_{2a}(\theta, \phi)\tau_2) \exp(\omega_i \tau_3) \tag{14}$$

where

$$\tau_1 = P_2(\cos\beta)pt_1 \qquad \tau_2 = P_2(\cos\beta)t_2 \qquad \tau_3 = pt_1 + t_2 \tag{15}$$

Equation (14) has the form of the signal from a three-dimensional experiment with the time variables defined by Eq. (15). The three-dimensional time domain dataset implied by these variables can be collected by recording

normal two-dimensional exchange spectra for different spinning angles, β. The final three-dimensional dataset so obtained is then interpolated onto a regular Cartesian grid so that it can be Fourier transformed in the normal manner. In the resulting three-dimensional frequency spectrum, the (ω_1, ω_2) plane contains two-dimensional exchange spectra (with projections of chemical shift anisotropy powder patterns on each of the ω_1 and ω_2 axes) separated in the ω_3 dimension according to the isotropic chemical shift, ω_i. Complete details of the processing for the three-dimensional dataset are given in reference 56.

One of the most ingenious experiments for improving resolution is the ODESSA (one-dimensional exchange spectroscopy by sideband alternation) experiment.[57] This experiment achieves resolution by slow magic-angle spinning so that the powder pattern for each chemical site is broken up into a series of spinning sidebands and, in being so, resolves the signals from each site. The experiment takes the form of a normal two-dimensional exchange experiment (Fig. 19) except that the variable delay t_1 is now fixed at half a rotor period, $\tau_R/2$, and the mixing time, τ_m, is an integer number of rotor periods. After transfer of the magnetization to the z-axis, the t_1 delay of half a rotor period causes the magnetization associated with the different spinning sidebands to be polarized in alternate directions at the beginning of the mixing time, τ_m. During the mixing time, dynamic processes redistribute the polarization, resulting in a modified spinning sideband pattern in t_2. Analysis of these spinning sidebands then allows details of the reorientation process to be determined. Equations for simulating the spinning sideband patterns are derived in reference 57; each pattern consists of a sum of subspectra, one arising from those molecules that have not moved in the mixing time and others arising from molecules that have moved in some way. The experiment is applied to both ^{13}C and ^{2}H in dimethylsulfone (DMS) in this work.[57]

Another one-dimensional experiment, which improves resolution for spin-$\frac{1}{2}$ nuclei, is the CODEX NMR (centreband only detection of exchange) experiment.[58] The pulse sequence for this experiment is shown in Fig. 27. It is carried out under rapid magic-angle spinning, so that only the centrebands at the isotropic chemical shift for each chemical site remain in the spectrum. For an initial $N/2$ rotor periods, the spins evolve under the anisotropic chemical shift, which is refocused through the magic-angle spinning by two 180° pulses per rotor cycle. The magnetization is then stored along z as usual in an exchange experiment, for a mixing time that is an integral number of rotor periods. The magnetization is then returned to the transverse plane and allowed to evolve for a further $N/2$ rotor periods under the anisotropic chemical shift (by virtue of two 180° refocusing pulses per rotor cycle again). Finally a zero-quantum or z-filter is used to remove the effects of unwanted coherences. If there is no molecular reorientation during the mixing time, the (anisotropic) chemical shift associated with a given crystallite is the same before and after

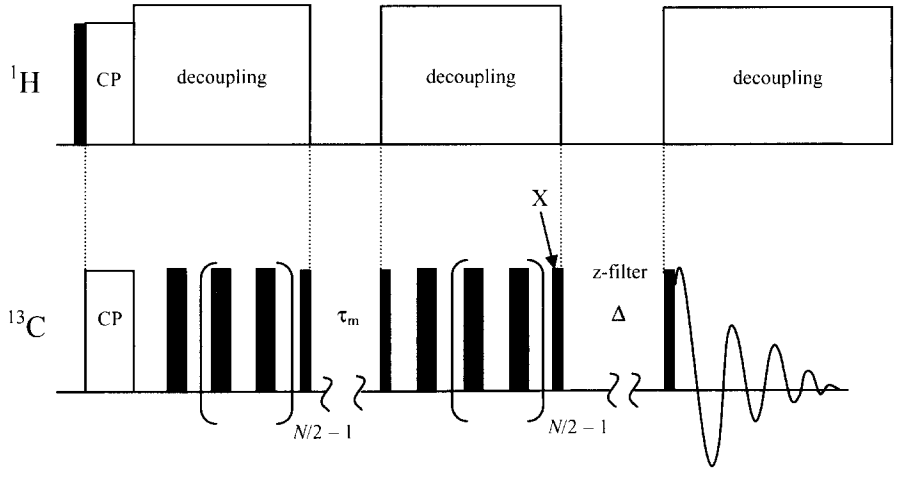

Fig. 27. The pulse sequence for the one-dimensional CODEX (centreband only detection of exchange) for spin-$\frac{1}{2}$ nuclei.[58] The experiment is conducted under rapid magic-angle spinning, so that only isotropic signals are recorded in the FID. The broad pulses are 180° pulses; the narrow ones are 90° pulses. All the gaps between the ^{13}C 180° pulses are $\tau_R/2$, where τ_R is the rotor period. The mixing time τ_m and z-filter delay Δ are both integral numbers of rotor periods. The series of ^{13}C 180° pulses either side of the mixing time refocus the chemical shift anisotropy during these periods. Any motion during the mixing time, τ_m then prevents complete refocusing of the chemical shift anisotropy at point X, immediately prior to recording the isotropic FID. This results in a loss of intensity in the corresponding isotropic signal. Repeating the experiment for different mixing times τ_m then allows the correlation time for the motion to be determined. Varying N, the number of rotor periods for which the chemical shift anisotropy is refocused, and/or τ_R, the rotor period, allows the geometry of the motion to be determined.

the mixing time. Then, the evolution under the reintroduced chemical shift anisotropy is refocused at the end of the second sequence of $N/2$ rotor periods. If, however, the chemical shift changes during the mixing time as a result of molecular reorientation, the chemical shift anisotropy is not completely refocused at this point. The resulting dephasing is observed as a decrease in the intensity of the isotropic chemical shift line observed via the recorded FID. The signal from immobile sites is removed from the final spectrum by subtracting a reference spectrum containing only signals from immobile sites, so that this final spectrum contains only intensity from sites that have suffered reorientation during the mixing time, τ_m. The reorientation rate can be determined by varying τ_m in the normal manner for exchange spectra, and the reorientation angle by varying $N\delta\tau_R$, where δ is the chemical shift anisotropy and τ_R is the rotor period. Thus, the reorientation rate can be found from plots of the CODEX intensity (for each site) as a function of τ_m, while the reorientation angle is determined from plots of the CODEX intensity as a function of $N\delta\tau_R$.

Trials on DMS[58] show that the CODEX intensity is a very sensitive function of these parameters, allowing very accurate determination of the motional details.

5. POLYMERS

In the review period there have been several extensive reviews of NMR applied to polymers, which include studies of molecular dynamics in such systems.[59,60] In addition, a book on the subject has been published[20] that is essential reading for anyone interested in this area.

The solid-state NMR techniques that are primarily used on polymers reflect the fact that motions of the polymer backbone are often relatively slow, with correlation times of the order of milliseconds to seconds. Accordingly, the main techniques used are two-dimensional exchange, both static[61–66] and magic-angle spinning[67,68] versions, with ^{13}C and ^{2}H; rotating frame relaxation ($T_{1\rho}$)[69–73] and transverse relaxation (T_2)[70] measurements and some ^{2}H lineshape analysis.[74–77] One particularly interesting application of ^{2}H lineshape analysis is the investigation of why 1,4-bis(1,3-octadecadiynyl)benzene cannot be made to undergo solid-state polymerization.[77] The study found that the motion of the monomers is simply too restricted at all temperatures to allow the molecules to attain the alignment needed for polymerization.

Spin–lattice relaxation measurements (T_1) are also common,[78–83] though these of course monitor more rapid motions. Spin–lattice relaxation times have nevertheless proved a simple but effective means of distinguishing different structural regions within polymer samples, i.e. crystalline and amorphous regions and interfacial regions between crystalline and amorphous parts.

Two-dimensional wideline ^{1}H spectroscopy (WISE) (see Section 2) is used to identify regions of high mobility (amorphous regions) from regions of low mobility (crystalline regions).[84,85] One particular study[86] examined the molecular mobilities in polyrotaxanes prepared by polymerizing acrylonitrile in the presence of 60-crown-20. For the resulting poly(acrylonitrile)$_n$-rotaxa-(60-crown-20)$_x$ with $x/n = 0.01$, the 60-crown-20 was, with WISE experiments, found to be phase separated, amorphous and highly mobile. A second less mobile region was identified and attributed to an interfacial region between the two components. In this particular system, the glass transition of the poly(acrylonitrile) was undetectable by DSC (differential scanning calorimetry), so ^{1}H NMR was employed instead to identify this transition.

Dipolar filter techniques (see Section 3) are becoming more common for examining regions of different mobility in polymers.[87] In one particular study,[88] a dipolar filter is used initially to select ^{1}H spins from mobile regions of core–shell latex systems. Dipolar filters of increasing strength are then applied so as to obtain a characteristic decay curve for each sample. This enabled the mobility of the various components in the system to be compared with the respective pure substances, so that the effect of mixing could be assessed.

Another study used the VACSY experiment discussed in Section 2.2 to examine the molecular motion in the crystalline region on poly(ε-caprolactone) via lineshape analysis of ^{13}C chemical shift anisotropy powder patterns.[79]

One of the biggest advances was in the development of experiments to examine the dynamic heterogeneity in polymer systems, particularly close to the glass transition. As discussed in Section 4, NMR experiments performed on polymer systems in this phase region generally result in the conclusion that there exists a distribution of motional correlation times.[89–91] The question is then how to interpret this distribution. It could reflect a spatial heterogeneity, or a molecular motion with an intrinsically nonexponential correlation function, or could arise from the dynamics at any given polymer segment changing with time. Three- and four-dimensional exchange and stimulated echo experiments have been developed to answer these questions as discussed in Section 4, and result in very detailed descriptions of the molecular dynamics in a polymer system, and in particular of the rate 'memory' within the system.[92–96]

The reasons for examining polymer dynamics are many and varied. There has been much emphasis of late in identifying the molecular processes underlying α- and β-relaxation processes in polymers, as described elsewhere in this review.[19,97] The segmental reorientation related to the α-relaxation process near the glass transition in supercooled poly(vinyl acetate) was examined using two-dimensional ^{13}C echo measurements.[98] It was found that the dynamics consisted of a superposition of $\sim 10^\circ$ angular jumps and rotational diffusion, both processes being related to the α-relaxation process. Related to this is a truly novel experiment in which ^{2}H powder lineshapes were used to monitor the relaxation behaviour of stress on a polymer (polybutadiene with 4-(3,5-dioxo-1,2,4-triazolidin-4-yl) benzoic or isophthalic acid units randomly attached) while the polymer was being subjected to a strain in a step-strain experiment.[99]

There is also considerable interest in examining the changes in molecular dynamics that occur upon curing as a result of increased cross-linking,[100] or that occur upon blending.[101,102] In one example, the effects of complexation on the mobilities of the individual components in a poly(acrylic acid)/poly(ethylene oxide) complex are studied via ^{13}C T_2 measurements.[103] In another, ^{13}C $T_{1\rho}$ measurements are used to monitor the effects of blending on molecular motion in poly(ethylene oxide)/poly(vinylphenyl) blends; here, blending was found to affect the proportion of phenyl rings undergoing librational motions, in addition to other effects on the polymer main chains.[104] The effect of the mode of crystallization of polymers upon the molecular mobility in the final material has also been investigated.[105]

A new area that has been examined is that of molecular dynamics in polyelectrolytes,[106] where the molecular motions responsible for the glass transition have been identified. Another interesting study is the effect of molecular motion upon the ingress of solvent into polymer material, as a function of cross-linking density.[107] In the particular case studied, of dioxane

diffusing into polystyrene, it was found that the density of cross-linking affected the phenyl ring motion, which in turn determined what type of diffusion process dominated.

6. BIOLOGICAL MATERIALS

The interest in studying biomolecules in the solid-state with NMR has grown hugely in the last five years, and this is fast becoming a dominant area of study. Most of the work to date aims at elucidating molecular structures by solid-state NMR, which is outside the scope of this review. However, there have been a significant number of motional studies, some of which show real promise for the utility of dynamic NMR studies in solid biological samples.[108] For many biomolecules, local internal molecular dynamics are important to the biological function. In solution-state studies, it can sometimes be difficult to separate whole-molecule reorientations from local oscillations. Solid-state studies largely circumvent this problem in many cases by reducing the rate and amplitude of whole-molecule rotations to a level where they have little effect on NMR spectra.

One of the principal areas of interest is, not surprisingly, the study of liquid-crystal-like phospholipid bilayers, which, at least to some extent, model phospholipid membranes in naturally occurring systems. Solid-state NMR has been used to examine the effect of binding proteins, carbohydrates and other species to phospholipid bilayers, in the form of liposomes in aqueous medium. A typical study is that examining the effect on phospholipid dynamics of adding myosin or casein to liposomes consisting of pure dimyristoylphosphatidylcholine (DMPC) or DMPC and dimyristoylphosphatidylglycerol (DMPG) in 1 : 1 molar ratio.[109] Two differently labelled DMPC molecules were used in the study, one with the headgroup α and β hydrogens deuterated (d_4-DMPC) and one with the γ hydrogens deuterated (d_9-DMPC), so that different regions of the headgroup could be studied separately. Any changes in the DMPC motion are then detected via changes in ^{2}H lineshapes or ^{2}H T_1. There was no change to any ^{2}H NMR parameters when myosin was added to the pure DMPC liposomes, but in the DMPC/DMPG liposomes changes were observed in both the ^{2}H quadrupole splittings and T_1 times for all DMPC headgroup segments. The interaction of the myosin was suggested to be electrostatic via the positively charged lysine residues located in the tail domain of myosin. β-Casein was found to interact with both DMPC and DMPC/DMPG liposomes, although the interaction was more pronounced with the charged liposomes.

Another study on this same theme examined the effects of trehalose, glucose and hydroxyethyl starch on the motional properties of the phosphate headgroup of freeze-dried dipalmitoylphosphatidylcholine (DPPC) liposomes, this time employing ^{31}P NMR.[110] The work aimed to examine whether there

was any correlation between the glass-forming tendency of the carbohydrate and the effect of the carbohydrate on the motions of the phospholipid headgroup. ^{31}P chemical shift anisotropy lineshapes were studied as a function of temperature; trehalose, which is a strong glass former, was found to elevate the onset of headgroup rotations. Moreover, it preserves the mobility of the phosphate headgroups after cooling from the liquid-crystal phase. Hydroxyethyl starch, on the other hand, has little effect on the headgroup dynamics, despite being a good glass former. Glucose is a very effective depressant of the phase transition temperature of freeze-dried DPPC and elevates the onset of headgroup rotations. However, it does not preserve the headgroup disordering when cooled from the liquid-crystal phase. An earlier very detailed study also used ^{31}P NMR, this time to examine the interaction of cytochrome *c* with phospholipid bilayers.[111] This work utilized ^{31}P T_1 relaxation times in addition to chemical shift anisotropy lineshapes.

Another study examined the effect of the anaesthetic steroid alphaxalone and its inactive congener, δ_{16}-alphaxalone in DPPC model membranes via ^{13}C cross-polarization, magic-angle spinning experiments.[112] Here, ^{13}C NMR spectra of the alphaxalone-containing membrane show a pretransition region before the main phase transition. Furthermore, ^{13}C chemical shift changes show that the populations of *trans* and *gauche* isomers of the lipid alkyl chains vary with temperature, presumably through some dynamic process. The respective ^{13}C NMR spectra of the alphaxalone- and δ_{16}-alphaxalone-containing membranes show that the two molecules have very different mobilities in the phospholipid bilayers, which may go some way towards explaining their different biological effects.

Small amounts of non-ionic surfactant (tetraethyleneglycol mono-*n*-dodecyl ether) are found to have a pronounced effect on DPPC bilayers.[113] In particular, the order parameter of the lipid chains measured via ^{2}H NMR is found to be significantly reduced, suggesting that the slower chain motions are affected by the surfactant. T_1 studies, though, show that the high-frequency motions, which are dominated by kink motions of the lipid chains, are unaffected.

Another important area of dynamic studies in biological samples is the effect of hydration upon molecular mobility in proteins and carbohydrates. The reason for these studies is primarily that protein dynamics, in particular, are crucial to their function, and so examining factors, such as the degree of hydration, that affect their dynamics is very important. However, it is obviously near-impossible to study dynamics in aqueous solution as a function of degree of hydration, and, since most proteins are not soluble in nonaqueous solvents, solid-state studies must be used. The motions at three methionine (Met) residues in *Streptomyces* subtilisin inhibitor (SSI) were studied with ^{2}H NMR using a sample in which the Met residues at two crucial enzyme recognition sites (P1 and P4) were specifically deuterated, along with one in the hydrophobic core.[114] The motions of the Met side-chains were then examined

in crystalline and powder samples as a function of hydration. Immediately after lyophilization, the ^{2}H lineshapes showed that the motions of all three Met side-chains were effectively quenched. However, as the hydration level is increased, the methyl group axes in the Met residues at the P1 and P4 sites undergo orientational fluctuation. This increases in both amplitude and frequency as the hydration increases, so that, near to saturating hydration, the rate of reorientation is of the order 10^6 Hz. Meanwhile, ^{2}H T_1 studies yield correlation times for methyl group threefold rotations between 10^{-8} and 10^{-10} s, which are comparable with those in solution.

Another study used ^{1}H T_1, T_2 and ^{13}C T_1, $T_{1\rho}$ measurements to assess the molecular dynamics in dry and wet solid proteins: bacterial RNAase, lysozyme and bovine serum albumin.[115] All relaxation time data were analysed assuming three components for the molecular motion: methyl group rotation and slow and fast oscillations of all atoms. An inhomogeneous distribution of correlation times was found for all samples, not surprisingly given the inhomogeneous nature of the samples. Interestingly, it was found that dehydration affected only the slow internal motions of the proteins and that the fast ones remained unaltered.

The one-dimensional exchange experiment ODESSA (see Section 2.4) was used in a study of the effects of hydration in the protein barstar and the polypeptide polyglycine.[116] For the experiments on barstar, a uniformly labelled ^{15}N sample was used, and natural-abundance ^{13}C was used for polyglycine. Only the wet barstar sample showed any signs of molecular reorientation in this case, with correlation times between 50 and 100 ms.

Studies of dynamics in wet and dry carbohydrates have also been performed. Slow motions of polysaccharide chains in native starch and retrograding starch gels were monitored with two-dimensional ^{2}H exchange and stimulated echo experiments.[117] The effects of hydration on the dynamics of β-cyclodextrin polymers have been examined with ^{13}C T_1 and ^{1}H $T_{1\rho}$ measurements,[118] and WISE experiments were used to probe the effects of hydration on polysaccharide chains in maize starch forms A and B.[119]

Another very interesting area concerns the study of molecular dynamics in DNA oligomers. Any dynamics at a molecular level must have some effect on the DNA sequence-specific recognition, if only in so far that incoherent motions between a protein and its docking site on DNA make the probability of binding much smaller. ^{2}H NMR has been used to study the local mobility at the C9pG10 step (see Fig. 28) in the DNA dodecamer $[d(CGCGAATTTCCCG)]_2$.[120] The study concludes that the furanose ring and helix backbone of dC9 display large-amplitude motions on 0.1 ms timescale for hydration levels characteristic of the B form structure (i.e. the biologically active form), though both the rate and amplitude of the motions are dependent on the degree of hydration. One particularly important result from this work is the finding that the amplitudes of local reorientational motions of the C–D bonds in the furanose ring and backbone of dC9 are larger than those of the C–D bonds in the cytosine base of

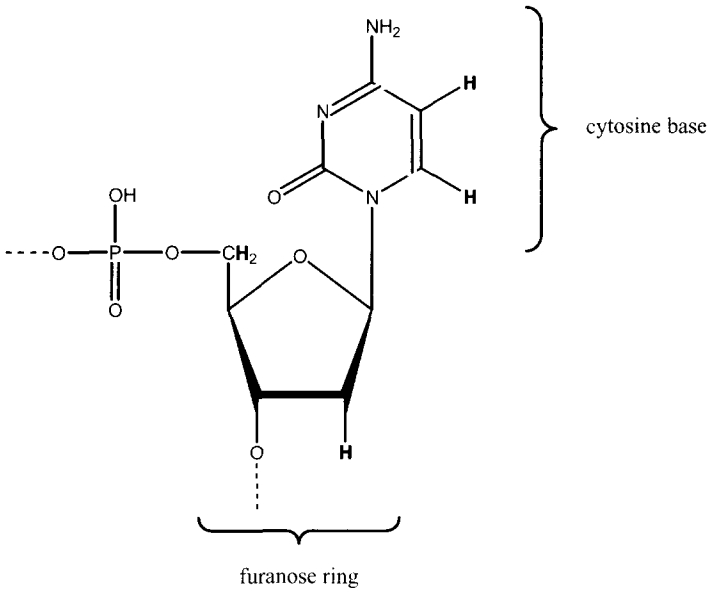

Fig. 28. The C9pG10 step in the DNA dodecamer [d(CGCGAATTTCCCG)]$_2$. Shown is the C9 nucleotide, with its cytosine base, furanose ring and linking phosphate group (C9pG10) which forms the phosphodiester backbone. The hydrogens in bold are the ones deuterated in the study of reference 120.

dC9. Therefore, the nucleotide unit does not move as a rigid entity but intersects a locally flexible region of the phosphodiester backbone. A similar study was performed on an RNA oligonucleotide, for which ^{2}H T_1 measurements were also used.[121]

In other studies, monitoring molecular dynamics can give vital information on bonding within biomolecules. In methyl-d_3-cobalamin, measurements of the anisotropic ^{2}H T_1 yields detailed information on the methyl group rotation (threefold jump, rather than rotational diffusion, with an activation energy of 8.3 ± 1.3 kJ mol^{-1}).[122] The energy barrier to the motion will clearly depend on the electronic character of the Co–C bond. Thus, it was proposed[125] that following changes in the activation energy for methyl group could probe changes in electronic character of the Co–C bond that accompany its biological role in enzymes such as methionine synthase.

The hydrogen bonding of serine side-chains in *Bombyx mori* and *Samia cynthia ricini* silk fibroin has been examined by looking for restricted mobility, which is presumed to arise from hydrogen bonding.[123] ^{2}H lineshapes (using [3,3-$^2H_2$]serine-labelled samples) were used to monitor serine side-chain motions. The lineshapes could be simulated assuming that 25% of the serine side-chains were undergoing rapid three-site motion and the remaining 75% a slow exchange between sites of unequal occupation with a small angle of

libration. The former component can be assumed to be uninvolved in hydrogen bonding, while the latter presumably has some degree of hydrogen bonding.

Reference 48, discussed previously in connection with ^2H T_1 anisotropy measurements, represents an example of using molecular dynamics to infer details of molecular structure.

7. HOST–GUEST COMPOUNDS

A vast range of guest molecule motions in inclusion compounds, zeolites and clay minerals have been studied over the years since solid-state NMR became more widely available in chemistry laboratories.

In the case of inclusion compounds, studying the dynamics of the guest molecule as a function of temperature, and indeed as a function of guest molecule, can reveal valuable information on the interaction between host and guest. This in turn yields some insight into the factors determining the stability of the inclusion compound.

Zeolites and related materials are used as molecular sieves and catalysts, so movement of molecules inside zeolite channels and cages is clearly an important subject. However, the motions of interest in this case would be largely translational. Such motions cannot be studied by solid-state NMR; only those motions that involve a specific change of molecular orientation or change of molecular site sufficiently drastic to cause a change in isotropic chemical shift can reasonably be studied by solid-state NMR. There are innumerable examples in the literature of solid-state NMR studies of the dynamics of small organic molecules in various zeolites, the vast majority of them being ^2H lineshape analyses. It has to be said that the motivation behind many of these studies is not obvious. It can reasonably be argued that studying the host dynamics in such systems gives generic information on the potential exerted by the host, which is then useful in understanding sieve and catalytic properties. However, to gain this type of detailed information, one would need to perform dynamic studies at many different guest loadings. All guest molecules in zeolite systems have preferred occupation sites and may well even have preferred orientations. Studies at a single guest concentration will probe only those sites then occupied. Only by varying the loadings can large parts of the channel/cage system really be explored, by forcing molecules into all parts of the host system and varying the populations at any one site. Moreover, interactions between guest molecules will also affect any NMR spectrum, and such effects cannot be extracted from host–guest interactions if only single guest loadings are studied.

In the review period, studies on zeolite systems have proceeded much as before; ^2H NMR lineshape studies still predominate. However, the organic guest molecules now being considered are larger than previously. This brings with it added complications for the ^2H lineshape analysis, at least for uniformly

labelled molecules. There are in general several different ^2H sites in the organic molecule, each of which contributes to the observed ^2H powder pattern. Add to this the fact that there may be several different sites within the zeolite for the guest molecule, each having different molecular dynamics associated with it, and it soon becomes apparent that unambiguous analysis of the net ^2H lineshape is highly unlikely. There are many examples in the literature of the review period where broad, rather featureless ^2H powder patterns, arising from the sum of contributions from many different ^2H sites, are analysed in terms of very detailed and specific motional models. Often, the possibility of different sites for the guest molecule is overlooked completely. In consequence, there are many studies in this area that cannot really be said to contribute any useful insight into the systems studied. One clear exception to this[124] (and there are others) examines the reorientational mobility of *n*-hexane and *n*-pentanol in Dianin's compound and in zeolite 5A. This work begins by using molecular mechanics calculations of the host–guest systems to produce minimum-energy structures, and then molecular dynamics calculations (20–100 ps trajectories at temperatures of 300 K and 77 K) to identify the fast motions in the system at the temperatures of calculation. This process yielded the following results for the Dianin inclusion compounds:

- The all-*trans* conformation of both guest molecules was maintained throughout the simulation period, but the molecular axis jumped several times between three symmetry-related sites; this corresponds to a rate of 10^{10}–10^{12} s^{-1}.
- The methyl groups of both guest molecules rotated, though this process was slower than the molecular reorientation described above.
- For the pentanol hydroxyl group, the hydrogen atom is preferentially in the *gauche* conformation and exhibits $g^+ - g^-$ jumps. This process was faster than any other and the only one exhibited at 77 K.

Similar detail was extracted for the zeolite host–guest system. These motional details were then used as the starting point in ^2H lineshape analyses. The fact that at least the fast motions at each temperature can be assumed to be similar to those found in the molecular dynamics calculations goes a long way to removing ambiguity from the analysis. Furthermore, the sites of the guest molecules can be taken from the molecular dynamics calculations. This particular work took the form of a 'proof of concept', and indeed showed very clearly that the ^2H lineshapes in the fast motion limit could be analysed assuming the motions deduced from the molecular dynamics calculations. The ^2H lineshapes at lower temperatures were then successfully simulated assuming that these motions slowed down. Slower motions present in the system would not, of course, be picked out by the molecular dynamics calculations. However, the contributions of the fast motions to the ^2H lineshapes can be extracted out with the aid of the molecular dynamics calculations, so leaving only the slow motions to be determined from the ^2H lineshapes.

In summary, for this area to move forward, methods need to be introduced to provide information additional to ^2H lineshapes when studying more complex systems. Calculations such as those just described are one real possibility; experimental possibilities include use of magic-angle spinning ^2H NMR, and using the full anisotropy of ^2H T_1 measurements and ^{13}C NMR. A very nice illustration of the use of several different techniques in a motional study examined the slow alkane motions in a urea/alkane inclusion compound via ^2H relaxation measurements, selective inversion experiments and two-dimensional ^2H exchange.[125]

8. ORGANOMETALLIC COMPOUNDS

Molecular dynamics in organometallic compounds is a potentially important area, as it can influence the course of solid-state reactions, and there are many such reactions known for organometallic compounds. Studying molecular dynamics can also give useful information on both intra- and intermolecular interactions, which between them govern molecular dynamics. This subject has been reviewed extensively elsewhere.[126]

A particularly good example of such use is in the investigation of agostic hydrogen interactions.[127] Interactions of β-hydrogens in alkyl ligands with metals in organometallic complexes are well documented. There is some controversy over whether agostic α-hydrogen interactions exist. If such interactions do exist, they might explain, for instance, the enhanced acidity of some alkyl complexes of tantalum and tungsten, and their tendency to form alkylidene complexes on addition of base. However, the evidence for agostic α-hydrogen interactions in monomeric complexes is slim at present. This particular study examined the motions of the methyl ligands in $[W(\eta^5\text{-}C_5Me_5)Me_4][PF_6]$ (Fig. 29). This tungsten complex is trigonal bipyramidal, with one axial and three equatorial methyl ligands. In one sample, the methyl ligands were ^{13}C-enriched. The ^{13}C NMR spectra showed a temperature-dependent line broadening of the axial methyl ligand signal, as a result of interference between the ^1H decoupling and methyl group motion.[128] This type of effect occurs when the rate of motion is comparable to the ^1H decoupling nutation frequency, and so this experiment in itself gives an indication of the rate of the axial methyl ligand motion. This motion was examined in more detail with ^2H lineshape analysis and ^2H T_1 measurements. The anisotropy in the ^2H T_1 indicated that the methyl group motion consisted of discrete three-site hopping, rather than continuous rotational diffusion. Detailed analysis of the partially relaxed ^2H lineshapes from inversion recovery experiments at higher temperatures and quadrupole-echo lineshape analysis at lower temperatures gave motional rates of $10^7\ s^{-1}$ at 297 K and $10^3\ s^{-1}$ at 348 K. The activation energy for the axial methyl ligand rotation was determined to be $26.8 \pm 1.7\ kJ\,mol^{-1}$. This is very high, the activation

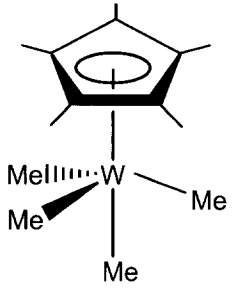

Fig. 29. The structure of the $[W(\eta^5\text{-}C_5Me_5)Me_4]^+$ cation.

energies for methyl group rotations normally being between 8 and 12 kJ mol^{-1}; indeed that for the equatorial methyl ligand rotation is determined to be 10.9 ± 0.4 kJ mol^{-1} from this same study. This may indicate that the axial methyl ligand is involved in some sort of agostic hydrogen interaction with the tungsten. This same work[127] also examined methyl ligand exchange in the $[W(\eta^5\text{-}C_5Me_5)Me_4]^+$ complex via selective ^{13}C inversion recovery experiments. The axial methyl ^{13}C resonance was selectively inverted using a DANTE pulse sequence. Any decrease in intensity of the equatorial methyl signal as the axial methyl signal recovers then indicates that magnetization has transferred from equatorial to axial ligands. At temperatures below room temperature, the equatorial methyl ^{13}C signal certainly show decreases in intensity as the axial signal recovers, but these changes in intensity are independent of temperature, indicating that the dominant process here is one of spin diffusion. Above room temperature, however, temperature-dependent intensity changes occur. From the timescale of the inversion recovery experiments, this shows that axial–equatorial ligand exchange occurs on the timescale of 1–5 s. Another interesting point arising from this work[127] is the fact that the ^2H powder lineshape from the equatorial methyl ligands shows a pronounced asymmetry in the fast-motion limit of methyl group rotation. This probably arises from these methyl groups being distorted from local threefold symmetry, presumably as a result of interactions between ligands, or maybe even agostic hydrogen interactions between the equatorial methyl ligand hydrogens and the metal.

Another interesting study examines the exchange of carbonyl ligands in $Cr(\eta^6\text{-arene})(CO)_3$ complexes.[130] The CO ligand dynamics were studied through ^{13}C chemical shift anisotropy sideband patterns from magic-angle spinning experiments. It was found that the relative ease of CO exchange depends upon the methyl substitution of the arene ring, with the exchange being more facile in complexes with less-symmetric rings. Whether this effect is due to differences in the metal–ligand bonding or in intermolecular packing is not clear.

ACKNOWLEDGEMENT

The author gratefully acknowledges the help of Mr J. H. Duer in the preparation of this manuscript.

REFERENCES

1. A. Schmidt and S. Vega, *J. Chem. Phys.*, 1987, **87**, 6895.
2. M. J. Duer and M. H. Levitt, *Solid-State NMR*, 1992, **1**, 211.
3. J. Clauss, M. J. Duer, L. F. Gladden, A. C. Griffin, C. P. Jariwala and C. Stourton, *J. Chem Soc., Faraday Trans.*, 1996, 803.
4. A. Abragam, *Principles of Nuclear Magnetism*, Clarendon Press, Oxford, 1961.
5. H. Sillescu, *J. Chem. Phys.*, 1971, **54**, 2110.
6. J. H. Kristensen, G. L. Hoatson and R. L. Vold, *J. Chem. Phys.*, 1999, **110**, 4533.
7. K. J. Hallock, D. K. Lee and A. Ramamoorthy, *Chem. Phys. Lett.*, 1999, **302**, 175.
8. D. K. Lee and A. Ramamoorthy, *J. Magn. Reson.*, 1998, **133**, 204.
9. I. Holleman, P. Robyr, A. P. M. Kentgens, B. H. Meier and G. Meijer, *J. Am. Chem. Soc.*, 1999, **121**, 199.
10. I. Holleman, G. von Helden, E. T. H. Olthof, P. J. M. van Bentum, R. Engeln, G. H. Nachtegaal, A. P. M. Kentgens, B. H. Meier, A. van der Avoird and G. Meijer, *Phys. Rev. Lett.*, 1997, **79**, 1138.
11. R. K. Harris and L. A. Crowe, *J. Chem. Soc., Dalton Trans.*, 1999, 4315.
12. K. Müller, H. Zimmermann, C. Krieger, R. Poupko and Z. Luz, *J. Am. Chem. Soc.*, 1996, **118**, 8006.
13. R. Poupko, K. Müller, C. Krieger, H. Zimmermann and Z. Luz, *J. Am. Chem. Soc.*, 1996, **118**, 8015.
14. R. Tycko, G. Dabbagh and P. A. Mirau, *J. Magn. Reson. A*, 1989, **85**, 265.
15. L. Frydman, G. C. Chingas, Y. K. Lee, P. J. Grandinetti, M. A. Eastman, G. A. Barrall and A. Pines, *J. Chem. Phys.*, 1992, **97**, 4800.
16. Z. Gan, *J. Am. Chem. Soc.*, 1992, **114**, 8307.
17. L. Frydman, S. Vallabhaneni, Y. K. Lee and L. Emsley, *J. Chem. Phys.*, 1994, **101**, 111.
18. M. J. Duer, *J. Magn. Reson. A*, 1996, **119**, 204.
19. W.-G. Hu, C. Boeffel and K. Schmidt-Rohr, *Macromolecules*, 1999, **32**, 1611.
20. K. Schmidt-Rohr and H. W. Spiess, *Multidimensional Solid-State NMR and Polymers*, Academic Press, London, 1994.
21. K. Schmidt-Rohr, J. Clauss and H. W. Spiess, *Macromolecules*, 1992, **25**, 3273.
22. I. Quijada-Garrido, M. Wilhelm, H. W. Spiess and J. M. Barrales-Rienda, *Macromolecules Chem. Phys.*, 1998, **199**, 985.
23. M. Wilhelm, S. Lehmann, C. Jager, H. W. Spiess and R. Jerome, *Magn. Reson. Chem.*, 1994, **32**, S3.
24. H. Geen, J. T. Titman, J. Gottwald and H. W. Spiess, *Chem. Phys. Lett.*, 1994, **227**, 79.
25. H. Geen, J. T. Titman, J. Gottwald and H. W. Spiess, *J. Magn. Reson.*, 1995, **114**, 264.
26. S. P. Brown, I. Schnell, J. D. Brand, K. Müller and H. W. Spiess, *J. Am. Chem. Soc.*, 1999, **121**, 6712.
27. B. Alemany, D. M. Grant, T. D. Alger and R. J. Pugmire, *J. Am. Chem. Soc.*, 1983, **105**, 6697.
28. G. A. Facey, C. I. Ratcliffe and J. A. Ripmeester, *J. Phys. Chem.*, 1995, **99**, 12249.
29. J. H. Kristensen, H.Bildsøe, H. J. Jakobsen and N. C. Nielsen, *J. Magn. Reson.*, 1992, **100**, 437.
30. O. Weintraub and S. Vega, *Solid-State NMR*, 1995, **4**, 341.
31. J. H. Kristensen, G. L. Hoatson and R. L. Vold, *Solid-State NMR*, 1998, **13**, 1.

32. F. H. Larsen, H. J. Jakobsen, P. D. Ellis and N. C. Nielsen, *J. Phys. Chem. A*, 1997, **101**, 8597.
33. F. H. Larsen, H. J. Jakobsen, P. D. Ellis and N. C. Nielsen, *Chem. Phys. Lett.*, 1998, **292**, 467.
34. T.-H. Lin and R. R. Vold, *J. Magn. Reson.*, 1995, **113**, 271.
35. J. A. DiNatale and R. R. Vold, *J. Magn. Reson. A*, 1995, **117**, 304.
36. W. S. Price and K. Hayamizu, *J. Magn. Reson. A*, 1995, **114**, 73.
37. M. J. Duer and E. C. Stourton, *J. Magn. Reson.*, 1997, **129**, 44.
38. D. Sandström, M. Hong and K. Schmidt-Rohr, *Chem. Phys. Lett.*, 1999, **300**, 213.
39. C. P. Slichter, *Principles of Magnetic Resonance*, Springer-Verlag, Berlin, 1992.
40. G. L. Hoatson and R. L. Vold, *NMR: Basic Principles and Progress*, 1994, **32**, 1.
41. R. L. Vold, G. L. Hoatson and T. Y. Tse, *Chem. Phys. Lett.*, 1996, **263**, 271.
42. G. L. Hoatson, R. L. Vold and T. Y. Tse, *J. Chem. Phys.*, 1994, **100**, 4756.
43. A. Scheicher, K. Müller and G. Kothe, *J. Chem. Phys.*, 1990, **92**, 6432.
44. D. A. Torchia and A. Szabo, *J. Magn. Reson.*, 1991, **94**, 152.
45. V. Copié, A. E. McDermott, K. Beshah, J. C. Williams, M. Spijker-Assink, R. Gebhard, J. Lugtenberg, J. Herzfeld and R. G. Griffin, *Biochemistry*, 1994, **33**, 3281.
46. M. J. Brown, R. L. Vold and G. L. Hoatson, *Solid-State NMR*, 1996, **6**, 167.
47. M. J. Brown, G. L. Hoatson and R. L. Vold, *J. Magn. Reson. A*, 1996, **122**, 165.
48. C.-G. Hoelger, B. Wehrle, H. Benedict and H.-H. Limbach, *J. Phys. Chem.*, 1994, **98**, 843.
49. T. Fritzhanns, D. E. Demco, S. Hafner and H. W. Spiess, *Mol. Phys.*, 1999, **97**, 931.
50. X. Helluy, J. Kümmerlen and A. Sebald, *Organometallics*, 1998, **17**, 5003.
51. D. Schaefer, J. Leisen and H. W. Spiess, *J. Magn. Reson. A*, 1995, **115**, 60.
52. A. Heuer, J. Leisen, S. C. Kueber and H. W. Spiess, *J. Chem. Phys.*, 1996, **105**, 7088.
53. K. Schmidt-Rohr and H. W. Spiess, *Phys. Rev. Lett.*, 1991, **66**, 3020.
54. U. Tracht, M. Willhelm, A. Heuer, H. Feng, K. Schmidt-Rohr and H. W. Spiess, *Phys. Rev. Lett.*, 1998, **81**, 2727.
55. U. Tracht, M. Willhelm, A. Heuer and H. W. Spiess, *J. Magn. Reson.*, 1999, **140**, 460.
56. Y. K. Lee, L. Emsley, R. G. Larsen, K. Schmidt-Rohr, M. Hong, L. Frydman, G. C. Chingas and A. Pines, *J. Chem. Phys.*, 1994, **101**, 1852.
57. V. Gérardy-Montouillot, C. Malveau, P. Tekely, Z. Oleander and Z. Luz, *J. Magn. Reson. A*, 1996, **123**, 7.
58. E. R. deAzevedo, W.-G. Hu, T. J. Bonagamba and K. Schmidt-Rohr, *J. Am. Chem. Soc.*, 1999, **121**, 8411.
59. K. Schmidt-Rohr, *ACS Symp. Ser.*, 1995, **598**, 191.
60. H. W. Spiess, *Ber. Buns. Gesell. Phys. Chem. Chem. Phys.*, 1997, **101** 153.
61. S. C. Kuebler, D. J. Schaefer, C. Boeffel, U. Pawelzik and H. W. Spiess, *Macromolecules*, 1997, **30**, 6597.
62. C. A. Veracini, C. Boeffel and H. W. Spiess, *Mol. Cryst. Liquid Cryst. A*, 1995, **266**, 47.
63. M. Willhelm and H. W. Spiess, *Macromolecules*, 1996, **29**, 1088.
64. A. Dardin, C. Boeffel, H. W. Spiess, R. Stadler and E. T. Samulski, *Acta Polym.*, 1995, **46**, 291.
65. K. Schmidt-Rohr, A. S. Kulik, H. W. Beckham, A. Ohlemacher, U. Pawelzik, C. Boeffel and H. W. Spiess, *Macromolecules*, 1994, **27**, 4733.
66. A. S. Kulik, H. W. Beckham, K. Schmidt-Rohr, D. Radloff, U. Pawelzik, C. Boeffel and H. W. Spiess, *Macromolecules*, 1994, **27**, 4746.
67. H. W. Beckham, K. Schmidt-Rohr and H. W. Spiess, *ACS Symp. Ser.*, 1995, **598**, 243.
68. K. Hirao, Y. Ishii, T. Terao, Y. Kishimoto, T. Miyatake, T. Ikariya and R. Noyori, *Macromolecules*, 1998, **31**, 3405.
69. S. Ando, R. K. Harris, G. A. Monti and S. A. Reinsberg, *Magn. Reson. Chem.*, 1999, **37**, 709.
70. L. Abis, G. Floridi, E. Merlo, R. Po and C. Zannoni, *J. Polym. Sci. B Polym. Phys.*, 1998, **36**, 1557.
71. G. Vho, A. Natansohn, T. Ho and K. J. Wynne, *Macromolecules*, 1996, **29**, 2563.

72. J. C. Moreland, G. L. Wilkes, C. G. Moreland, S. S. Sankar, E. O. Stejskal and R. B. Turner, *J. Appl. Polym. Sci.*, 1994, **52**, 1175.
73. S. H. Zhu, M. K. Cheung and C. M. Chan, *Polymer*, 1998, **39**, 6099.
74. V. M. Litvinov, V. Macho and H. W. Spiess, *Acta Polym.*, 1997, **48**, 471.
75. U. Wiesner, H. W. Spiess, M. Muller, F. Kremer, F. Laupretre, J. L. Hallary and L. Monnerie, *Acta Polym.*, 1996, **47**, 429.
76. F. Horii, H. Kaji, H. Ishida, K. Kuwabara, K. Masuda and T. Tai, *J. Mol. Struct.*, 1998, **441**, 303.
77. S. Kitazawa, T. Hiraoki and A. Tsutsumi, *J. Mol. Struct.*, 1995, **355**, 87.
78. M. Kobayashi, I. Ando, T. Ishii and S. Amiya, *J. Mol. Struct.*, 1998, **440**, 155.
79. H. Kaji and F. Horii, *Macromolecules*, 1997, **30**, 5791.
80. S. Kitazawa, T. Hiraoki, T. Hamada and A. Tsutsumi, *Polymer J.*, 1994, **26**, 1213.
81. H. Kurosu, K. Suzuki, I. Ando and T. Otsu, *J. Mol. Struct.*, 1994, **321**, 229.
82. F. O. Garces, K. Sivadasan, P. Somasundaran and N. J. Turro, *Macromolecules*, 1994, **27**, 272.
83. D. Inoue, H. Kurosu, Q. Chen and I. Ando, *Acta Polym.*, 1995, **46**, 420.
84. I. Quijada-Garrido, M. Wilhelm, H. W. Spiess and J. M. Barrales-Rienda, *Macromolecules, Chem. Phys.*, 1998, **199**, 985.
85. K. Nagapudi, J. Hunt, C. Shepherd, J. Baker and H. W. Beckham, *Macromol. Chem. Phys.*, 1999, **200**, 2541.
86. K. Nagapudi, J. Leisen, H. W. Beckham and H. W. Gibson, *Macromolecules*, 1999, **32**, 3025.
87. K. Landfester, C. Boeffel, M. Lambla and H. W. Spiess, *Macromolecules*, 1996, **29**, 5972.
88. F. Mellinger, M. Wilhelm, P. Belik, H. Schwind and H. W. Spiess, *Macromol. Chem. Phys.*, 1999, **200**, 2454.
89. P. G. Klein, B. W. Evans and I. M. Ward, *Polymer*, 1998, **39**, 3349.
90. R. D. O'Connor, F. D. Blum, E.Ginsberg and R. D. Miller, *Macromolecules*, 1998, **31**, 4852.
91. S. Saxena, D. Cizmeciyan and J. A. Kornfield, *Solid-State NMR*, 1998, **12**, 165.
92. S. C. Kuebler, A. Heuer and H. W. Spiess, *Phys. Rev. E*, 1997, **56**, 741.
93. A. Heuer, M. Wilhelm, H. Zimmermann and H. W. Spiess, *Phys. Rev. Lett.*, 1995, **75**, 2851.
94. J. Leisen, K. Schmidt-Rohr and H. W. Spiess, *J. Non-Cryst. Solids*, 1994, **172**, 737.
95. H. Sillescu, *J. Chem. Phys.*, 1996, **104**, 4877.
96. G. Hinze, R. Böhmer, G. Diezemann and H. Sillescu, *J. Magn. Reson.*, 1998, **131**, 218.
97. H. Y. Chien, D. McIntyre, J. L. Cheng and M. Fone, *Polymer*, 1995, **36**, 2559.
98. U. Tracht, A. Heuer and H. W. Spiess, *J. Chem. Phys.*, 1999, **111**, 3720.
99. A. Dardin, H. W. Spiess, R. Stadler and E. T. Samulski, *Polym. Gels Networks*, 1997, **5**, 37.
100. M. C. S. Perera, *Polymer*, 1999, **40**, 1667.
101. A. Tezuka, K. Takegoshi and K. Hikichi, *J. Mol. Struct.*, 1995, **355**, 1.
102. K. Takegoshi, K. Tauchiya and K. Hikichi, *Polymer J.*, 1995, **27**, 284.
103. T. Miyoshi, K. Takegoshi and K. Hikichi, *Polymer*, 1997, **38**, 2315.
104. K. S. Jack and A. K. Whittaker, *Macromolecules*, 1997, **30**, 3560.
105. F. G. Morin, G. Delmas and D. F. R. Gilson, *Macromolecules*, 1995, **28**, 3248.
106. R. R. Rietz, K. Schmidt-Rohr, W. H. Meyer, H. W. Spiess and G. Wegner, *Solid-State Ionics*, 1994, **68**, 151.
107. M. Ilg, B. Pfleiderer, K. Albert, W. Rapp and E. Bayer, *Macromolecules*, 1994, **27**, 2778.
108. D. J. Siminovitch, *Biochem. Cell Biol.*, 1998, **76**, 411.
109. J. A. G. Areas, G. J. Grobner, L. B. Pellacani, C. Glaubitz and A. Watts, *Magn. Reson. Chem.*, 1997, **35**, 5119.
110. N. M. Tsvetkova, B. L. Phillips, L. M. Crowe, J. H. Crowe and S. H. Risbud, *Biophys. J.*, 1998, **75**, 2947.
111. T. U. T. Pinheiro and A. Watts, *Biochemistry*, 1994, **33**, 2451.
112. T. Mavromoustakos, E. Theodoropoulou and D. P. Yang, *Biochim. Biophys. Acta Biomembr.*, 1997, **1328**, 65.

113. C. Gliss, H. Casalta and T. M. Bayerl, *J. Phys. Chem. B*, 1999, **103**, 8908.
114. A. Tamura, M. Matsushita, A. Naito, S. Kojima, K. I. Miura and K. Akasaka, *Protein Sci.*, 1996, **5**, 127.
115. A. G. Krushelnitsky, V. D. Fedotov, J. Spevacek and J. Staka, *J. Biomol. Struct. Dynam.*, 1996, **14**, 211.
116. A. Krushelnitksy, D. Reichert, G. Hempel, V. Fedotov, H. Schneider, L. Yagodina and A. Schulga, *J. Magn. Reson.*, 1999, **138**, 244.
117. A. S. Kulik and J. Haverkamp, *Carbohydr. Polym.*, 1997, **34**, 49.
118. G. Crini, C. Cosentino, S. Bertini, A. Naggi, G. Torri, C. Vecchi, L. Janus and M. Morcellet, *Carbohydr. Res.*, 1998, **308**, 37.
119. A. S. Kulik, J. R. C. Decosta and J. Haverkamp, *J. Agric. Food Chem.*, 1994, **42**, 2803.
120. M. E. Hatcher, D. L. Mattiello, G. A. Meints, J. Orban and G. P. Drobny, *J. Am. Chem. Soc.*, 1998, **120**, 9850.
121. A. C. Wang, M. A. Kennedy, B. R. Reid and G. P. Drobny, *J. Magn. Reson. B*, 1994, **105**, 1.
122. J. R. Garbutt, G. R. Goward, C. W. Kirby, W. P. Power, *Biochem. Cell Biol.*, 1998, **76**, 423.
123. T. Kameda, Y. Ohkawa, K. Yoshizawa, J. Naito, A. S. Ulrich and T. Asakura, *Macromolecules*, 1999, **12**, 7166.
124. E. Zaborowski, H. Zimmermann and S. Vega, *J. Am. Chem. Soc.*, 1998, **120**, 8113.
125. K. A. Bell, G. L. Hoatson and R. L. Vold, *J. Magn. Reson. A*, 1994, **108**, 238.
126. M. J. Duer, in *Solid-State Organometallic Chemistry: Methods and Applications* (eds. M. Gielen, R. Willem and B. Wrackmeyer), Wiley, Chichester, 1999.
127. D. C. Maus, V. Copié, B. Sun, J. M. Griffiths, R. G. Griffin, S. Luo, R. R. Schrock, A. H. Liu, S. W. Seidel, W. M. Davis and A. Grohmann, *J. Am. Chem. Soc.*, 1996, **118**, 5665.
128. W. P. Rothwell and J. S. Waugh, *J. Chem. Phys.*, 1981, **74**, 2721.
129. P. J. Barrie, C. A. Misopoulou, M. Motevalli and E. W. Randall, *J. Chem. Soc. Dalton Trans.*, 1997, 353.

NMR Lineshapes and Lineshape Fitting Procedures

JOHN HIGINBOTHAM[1] and IAN MARSHALL[2]

[1] *School of Applied Mathematical and Physical Sciences, Napier University, 10 Colinton Road, Edinburgh EH10 5DT, UK*

[2] *Department of Medical Physics and Medical Engineering, The University of Edinburgh, Western General Hospital, Crewe Road, Edinburgh, EH4 2XU, UK*

Abbreviations and symbols 60
1. Introduction 63
2. NMR lineshapes 65
   2.1. Lorentzian lineshape 65
   2.2. Gaussian lineshape 66
   2.3. Voigt lineshape 68
   2.4. Convolution of Gaussian and rectangular lineshapes 69
   2.5. Lineshapes due to exchange narrowing 70
   2.6. Powder lineshape 73
   2.7. Quadrupolar lineshape 75
   2.8. Lineshape due to Brownian motional narrowing 79
   2.9. Comparison of various lineshapes 81
3. Approximations to NMR lineshapes 84
   3.1. Approximations to the Voigt lineshape 84
   3.2. Moment expansions 85
   3.3. Rational function expansions 88
4. Lineshape fitting procedures 93
   4.1. Criteria for a good fit 93
   4.2. Nonlinear least-squares fitting in the time domain (Levenberg–Marquardt method) 94
   4.3. Nonlinear least-squares fitting in the frequency domain (Levenberg–Marquardt method) 97
   4.4. VARPRO 98
   4.5. Linear prediction and related techniques 100
   4.6. Maximum-entropy techniques 109
5. Summary 111
   Acknowledgements 116
   References 116

ANNUAL REPORTS ON NMR SPECTROSCOPY
VOLUME 43 ISBN 0-12-505343-6

ABBREVIATIONS AND SYMBOLS

a	Voigt parameter (also a parameter associated with exchange narrowing)
$\mathbf{a}$	Vector of prediction coefficients
$A(f)$	Absorption signal in the frequency domain
a_k	Amplitude of the kth component in the frequency domain
A_k	Amplitude of the kth component in the time domain
a_m	Linear prediction coefficient
b	Half width of rectangular lineshape
$\mathbf{B}_0$	Magnetic induction of the main magnetic field
b_k	Damping factor
$\mathbf{c}$	Vector of complex coefficients
c, c_k	Amplitude or complex amplitude
CW	Continuous wave
$D(f)$	Dispersion signal in the frequency domain
DFT	Discrete Fourier transform
DMPC	Dimyristoylphosphatidylcholine
$E(m)$	Energy of the state whose z component of angular momentum is $\hbar m$
$e(t)$	White noise (zero mean, normally distributed)
ESR	Electron spin resonance (also known as electron paramagnetic resonance (EPR))
$\mathbf{F}$	Matrix of basis functions
$\mathbf{F}^{\mathrm{T}}$	Transpose of $\mathbf{F}$
f_0	Frequency of the centre of a resonance in Hz
$f_{\parallel}$	Frequency parallel to the axis of symmetry
$f_{\perp}$	Frequency perpendicular to the axis of symmetry
f_k	Basis function
f_{Q}	Rescaled quadrupolar coupling constant
FD	Frequency domain
FFT	Fast Fourier transform
FID	Free induction decay
FT	Fourier transform
FWHM	Full width at half maximum height
$g(f)$	Normalized lineshape function in the frequency domain
$G(t)$	The Fourier transform of $g(f)$
$g_{\mathrm{G}}(f)$	Normalized Gaussian lineshape function as a function of frequency
$g_{\mathrm{L}}(f)$	Normalized Lorentzian lineshape function as a function of frequency
$g_{\mathrm{R}}(f)$	Normalized rectangular lineshape function as a function of frequency

h	Planck constant
$\mathcal{H}_1'$	Hamiltonian operator equal to $\alpha + \beta$
HLSVD	Hankel–Lanczos singular value decomposition
HSVD	Hankel singular value decomposition
HTLS	Hankel total least-squares
i	Square root of -1
I	Nuclear spin quantum number
$I(f)$	Intensity function for a powder lineshape
IR	Infrared
J_{12}	J-coupling
K	Number of signal components
k	Denotes kth signal component
LP	Linear prediction
LPSVD	Linear prediction singular value decomposition
LPTLS	Linear prediction total least-squares
LS	Least-squares
M	Linear prediction length (also degree of polynomial $P(x)$ and number of parameters)
m	Denotes mth linear prediction coefficient
$M(f)$	Magnitude signal in the frequency domain
M_n	nth moment of the lineshape
$\mathcal{M}_x$	Operator corresponding to the x component of the magnetization
MEM	Maximum-entropy method
MRS	Magnetic resonance spectroscopy
N	Number of data points (also degree of polynomial $Q(x)$)
n	Denotes nth data point
NAA	N-acetylaspartate
NMR	Nuclear magnetic resonance
p	Probability
$P(f)$	Power spectrum
$P(x)$	Polynomial of degree M
Q	Nuclear quadrupole moment
$Q(x)$	Polynomial of degree N
QR	Householder triangularization
r	Fractional parameter giving proportion of Lorentzian lineshape
RF	Radiofrequency
rms	Root mean square
$S(p)$	Entropy function
SNR	Signal-to-noise ratio
SVD	Singular value decomposition
T_2	Transverse relaxation time
T_2^*	Effective transverse relaxation time

TD	Time domain
TDFD	Time domain–frequency domain
TLS	Total least-squares
t_n	Time of nth sample
$\mathbf{U}_k$	Result of singular value decomposition
V	Electrostatic potential
$V(f)$	Voigt function
$V'(f)$	Approximation to the Voigt function
$\mathbf{V}_k$	Result of singular value decomposition
VARPRO	Variable projection method
voxel	Volume element
W	FWHM of a Voigt lineshape function (Hz)
W_G	FWHM of a Gaussian (Hz)
W_L	FWHM of a Lorentzian (Hz)
$\mathbf{x}$	Data vector
$\mathbf{X}$	Data matrix
$\mathbf{X}_l$, $\mathbf{X}_r$	Left and right decomposition of $\mathbf{X}$
x_n	nth experimental data point
$\hat{x}_n$	nth model data point
$\mathbf{Z}$	Matrix of signal poles z_k
Z_k	Signal pole
α	First Euler angle (also a term in a Hamiltonian)
β	Second Euler angle (also a term in a Hamiltonian)
γ	Gyromagnetic ratio of a nucleus
γ_k	General nonlinear parameter
Δf	Total anisotropy in frequency units (Hz)
Δt	Sampling period
$\Delta\omega$	Total anisotropy
λ	Deformation (also Lagrange multiplier)
Λ_k	Result of singular value decomposition (singular value matrix)
σ	Standard deviation
σ_{ii}	Principal axes values of the chemical shielding tensor
τ_A	Lifetime of a nucleus in state A
τ_c	Correlation time associated with diffusion
ϕ_k	Phase
χ	Static quadrupole coupling constant
χ'	Real part of the magnetic susceptibility
χ''	Imaginary part of the magnetic susceptibility
ψ_f	SNR in the frequency domain
ψ_t	SNR in the time domain
ω, ω_k	Angular frequency
ω_{ii}	Angular frequency tensor component
$\omega_{\|\|}$	Angular frequency parallel to the axis of symmetry
$\omega_\perp$	Angular frequency perpendicular to the axis of symmetry

1. INTRODUCTION

This report on lineshapes and lineshape fitting procedures is intended to give an appropriate overview for use by someone commencing research in this area. For this reason, references to text books are given and original articles are cited to facilitate the examination of concepts by research workers. Although many of the details given relate to NMR, the principles cover numerous applications, including x-ray, infrared (IR), electron spin resonance (ESR) and astronomical spectra. The area of each line in the frequency domain (FD) is proportional to the quantity of a particular entity, whereas the shape and width of a line reveal information about relaxation processes. Hence, in order to extract as much information as possible from the data, an accurate and reliable fit must be made to each resonance line.

In order to obtain the most satisfactory fit in the presence of noise, it is advantageous to make use of as much prior knowledge about the component lineshapes as possible. In the case of high-resolution solution NMR, the spectra can normally be assumed to be a superposition of Lorentzian lineshapes. In other cases, much more complicated lineshapes can be involved.

If more than one line-broadening mechanism, such as magnetic field inhomogeneity, is present, then the resulting lineshape consists of the convolution of the intrinsic lineshape, such as a Lorentzian, with each of the line-broadened lineshapes. In general, this can lead to extremely complicated lineshapes. The observed shape of the continuous wave (CW) NMR lineshape under various conditions of modulation amplitude, radiofrequency (RF) level, sweep rate and filter time constant has been studied extensively.[1–4] For simple saturation and measurement conditions, such as slight saturation under intermediate passage conditions, the effects are readily described in terms of the Bloch equations.[5,6] For more complicated saturation and measurement conditions in CW NMR, the Provotorov theory[7,8] is required. It should be noted that the absorption signal is proportional to the imaginary part of the magnetic susceptibility, χ'', whereas the dispersion signal is proportional to the real part of the magnetic susceptibility χ'. Since χ'' and χ' are related by the Kramers–Kronig relations, they are not independent.[9] Under conditions of negligible saturation in a slow passage CW measurement, χ'' is proportional to the lineshape function $g(f)$.[5] The conditions under which the pulse measurements are identical to the Fourier transform (FT) of the CW measurements in the high-temperature limit have been discussed extensively.[10–12] This report will deal mainly with lineshapes arising from the use of pulsed NMR, because of the current almost universal usage of pulsed NMR.

If, in a pulsed NMR experiment, the steady magnetic induction[13] $\mathbf{B}_0$ is applied along the z-direction and the oscillating component of the magnetic induction, $\mathbf{B}_1$ is applied along the x-direction in the rotating frame,[14] then the free induction decay (FID) observed along the y-direction, detected in the in-phase channel in quadrature detection, is proportional to $G(t)$, the Fourier transform of $g(f)$,[9] and

is known as the absorption signal in the time domain, $A(t)$. The corresponding signal in the quadrature channel is the corresponding dispersion signal $D(t)$.[15–17] Normally, NMR spectra are displayed in the form of the absorption signal in the frequency domain, which is proportional to $g(f)$. Sometimes, however, the magnitude spectra[18] $M(f) = [A(f)^2 + D(f)^2]^{1/2}$ or the power spectra[19] $P(f) = M(f)^2$ are displayed, both of which give signals that are broader than the corresponding absorption signals and lack any phase information.

Many methods for the fitting of data obtained from pulsed NMR have been described in the literature. The methods may, for example, be classified as either time domain (TD) or FD methods. Alternatively, they may be described as black-box methods or as interactive methods. An excellent review is given by de Beer and van Ormondt.[20] There is now a consensus[21] that FD and TD fitting methods are equivalent in terms of χ^2 parameter estimation if potential artifacts introduced by Fourier transformation are handled properly. TD and FD fitting can truly be equivalent (i.e. same χ^2 minima) if χ^2 is determined over the whole data range (a consequence of the power theorem on the Fourier transform) and if the model used to fit the experimental spectrum is correct. Very often, however, the model used is only an approximation.

Several algorithms for the least-squares fitting of high-resolution NMR spectra have been developed, where a Lorentzian lineshape is normally assumed.[22] The corresponding computer programs yield the centre frequencies of the transitions and the scalar coupling constants. An excellent review of both FD and TD fitting is given by Gesmar *et al.*[23] As pointed out in another excellent review by Stephenson[24] of linear prediction (LP) and maximum entropy techniques, LP works well only for a large signal-to-noise ratio (SNR). Care should be taken in calculating the uncertainties of the parameters of interest. For example, in strongly *J*-coupled AB systems[25] the covariances play a decisive role in the propagation of errors from the set $\{f_1, f_2, J_{12}\}$ to the set $\{\delta, s, J_{12}\}$ where $\delta = f_1 - f_2$ is the chemical shift and $s = (f_1 + f_2)/2$ is the centre of the spectrum, and J_{12} is the J-coupling.

When the SNR is poor, and when instrumental effects are significant, e.g. in magnetic resonance spectroscopy (MRS), great care must be taken in the selection of the fitting technique used. As is well known,[26] the uncertainty in the model parameters increases with the number of parameters estimated. If this number can be reduced, the uncertainty in the estimated model parameters will be reduced. That is, it is *always advantageous* to make use of *prior knowledge*. It is possible to combine the advantages of TD fitting, e.g. ease of handling missing data points, with the advantages of FT fitting, e.g. ability to ignore unwanted resonances. This is known as TDFD fitting.[26]

The application of the reference deconvolution technique to overcome the effect of magnetic field inhomogeneity in high-resolution NMR has recently been reviewed by Metz *et al.*[27] In this technique, the observed resonance lineshape from a single resonance line is used to deconvolve the observed lineshapes to produce the Lorentzian lineshapes associated with liquid samples.

In another approach, the actual experimental lineshapes in accurately prepared sample solutions are used to fit the spectrum containing unknown concentrations of the same chemical species.[28] This approach relies on the experimental artefacts causing line broadening to be the same for both measurements. This technique has been applied to MRS spectra where model spectra of metabolite solutions *in vitro* have been used as a basis set of spectra to fit the *in vivo* spectra.[29]

When evaluating a fitting technique, three levels of robustness may be considered as follows:

(1) An ideal spectrum with normally distributed random noise with poor SNR.
(2) As above but with the addition of resonances that are not able to be modelled. This can occur in MRS where not all the chemical compounds involved are known.
(3) As above, but with the further addition of spurious signals due to measurement artifacts, e.g. signals resulting from the eddy currents caused by the rapid switching of gradient coils in MRS.

Although different fitting methods may produce estimates of parameters with the same uncertainties, the methods may differ greatly in reliability. It is thus of prime importance to choose an accurate method that has the greatest robustness for the application being considered.

Before the fitting process is commenced, it is important that any artifacts are removed from the data. For example, in MRS the effects of eddy currents can normally be removed by using the phase information taken from an unsuppressed water signal.[30]

2. NMR LINESHAPES

2.1. Lorentzian lineshape

The Lorentzian lineshape is obtained for liquid samples under ideal high-resolution NMR conditions[10] and is readily derived from the Bloch equations.[31] The normalized Lorentzian lineshape function in the frequency domain is given by

$$g(f) = \frac{2}{\pi W_L} \frac{1}{1 + \left(\frac{f - f_0}{W_L/2} \right)^2} \tag{1}$$

where W_L is the full width at half maximum height (FWHM) (Hz) and f_0 is the frequency (Hz) at the centre of the resonance. Note that if the normalized

lineshape function is expressed in angular frequency units then its amplitude is divided by 2π as W_L must then be expressed in rad s^{-1} instead of Hz. As shown in Table 1, in the TD the Lorentzian lineshape corresponds to the exponential decay of the FID envelope, with a time constant equal to T_2. The transverse relaxation time, T_2 is given by

$$T_2 = 1/(\pi W_L) \tag{2}$$

The Lorentzian lineshape is shown in Fig. 1 (dashed line).

2.2. Gaussian lineshape

Random broadening effects can dominate the lineshape and lead to a lineshape that is almost Gaussian. This is often the case in MRS.[32] The Gaussian lineshape is also a convenient approximation to the lineshape for some solids.[10] The normalized Gaussian lineshape function in the frequency domain is given by

$$g(f) = \frac{2}{W_G}\sqrt{\frac{\ln 2}{\pi}}\exp\left[-\ln 2\left(\frac{f-f_0}{W_G/2}\right)^2\right] \tag{3}$$

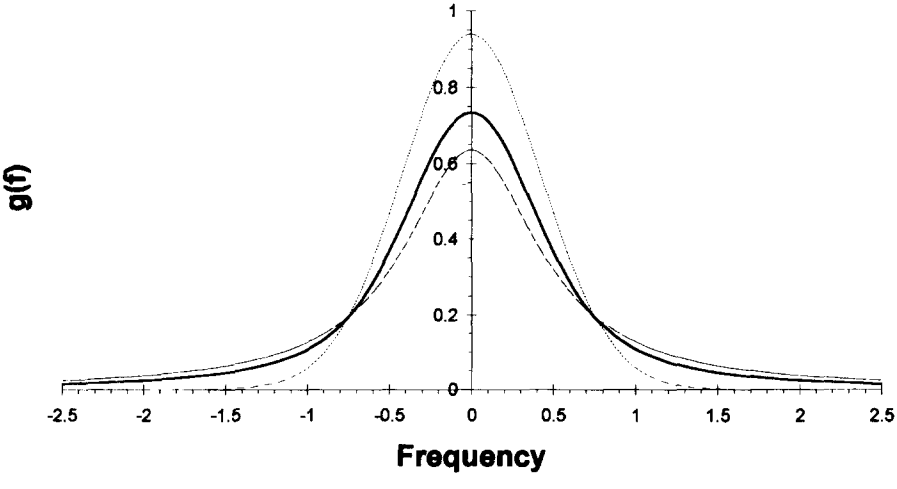

Fig. 1. The Voigt lineshape is plotted for three different values of the Voigt parameter, $a = W_L/W_G$, namely $a = 0$ (Gaussian, dotted line), $a = 1$ (solid line, with the component Lorentzian and Gaussian lineshapes having an equal width given by $W_G = W_L = 0.6107W$) and $a = \infty$ (Lorentzian, dashed line). The frequency scale is given in units of the FWHM of the Voigt lineshape, W.

Table 1. Various lineshapes in the frequency and time domains. In the frequency domain $g(f)$ corresponds to absorption mode lineshape and in the time domain $G(t)$ corresponds to the in-phase component of the FID

Shape	$g(f)$	$G(t)$
Lorentzian	$\frac{2}{\pi W_L}\frac{1}{1+\left(\frac{f}{W_L/2}\right)^2}$	$\exp(-\pi W_L t)$
Gaussian	$\frac{2}{W_G}\sqrt{\frac{\ln 2}{\pi}}\exp\left[-\left(\frac{f}{W_G/(2\sqrt{\ln 2})}\right)^2\right]$	$\exp\left[-\left(\frac{\pi W_G t}{2\sqrt{\ln 2}}\right)^2\right]$
Voigt	$\frac{2\mu^2}{W_L\pi^{3/2}}\int_{-\infty}^{\infty}\frac{\exp(-\zeta^2)\,d\zeta}{\mu^2+(f\sqrt{\ln 2}/W_G-\zeta)^2}$ where $\mu=\sqrt{\ln 2}W_L/W_G$	$\exp(-\pi W_L t)\exp\left[-\left(\frac{\pi W_G t}{2\sqrt{\ln 2}}\right)^2\right]$
Rectangle	$1/(2b)$ for $\lvert f/b\rvert<1$ $1/(4b)$ for $\lvert f/b\rvert=1$ 0 for $\lvert f/b\rvert>1$	$\mathrm{sinc}(bt)=\frac{\sin(bt)}{bt}$
Truncated Lorentzian	$\frac{1}{W_L\tan^{-1}(2f^*/W_L)}\frac{1}{1+\left(\frac{f}{W_L/2}\right)^2}$ for $f\leqslant f^*$ 0 for $f>f^*$	$\mathrm{sinc}(f^*t)\otimes\exp(-\pi W_L t)$

Note: The FT[41] of a symmetrical FD signal is a symmetrical echo signal in the TD. Hence, the FT of the FID in the TD, which exists only for positive time values, yields a FD signal of area 0.5.

where W_G is the FWHM and f_0 is the frequency (Hz) of the centre of the resonance. The Gaussian lineshape is shown in Fig. 1 (dotted line).

As shown in Table 2, the standard deviation, σ of the lineshape in the FD is given by

$$\sigma = \frac{W_G}{2\sqrt{2\ln 2}} \tag{4}$$

2.3. Voigt lineshape

Although an NMR line may have an intrinsic Lorentzian shape, it may be broadened by imperfect shimming and susceptibility variations. This is often the case for MRS.[32] If these broadening processes have a random nature, then the

Table 2. Amplitude and moments of various lineshapes

Quantity	Gaussian[10,50]	Lorentzian	Truncated Lorentzian[10]	Voigt
$g(0)$	$\frac{2}{W_G}\sqrt{\frac{\ln 2}{\pi}}$	$\frac{2}{\pi W_L}$	$\frac{1}{W_L \tan^{-1}(2f^*/W_L)}$	$\frac{2\mu^2}{\pi^{3/2} W_L}\int_{-\infty}^{\infty}\frac{\exp(-x^2)}{\mu^2+x^2}\,dx$
				$=\frac{2}{\pi W_L}$ for $\mu \to \infty$
				$=\frac{2}{W_G}\sqrt{\frac{\ln 2}{\pi}}$ for $\mu \to 0$
				$=0.735/W$ for $\mu=\sqrt{\ln 2}$
				i.e. $W_L = W_G$
M_2	$\frac{W_G^2}{8\ln 2}=\sigma^2$	∞	$2f^*W_L$	∞
M_4	$\frac{3W_G^4}{64(\ln 2)^2}=3\sigma^4$	∞	$2f^{*3}W_L/3$	∞

Notes

(1) The truncated Lorentzian is defined by

$$g(f) = \begin{cases} g_L(f) & |f| \leqslant f^* \\ 0 & |f| > f^* \end{cases}$$

(2) Since $g(f)$ is normalized, $M_0 = G(0) = 1$, except for the special case of the unnormalized truncated Lorentzian lineshape.

broadening function will have a Gaussian shape, leading to a Voigt lineshape, which is the convolution of the Lorentzian and Gaussian lineshapes.[33–35] The Voigt lineshape is also associated with the Lorentz–Gauss transformation sometimes used for resolution enhancement in NMR spectroscopy.[36] The normalized Voigt lineshape[37] in the frequency domain is given by[38]

$$V(a,f) = \frac{2\mu^2}{\pi^{3/2} W_L} \int_{-\infty}^{\infty} \frac{\exp(-\zeta^2)}{\mu^2 + (q-\zeta)^2} \, d\zeta \tag{5}$$

where W_L and W_G are the Lorentzian and Gaussian FWHM, respectively and where

$$\mu = \sqrt{\ln 2} \left(\frac{W_L}{W_G} \right) = \sqrt{\ln 2}\, a \tag{6}$$

$$\zeta = \frac{2\sqrt{\ln 2}}{W_G} f' \tag{7}$$

$$q = \frac{2\sqrt{\ln 2}(f - f_0)}{W_G} \tag{8}$$

where f_0 is the frequency (Hz) at the centre of the resonance, a is the Voigt parameter, and f' is the frequency shift of the functions in the convolution integral (i.e. the variable of integration). The Voigt lineshape is shown in Fig. 1 for three different values of the Voigt parameter, a, namely $a = 0$ (Gaussian), $a = 1$ and $a = \infty$ (Lorentzian).

2.4. Convolution of Gaussian and rectangular lineshapes

For a spin system in a solid where the lineshape is determined by the magnetic dipole–dipole interaction, the lineshape function in the FD can be approximated by a Gaussian function g_G convolved with a rectangular envelope g_R:[10]

$$g(f) = g_G(f) \otimes g_R(f) \tag{9}$$

where the convolution of g_G with g_R is defined by[39,40]

$$g_G(f) \otimes g_R(f) = \int_{-\infty}^{\infty} g_G(f - f') g_R(f') \, df' \tag{10}$$

The rectangular envelope of width $2b$ is given in Table 1.

By taking the Fourier transform of this lineshape, we can express it in the time domain as follows:

$$g_G(f) \otimes g_R(f) \xrightarrow{\mathcal{F}^-} G_G(t)G_R(t) \tag{11}$$

where $G_G(t)$ and $G_R(t)$ are the Fourier transforms of $g_G(f)$ and $g_R(f)$, respectively.

The Fourier transform and its inverse are defined by[31]

$$g(f) = \int_{-\infty}^{\infty} G(t) \exp(-2\pi i f t)\, dt \equiv \mathcal{F}^+ G(t) \tag{12}$$

and

$$G(t) = \int_{-\infty}^{\infty} g(f) \exp(2\pi i f t)\, df \equiv \mathcal{F}^- g(f) \tag{13}$$

Thus, in the time domain, the lineshape is given by[41]

$$G(t) = \exp\left[-\left(\frac{\pi W_G t}{2} \right)^2 \Big/ \ln 2 \right] \operatorname{sinc}(bt) \tag{14}$$

where $\operatorname{sinc} x = (\sin x)/x$.

An example of the application of this lineshape is shown in Fig. 2a for the free induction decay of ^{19}F in a single crystal of CaF_2 for $\mathbf{B}_0$ along the [1, 0, 0] direction.[10] Equation (14) has been used for the calculated lineshape with $b/W_G = 2.5$. The corresponding lineshape in the frequency domain is shown in Fig. 2b. Using Eq. (14), the value of the width parameter, b, used in Fig. 2b was calculated from the position of the first zero of $G(t)$ in Fig. 2a, giving $b = \pi/20$ MHz.

2.5. Lineshapes due to exchange narrowing

In some molecules, nuclei such as protons undergo magnetic site exchange.[31] In the case of spin-$\frac{1}{2}$ nuclei, random magnetic site exchange between two equally populated sites A and B gives rise to the following lineshape function.[31,42–45]

$$g(f) = \frac{\frac{1}{2}\tau_A (f_A - f_B)^2}{[f - \frac{1}{2}(f_A + f_B)]^2 + \pi^2 \tau_A^2 (f - f_A)^2 (f - f_B)^2} \tag{15}$$

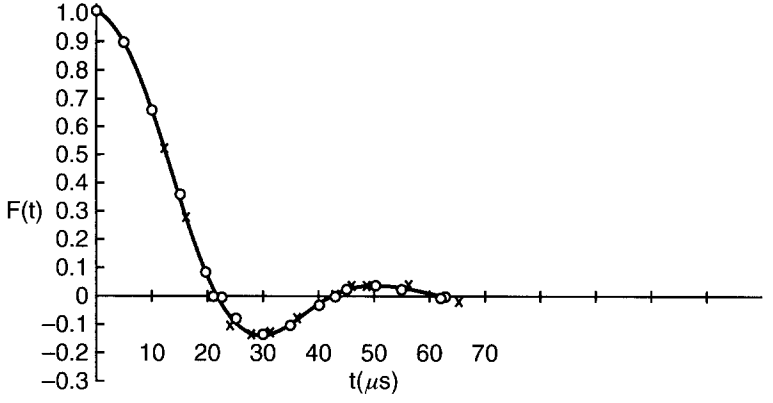

(a)

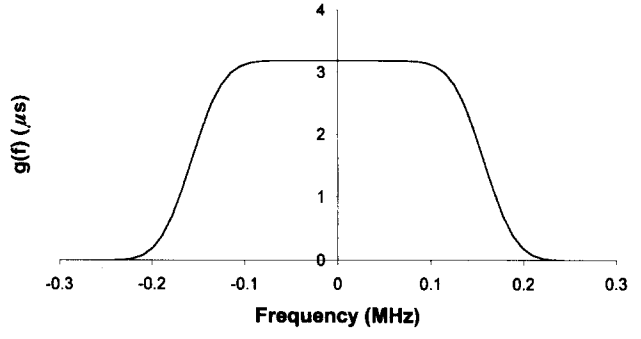

(b)

Fig. 2. (a) The free induction decay, $G(t)$ for ^{19}F in a single crystal of CaF_2 for $\mathbf{B}_0$ along [1, 0, 0]. The experimental points are given by circles and crosses from the CW and pulse measurements, respectively, and the theoretical curve is that of Eq. (14), corresponding to an exponential decay multiplied by a sinc function. Note that $F(t)$ is equivalent to $G(t)$ in the present notation. Reproduced with permission from A. Abragam, *The Principles of Nuclear Magnetism*, p. 121, Oxford University Press, London, 1961. (b) The lineshape in the frequency domain corresponding to the Fourier transform of the theoretical curve.

where f_A and f_B are the resonant frequencies at sites A and B, respectively, and τ_A is the lifetime of a nucleus in state A associated with site A.[46] In this expression, the contribution of the intrinsic width of the resonances has been neglected. The expression for the lineshape can be written in a more compact form by making the following substitutions:

$$f' = \tfrac{1}{2}(f_A - f_B) \tag{16}$$

$$\Delta f = f - \tfrac{1}{2}(f_A + f_B) \tag{17}$$

$$a = \pi f' \tau_A \tag{18}$$

$$x = \Delta f / f' \tag{19}$$

This gives

$$g(f) = \frac{2\tau_A}{x^2 + a^2(x^2 - 1)^2} \tag{20}$$

The normalization is that giving an area of 2, since for a large the lineshape consists of two separated Lorentzian resonances, as shown in Fig. 3.

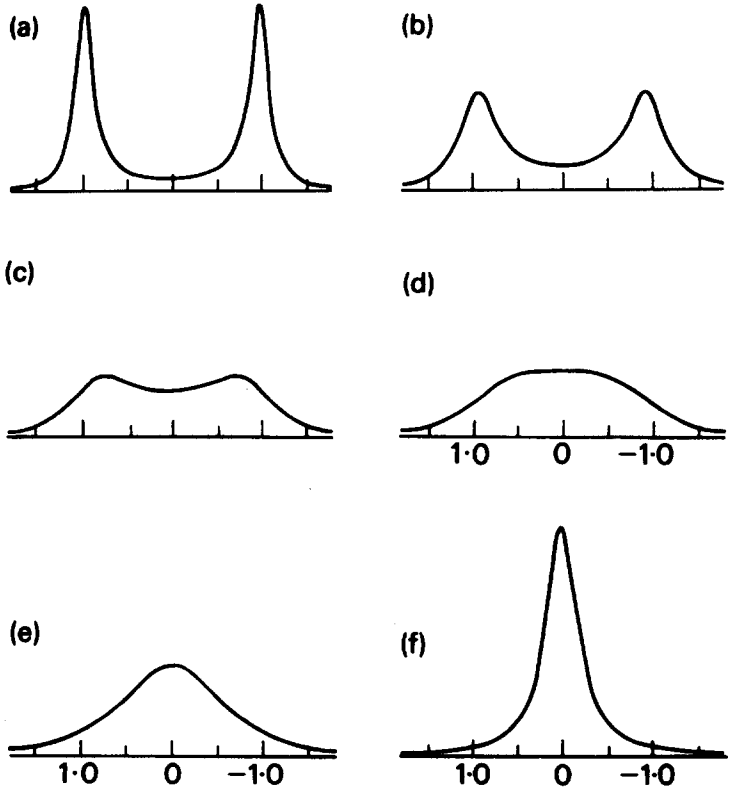

Fig. 3. Calculated NMR lineshapes for equally populated two-site exchange as a function of the dimensionless parameter $a = \pi f' \tau_A$. The abscissa is the dimensionless relative offset parameter, $x = \Delta f / f'$ (see Eq. (18)). (a) $a = 4$; (b) $a = 2$; (c) $a = 1$; (d) $a = 1/\sqrt{2}$; (e) $a = 0.5$; (f) $a = 0.2$. Spectra (a) and (f) are near the slow and fast exchange limits, respectively. Reproduced with permission from R. K. Harris, *Nuclear Magnetic Resonance Spectroscopy: A Physicochemical View*, p. 124, Longman Scientific and Technical, Harlow, 1986.

More general situations of multiple site exchanges with unequal populations where the intrinsic widths of the resonances are taken into account have been treated in detail by Sandstrom.[45] Numerous applications are given in the review by Binsch and Kessler.[47] A computer program to calculate chemical exchange lineshapes, taking all relaxation mechanisms rigorously into account, has recently been produced by Cuperlovic *et al.*[48]

2.6. Powder lineshape

The observed magnitude of the angular frequency, ω of a spectral line of negligible width can be expressed by the Euler angles (α, β), which relate the principal axes values of the angular frequency tensor $(\omega_{11}, \omega_{22}, \omega_{33})$ to the laboratory frame as

$$\omega = \omega_{11} \cos^2 \alpha \sin^2 \beta + \omega_{22} \sin^2 \alpha \sin^2 \beta + \omega_{33} \cos^2 \beta \tag{21}$$

with the convention $\omega_{33} \geqslant \omega_{22} \geqslant \omega_{11}$.[49–51] The angular frequency tensor is related to the principal axes values of the chemical shielding tensor $(\sigma_{11}, \sigma_{22}, \sigma_{33})$ by

$$\omega_{ii} = |\gamma| B_0(1 - \sigma_{ii}) \qquad \text{for} \quad i = 1, 2, 3 \tag{22}$$

For an axially symmetric tensor, we have

$$\omega = (\omega_{||} - \omega_{\perp}) \cos^2 \beta + \omega_{\perp} = \tfrac{1}{3}(\omega_{||} + \omega_{\perp}) + \tfrac{2}{3}(\omega_{||} - \omega_{\perp}) P_2(\cos \beta) \tag{23}$$

where β is the angle between the 3-axis and the direction of the magnetic field $\mathbf{B}_0$ (z-axis), and the Legendre polynomial is given by[52]

$$P_2(\cos \beta) = (3 \cos^2 \beta - 1)/2 \tag{24}$$

and where, for example,

$$\omega_{||} = \omega_{33} \tag{25a}$$

$$\omega_{\perp} = \omega_{11} = \omega_{22} \tag{25b}$$

This leads to the definition of the total anisotropy, $\Delta\omega$, as

$$\Delta\omega = \omega_{||} - \omega_{\perp} \tag{26}$$

or, in frequency units,

$$\Delta f = f_{||} - f_{\perp} \tag{27}$$

For an axially symmetric tensor, the lineshape function or intensity function $I(f)$ is given by[9, 51, 53]

$$I(f) = \tfrac{1}{2}[(f_{\|} - f_{\perp})(f - f_{\perp})]^{-1/2} = \tfrac{1}{2}[\Delta f(f - f_{\|} + \Delta f)]^{-1/2} \qquad \text{for} \quad f_{\|} \geqslant f > f_{\perp} \tag{28}$$

In the general case $f_{33} > f_{22} > f_{11}$ and the intensity function has a different functional form for each of the two available frequency ranges. For the higher frequency range $f_{33} \geqslant f > f_{22}$,

$$I(f) = \pi^{-1}[(f - f_{11})(f_{33} - f_{22})]^{-1/2} K(m) \tag{29}$$

with

$$m = \frac{(f_{22} - f_{11})(f_{33} - f)}{(f_{33} - f_{22})(f - f_{11})} \qquad \text{for} \quad f_{33} \geqslant f > f_{22} \tag{30}$$

For the lower frequency range $f_{22} > f \geqslant f_{11}$,

$$I(f) = \pi^{-1}[(f_{33} - f)(f_{22} - f_{11})]^{-1/2} K(m) \tag{31}$$

with

$$m = \frac{(f - f_{11})(f_{33} - f_{22})}{(f_{33} - f)(f_{22} - f_{11})} \qquad \text{for} \quad f_{22} > f \geqslant f_{11} \tag{32}$$

and

$$I(f) = 0 \qquad \text{for} \quad f > f_{33} \qquad \text{and} \qquad f < f_{11} \tag{33}$$

where

$$K(m) = \int_{\sigma}^{\pi/2} [1 - m^2 \sin \phi]^{1/2} \, \mathrm{d}\phi \tag{34}$$

Note that $0 \leqslant m < 1$.

Since the intrinsic lineshape has finite width, the experimentally observed lineshape is the convolution of $I(f)$ with one of the lineshape functions $g(f)$. A powder lineshape for an axially symmetric chemical shielding tensor is shown in Fig. 4 and a typical example of a general powder lineshape is shown in Fig. 5. Many systems yield lineshapes close to that of a powder pattern and the mathematical properties of these lineshapes are discussed in detail by Alexander *et al.*[54]

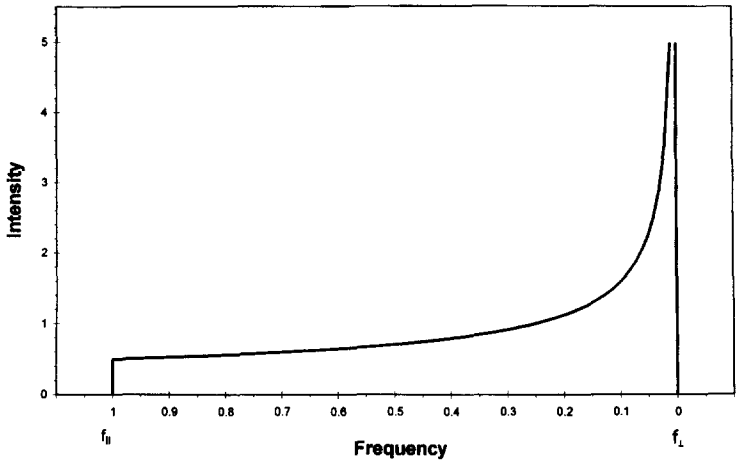

Fig. 4. A powder lineshape for an axially symmetric tensor shown as a function of frequency. The frequency scale is given in units of Δf, hence the intensity scale is in units of $1/\Delta f$. The frequency is shown increasing to the left, since it is conventional to display NMR spectra as if they were measured under CW conditions with the frequency held constant and the magnetic induction shown increasing to the right.

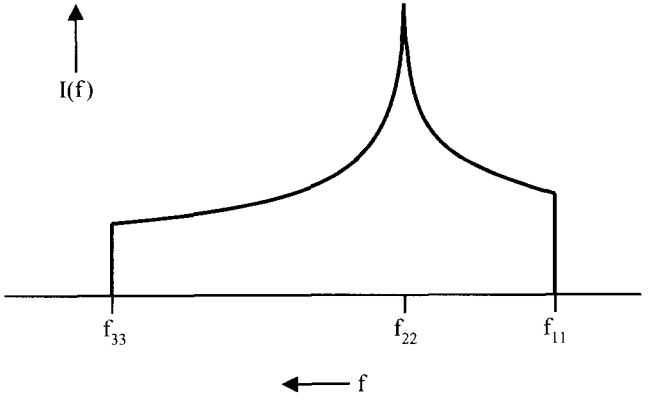

Fig. 5. A general powder lineshape. The shape is given by Eqs (29) to (34).

2.7. Quadrupolar lineshape

A nucleus with a nuclear spin $I > \frac{1}{2}$ may possess a charge distribution that has a nuclear quadrupolar moment, Q. Such a nucleus may interact with a nonhomogeneous electric field possessing an electric field gradient, which can be expressed in terms of the second derivative of the electrostatic potential, V.[31]

For convenience, the quantity q_{zz} is defined in terms of the electronic charge, e, to be proportional to the electric field gradient in the z-direction as follows:

$$eq_{zz} = \frac{d^2V}{dz^2} \tag{35}$$

The energy levels for the Zeeman–Quadrupolar Hamiltonian are given by[31,55]

$$E(m) = -f_0 mh + \frac{\chi[3m^2 - I(I+1)]}{8I(2I-1)}(3\cos^2\theta - 1)h \qquad \text{for} \quad -I \leqslant m \leqslant I \tag{36}$$

where

$$f_0 = |\gamma| \mathbf{B}_0(1-\sigma)/2\pi \tag{37}$$

and

$$\chi = e^2 Q q_{zz}/h \tag{38}$$

is the static quadrupolar coupling constant ($\sim$168 kHz) for ^{2}H.[56–58] That is,

$$E(m) = -f_0 mh + \frac{\chi[3m^2 - I(I+1)]}{4I(2I-1)} P_2(\cos\theta)h \tag{39}$$

where the Legendre polynomial is given by Eq. (24) and θ is the angle between $\mathbf{B}_0$ and q_{zz}.

For $I = 1$, we have

$$E(m) = -f_0 mh + \frac{\chi}{4}[3m^2 - 2]P_2(\cos\theta)h \tag{40}$$

Therefore,

$$E(-1) = f_0 h + \frac{\chi}{4} P_2(\cos\theta)h \tag{41a}$$

$$E(0) = 0 - \frac{\chi}{2} P_2(\cos\theta)h \tag{41b}$$

$$E(1) = -f_0 h + \frac{\chi}{4} P_2(\cos\theta)h \tag{41c}$$

$$f_{0\to -1} = \frac{E(-1) - E(0)}{h} = f_0 + \frac{3\chi}{4} P_2(\cos\theta) \tag{42a}$$

$$f_{1\to 0} = \frac{E(0) - E(1)}{h} = f_0 - \frac{3\chi}{4} P_2(\cos\theta) \tag{42b}$$

where the subscripts attached to f indicate the change in the values of m associated with the transition.

The energy levels are shown in Fig. 6 and the corresponding spectrum is shown in Fig. 7. From Eq. (39) it follows that the extreme positions ($f_{\|}$ and $f_{\perp}$) of the two lines in the spectrum occur for

(i) $\theta = 0$, thus $P_2(\cos\theta) = 1$, giving $f_{\|}$ and
(ii) $\theta = \pi/2$, thus $P_2(\cos\theta) = -1/2$, giving $f_{\perp}$

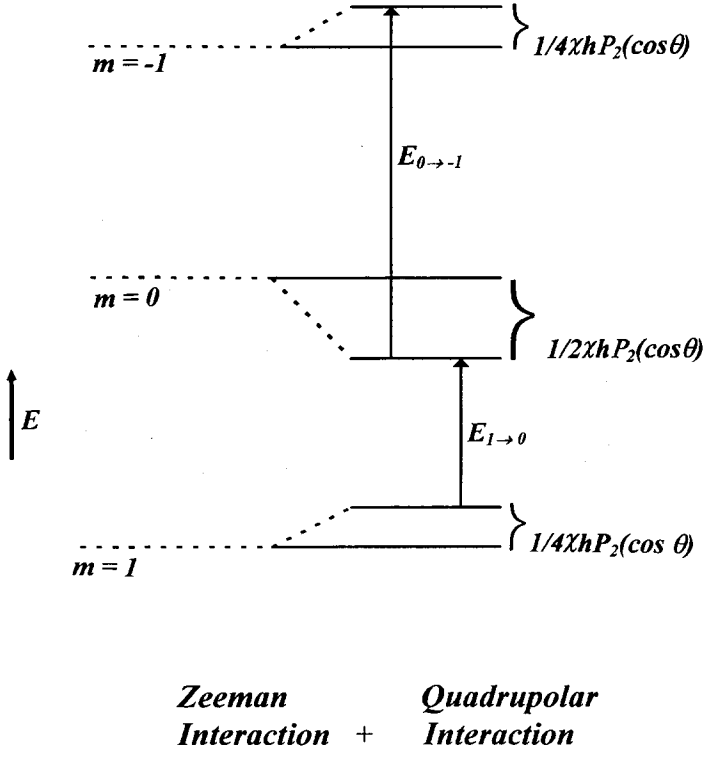

Fig. 6. Energy level splitting due to the Zeeman interaction and the quadrupolar interaction for a spin-1 nucleus. The scale has been exaggerated for clarity.

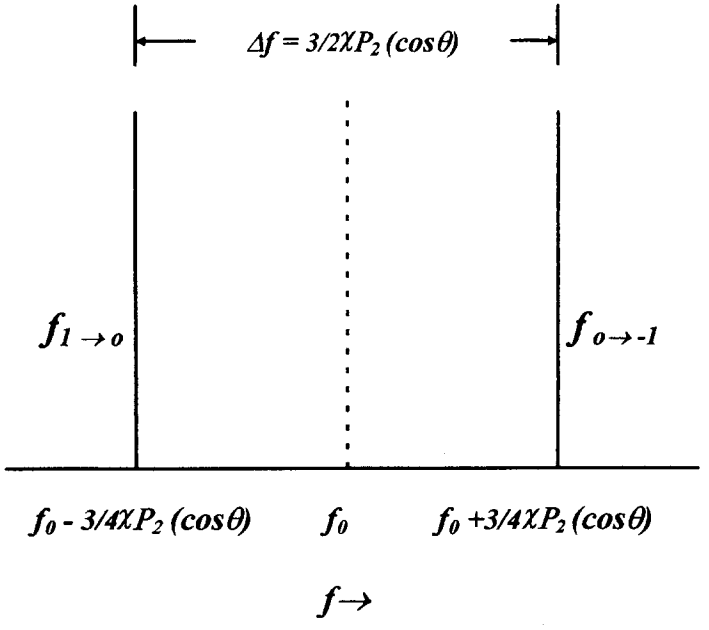

Fig. 7. Transition frequencies resulting from the Zeeman interaction and the quadrupolar interaction for a spin-1 nucleus.

The powder pattern for an $I = 1$ quadrupolar interaction can be obtained by reflecting the axially symmetric chemical shielding powder pattern about its average value,[53] as shown in Fig. 8. This follows from Eqs (42a) and (42b) having the same functional form as that of Eq. (24). From Eq. (42b) we obtain

$$f_{\|} - f_{\perp} = -\left[\frac{3}{4} - \left(-\frac{3}{8}\right)\right]\chi = -\frac{9\chi}{8} \qquad \text{for} \quad f_{1\to 0} \tag{43}$$

That is,

$$f_{\|} - f_{\perp} = +\frac{9\chi}{8} \qquad \text{for} \quad f_{0\to -1} \tag{44}$$

i.e. $\omega_{\|} > \omega_{\perp}$ as used in Eq. (23)

The lineshape for $f_{0\to -1}$ is thus given from Eq. (28) by

$$I(f_{0\to -1}) = \tfrac{1}{2}[(f_{\|} - f_{\perp})(f - f_{\perp})]^{-1/2} \qquad \text{for} \quad f_{\perp} \leqslant f \leqslant f_{\|} \tag{45}$$

where

$$f_{\|} - f_{\perp} = \frac{9\chi}{8} \tag{46a}$$

$$f_{\perp} = f_0 - \frac{3\chi}{8} \tag{46b}$$

The lineshape for $f_{1\to 0}$ is given from Eq. (28) by

$$I(f_{1\to 0}) = \tfrac{1}{2}[(f_{\|} - f_{\perp})(f - f_{\perp})]^{-1/2} \qquad \text{for} \quad f_{\|} \leqslant f \leqslant f_{\perp} \tag{47}$$

where

$$f_{\|} - f_{\perp} = -\frac{9\chi}{8} \tag{48a}$$

$$f_{\perp} = f_0 + \frac{3\chi}{8} \tag{48b}$$

The total lineshape is thus the sum of these two components and is given by

$$I(f) = \tfrac{1}{2}[I(f_{0\to 1}) + I(f_{-1\to 0})] \tag{49}$$

This lineshape is often referred to as a Pake doublet or Pake pattern[59] and is shown in Fig. 8.

2.8. Lineshape due to Brownian motional narrowing

In many crystals, the lineshape is affected by self-diffusion of the atoms from one crystal site to another. The resulting lineshape can be expressed in the time domain as[10]

$$G(t) = \exp\{-\omega_p^2 \tau_c^2 [\exp(-t/\tau_c) - 1 + (t/\tau_c)]\} \tag{50}$$

where τ_c is the correlation time associated with the diffusion and ω_p^2 is the second moment of the intrinsic line. We see that, in the limit of negligible diffusion,

$$\lim_{1/\tau_c \to 0} G(t) = \exp(-\omega_p^2 t^2/2) \tag{51}$$

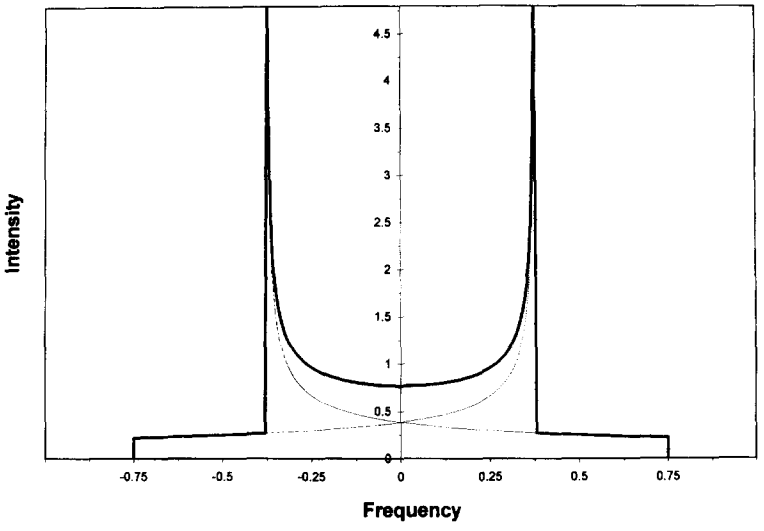

Fig. 8. The powder pattern for an $I = 1$ quadrupolar interaction. The two components of the lineshape given in Eq. (49) are also shown as dashed lines. The frequency scale is in units of χ, hence the intensity scale is in units of $1/\chi$. The centre of the spectrum is located at the frequency f_0.

Thus, for $\omega_p \tau_c$ large, $G(t)$ becomes a Gaussian. By comparison with Eq. (14), we see that the rms width ω_p given by

$$\omega_p = \pi W_G / \sqrt{2 \ln 2} \tag{52}$$

This long correlation time regime corresponds to that found in solids, where wide resonance lines are obtained, which may be approximately Gaussian in shape.

Also, we have

$$\lim_{\omega_p \tau_c \to 0} G(t) = \exp(-\omega_p^2 \tau_c t) \tag{53}$$

Thus for $\omega_p \tau_c$ small, we see from Table 1 that $G(t)$ corresponds to a Lorentzian, $g_L(f)$ with FWHM given by

$$W_L = \omega_p^2 \tau_c / \pi \tag{54}$$

This short correlation time regime corresponds to that found in liquids, where narrow resonance lines with a Lorentzian shape are observed.

Since the even moments, M_{2n} are given by[10]

$$M_{2n} = (-1)^n \left(\frac{\mathrm{d}^{2n} G}{\mathrm{d}t^{2n}} \right)_{t=0} \tag{55}$$

we find from Eq. (50) that

$$M_2 = \omega_\mathrm{p}^2 \tag{56a}$$

and

$$M_4 = 3\omega_\mathrm{p}^4 - \omega_\mathrm{p}^2/\tau_\mathrm{c}^2 \tag{56b}$$

for all values of $\tau_\mathrm{c} > 0$. Thus $G(t)$ corresponds to a lineshape having finite second and fourth moments, as required by quantum mechanics, yet yields a Lorentzian shape in the limit of a short correlation time.

2.9. Comparison of various lineshapes

Some of the most common lineshapes are tabulated in Table 1. The Lorentzian, Gaussian and Voigt lineshapes are shown in Fig. 1. The use of an approximation to the Voigt function is shown in Fig. 18. A detailed tabulation of the properties of the Gaussian and Lorentzian lineshapes and their first and second derivatives is given by Poole.[50] The FWHM of the Voigt function, W, in terms of the FWHM of the component Lorentzian, W_L, and that of the component Gaussian, W_G, is given both in tabular and graphical form by Van de Hulst and Reesinck.[34]

In Table 1, the frequency is measured from the centre of the resonance, which is taken as the origin. For the more general case where the centre of the resonance occurs at a frequency f_0, f in $g(f)$ is simply replaced by $(f - f_0)$ and $G(t)$ is multiplied by $\cos(2\pi f_0 t)$. This latter result is a consequence of the Fourier transform frequency-shifting theorem applied to the even function $g(f)$.[41] The lineshape functions in the TD are those associated with a pulse and are defined for $t \geqslant 0$. The lineshapes for the corresponding spin echo signal, for which $-\infty < t < \infty$, are obtained by replacing t by $|t|$ in the expressions given, provided $T_2 \gg T_2^*$, where T_2^* is the effective value of T_2.[31] Other more complicated lineshapes occur in particular situations. For example, under certain conditions a super-Lorentzian lineshape occurs for vesicles,[60–63] given by

$$g(f) = \frac{2}{\pi W_\mathrm{L}} \int_0^1 \frac{1 + Q\,|\,P_2(\mu)\,|^2}{1 + Q\,|\,P_2(\mu)\,|^2 + \left(\dfrac{f}{W_\mathrm{L}/2} \right)^2} \,\mathrm{d}\mu \tag{57}$$

where $\mu = \cos\theta$ and $Q = M_{2r}\tau_c T_2$ where M_{2r} is the residual second moment and τ_c is a correlation time associated with the rotational diffusion equation. This lineshape is shown in Fig. 9.

Another example is the deuterium NMR lineshape from chain segments in a deformed elastomer, which can be expressed in terms of the deformation, λ, as[64]

$$g(f,\lambda) = \left(\frac{3N\pi}{2f_1}\right)\left[2\lambda + \frac{1}{\lambda^2}\right]^{-1/2}\left[g_+\left(|f| + \frac{\Delta f}{2}, \lambda\right) + g_-\left(|f| - \frac{\Delta f}{2}, \lambda\right)\right] \tag{58}$$

where

$$\Delta f = \left|\frac{2f_Q}{\pi}\langle P_2(\cos\theta)\rangle_v\right| \tag{59}$$

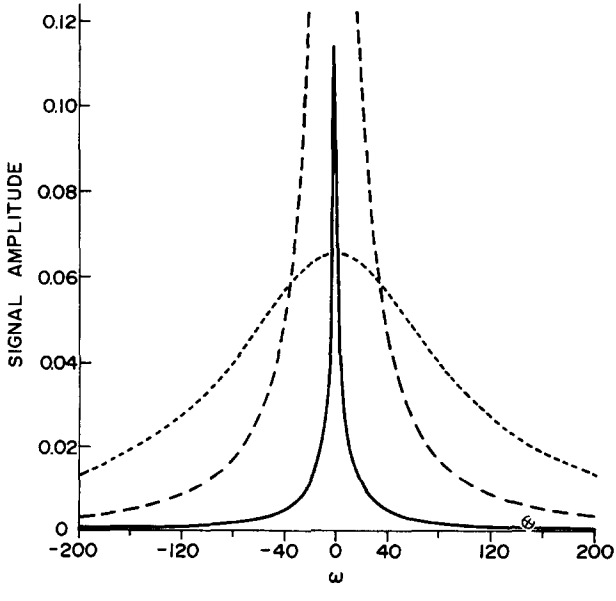

Fig. 9. The solid curve depicts the super-Lorentzian lineshape $g(\omega)$ for a single spin species in vesicles according to Eq. (57) for $Q = 100$. The frequency scale is given in units of $1/T_2$. The wide skirts on which the sharp line is superimposed are illustrated by the plot of $10g(\omega)$ versus ω (dashed curve). A Lorentzian line ($\times$ 10) of width $100/T_2$ is shown for comparison (small-dashed curve). Reproduced with permission from M. Bloom, *Chem. Phys. Lipids*, 1975, **14**, 107. © 1975 American Chemical Society.

with

$$g_+(f, \lambda) = \exp[-3N\pi\lambda f/f_Q] \tag{60}$$

When

$$|f| \leqslant \frac{\Delta f}{2},$$

$$g_-(f, \lambda) = \exp[3N\pi\lambda f/f_Q] \tag{61}$$

and when

$$|f| \geqslant \frac{\Delta f}{2},$$

$$g_-(f, \lambda) = \exp[3N\pi\lambda f/f_Q]\left\{1 - \operatorname{erf}\left[z(f)\sqrt{\frac{3}{2}\left(2\lambda + \frac{1}{\lambda^2}\right)}\right]\right\} \tag{62}$$

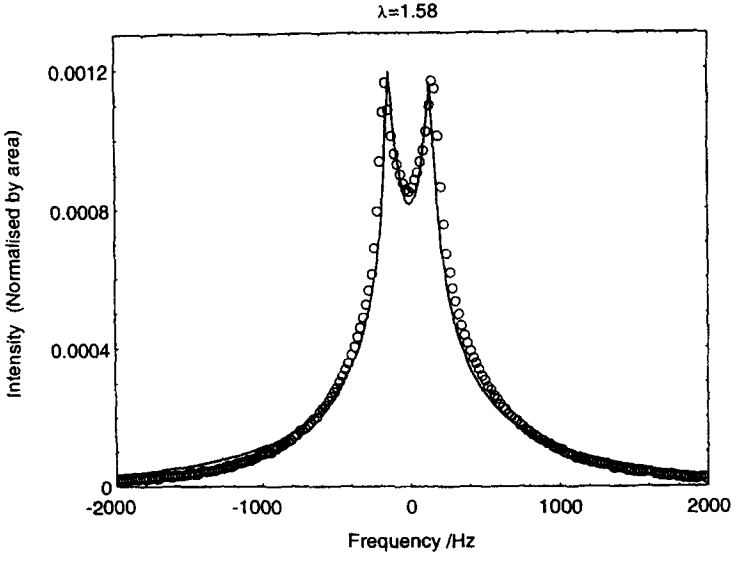

Fig. 10. Circles show the data from a strained poly(butadiene) network with the corresponding theoretical fit for the deformation ratio $\lambda = 1.58$. Reproduced with permission from M. E. Ries, M. G. Brereton, P. G. Klein, I. M. Ward, P. Ekanayake and H. Schneider, *Macromolecules*, 1999, **32**, 4961.

with

$$z(f) = \sqrt{\frac{N\pi}{f_Q}} \tag{63}$$

where f_Q is the rescaled quadrupolar coupling constant,[65] N is the number of statistical segments between cross-links, erf is the error function[66] and the Legendre polynomial is given by Eq. (24). Note that the symbol v in Eq. (59) indicates that the excluded volume interactions are taken into account. The deformation λ is given by the length of the deformed sample divided by its initial undeformed length. The experimental data and corresponding theoretical fit for a strained poly(butadiene) network for $\lambda = 1.58$ is shown Fig. 10. Other examples of complicated lineshapes are the Gauss–Lorentz product curve[37] and the Kubo–Tomita curve.[67] Since a lineshape can be expressed in terms of its moments, the moments of some of the most commonly used lineshapes are given in Table 2.

3. APPROXIMATIONS TO NMR LINESHAPES

3.1. Approximations to the Voigt lineshape

The Voigt function can be expressed in terms of the real part of the complex error function,[68–71]

$$V(a,f) = \frac{2\mu}{\pi^{3/2} W_L} \Re\left\{ i \int_{-\infty}^{\infty} \frac{\exp(-\xi^2)\, d\xi}{z - \xi} \right\} \tag{64}$$

where $z = q + i\mu$ and the other symbols are defined in Eqs (5) to (8). This can be written as[38,69]

$$V(a,f) = \frac{2\mu}{\pi^{1/2} W_L} \Re\{\exp(-z^2)\ \mathrm{erfc}(-iz)\} \tag{65}$$

where erfc is the complementary error function. The Voigt function can then be approximated by an appropriate complex Taylor series expansion.[70] A numerical tabulation of the dimensionless form of the Voigt function has been given by Faddeyeva and Terent'ev.[72] The Voigt function can also be expressed as a series expansion.[73] Using a Taylor series expansion valid for $\mu \gg 1/\sqrt{2}$, the width of the Voigt function, W can be approximated by[74,75]

$$W \cong W_L \left(1 + \frac{3}{4\mu^2} \right) \qquad \text{for} \quad \mu \gg \frac{1}{\sqrt{2}} \tag{66}$$

For a Voigt function that is almost Lorentzian, the extent of Gaussian broadening can be visualized by plotting the dispersion of the lineshape, $D(f)$ against the absorption, $A(f)$.[76,77] For a pure Lorentzian lineshape, a circle is obtained. Hence, the extent of the departure from this circular shape indicates the extent of the Gaussian broadening.

Using a Taylor series expansion in the TD it can be shown that, to a good approximation,[78] the Voigt function can be written as V', a linear combination of Lorentzian, $g_L(f)$ and Gaussian $g_G(f)$ functions having the same width, $W = W_L = W_G$, namely

$$V'(f) = rg_L(f) + (1 - r)g_G(f) \tag{67}$$

where r is the fractional parameter that varies the relative contributions of $g_L(f)$ and $g_G(f)$. Since the use of V' instead of V results in errors of less than 0.72% in the calculation of the area of the lineshape over the full range of the Voigt parameter, as shown in Fig. 11, this approximation is appropriate to minimize computational time. A more general numerical approximation to the Voigt function in which $W_L \neq W_G$ has also been evaluated.[75]

3.2. Moment expansions

The lineshape of a crystalline solid can be expressed in terms of a moment expansion[10,62]

$$G(t) = \sum_{n=0} (-1)^n \frac{M_{2n} t^{2n}}{2n!} \tag{68}$$

where the moments are defined by

$$M_n = \int (\omega - \omega_0)^n g(\omega)\, \mathrm{d}\omega \tag{69}$$

Note that $G(t)$ is also the reduced autocorrelation function.[10] The above series, however, converges very slowly. In practice it is therefore necessary to use a modified moment expansion that converges more rapidly. In order to obtain an explicit expression for $G(t)$, we consider a single crystal containing only one species of nuclei with spin $\frac{1}{2}$ such that the nuclei are located at the points of a lattice. We further assume that the only interaction present is the nuclear dipole–dipole interaction. It can be shown that[10]

$$G(t) = \mathrm{tr}\{\exp(\mathrm{i}\mathcal{H}'_1 t)\mathcal{M}_x \exp(\mathrm{i}\mathcal{H}'_1 t)\mathcal{M}_x\} \tag{70}$$

where $\mathcal{M}_x$ is the operator corresponding to the x component of the magnetization and tr stands for trace.

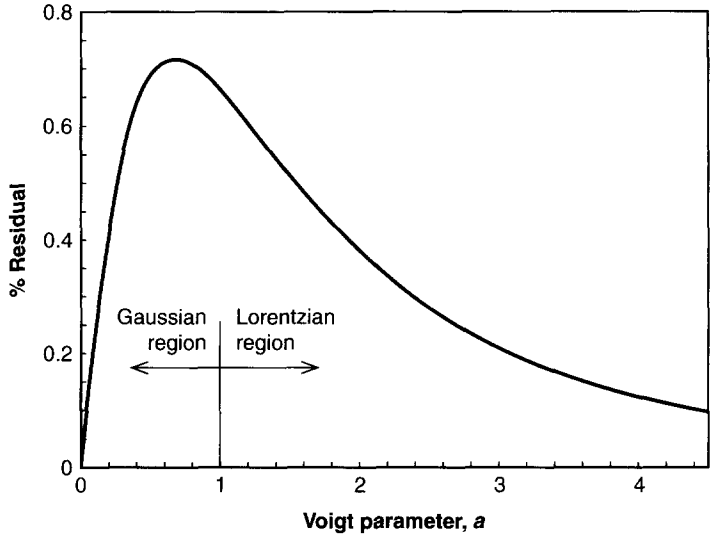

Fig. 11. The peak area residual between the Voigt function and the approximated Voigt function is shown as a function of the Voigt parameter, *a*. This diagram was obtained by replotting the information in S. Bruce, J. Higinbotham, I. Marshall and P. H. Beswick, *J. Magn. Reson.*, 2000, **142**, 57.

The secular part $\mathcal{H}_1'$ is a sum of two terms α and β:[10]

$$\alpha = -\frac{\gamma^2\hbar^2\mu_0}{12\pi}\sum_{j<k} b_{jk} I^j \cdot I^k \tag{71a}$$

$$\beta = \frac{\gamma^2\hbar^2\mu_0}{4\pi}\sum_{j<k} b_{jk} I_z^j I_z^k \tag{71b}$$

where

$$b_{jk} = \tfrac{3}{2}(1 - 3\cos^2\theta_{jk})/r_{jk}^3 \tag{71c}$$

and I^j is the spin operator of the jth nucleus, r_{jk} is the vector separation of the jth nucleus from the kth nucleus, θ_{jk} is the angle between r_{jk} and $\mathbf{B}_0$, γ is the gyromagnetic moment of the nucleus,

$$[\alpha, \mathcal{M}_x] = 0 \tag{72a}$$

$$[\beta, \mathcal{M}_x] \neq 0 \tag{72b}$$

$$[\alpha, \beta] \neq 0 \tag{72c}$$

Because of Eq. (72c) we expand the exponential $\exp[it(\alpha+\beta)]$ as

$$\exp[it(\alpha+\beta)] = \exp(i\beta t)X(t)\exp(i\alpha t) \tag{73}$$

where $X(t)$ is a correction term to take care of the noncommutability of α and β, given by

$$X(t) = \exp(-i\beta t)\exp[it(\alpha+\beta)]\exp(-i\alpha t) \tag{74}$$

This correction term is now approximated by a power series

$$X(t) = 1 + \sum_n \frac{c_n}{n!} t^n \tag{75}$$

This leads to $G(t)$ being expressed as a series expansion:[10]

$$G(t) = \sum_n \frac{F_n(t)t^n}{n!} \tag{76}$$

The series in Eq. (76) converges more rapidly than that in Eq. (68) owing to the presence of trigonometric functions of time in $F_n(t)$. For the case of a simple cubic lattice, we obtain[12]

$$G(t) = U(t)V(t) \tag{77}$$

where

$$U(t) = \prod_j{}' \cos(\omega_{jk}t) \tag{78}$$

and

$$\begin{aligned} V(t) = 1 - \frac{1}{6}\Bigg[& \left\{ \sum_k{}' \omega_{jk}t \tan(\omega_{jk}t) \right\}^2 - \sum_k{}' \{\omega_{jk}t \tan(\omega_{jk}t)\}^2 \\ & + \frac{2}{9}\Bigg[\left(\sum_k{}' (\omega_{jk}t)^2 \right) \left\{ \sum_k{}' \omega_{jk}t \tan(\omega_{jk}t) \right\} \\ & - \sum_k{}' (\omega_{jk}t)^3 \tan(\omega_{jk}t) \Bigg] \\ & - \frac{1}{12}\Bigg[\left(\sum_k{}' (\omega_{jk}t)^2 \right)^2 - \sum_k{}' (\omega_{jk}t)^4 \Bigg] \end{aligned} \tag{79}$$

and where

$$\omega_{jk} = \frac{3\mu_0}{16\pi}(\gamma^2\hbar/r_{jk}^3)(1 - 3\cos^2\theta_{jk}) \tag{80}$$

where r_{jk} is the distance between the kth and jth nuclei and θ_{jk} is the angle between $\mathbf{r}_{jk}$ and $\mathbf{B}_0$. The prime notation indicates the exclusion of the diagonal term $j = k$. In order to evaluate Eq. (79) for ^{19}F nuclei in CaF_2, the terms corresponding to the first 26 closest fluorine nuclei were evaluated individually, and the terms corresponding to more remote nuclei were collected into another sum by a power series expansion. This latter quantity was found to be isotropic to within ±5% for the orientations considered. The fluorine nearest-neighbour separation was taken to be 272.5 pm. The results for $\mathbf{B}_0$ along the [1, 0, 0] direction are shown in Fig. 12.[10]

3.3. Rational function expansions

The NMR lineshapes obtained in MRS are often assumed to have a Voigt lineshape.[32,79] The Voigt lineshape, however, does not have a simple analytical form. None the less, as shown earlier, the Voigt lineshape can conveniently be approximated as a linear sum of Gaussian and Lorentzian lineshapes.[33,78]

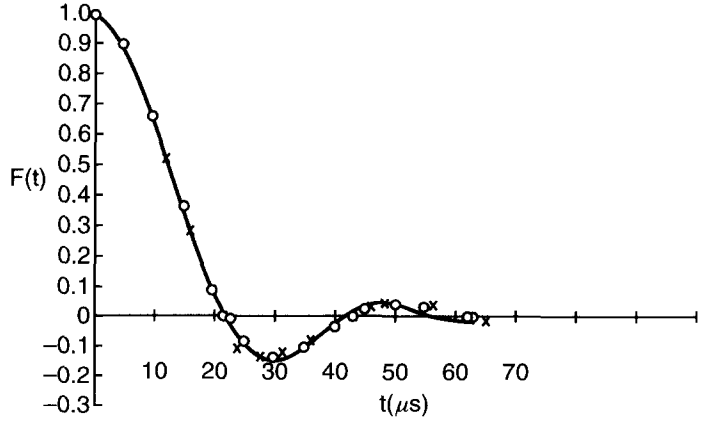

Fig. 12. The free induction decay of ^{19}F in a single crystal of CaF_2 with $\mathbf{B}_0$ along the [1, 0, 0] direction. The crosses and circles correspond to the experimental data and the solid line is calculated from Eq. (76) using only terms up to t^4. Note that $F(t)$ is equivalent to $G(t)$ in the present notation. Reproduced with permission from A. Abragam, *The Principles of Nuclear Magnetism*, p. 118, Oxford University Press, London, 1961.

Rational functions were introduced by Maltempo[80] for approximating resonances having generalized spectroscopic lineshapes. These functions have two main advantages, namely being entirely general even if the lineshape is asymmetric and not requiring any preliminary knowledge of parameters.

To describe symmetric lineshapes, Maltempo[80] defined linear combinations of normalized Lorentzian and Gaussian lineshapes (hybrid lineshapes) as the function

$$g(f) = rg_L(f) + (1 - r)g_G(f) \tag{81}$$

with the lineshapes having a common width parameter, σ' in magnetic induction units given from Eq. (22) by

$$\sigma' = \pi W_L/\gamma = \pi W_G/(\gamma\sqrt{\ln 2}) \tag{82}$$

The rational function approximations to the Lorentzian and Gaussian lineshapes were written as

$$S(u, \beta_i) = \frac{1}{\sigma'\sqrt{\pi}} \frac{\beta_1 + \beta_2 u^2}{\beta_3 + \beta_4 u^2 + \beta_5 u^4} \tag{83}$$

with the coefficients as given in Table 3, where the function has been fitted over the range $-1.86\sigma'$ to $+1.86\sigma'$ for the variable $u = B/\sigma'$ and where the magnetic induction is measured from the centre of the resonance.[80]

The resulting fit for the case of the Gaussian is shown in Fig. 13. For the same fitting range, various hybrid lineshapes, corresponding to different values of r, were also fitted by rational functions and are shown in Fig. 14.

Bergmann *et al.*[81] have investigated two overlapping resonances of Lorentzian shape using rational functions. More recently, Roberts *et al.*[82] have introduced a method that can be applied, in principle, to any number of overlapping resonances. This is an iterative method of determining a rational function that fits a given lineshape in a least-squares sense. For the case of m Lorentzian lines, the degree N of the denominator is $2m$, while that of the

Table 3. Coefficients of the rational function approximation

$$S(u, \beta_i) = \frac{\beta_1 + \beta_2 u^2}{\beta_3 + \beta_4 u^2 + \beta_5 u^4}$$

	β_1	β_2	β_3	β_4	β_5
Gaussian (G)	1	−0.203 659	0.997 332	0.674 201	0.519 307
Lorentzian (L)	1	0	1.772 45	1.772 45	0

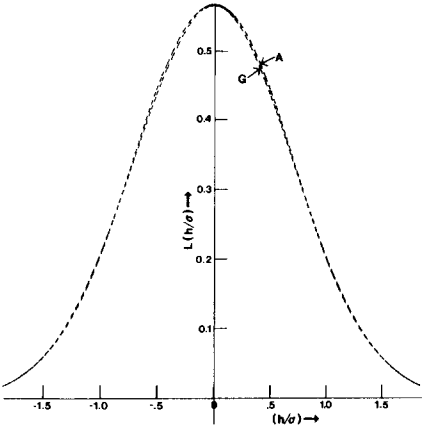

Fig. 13. Normalized Gaussian (G) lineshape $(1/\sigma'\sqrt{\pi})\exp(-B/\sigma')^2$ and rational function (A) approximation $(1/\sigma'\sqrt{\pi})S(B/\sigma', \beta_i)$ for $C = 1.86$ $(m = 1)$. Note that $\sigma' = \sqrt{2}\sigma$ where σ is the standard deviation of the Gaussian in magnetic induction units and Maltempo uses h to represent B. Reproduced with permission from M. M. Maltempo, *J. Magn. Reson.*, 1986, **68**, 102.

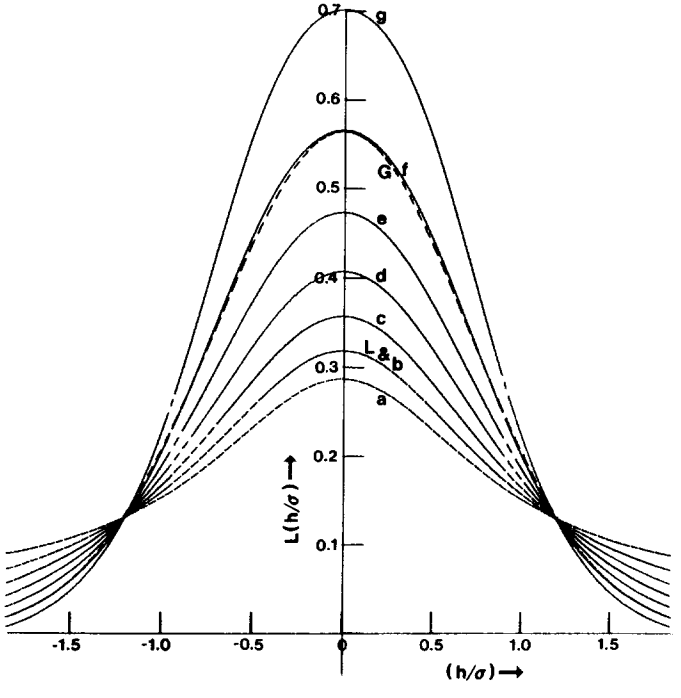

Fig. 14. Normalized Gaussian (G), normalized Lorentzian (L), and hybrid lineshapes for various values of m $(C = 1.86)$; (a) $m = 0.25$, (b) $m = 0$, (c) $m = 0.25$, (d) $m = 0.5$, (e) $m = 0.75$, (f) $m = 1.0$, (g) $m = 1.25$. Reproduced with permission from M. M. Maltempo, *J. Magn. Reson.*, 1986, **68**, 102.

numerator, M is $2m-2$. In partial fraction form, the lineshape, $g(x)$ is described by

$$g(x) = \sum_{k=1}^{m} \frac{A_k}{(x-\alpha_k)^2 + (\beta_k)^2} \tag{84}$$

where the *real* numbers A_k, α_k and β_k ($k = 1, 2, \ldots, m$), are to be estimated from the fit.

From a computational point of view it is important to ensure that the problem is not ill-conditioned so as to maintain numerical stability. Therefore, the use of rational functions as proposed by Bergmann *et al.*[81] is combined with the established practice of fitting polynomials to given data using orthogonal polynomial bases.[83] A system of linear equations is solved at each iteration.[81] Hence, the condition number[83] of this system may be used to monitor numerical stability.

The outline of this method is as follows. For the given data (x_i, f_i), $i = 1, \ldots, n$, two polynomials $P(x)$ and $Q(x)$ of maximum degrees M and N, respectively, are sought so that the quantity

$$L = \sum_{i=1}^{n} \left[f_i - \frac{P(x_i)}{Q(x_i)} \right]^2 \tag{85}$$

is a minimum. In terms of the equations determining the coefficients of the numerator and denominator polynomials, this is a nonlinear problem. It may, however, be reduced to a sequence of linear problems by considering the following quantities for the kth iteration:[81]

$$L^{(k)} = \sum_{i=1}^{n} W^{(k)}(x_i)[f_i Q^{(k)}(x_i) - P^{(k)}(x_i)]^2 \qquad k = 1, 2, \ldots \tag{86}$$

where

$$W^{(k)}(x) = [Q^{(k-1)}(x)]^{-2} \tag{87}$$

An iteration is begun by providing a reasonable starting form for the denominator polynomial $Q^{(0)}(x)$. For example, the results presented were obtained using $Q^{(0)}(x) = 1 + x + x^2 + \cdots + x^N$. Since, at the kth iteration stage, $W^{(k)}(x)$ is known, $L^{(k)}$ may then be minimized to obtain $P^{(k)}(x)$ and $Q^{(k)}(x)$ by solving a system of linear equations. Termination is reached when corresponding polynomials of consecutive steps are sufficiently close to each other. There is no guarantee, however, that this will happen, although numerical experiments indicate that this is usually the case.

This method is illustrated in Fig. 15 for the simulated spectra for the AA′B type spectrum for C26 and C27 of 16.67 mol% [25,26,27-^{13}C]cholesterol in dimyristoylphosphatidyl choline (DMPC) vesicles at 90 MHz. The simulated spectrum is plotted using 100 data points, where 1% noise (i.e. SNR of 100) has been added. The solid line represents the fitted lineshape. The parameters obtained from the fit are compared with their known values in Table 4. Since each component in the spectrum corresponds to a quadratic factor of the denominator polynomial (cf. Eq. (84)), estimates of the position and width of a line may be determined from the real and imaginary parts, respectively, of the appropriate zeros of the denominator polynomials ($\alpha_k \pm i\beta_k, k = 1, \ldots, m$).

It should be emphasized that for this approach to be successful, several data points per peak and a relatively high SNR are required. Under these conditions, a fit by a rational function provides a robust method for obtaining starting values for the nonlinear least-squares fitting techniques listed in

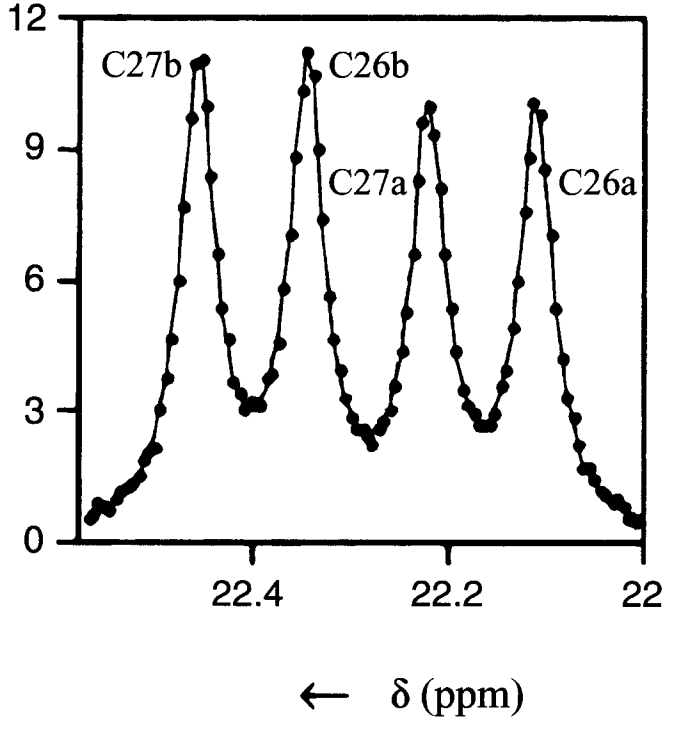

Fig. 15. Simulated spectra for C26 and C27 of 16.67 mol% [25,26,27-^{13}C]cholesterol in DMPC vesicles for a spectrometer operating at a frequency of 90 MHz. The simulated spectrum is plotted using 100 data points, where 1% noise (i.e. S/N ratio of 100) has been added. The solid line represents the fitted lineshape. Reproduced with permission from D. E. Roberts, Y. Z. Wu, R. Yusaf, J. Higinbotham, A. J. Shand and I. C. Malcolm, 1997, *Magn. Reson. Chem.*, **35**, 468. © 1997 John Wiley and Sons Ltd.

Table 4. Averages of parameter values obtained from the rational function fitting procedure from 100 sets of data with SNR = 100

Parameters	Species	Exact value	Fitted value
Intensities	C26a	1.007	0.999 ± 0.037
	C27a	1.023	1.029 ± 0.042
	C26b	1.228	1.230 ± 0.036
	C27b	1.210	1.200 ± 0.028
Positions (ppm)	C26a	22.0293	22.0361 ± 0.03
	C27a	22.1401	22.1306 ± 0.03
	C26b	22.4165	22.4170 ± 0.001
	C27b	22.5272	22.5290 ± 0.001
Widths (ppm)	C26a	0.035 575	0.0357 ± 0.0013
	C27a	0.035 575	0.0368 ± 0.0017
	C26b	0.035 575	0.0371 ± 0.0011
	C27b	0.035 575	0.0354 ± 0.0001

C26 and C27 of [25,26,27-^{13}C]cholesterol.

Table 5. Note that in the paper by Roberts *et al.*,[82] a factor of $1/n$ is missing in the definition of E in Eq. (18) in that paper.

4. LINESHAPE FITTING PROCEDURES

4.1. Criteria for a good fit

The essential criteria for a good fit are that the returned parameters should be as accurate as permitted by the data and that the fitting process should be robust. The theoretical limit on the uncertainties of each of the parameters in the model is given by the Cramér–Rao lower bound. The Cramér–Rao bound applies to any unbiased estimator $\hat{\theta}(y)$ of a parameter vector, θ, using measurements, y. The measurements are described by their joint probability density function $p(y \mid \theta)$, which is influenced by θ.

Providing $p(y \mid \theta)$ is sufficiently 'well behaved' the Cramér–Rao bound is given by

$$\operatorname{cov} \theta(y) \geqslant F^{-1} \tag{88a}$$

where the Fischer information matrix[84] is given by

$$F = E_{y \mid \theta}\left\{ \frac{\partial}{\partial \theta} \ln p(y \mid \theta) \left(\frac{\partial}{\partial \theta} \ln p(y \mid \theta) \right)^{\mathrm{T}} \right\} \tag{88b}$$

where $E_{y|\theta}$ is the expectation value associated with the measurements, y, and parameters, θ, for the function shown in braces.[84] In the case of Gaussian noise, nonlinear least-squares fitting in the frequency domain yields parameter estimates whose standard deviations approach those given by the Cramér–Rao lower bounds.[20] Note that using prior knowledge reduces the number of parameters to be fitted and this in turn lowers the Cramér–Rao lower bounds.[20]

4.2. Nonlinear least-squares fitting in the time domain (Levenberg–Marquardt method)

Probably the most straightforward method of performing a nonlinear least-squares fit is to use the well-established Levenberg–Marquardt method.[85–87] The Levenberg–Marquardt algorithm employs an appropriate compromise between the downhill gradient direction and the direction given by the Gauss–Newton algorithm.[84] The objective is to minimize the value of χ^2 (see Eq. (96)). If the static magnetic induction $\mathbf{B}_0$ is homogeneous and is taken to be along the z-direction and the RF magnetic induction $\mathbf{B}_1$ is taken to be along the x-direction in the rotating frame, then the measured real component of the free induction decay resulting from an RF pulse is proportional to the y component of the magnetization and can be written in the time domain as

$$M_y(t) = \sum_{k=1}^{K} A_k \cos(2\pi f_k t) \exp(-t/T_2^*) + e(t) \tag{89}$$

where K is the number of resonances, $e(t)$ is the noise, A_k is the amplitude, f_k is the frequency and T_2^* is the effective transverse relaxation time of the kth resonance. In Eq. (89) each resonance is assumed to have the same value of T_2^*, as this is often a good approximation in MRS.

The Fourier transform of $M_y(t)$ is given by

$$M_y(f) = \sum_{k=1}^{K} a_k[1 + [2\pi T_2^*(f - f_k)]^2]^{-1} + e(f) \tag{90}$$

where $e(f)$ is the noise in the frequency domain and

$$a_k = A_k T_2^*/\Delta t \tag{91}$$

where Δt is the sampling interval.

It can be shown that the standard deviation of the noise in the time domain, σ_t is related to the standard deviation of the noise in the frequency domain, σ_f by[88]

$$\sigma_f = \sqrt{N}\sigma_t \tag{92}$$

where N is the number of data points.

For each resonance, k, the SNR in the time domain, Ψ_{t_k} is defined by

$$\Psi_{t_k} = A_k/\sigma_t \tag{93}$$

Similarly, the corresponding SNR in the frequency domain, Ψ_{f_k} is defined by

$$\Psi_{f_k} = a_k/\sigma_f \tag{94}$$

From Eqs (91) and (94) we obtain, for all resonances,

$$\Psi_t/\Psi_f = \sqrt{N}\,\Delta t/T_2^* \tag{95}$$

The procedure was tested on simulated time domain MRS data where the model data consisted of metabolite peaks at 3.2, 3.0 and 2.0 ppm representing choline, creatine and *N*-acetylaspartate (NAA) respectively, with corresponding values of A_k of 1.0, 1.0 and 3.0 units.[89] White noise of specified standard deviation, σ_t, was then added. The Levenberg–Marquardt method requires suitable initial values for each of the nine parameters being fitted. The initial values of the three frequencies were taken as their known values. An exponentially decaying curve with a constant offset parameter was fitted, using a nonlinear least-squares fit, to the envelope of the free induction decay, $M_y(t)$, in order to obtain an initial value for T_2^* and for the amplitudes, each of which was taken to be one-third of the amplitude of the envelope. The constant offset was added to account for the presence of the noise.

For each fit, the normalized value of χ^2 was calculated using

$$\chi^2 = [1/(N-M)] \sum_{i=1}^{N} [[M_y(t_i) - M'_y(t_i)]/\sigma_t]^2 \tag{96}$$

where $M = 9$ is the number of parameters and M'_y is the fitted function dependent on the M parameters.

For the simulated data, for each SNR, 50 data sets were created, each with $T_2^* = 100$ ms and each with a different noise component with the same σ_t. The values of Ψ_t for NAA used were 6, 3, 1.5, 1.0 and 0.75. For the fit corresponding to $\Psi_t = 6$, a value of 1.08 for χ^2 was obtained. The calculated values of all nine parameters were found to agree with the known values within the calculated error limits. As the SNR is decreased, the fit became progressively less satisfactory, as expected. The fit for $\Psi_t = 1.5$ is shown in

Fig. 16a, with the corresponding frequency domain plot shown in Fig. 16b. In this case, all the calculated values of the parameters were found to agree with the known values, within the calculated error limits, except for the T_2^* values for the creatine and NAA peaks. The robustness of the technique is shown by

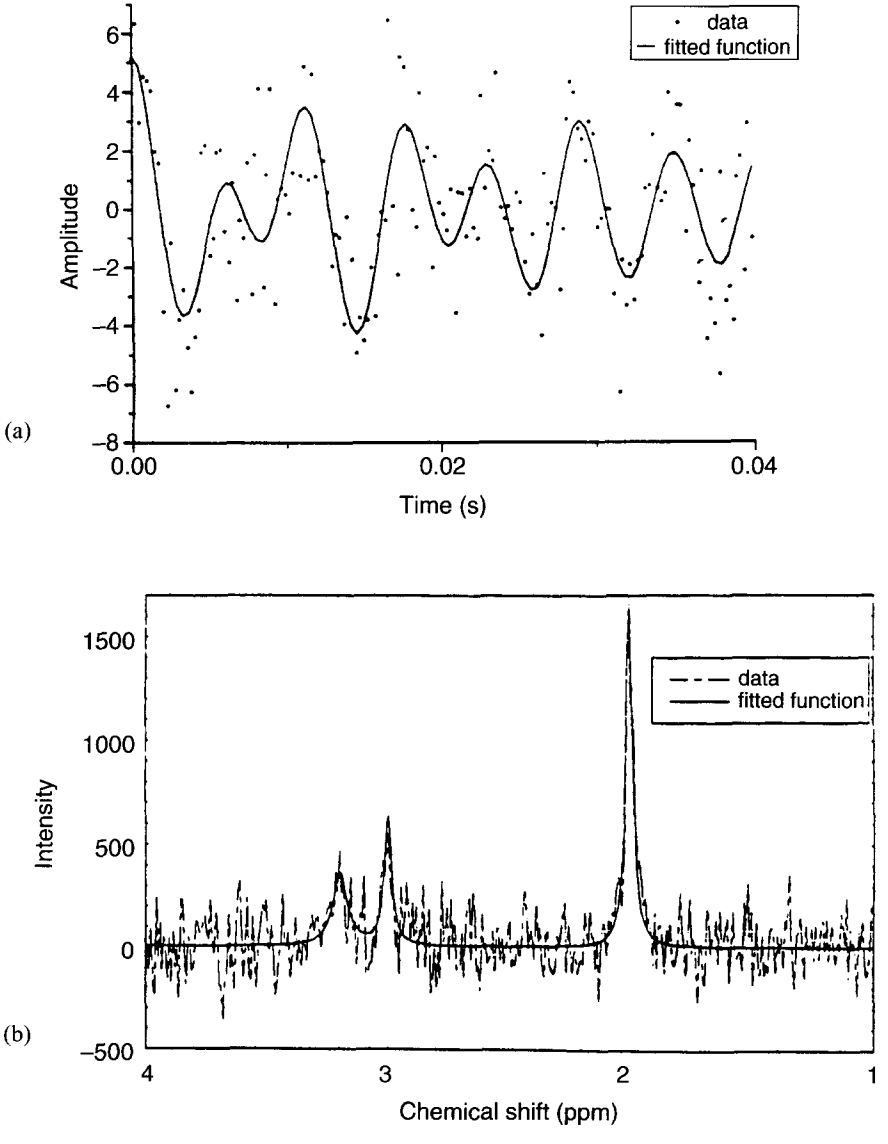

Fig. 16. (a) Fit of synthetic data in the time domain for which the SNR of the NAA peak in the time domain is 1.5. (b) The fit shown in (a) plotted in the frequency domain.

the dependence of the calculated parameters on the actual noise added for a particular value of σ_t. The dependence of the amplitude of the NAA peak on the actual noise added is shown in Fig. 17. Notice that even for $\Psi_t = 1.5$, one of the 50 values of A_3 was spurious, indicating a lack of robustness. The fitted values for each of the nine parameters were found to be centred about their known values, as shown in Fig. 17 for A_3; that is, the fit was unbiased, as required. Substituting the values $N = 4096$, $\Delta t = 0.25$ ms and $T_2^* = 100$ ms into Eq. (95), we obtain $\Psi_f/\Psi_t = 6.25$. For the data shown in Fig. 16, the measured value of Ψ_f/Ψ_t was 6.6 ± 0.3, in agreement with the calculated value. It should be noted that in order also to obtain a satisfactory estimate of the corresponding T_2^* values, a SNR greater than 1.0 was required.

The model function of a sum of exponentially decaying sinusoids can be approximated by a first-order Taylor expansion. In this way the nonlinear dependence on parameters is approximated by linear dependence on small updates of these parameters.[20]

4.3. Nonlinear least-squares fitting in the frequency domain (Levenberg–Marquardt method)

Fitting in the frequency domain is readily visualized graphically and the well-established Levenberg–Marquardt method[85] is straightforward to implement. This method is applicable to any lineshape function. For example, Marshall *et al.*[32] have used $V'(f)$, an approximation to the Voigt function, when fitting

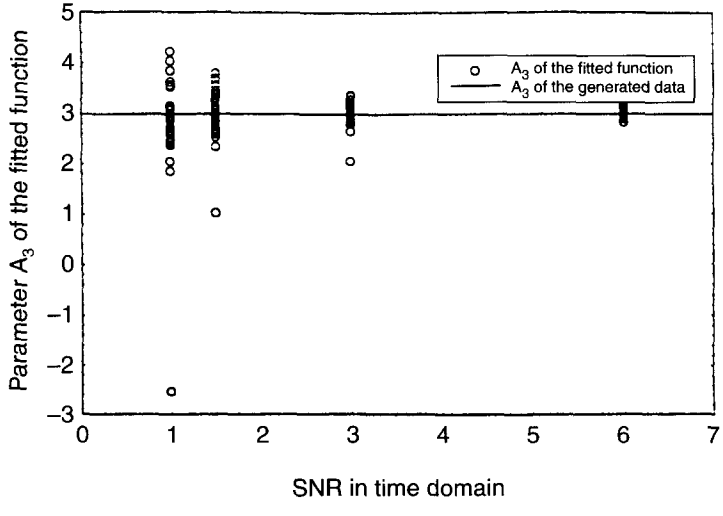

Fig. 17. The dependence of the amplitude of the NAA peak, A_3, on the actual noise added for various SNRs.

MRS spectra from the human brain. In order to improve the robustness of the χ^2 minimization, an internal parameter R was used, defined by $r = \exp(-|R|)$. The arctangent function, however, is preferable as it has a continuous derivative around $R = 0$. The equal asymptotic behaviour of this function towards 0 and 1 ensures that r remains within this valid range. We have subsequently found that using $r = (\arctan(R) + \pi/2)/\pi$ gives better performance. The fit can be conveniently performed using only the real part of the complex spectrum. Thus the normalized χ^2 is given by

$$\chi^2 = \frac{1}{N - M} \sum_{i=1}^{N} \left[\frac{\sum_{k=1}^{K} A_k g_{v'_i}(f_{0_k}, W_k, r_k) - M_{y_i}}{\sigma} \right]^2 \tag{97}$$

where N is the number of data points and K is the number of resonances and where, for the ith point, σ is the standard deviation of the noise, M_{y_i} is the measured real part of the magnetization in the frequency domain, and $g_{v'_i}$ is the approximation to the Voigt lineshape. Further, for the kth resonance, A_k is the area, f_{0_k} the frequency at the centre, W_k the FWHM and r_k the fractional parameter. The number of parameters, M, depends on whether parameters such as W_k are taken to be the same for two or more resonances. All the parameters were normalized internally so that they had equal weight in the fitting algorithm. Convergence of the Levenberg–Marquardt algorithm was usually achieved within one minute, when the change in model parameters fell below the 1 part in 10^4 limit. An example of the fit of $V'(f)$ to a simulated Voigt function, $V(f)$, for the three metabolites choline, creatine and NAA is shown in Fig. 18. The value of 1.01 obtained for χ^2 indicates a satisfactory fit.

This technique has been extended to the fitting of two-dimensional NMR spectra.[90] In the cores of large molecules such as peptides and proteins, well-chosen areas need to be selected in order to avoid exorbitant computation time. Initial parameter estimates corresponding to the appropriate portion of the multidimensional χ^2 surface are of crucial importance to ensure convergence to the global minimum corresponding to the correct parameter set.

4.4. VARPRO

The variable projection (VARPRO) method was devised by Golub and Pereyra.[91] Subsequent authors have given less rigorous but more readable accounts.[92–94] Essentially, this is a nonlinear method, but the amplitude parameters, which appear in a linear fashion, are treated separately with a subsequent reduction in the dimensionality of the least-squares fitting problem.

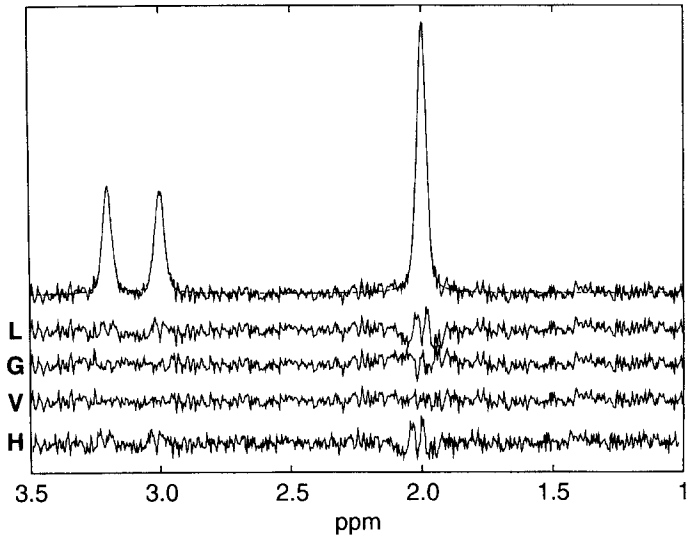

Fig. 18. Example of synthetic ^{1}H NMR spectrum, consisting of metabolite peaks at 3.2, 3.0 and 2.0 ppm representing choline, creatine and NAA, respectively. The metabolites have peak areas corresponding to time domain amplitudes of 1.0, 1.0 and 2.5 units, respectively, and all have a T_2 value of 300 ms. In this case, 2 Hz Gaussian line broadening has been applied to simulate the effect of imperfect shimming, and normally distributed random noise of amplitude 0.2 units has been added. The result of fitting with the Voigt approximation lineshape model is shown in dashed line. Also shown are the residuals for the Lorentzian (L), Gaussian (G), Voigt (V) and HLSVD (H) models. Reproduced with permission from I. Marshall, J. Higinbotham, S. Bruce and A. Freise, *Magn. Reson. Med.*, 1997, **37**, 651. © 1997 John Wiley and Sons.

The data model is

$$\hat{x}_n = \sum_{k=1}^{K} c_k f_k(\gamma_k, t_n) \tag{98}$$

where the $\hat{x}_n$ are the model data points ($n = 0, 1, \ldots, N-1$) as a function of the sample times t_n, the c_k are the (complex) amplitude coefficients, and the f_k are user-defined *basis functions* ($k = 1, 2, \ldots, K$) that involve the parameters γ_k in an arbitrary, nonlinear fashion. The method could also be applied in the frequency domain, in which case the samples would be at discrete frequencies. In matrix form, Eq. (98) can be written as

$$\hat{\mathbf{x}} = \mathbf{F}\mathbf{c} \tag{99}$$

where $\hat{\mathbf{x}}$ is the model data vector, $\mathbf{F}$ is the matrix of basis functions evaluated at the sample times, and $\mathbf{c}$ is the vector of complex coefficients. Rather than carry

out a complete nonlinear least-squares fit of the experimental data vector $\mathbf{x}$ to the model (i.e. minimizing $|\mathbf{x}-\hat{\mathbf{x}}|^2$), the complex amplitudes are removed from the expression by substituting $\mathbf{c}=(\mathbf{F}^T\mathbf{F})^{-1}\mathbf{F}^T\mathbf{x}$, where $\mathbf{F}^T$ represents the transpose of $\mathbf{F}$. This expression arises from the normal equations of the least-squares criterion,[85] and substitution leads to

$$|\mathbf{x}-\hat{\mathbf{x}}|^2=|\mathbf{x}-\mathbf{F}(\mathbf{F}^T\mathbf{F})^{-1}\mathbf{F}^T\mathbf{x}|^2 \tag{100}$$

This expression is minimized to find the nonlinear parameters γ_k. The amplitudes are then solved for in a linear fashion. Removing the amplitude parameters from the nonlinear fit saves computing time, as fewer parameters need to be fitted simultaneously and starting values are not required. Starting values are, however, required for the nonlinear parameters, and they may be obtained from, say, a preceding linear fit using linear prediction singular value decomposition (LPSVD), for example.[92]

It is possible, and indeed desirable, to incorporate prior knowledge in the nonlinear fit. This knowledge will typically relate to the phases and multiplet structure of spectral resonances. The aim is to determine the best fit of the data to a physically meaningful model, which may not be the best fit in a purely mathematical sense. Thus Hankel–Lanczos singular value decomposition (HLSVD) (which is unable to use *a priori* knowledge) has been shown to produce unphysical fits at low SNR, whereas VARPRO (using prior knowledge) gave much better results with the same data.[95] Similarly, VARPRO produces better results than noniterative methods when applied to strongly overlapping resonances.[96] In fitting the many spectra produced by a chemical shift imaging experiment, Spielman *et al.*[97] saved processing time by assuming that all the metabolite resonance frequencies were fixed relative to the water resonance frequency of each spectrum.

Although most implementations of VARPRO have concentrated on using exponentially damped sinusoids for the basis functions (i.e. Lorentzian lineshapes), there is no reason why more realistic models (e.g. Gaussian or Voigt[32]) should not be used.

More recently, it has been shown that solving the complete nonlinear least-squares problem (i.e. minimizing $|\mathbf{x}-\hat{\mathbf{x}}|^2$) is more robust than the VARPRO technique.[98]

4.5. Linear prediction and related techniques

Linear prediction and state-space methods are grouped together here because, although the philosophy behind the two methods is different, the mathematics involved is very similar. In both cases, the data-fitting problem is made linear by constructing a matrix from the observed data points, and the model equation is then solved by linear means. The nonlinear model parameters are

extracted from the eigenvalues of the matrix equation, and it is in this step that the two methods differ. The methods are noniterative, and starting values are not required. It is, however, not easily possible to make use of *a priori* information about the nature of the signal.

The original linear prediction and state-space methods are known in the nuclear magnetic resonance literature as LPSVD and Hankel singular value decomposition (HSVD), respectively, and many variants of them exist. Not only do these methods model the data, but also the fitted model parameters relate directly to actual physical parameters, thus making modelling and quantification a one-step process. The analysis is carried out in the time domain, although it is usually more convenient to display the results in the frequency domain by Fourier transformation of the fitted function.

In both cases, the model in question is a summation of K exponentially decaying sinusoids

$$\hat{x}_n = \sum_{k=1}^{K} c_k \exp[(b_k + \mathrm{i}\omega_k)t_n + \mathrm{i}\phi_k] \tag{101}$$

where the model data points are $\hat{x}_n$ ($n = 0, \ldots, N-1$), and the K amplitudes, damping factors, angular frequencies and phase angles are c_k, b_k, ω_k and ϕ_k respectively ($b_k < 0$). The sample times are $t_n = n\,\Delta t$, where Δt is the sampling interval. The model spectrum thus consists of Lorentzian lineshapes. An overview is given by Hoch and Stern.[99]

Linear prediction (LPSVD and derivatives)

The linear prediction (LP) method stems from work by Kumaresan and Tofts,[100] and was introduced into the NMR literature by Barkhuijsen and colleagues.[101] In essence, the method is a descendant of Prony's method. De Beer has written useful reviews of the method.[20,93]

For a noiseless signal consisting of a sum of decaying sinusoids described in Eq. (101), each measured (complex) signal value x_n can be written as a weighted sum of the M preceding data points as

$$x_n = \sum_{m=1}^{M} a_m x_{n-m} \tag{102}$$

where M is the prediction length, the a_m ($m = 1, \ldots, M$) are the linear prediction coefficients, and n can take any value between M and $N-1$. In general, the variables are complex.

This is known as the (forward) linear prediction equation, because the time series can be used to predict subsequent data points. For a single sinusoidal component, Eq. (101) reduces to $\hat{x}_n = c \exp[(b + \mathrm{i}\omega)n\,\Delta t]$, where the phase

factor is absorbed into the constant c. It is immediately evident that we may write $\hat{x}_n = \hat{x}_{n-1} \exp[(b + i\omega)\Delta t]$. Thus each data point can be predicted exactly from the previous one, and the prediction length M is equal to 1. Obviously, it is not possible to infer the initial amplitude of the signal directly from the prediction coefficients. The *linear* combination of components in Eq. (101) ensures that Eq. (102) also holds for the complete model function with a prediction length of M.

If N data points are sampled during a FID, then it is possible to write a total of $(N - M)$ linear prediction equations of the form of Eq. (102). The resulting matrix equation is

$$\begin{bmatrix} x_1 & x_2 & \cdot & x_M \\ x_2 & x_3 & \cdot & x_{M+1} \\ \cdot & \cdot & \cdot & \cdot \\ x_{N-M-1} & x_{N-M} & \cdot & x_{N-2} \\ x_{N-M} & x_{N-M+1} & \cdot & x_{N-1} \end{bmatrix} \begin{bmatrix} a_M \\ a_{M-1} \\ \cdot \\ a_2 \\ a_1 \end{bmatrix} = \begin{bmatrix} x_{M+1} \\ x_{M+2} \\ \cdot \\ x_{N-1} \\ x_N \end{bmatrix} \tag{103a}$$

or

$$\mathbf{Xa} = \mathbf{x} \tag{103b}$$

where $\mathbf{X}$ is an $(N - M)$ by M matrix having Hankel structure, i.e. the entries along any antidiagonal are equal, $\mathbf{a}$ is a vector of dimension M containing the required prediction coefficients, and $\mathbf{x}$ is a vector of $(N - M)$ data points.

For a signal with a relatively small (but generally unknown) number K of components, Eq. (103) forms an overdetermined set that can be solved in the presence of experimental noise in a least-squares sense. The inversion of matrix $\mathbf{X}$ required to solve the equation is generally carried out by singular value decomposition[102] (SVD; hence the acronym LPSVD), which is both robust and allows one to estimate K from the relative sizes of the eigenvalues. SVD is a factorization method for ordinary least-squares that can indicate where the cause of any ill-conditioning lies[84] and it plays a vital role in reducing the ill-conditioning associated with the LP technique.[103] SVD is usually provided as a 'black box' function in numerical analysis packages, with the intermediate step of reduction of the matrix to bidiagonal form[104] being hidden. For perfect, noiseless data, there are exactly K nonzero eigenvalues, and the rank of the matrix equation can accordingly be reduced by truncation. In the presence of noise, the first K eigenvalues correspond to the signal components, while the remaining ones correspond to noise. These latter ones will be smaller, and inspection of the relative values allows reduction of the rank of Eq. (103) by setting them to zero. SVD and truncation of matrix $\mathbf{X}$ gives the matrices $\mathbf{U}_K \Lambda_K \mathbf{V}_K^T$, which are shown schematically in Fig. 19.

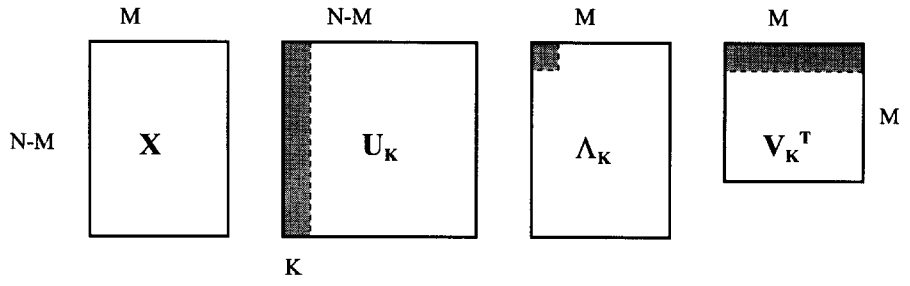

Fig. 19. Singular value decomposition of matrix **X**. The number of data points is N, the model order is M, and the rank is K ($N \gg M > K$). The signal information is contained in the shaded regions. The remaining rows and columns contain noise information and may be discarded. Adapted from de Beer and van Ormondt, in *NMR: Basic Principles and Progress*, Vol. 26 (eds Diehl *et al.*), p. 202, Springer-Verlag, Berlin, 1992. © 1992 Springer-Verlag.

It can be shown that the roots of the characteristic polynomial of Eq. (103) give the various frequencies and damping constants.[100] Thus the next step is to calculate the roots of

$$z^M - a_1 z^{M-1} \cdots - a_M = 0 \tag{104}$$

Depicting the roots as vectors in the complex (z) plane, the frequencies are found from the angular arguments and the damping factors from the respective radii. Having found the frequencies and damping constants, only the signal amplitudes and phases (i.e. the complex amplitudes) remain to be found. Because the amplitudes appear linearly in the model, as shown in Eq. (101), they can be found by a simple matrix inversion, after substitution of the frequencies and damping factors for all N data points. In the presence of noise, a least-squares procedure is used to find the most likely solution.

In the presence of noise, and without knowledge of the number of components, the prediction order M is taken to be greater than the suspected maximum number. A problem with the LPSVD method is the difficulty of clearly distinguishing the signal roots from spurious roots due to noise. All stable signals are decaying (i.e. $b_k < 0$), so that the roots corresponding to true signal components can be made to lie outside the unit circle by *backward* prediction. By contrast, spurious roots due to noise lie within the unit circle[100] and hence can be distinguished. The distinction becomes blurred as the SNR falls. Delsuc[105] proposed carrying out both forward and backward prediction to assist in picking the correct roots, since the signal roots will be reflected across the unit circle whereas the noise-related roots are insensitive to the prediction direction.[100] Various other strategies for root picking and correction are possible, for example, with forward LP, replacing each (noise-related) root

outside the unit circle with either its reflection into the unit circle, or by a corresponding point on the unit circle.

The computational efficiency of LPSVD has been discussed by several authors.[106,107] The singular value decomposition is the limiting step, requiring of order (N^3) calculations. For large prediction lengths, M, the polynomial rooting time also becomes significant.[106]

Tang[108] suggested using a Householder triangularization (QR) decomposition[66] of the data matrix **X** instead of a full SVD. This offers a reduction in computation time, but at the expense of reduced accuracy, especially when the signal-to-noise ratio is low.

In an analysis of errors, Barkhuijsen and colleagues[109] showed that the Cramér–Rao bounds can be used as estimates of the random errors in the parameter estimates.

Various refinements to the basic LPSVD method include using the noise singular values to correct the signal singular values,[100,101,109] restoration of the Hankel structure of **X** after truncation of the noise singular values,[110,111] and regularization of Eq. (103) to determine K.[111,112]

Although it is customary to solve the matrix equation (103) by the least-squares method, this is actually not quite correct. The data points in the vector **x** are also contaminated by noise, and so in fact a total least-squares (TLS) method (LPTLS) is more appropriate.[113–119] It can be shown that the TLS method minimizes the effects of noise in the LP solution vector by subtracting the effects from the singular values, resulting in an improved estimate of the spectral parameters. Least-squares does not perform a similar noise-compensating procedure, and for this reason TLS produces better results than least-squares for data with a poor SNR.[114] A general explanation of the solution of the total least-squares problem is given by Golub and van Loan.[120] A geometric interpretation of the difference between LS and TLS is possible.[121]

Prior knowledge may in fact be used even though LPSVD is a linear procedure. The number of spectral components K may be known exactly, thus guiding the truncation of the SVD. Furthermore, the frequencies of the spectral components may be known, so that the correct roots can be readily picked (or replaced with the theoretical values) during the polynomial rooting.[118]

State-space method (HSVD and derivatives)

One of the weaknesses of the linear prediction method is the need to find the M (complex) roots of a polynomial. In the presence of noise, it is difficult to separate the true signal-related roots from the spurious roots due to the noise. A rather different approach to the signal identification problem was proposed by Kung,[122] and introduced into NMR by Barkhuijsen and colleagues.[123] Despite its origins in state-space theory, many of the processing steps involved are markedly similar to those of the linear prediction method. Useful reviews are those by de Beer and colleagues.[20,23]

The time-domain signal model is again given by Eq. (101), which can also be written as

$$\hat{x}_n = \sum_{k=1}^{K} c_k z_k^n \tag{105}$$

where the z_k are the signal poles defined as $z_k = \exp((b_k + i\omega_k)\Delta t)$, and b_k and ω_k are, as previously, the damping factors and angular frequencies, respectively. The c_k are now complex amplitudes, having absorbed the phase factors ϕ_k of Eq. (101).[93]

A data matrix **X** is formed from the N data points exactly as in Eq. (103).

The essence of the HSVD method is that **X** can be written as the product of two matrices $\mathbf{X} = \mathbf{X}_l\mathbf{X}_r$, in which the left-hand matrix $\mathbf{X}_l$ has Vandermonde structure, with each row being equal to the previous one postmultiplied by **Z**, where **Z** is a K by K diagonal matrix whose diagonal elements are the z_k ($k = 1, ..., K$).[123] The required signal frequencies and damping factors are then immediately available without the need of polynomial rooting and root selection. There is, however, no direct method of performing the Vandermonde decomposition of **X**. Instead, a singular value decomposition is first carried out (hence the acronym HSVD), after which **Z** can be calculated from the left-hand signal vectors.[123] Truncation of the decomposed matrix eliminates the noise-related components just as for the LPSVD method. The signal poles z_k (i.e. the frequencies and damping factors) may then be used in Eq. (105) to perform a least-squares fit to the data and hence determine the amplitudes c_k. Prior knowledge may be used at this stage, for example by replacing the estimated frequencies by theoretical values. Alternatively, the amplitudes may be obtained from the first column of $\mathbf{X}_r$.

The most time-consuming stage in HSVD (and indeed in LPSVD) is the singular value decomposition of the data matrix **X**. In general, the number of operations needed for SVD is proportional to the cube of the matrix dimensions, and so decomposition times rapidly become impractical for long data sets. The Lanczos algorithm,[124] however, can be used to exploit the special Hankel structure of **X**.[125,126] The SVD diagonalization can be carried out by an iterative process in which the larger eigenvalues (corresponding to the true signal components) are found long before the noise-related eigenvalues. The process can be stopped before total conversion has been achieved, with significant saving of computation time. Furthermore, each iteration requires the multiplication of a circulant matrix with a vector, which can be carried out efficiently by a fast Fourier transform.[127] This approach has become known as the Hankel–Lanczos SVD (HLSVD) method. The time taken for the Lanczos SVD algorithm is (ideally) proportional to the square of the matrix size, thus offering a substantial increase in speed over the conventional SVD. For noisy data, the increase in speed is less impressive, and HLSVD is not well suited to

finding all the singular values, as many iterations are necessary for evaluating the noise-related ones.[126] Close singular values are more efficiently determined using a low-rank revealing decomposition.[128]

Total least-squares has been applied to the HSVD method (HTLS),[117,118,129] and, as in LPSVD, has been found to improve its performance slightly. Van Huffel[117] found that the TLS-based LP method had better resolution and was more robust than LPSVD.

Applications

Linear time domain analysis of NMR signals has been popularized by Barkhuijsen and colleagues, who first applied the LPSVD method to synthetic data and to an *in vivo* ^{31}P signal obtained from a mouse[101] (Fig. 20). The spectrum was successfully modelled when compared with a conventional Fourier transform analysis. The method has been used with prediction lengths as great as 2400 for the analysis of complex ^{13}C signals,[130] with a computational time of approximately one day. In a later paper, a modified (fast) version was used with $M = 13\ 000$.[131] LPSVD has also been applied to the analysis of 2D NMR signals of liquids.[132]

With the introduction of the HSVD method, the difficult step of polynomial rooting was avoided. Comparisons of LPSVD and HSVD generally show that the results are very similar, with only minor differences in the parameters of the smallest spectral components[93] (Fig. 21). Incorporation of the Lanczos

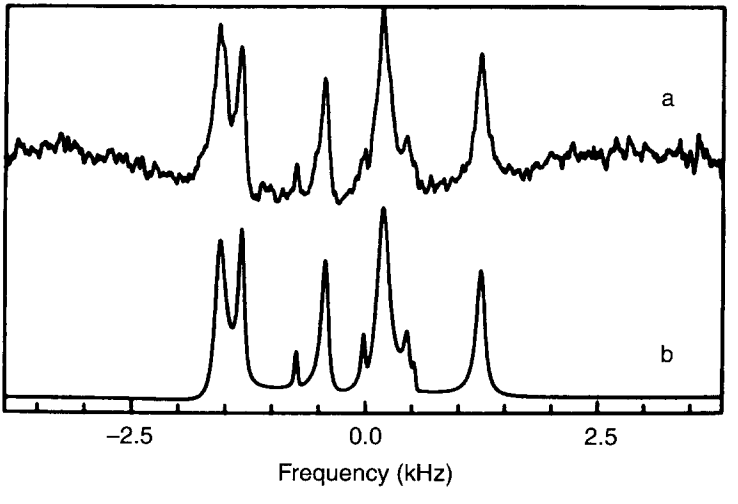

Fig. 20. LPSVD applied to an *in vivo* ^{31}P spectrum. Curve a, FFT of original signal with first three data points missing; curve b, FFT of LPSVD fit of same data. Reproduced with permission from Barkhuijsen *et al.*, *J. Magn. Reson.*, 1985, **61**, 465.

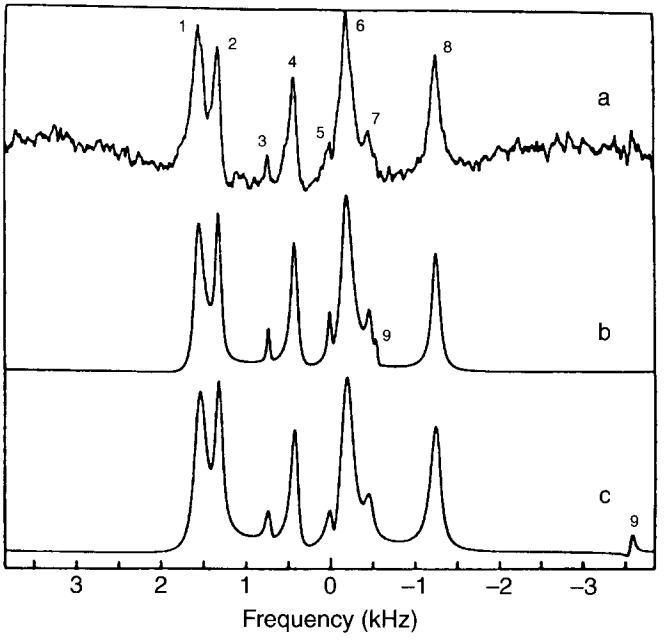

Fig. 21. Comparison of LPSVD and HSVD analysis of an *in vivo* ^{31}P spectrum. Curve a, FFT of original signal; curve b, LPSVD fit; curve c, HSVD fit. Note that LPSVD and HSVD select different features for the smallest (ninth) component. Reproduced with permission from de Beer *et al.*, *Israel J. Chem.*, 1988, **28**, 249.

algorithm[125,126] for rapidly finding the most significant signal components has made H(L)SVD analysis a practical proposition on commonly available computers.

When K is not known, it has been found preferable to set the prediction length M to approximately half the available number of data points N.[117,118]

Generally speaking, linear time domain analysis is able to determine the signal frequencies accurately, but the linewidth and amplitude estimates are not as good. The best results are obtained by using a total least-squares version, and applying prior knowledge as far as is possible with such noniterative techniques.[115,117,118] Koehl[115] found that using a total least-squares version of LPSVD reduced the bias in parameter estimates of a complicated simulated ^{13}C spectrum. Van Huffel[117] found that using HTLS instead of HLSVD reduced the errors in estimates of damping factors and amplitudes by 20–40% at low SNR (< 3 dB). At higher SNR there was little difference in the errors. Chen[118] showed that using prior knowledge of strong signal components gave an improvement in the estimation of neighbouring weaker signals.

At modest SNR, nonlinear least-squares methods (either in the time or the frequency domain) have been found to give more accurate results than linear

methods such as HLSVD.[133] For high-quality data the difference becomes negligible.

Both the linear prediction and state-space methods are directly applicable only to exponentially decaying sinusoidal signal components, which correspond to Lorentzian lineshapes. Non-Lorentzian (e.g. Gaussian or Voigt) lineshapes will be fitted by these techniques as linear sums of Lorentzian components. Although the data may be accurately modelled, the fits are then mathematical rather than having physical significance. One important application is in the removal of the residual water resonance from proton spectra.[20,134] As a result of experimental water suppression techniques, the residual water peak will have a non-Lorentzian lineshape, which may, however, be modelled as a sum of Lorentzian components. Removal of those components having central frequencies within a selected range around the ideal water resonance frequency then provides effective suppression of the residual water signal, including any long tails, regardless of its lineshape (Fig. 22). The same technique can be used to remove any unwanted spectral component whose model function is not known,[126] and this is probably one of the most useful applications of the methods discussed in this section.

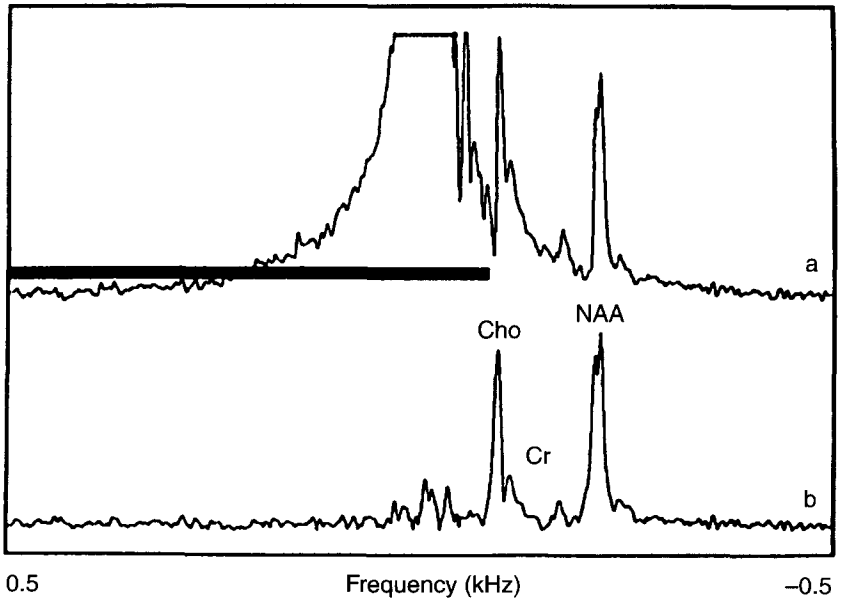

Fig. 22. Removal of residual water signal by HSVD. Curve a, FFT of original signal. The horizontal bar indicates the water region; curve b, FFT of the signal after water components have been identified by HSVD fitting and subtracted. Reproduced with permission from de Beer and van Ormondt, in *NMR: Basic Principles and Progress*, Vol. 26 (eds Diehl *et al.*), p. 202, Springer-Verlag, Berlin, 1992.

4.6. Maximum-entropy techniques

Unfortunately, there is great scope for confusion, as two distinct techniques include the phrase 'maximum entropy' in their names. The first technique, due to Burg,[135] uses the autocorrelation coefficients of the time series signal, and is effectively an alternative means of calculating linear prediction coefficients. It has become known as the maximum-entropy method (MEM). The second technique, which is more directly rooted in information theory, estimates a spectrum with the maximum entropy (i.e. assumes the least about its form) consistent with the measured FID. This second technique has become known as maximum-entropy reconstruction (MaxEnt). The two methods will be discussed only briefly here. Further details can be found in references 24, 99, 136 and 137. Note that Laue *et al.*[136] describe the MaxEnt technique although they refer to it as MEM.

Maximum-entropy method (MEM)

Burg[135] derived a means of estimating a power spectrum from the limited number of autocorrelation coefficients of a short time series, without adding extra information. It can be shown that this approach leads to equations identical to an autoregressive LP method, with the power spectrum $P(f)$ given by

$$P(f) = \frac{a_0}{\left| 1 + \sum_{k=1}^{M} a_k z^k \right|^2} \tag{106}$$

Here, M is the model order, and z the complex variable as usual. This is an efficient way of representing a spectrum $P(f)$ that consists mainly of sharp peaks, and is known as the all-poles or autoregressive model. Once the coefficients a of the model have been found, the spectrum can be evaluated at arbitrary frequencies within the sampling range, to ensure that no narrow details are lost. By considering the linear prediction (LP) model (Section 4.5) as a filter in the time domain, it can be shown that the required coefficients are simply the negative of the LP coefficients. Alternatively, Burg[135] gave a recursive derivation. His algorithm was developed for stationary data, and is not particularly well suited to the decaying signals encountered in NMR.[99] The MEM method must be used with care, particularly in the choice of model order M. Usually, best results are achieved when M is set to about ten times the expected number of peaks. If set too low, smoothing of spectral details occurs, and, if too high, spurious peaks are created. Figure 23 shows the effect of varying M in the reconstruction of an *in vivo* proton spectrum. The computational burden is proportional to the product MN, where N is the number of data points, and so is generally much greater than for a (fast) Fourier transform.

Maximum-entropy reconstruction (MaxEnt)

In this technique, a spectrum is generated to have maximum entropy (in the information theory sense)[138] subject to being consistent with the observed FID.[136,139] This inverse problem is solved iteratively. At each stage, the inverse Fourier transform of the spectrum is taken as an estimate of the FID and

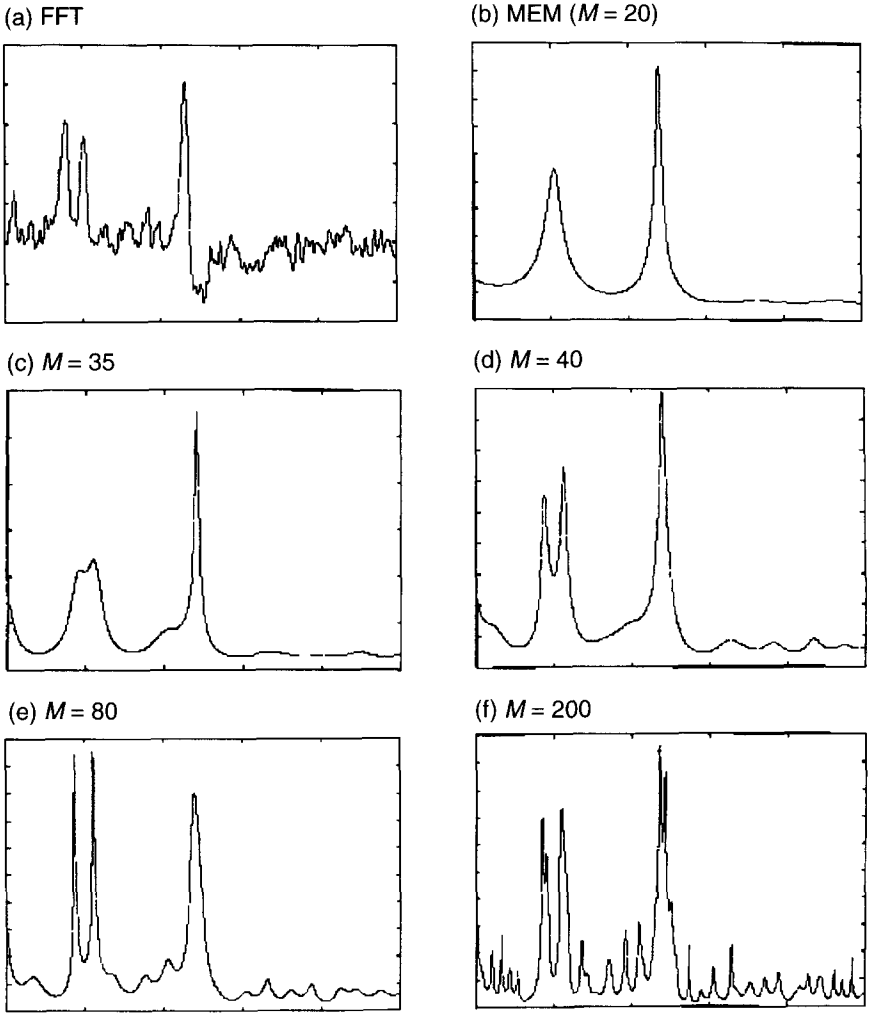

Fig. 23. Performance of maximum-entropy method (MEM) on an *in vivo* ^{1}H spectrum. Curve (a) FFT of original data; curves (e)–(f) MEM with reconstruction orders 20, 35, 40, 80 and 200, respectively. Reproduced with permission from J. Wild, PhD thesis, University of Edinburgh, 1998.

compared in a least-squares sense with the experimental FID, and the parameters are updated to improve the match.[20] Specifically, the function

$$S(p) - \lambda \sum_i | x_i - \hat{x}_i |^2 \tag{107}$$

is maximized, where $S(p)$ is the entropy of the model spectrum, λ is a Lagrange multiplier, x_i are the experimental data points, and $\hat{x}_i$ are the model data points found by inverse Fourier transformation of the spectrum. $S(p)$ is given by Shannon's expression[138]

$$S(p) = - \sum_n p_n \log p_n \tag{108}$$

Deconvolution of undesirable features using *a priori* knowledge (for example of decay rates or *J*-coupling) may be possible by modifying the inverse Fourier transformation step. Optimization of Eq. (107) is carried out by an iterative process[136,140] with several control parameters that can influence the resulting spectrum. The maximum-entropy reconstruction method is inherently non-linear, with both noise and signals near the baseline being attenuated relative to larger signals (and noise). Spectral quantification is therefore difficult. In addition, the computational load is high, typically two orders of magnitude greater than for the comparable FFT. MaxEnt is most useful when the time domain data are truncated, or when it is desired to incorporate *a priori* knowledge at the deconvolution stage.[141] Daniell and Hore[137] introduced a modified version that defines the entropy in terms of spin magnetizations rather than a power spectrum. This variation can deal with signals of arbitrary phase.

5. SUMMARY

Of the various common NMR lineshapes, the Lorentzian occupies a special place. It is the basic lineshape of high-resolution NMR, the easiest to fit accurately and reliably, and also the simplest to treat mathematically, being derived from the Bloch equations. One can, of course, consider both the Lorentzian and Gaussian lineshapes to be special cases of the Voigt lineshape. On the other hand, the lineshape consisting of the convolution of a Gaussian with a rectangular lineshape is fundamentally different in character from these shapes since, in the time domain, it contains negative portions.

Various least-squares techniques have been applied to fitting high-resolution spectra in the frequency domain.[142,143] Owing to the high SNR and artefact-free nature typical of high-resolution NMR spectra, fitting such spectra is

straightforward. If the spectrum includes CH_2 groups observed at short echo times, then the spectrum can have a complicated appearance and needs to be carefully modelled.[144] As an alternative to performing a conventional fit of high-resolution spectra, a line listing can be performed using the 1D filter diagonalization method.[145] This enables essential information, such as coupling constants, to be readily extracted.

Exchange-broadened NMR spectra have been fitted successfully using a nonlinear least-squares routine that uses an interpolation between the Gauss–Newton and negative gradient directions and that appears to be superior to the standard Levenberg–Marquardt algorithm.[142] Lineshapes that result from a two-site jump motion, based on the stochastic Liouville equation, can be calculated using commercial spreadsheet software.[146]

A comparison of the various fitting techniques is given in Table 5. Most of these techniques depend either explicitly or implicitly on a least-squares minimization. This is appropriate, provided the noise present is normally distributed. In this case, least-squares estimation is equivalent to maximum-likelihood estimation.[147] If the noise is not normally distributed, a least-squares estimation is inappropriate. Table 5 includes an indication of how each technique scales with N, the number of data points, for the case in which N is large. A detailed discussion on how different techniques scale with N and also with the number of parameters, is given in the PhD thesis of Vanhamme.[148]

In the TDFD technique, the model signals are calculated in the TD, simulating the sampling as closely as possible, and then Fourier transformed to obtain the discrete FD model spectra. The data are then fitted in the FD, with respect to TD model parameters, minimizing the value of χ^2. This method circumvents the main disadvantages of both FD and TD fitting, i.e. it can handle truncated data sets while retaining straightforward frequency-selected fitting.[26] This technique can fit any arbitrary lineshape, as can VARPRO. It can also cope with missing data points, due for example to water suppression artefacts[21] and is robust with respect to variations in the starting values used for fitting. This technique has been applied to Voigt lineshapes obtained from astronomical spectral data.[149]

When using 'black box' NMR spectra fitting procedures, e.g. those based on SVD, the use of prior knowledge decreases the Cramér–Rao bounds and improves the resolution and accuracy of the estimated parameters.[150] When estimating the signal parameters from time-domain data, an improvement in accuracy can be achieved by making use of known frequency *intervals* of the peak locations.[151] Continuous regularization can be used to improve the estimate of the number of component signals with poor SNR when using LPSVD. An enhancement procedure followed by LPSVD provides a maximum-likelihood estimator.[111] It is of interest to note that many of the ideas presented here are applicable to other disciplines. The maximum-entropy method of deconvolution, for example, has been applied to astronomy.[152]

Table 5. Comparison of lineshape fitting techniques

Technique	Domain	Restricted to Lorentzian lineshape	Uses prior knowledge	Starting values required	Iterative	Scaling with N	Underlying principle	Robustness
Non-linear least-squares fitting in f-domain	F	N	Y	Y	Y	N	Nonlinear least-squares fit	Good
Non-linear least-squares fitting in time domain	T	N	Y	Y	Y	N	Nonlinear least-squares fit	Poor
VARPRO	T	N	Y	Y	Y	N	Amplitude parameters appear linearly. Nonlinear least-squares fit	Good
TDFD	F, T	N	Y	Y	Y		Amplitude parameters appear linearly. Nonlinear least-squares fit	Good
LPSVD	T	Y	N	N	N	N^3	Linear prediction and polynomial rooting	Good
HSVD	T	Y	N	N	N	N^3	Linear prediction and Vandermonde decomposition	Good
HLSVD	T	Y	N	N	N	N^2	Fast version of HSVD	Good
Maximum-entropy (Max Ent)	F, T	N	Y	N	Y	$N \log N$	Maximum-entropy and nonlinear least-squares	Poor
HTLS	T	Y	N	N	N	N^3	Linear predication and Vandermonde decomposition (uses total least-squares)	Good

Notes on scaling:
(a) N is the number of data points.
(b) Scaling as N is a consequence of nonlinear least-squares fitting.
(c) Scaling as N^3 is a consequence of SVD matrix inversion.
(d) Scaling as N^2 is a consequence of the Lanczos algorithm for SVD matrix inversion.
(e) Scaling as $N \log N$ is a consequence of a FFT.

MRS spectra can also be fitted in the time domain using the heuristic optimization techniques of a genetic algorithm or simulated annealing. The simulated annealing algorithm has been found to be slightly more robust.[153] As an alternative to performing a fit of MRS spectra, an artificial neural network analysis can be performed.[154] This technique gives similar results to lineshape fitting but is more easily automated.[154] If a particular resonance is repeatedly measured, for example in a kinetic study, then principal-component analysis can be employed to obtain an accurate estimate of the amplitude of that resonance in each spectrum.[155,156]

Bayesian probability theory[157] can also be applied to the problem of NMR parameter estimation: this approach incorporates prior knowledge of the NMR parameters and is particularly useful at short aquisition times[158] and when the FID contains few data points.[159] Bayesian analysis gives more precise estimates of the NMR parameters than do methods based on the discrete Fourier transform (DFT).[160] The amplitudes can be estimated independently of the phase, frequency and decay constants of the resonances.[161] For the usual method of quadrature detection, it is appropriate to apply this technique to the two quadrature signals in the time domain.[162–164]

Systematic use of all available *a priori* information can enable complicated MRS spectra to be adequately characterized, even in the presence of large baseline signals and relatively poor signal-to-noise ratios.[165] In the automated spectral analysis used by Soher *et al.*,[165] the model is calculated in the time domain but the optimization is done in the frequency domain. The use of the time domain simplifies the inclusion of filtering and truncation effects. It also allows the efficient calculation of the Voigt (Lorentzian–Gaussian) lineshape. On the other hand, optimization in the frequency domain simplifies the incorporation of the baseline estimation procedure when using a wavelet shrinkage technique.[144] The process begins by correction of $\mathbf{B}_0$ frequency shift differences in a series of spectra from the same object, relative to tabulated values, producing a $\mathbf{B}_0$ map. The $\mathbf{B}_0$ map is then smoothed using a robust two-dimensional filtering technique.[166] Initial amplitude estimates are then made for the major identifiable metabolite peaks. Using these estimates, initial values are then calculated for any remaining metabolites, assuming that they exist in their normal concentrations relative to the main metabolites. A metabolite model spectrum is then subtracted from a copy of the input spectral data, giving the baseline and unresolved metabolite resonances. The wavelet technique, which scales as $N \log N$ is then used to estimate the baseline.[167] The estimate of the baseline is then subtracted from the original input spectrum and a Levenberg–Marquardt nonlinear least-squares fit is used to estimate the metabolite resonance parameters. On the other hand, using a polynomial fitting procedure to estimate the broad background features of a spectrum interferes with correct parameter estimation of broad NMR components.[168] Formation of a parametrized model for the baseline signal contributions is unlikely, owing to limited understanding of their origins as well as the

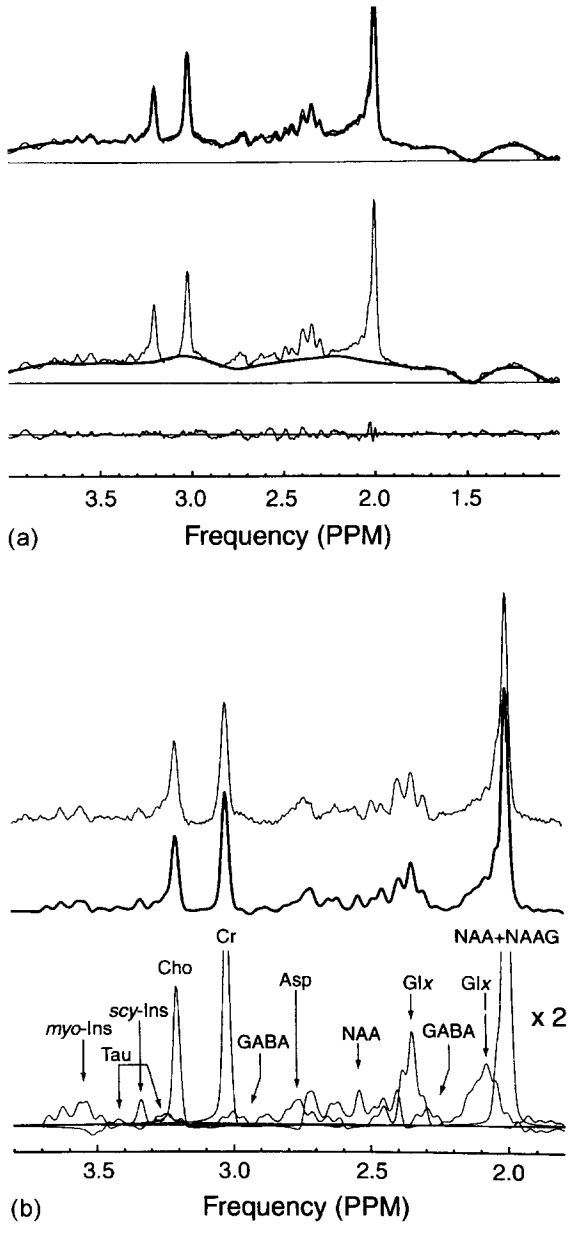

Fig. 24. Results from the fit of a single voxel from a *J*-refocused PRESS MRSI data set acquired at 4.1 T with 40 ms TE. (a) The top spectrum is the spectral data (thin line) overlaid with the fit result (heavy line), the middle spectrum is spectral data with only the baseline fit overlaid, and the bottom spectrum is the residual spectrum. (b) An expanded plot of the metabolite signal only (with baseline fit subtracted) in the top spectrum and the summed metabolite fits (without baseline) in the middle spectrum. The bottom spectrum contains the labelled, individual metabolite fits, with the vertical scale increased by 2. Reproduced with permission from B. J. Soher, K. Young, V. Govindaraju and A. A. Maudsley, *Magn. Reson. Med.*, 1998, **40**, 822. © 1998 John Wiley and Sons.

unpredictable effects of lipids and water suppression applied before data acquisition.[165] An example of the large number of metabolites that can be quantified in a single voxel is shown in Fig. 24.

Before a fitting routine is used on experimental data, it should always be tested first on trial data with known parameters and SNR. For each set of parameters for a given SNR, a set of, say, 50 spectra should be generated with different noise having the same standard deviation.[32] The distribution of each fitted parameter should be checked to verify that it is free from bias, relative to its known value, as shown in Fig. 17. If the fitting procedure has been correctly applied, then the uncertainties in the fitted parameters should satisfy the Cramér–Rao lower bounds. This procedure also checks the robustness of the fitting technique.

In conclusion, it is clear from all the considerations above that, before performing a NMR lineshape fitting procedure, it is essential to select an appropriate lineshape. The choice of the lineshape should be based on a proper understanding of the physical properties of the system. Using prior knowledge can improve the reliability of the fitted parameters significantly.[92] Finally, it should be stressed that both TD and FD fitting techniques give equivalent results provided potential artefacts are handled properly.[21]

ACKNOWLEDGEMENTS

Helpful suggestions by Dr I. C. Malcolm and valuable discussions with Dr W. Robin, both from the School of Mathematical and Physical Sciences, Napier University, are gratefully acknowledged by the authors.

REFERENCES

1. R. R. Ernst and W. A. Anderson, *Rev. Sci. Instrum.*, 1965, **36**, 1696.
2. G. W. Smith, *J. Appl. Phys.*, 1964, **35**, 1217.
3. M. Weger, *Bell System Tech. J.*, 1960, **39**, 1013.
4. R. R. Ernst, in *Advances in Magnetic Resonance* (ed. J. S. Waugh), Vol. 2, p. 1, Academic Press, New York, 1966.
5. G. E. Pake and T. L. Estle, *The Physical Principles of Electron Paramagnetic Resonance*, Benjamin, Reading, MA, 1973.
6. N. Bloembergen, E. M. Purcell and R. V. Pound, *Phys. Rev.*, 1948, **73**, 679.
7. B. N. Provotorov, *Sov. Phys., JEPT*, 1962, **14**, 1126.
8. M. Goldman, *Spin Temperature and Nuclear Magnetic Resonance in Solids*, Oxford University Press, London, 1970.
9. C. P. Slichter, *Principles of Magnetic Resonance*, Springer-Verlag, Berlin, 1990.
10. A. Abragam, *The Principles of Nuclear Magnetism*, Oxford University Press, London, 1961.
11. R. R. Ernst, W. P. Aue, E. Bartholdi, A. Hohener and S. Schaublin, *Pure Appl. Chem.*, 1974, **37**, 47.
12. I. Lowe and R. E. Norberg, *Phys. Rev.*, 1957, **107**, 46.

13. Bureau internationale de poids et mesures, *Le Système international d'unités (SI)*, Organisation Intergouvernemental de la Convention du Mètres, Sevres, 1998.
14. T. C. Farrar and E. D. Becker, *Pulse and Fourier Transform NMR*, Academic Press, New York, 1971.
15. E. Fukushima and S. B. W. Roeder, *Experimental Pulse NMR: A Nuts and Bolts Approach*, Addison-Wesley, London, 1981.
16. C. N. Chen and D. I. Hoult, *Biomedical Magnetic Resonance Technology*, Adam Hilger, Bristol, 1989.
17. H. Friebolin, *Basic One-and-Two-Dimensional NMR Spectroscopy*, VCH, Weinheim, 1993.
18. A. de Graaf, *In Vivo NMR Spectroscopy: Principles and Techniques*, Wiley, Chichester, 1998.
19. A. G. Marshall and F. R. Verdun, *Fourier Transforms in NMR, Optical and Mass Spectrometry*, Elsevier, Amsterdam, 1990.
20. R. de Beer and D. Van Ormondt, in *NMR Basic Principles and Progress* Vol. 26 (eds P. Diehl, E. Fluck, H. Gunther, R. Kosfeld and J. Seelig), p. 201, Springer-Verlag, Berlin, 1992.
21. L. Hofmann, J. Slotboom, C. Boesch and R. Kreis, *Abstracts of the 15th Annual Meeting, European Society for Magnetic Resonance in Medicine and Biology, Geneva*, p. 12, 1998.
22. P. Diehl, H. Kellerhals and E. Lustig, in *NMR Basic Principles and Progress*, Vol. 6 (eds P. Diehl, E. Fluck and R. Kosfeld), p. 1, Springer-Verlag, Berlin, 1972.
23. H. Gesmar, J. J. Led and F. Abildgaard, *Prog. NMR Spectrosc.*, 1990, **22**, 255.
24. D. S. Stephenson, *Prog. Nucl. Magn. Spectrosc.*, 1988, **20**, 515.
25. F. A. Bovey, *Nuclear Magnetic Resonance Spectroscopy*, Academic Press, New York, 1988.
26. J. Slotboom, C. Boesch and R. Kreis, *Magn. Reson. Med.*, 1998, **39**, 899.
27. K. R. Metz, M. M. Lam and A. G. Webb, *Concepts Magn. Reson.*, 2000, **12**, 21.
28. A. Maudsley, *J. Magn. Reson. B.*, 1995, **106**, 47.
29. S. W. Provencher, *Magn. Reson. Med.*, 1993, **30**, 672.
30. U. Klose, *Magn. Reson. Med.*, 1990, **14**, 26.
31. R. K. Harris, *Nuclear Magnetic Resonance Spectroscopy: A Physiochemical View*, Longman, Harlow, 1986.
32. I. Marshall, J. Higinbotham, S. Bruce and A. Freise, *Magn. Reson. Med.*, 1997, **37**, 651.
33. J. F. Kielkopf, *J. Opt. Soc. Am.*, 1973, **63**, 987.
34. H. C. Van de Hulst and J. J. M. Reesinck, *Astrophys. J.*, 1947, **106**, 121.
35. A. B. McLean, C. E. J. Mitchell and D. M. Swanston, *J. Electron. Spectrosc. Related Phenomena*, 1994, **69**, 125.
36. H. Gunther, *NMR Spectroscopy: Basic Principles, Concepts and Applications in Chemistry*, Wiley, Chichester, 1995.
37. K. Unterforsthuber and K. Bergmann, *J. Magn. Reson.*, 1979, **33**, 483.
38. B. H. Armstrong, *J. Quant. Spectrosc. Radiat. Transfer*, 1967, **7**, 61.
39. D. Shaw, *Fourier Transform NMR Spectroscopy*, Elsevier Scientific, Amsterdam, 1976.
40. P. A. Jansson (ed.), *Deconvolution with Applications in Spectroscopy*, Academic Press, Orlando, 1984.
41. E. O. Brigham, *The Fast Fourier Transform*, Prentice-Hall, Englewood Cliffs, NJ, 1974.
42. C. P. Poole and H. A. Farach, *Theory of Magnetic Resonance*, Wiley, New York, 1987.
43. E. D. Becker, *High Resolution NMR: Theory and Chemical Applications*, Academic Press, New York, 1980.
44. P. W. Anderson, *J. Phys. Soc. Japan*, 1954, **9**, 316.
45. J. Sandstrom, *Dynamic NMR Spectroscopy*, Academic Press, London, 1982.
46. J. J. Delpuech (ed.), *Dynamics of Solutions and Fluid Mixtures by NMR*, Wiley, Chichester, 1995.
47. G. Binsch and H. Kessler, *Agnew. Chem. Int. Ed. Engl.*, 1980, **19**, 411.
48. M. Cuperlovic, G. H. Meresi, W. E. Palke and J. T. Gerig, *J. Magn. Reson.*, 2000, **142**, 11.
49. D. G. Gorenstein (ed.), *Phosphorus-31 NMR: Principles and Applications*, Academic Press, Orlando, 1984.

50. C. P. Poole, *Electron Spin Resonance: A Comprehensive Treatise on Experimental Techniques*, Wiley, New York, 1967.
51. M. Mehring, *Principles of High Resolution NMR in Solids*, Springer-Verlag, Berlin, 1983.
52. M. L. Boas, *Mathematical Methods in the Physical Sciences*, Wiley, New York, 1983.
53. R. G. Griffin, *Methods Enzymol.*, 1981, **72**, 108.
54. S. Alexander, A. Baram and Z. Luz, *J. Chem. Phys.*, 1974, **61**, 992.
55. E. Grell (ed.), *Membrane Spectroscopy*, Springer-Verlag, Berlin, 1981.
56. J. A. Barry and K. Gawrisch, *Biochemistry*, 1995, **34**, 8852.
57. L. J. Burnett and B. H. Müller, *J. Chem. Phys.*, 1971, **55**, 5829.
58. L. L. Holte, A. P. Senaka, T. M. Sinnwell and K. Gawrisch, *Biophys. J.*, 1995, **68**, 2396.
59. H. W. Spiess, *Annu. Rep. NMR Spectrosc.*, 1997, **34**, 1.
60. E. G. Finer, A. G. Flook and H. Hauser, *Biochim. Biophys. Acta*, 1972, **260**, 59.
61. M. Bloom, E. E. Burnell, M. I. Valic and G. Weeks, *Chem. Phys. Lipids*, 1975, **14**, 107.
62. M. Bloom, E. E. Burnell, A. L. Mackay, C. P. Nicol, M. Valic and G. Weeks. *Biochemistry*, 1978, **17**, 5750.
63. H. Wennestrom, *Chem. Phys. Lett.*, 1973, **18**, 41.
64. M. E. Ries, M. G. Brereton, P. G. Klein, I. M. Ward, P. Ekanayake, H. Menge and H. Schneider, *Macromolecules*, 1999, **32**, 4961.
65. M. G. Brereton and M. E. Ries, *Macromolecules*, 1996, **29**, 2644.
66. E. Kreyszig, *Advanced Engineering Mathematics*, Wiley, New York, 1993.
67. R. Kubo and K. Tomita, *J. Phys. Soc. (Jpn)*, 1954, **9**, 888.
68. D. Bruggeman and M. Bollig, *J. Quant. Spectrosc. Radiat. Transfer*, 1992, **48**, 111.
69. J. T. Reilly, J. M. Walsh, M. L. Greenfield and M. D. Donohue, *Spectrochim. Acta*, 1992, **48A**, 1459.
70. Z. Shippony and W. G. Read, *J. Quant. Spectrosc. Radiat. Transfer*, 1993, **50**, 635.
71. J. P. Grivet, *J. Magn. Reson.*, 1997, **125**, 102.
72. V. N. Faddeyeva and N. M. Terent'ev, *Mathematical Tables: Tables of Values of the Function* $w(z) = \exp(-z^2)(1 + (2i/\sqrt{\pi}))\int_0^z \exp(t^2)\,dt$ *for Complex Argument*, Pergamon Press, London, 1961.
73. J. A. Gubner, *J. Phys. A: Math. Gen.*, 1994, **27**, L745.
74. H. Flores-Llamas, A. Cabral-Priesto, H. Jiminez-Dominguez and M. Torres-Valderrama, *Nucl. Instrum. Methods Phys. Res. A*, 1991, **300**, 159.
75. C. M. Teodorescu, J. M. Esteva, R. C. Karnatak and A. El Afif, *Nucl. Instrum. Methods Phys. Res. A*, 1994, **345**, 141.
76. A. G. Marshall and D. C. Roe, *Anal. Chem.*, 1978, **50**, 756.
77. H. Jimenez-Dominguez, S. Cruz-Jiminez and A. Cabral-Prieto, *Appl. Spectrosc.*, 1997, **51**, 37.
78. S. D. Bruce, J. Higinbotham, I. Marshall and P. H. Beswick, *J. Magn. Reson.*, 2000, **142**, 57.
79. A. Freise, E. Spencer, I. Marshall and J. Higinbotham, *Bull. Magn. Reson.*, 1995, **17**, 302.
80. M. M. Maltempo, *J. Magn. Reson.*, 1986, **68**, 102.
81. G. Bergmann, W. Dietrich, U. Gunther and M. Wiecken, *J. Magn. Reson.*, 1988, **76**, 193.
82. D. E. Roberts, Y. Z. Wu, R. Yusaf, J. Higinbotham, A. J. Shand and I. C. Malcolm, *Magn. Reson. Chem.*, 1997, **35**, 468.
83. A. Ralston and P. Rabinowitz, *A First Course in Numerical Analysis*, McGraw-Hill, New York, 1984.
84. J. P. Norton, *An Introduction to Identification*, Academic Press, London, 1986.
85. W. H. Press, S. A. Teukolsky, W. T. Vetterling and B. P. Flannery, *Numerical Recipes in C: The Art of Scientific Programming*, Cambridge University Press, Cambridge, 1999.
86. D. M. Bates and D. G. Watts, *Nonlinear Regression Analysis and Its Applications*, Wiley, New York, 1988.
87. J. E. Dennis, *Proc. IEEE*, 1984, **72**, 1765.
88. R. Pohmann, M. Von Kienlin, and A. Haase, *J. Magn. Reson.*, 1997, **129**, 145.

89. M. Szymanska, I. Marshall and J. Higinbotham, *Abstracts of the 18th International Conference on Magnetic Resonance in Biological Systems, Tokyo*, p. 33, 1998.
90. Z. L. Madi and R. R. Ernst, *J. Magn. Reson.*, 1988, **79**, 513.
91. G. H. Golub and V. Pereyra, *SIAM J. Num. Anal.*, 1973, **10**, 413.
92. J. W. C. Van der Veen, R. de Beer, P. R. Luyten and D. Van Ormondt, *Magn. Reson. Med.*, 1988, **6**, 92.
93. R. de Beer, D. van Ormondt, W. W. F. Pijnappel and J. W. C. van der Veen, *Israel J. Chem.*, 1988, **28**, 249.
94. A. van den Boogaart, M. Ala-Korpela, J. Jokisaari and J. R. Griffiths, *Magn. Reson. Med.*, 1994, **31**, 347.
95. A. van den Boogaart, F. A. Howe, L. M. Rodrigues, M. Stubbs and J. R. Griffiths, *NMR Biomed.*, 1995, **8**, 87.
96. C. Decanniere, P. van Hecke, F. Vanstapel, H. Chen, S. van Huffel, C. van der Voort, B. van Tongern and D. van Ormondt, *J. Magn. Reson. B*, 1994, **105**, 31.
97. D. Spielman, P. Webb and A. Macovski, *Magn. Reson. Med.*, 1989, **12**, 38.
98. L. Vanhamme, A. van den Boogaart and S. van Huffel, *J. Magn. Reson.*, 1997, **129**, 35.
99. J. C. Hoch and A. S. Stern, *NMR Data Processing*, Wiley-Liss, New York, 1996.
100. R. Kumaresan and D. W. Tufts, *IEEE Trans. Acoust. Speech Signal Process.*, 1982, **30**, 833.
101. H. Barkhuijsen, R. de Beer, W. M. M. J. Bovee and D. van Ormondt, *J. Magn. Reson.*, 1985, **61**, 465.
102. G. H. Golub and C. F. Van Loan, *Matrix Computations*, Johns Hopkins University Press, Batimore, MD, 1996.
103. D. W. Tufts and R. Kumaresan, *IEEE Trans. Acoust. Speech Signal Process.*, 1982, **30**, 671.
104. G. H. Golub and C. Reinsch, *Num. Math.*, 1970, **14**, 403.
105. M. A. Delsuc, F. Ni and G. C. Levy, *J. Magn. Reson.*, 1987, **73**, 548.
106. K. Steiglitz and B. Dickinson, *IEEE Trans. Acoust. Speech Signal Process.*, 1982, **30**, 984.
107. H. Barkhuijsen, R. de Beer and D. van Ormondt, *J. Magn. Reson.*, 1985, **64**, 343.
108. J. Tang, P. Lin, M. K. Bowman and J. R. Norris, *J. Magn. Reson.*, 1985, **62**, 167.
109. H. Barkhuijsen, R. de Beer and D. van Ormondt, *J. Magn. Reson.*, 1986, **67**, 371.
110. J. A. Cadzow, *IEEE Trans. Acoust. Speech Signal Process.*, 1988, **36**, 49.
111. A. Diop, W. Kolbel, D. Michel, A. Briquet and D. Graveron-Demitly, *J. Magn. Reson. B*, 1994, **103**, 217.
112. J. Totz, A. van den Boogaart, S. van Huffel, D. Graveron-Demilly, I. Dologlou, R. Heidler and D. Michel, *J. Magn. Reson.*, 1997, **124**, 400.
113. M. A. Rahman and K.-B. Yu, *IEEE Trans. Acoust. Speech Signal Process.*, 1987, **35**, 1440.
114. C. F. Tirendi and J. F. Martin, *J. Magn. Reson.*, 1989, **85**, 162.
115. P. Koehl, C. Ling and J. F. Lefevre, *J. Magn. Reson A.*, 1994, **109**, 32.
116. S. van Huffel and J. Vandewalle, *The Total Least Squares Problem: Computational Aspects and Analysis*, SIAM, Philadelphia, 1991.
117. S. van Huffel, H. Chen, C. Decanniere and P. van Hecke, *J. Magn. Reson. A*, 1994, **110**, 228.
118. H. Chen, S. van Huffel, D. van Ormondt and R. de Beer, *J. Magn. Reson. A*, 1996, **119**, 225.
119. T. Akkin and S. Saliu, *Med. Biol. Eng. Comput.*, 1998, **36**, 544.
120. G. H. Golub and C. F. Van Loan, in *Smoothing Techniques for Curve Estimation* (eds T. Gasser and M. Rosenblatt), p. 69, Springer-Verlag, New York, 1979.
121. G. H. Golub and C. F. Van Loan, *SIAM J. Num. Anal.*, 1980, **17**, 883.
122. S. Y. Kung, K. S. Arun and D. V. Bhaskar Rao, *J. Opt. Soc. Am.*, 1983, **73**, 1799.
123. H. Barkhuijsen, R. de Beer and D. van Ormondt, *J. Magn. Reson.*, 1987, **73**, 553.
124. C. Lanczos, *J. Res. Natl. Bur. Stand.*, 1950, **45**, 255.
125. G. L. Millhauser, A. A. Carter, D. J. Schneider, J. H. Freed and R. E. Oswald, *J. Magn. Reson.*, 1989, **82**, 150.
126. W. W. F. Pijnappel, A. van den Boogaart, R. de Beer and D. van Ormondt, *J. Magn. Reson.*, 1992, **97**, 122.

127. P. J. Davis, *Circulant Matrices*, Wiley, New York, 1979.
128. L. Vanhamme, R. D. Fierro, S. van Huffel and R. de Beer, *J. Magn. Reson.*, 1998, **132**, 197.
129. H. Chen, S. van Huffel, C. Decanniere and P. van Hecke, *J. Magn. Reson. A*, 1994, **109**, 46.
130. H. Gesmar and J. J. Led, *J. Magn. Reson.*, 1988, **76**, 183.
131. H. Gesmar and P. C. Hansen, *J. Magn. Reson. A*, 1994, **106**, 236.
132. H. Gesmar and J. J. Led, *J. Magn. Reson.*, 1989, **83**, 53.
133. M. Joliot, B. M. Mazoyer and R. H. Huesman, *Magn. Reson. Med.*, 1991, **18**, 358.
134. A. van den Boogaart, D. van Ormondt, W. W. F. Pijnappel, R. de Beer and M. Ala-Korpela, in *Mathematics in Signal Processing III* (ed. J. G. McWhirter), 175, Clarendon Press, Oxford, 1994.
135. J. P. Burg, *Proceedings of the 37th Meeting, Society of Exploration Geophysicists, Oklahoma City*, 1967.
136. E. D. Laue, J. Skilling, J. Staunton, S. Sibisi and R. G. Brereton, *J. Magn. Reson.*, 1985, **62**, 437.
137. G. J. Daniell and P. J. Hore, *J. Magn. Reson.*, 1989, **84**, 515.
138. C. E. Shannon, *Bell Syst. Tech. J.*, 1948, **27**, 379.
139. S. F. Gull and G. J. Daniell, *Nature*, 1978, **272**, 686.
140. J. Skilling and R. Bryan, *Mon. Not. R. Astron. Soc.*, 1984, **211**, 111.
141. J. A. Jones and P. J. Hore, *J. Magn. Reson.*, 1991, **92**, 276.
142. D. S. Stephenson and G. Binsch, *J. Magn. Reson.*, 1978, **32**, 145.
143. P. Diehl, S. Sykora and J. Vogt, *J. Magn. Reson.*, 1975, **19**, 67.
144. K. Young, B. J. Soher and A. A. Maudsley, *Magn. Reson. Med.*, 1998, **40**, 816.
145. H. Hu, Q. N. Van, V. A. Mandeshtam and A. J. Shaka, *J. Magn. Reson.*, 1998, **134**, 76.
146. C. Mayer, *J. Magn. Reson.*, 1999, **138**, 1.
147. A. Van Den Bos, *IEEE Trans., Instrum. Meas.*, 1989, **38**, 1005.
148. L. Vanhamme, PhD thesis, 1999, Katholicke Universiteit, Leuven, Belgium.
149. X. Ouyang and P. L. Varghese, *Appl. Opt.*, 1989, **28**, 1538.
150. S. Van Huffel, L. Lagae, L. Vanhamme, P. Van Heck, D. Van Ormondt and K. U. Leuven, *Abstracts of the 15th Annual Meeting, European Society for Magnetic Resonance in Medicine and Biology, Geneva*, p. 13, 1998.
151. Z. Bi, A. P. Bruner, J. Li, K. N. Scott, Z. S. Liu, C. B. Stopka, H. W. Kim and D. C. Wilson, *J. Magn. Reson.*, 1999, **140**, 108.
152. P. Magain, F. Courbin and S. Sohy, *Astrophys. J.*, 1998, **494**, 472.
153. O. M. Weber, C. O. Duc, D. Meier and P. Boesiger, *Magn. Reson. Med.*, 1998, **39**, 723.
154. J. Kaartinen, S. Mieriskova, J. M. E. Oja, J-P. Usenius, R. A. Kauppinen and Y. Hiltunen, *J. Magn. Reson.*, 1998, **134**, 176.
155. R. Stoyanova, A. C. Kuesel and T. R. Brown, *J. Magn. Reson.* A, 1995, **115**, 265.
156. T. R. Brown and R. Stoyanova, *J. Magn. Reson. B*, 1996, **112**, 32.
157. G. J. Erickson, J. T. Rychert and C. R. Smith (eds), *Maximum Entropy and Bayesian Methods*, Kluwer Academic Publishers, Dordrecht, 1998.
158. J. J. Kotyk, N. G. Hoffman, W. C. Hutton, G. L. Bretthorst and J. H. Ackerman, *J. Magn. Reson. A*, 1995, **116**, 1.
159. K. S. Vines, D. F. Evilla and S. L. Whittenburg, *J. Magn. Reson.*, 1992, **100**, 195.
160. J. J. Kotyk, N. G. Hoffman and W. C. Hutton, *J. Magn. Reson.*, 1992, **98**, 483.
161. G. L. Bretthorst, *J. Magn. Reson.*, 1992, **98**, 501.
162. G. L. Bretthorst, *J. Magn. Reson.*, 1990, **88**, 533.
163. G. L. Bretthorst, *J. Magn. Reson.*, 1990, **88**, 552.
164. G. L. Bretthorst, *J. Magn. Reson.*, 1990, **88**, 571.
165. B. J. Soher, K. Young, V. Govindaraju and A. A. Maudsley, *Magn. Reson. Med.*, 1998, **40**, 822.
166. W. S. Cleveland, *J. Am. Stat. Assoc.*, 1979, **74**, 829.
167. D. L. Donoho and I. M. Johnstone, *J. Am. Statist. Assoc.*, 1995, **90**, 1200.
168. R. de Beer, A. Van den Boogaart, E. Cady, D. Graveron-Demilly, A. Knijn, K. W. Landenberger, J. C. Lindon, A. Ohlhoff, H. Serrai and M. Wylezinskia-Arridge, *Magn. Reson. Imag.*, 1998, **16**, 1127.

Recent Progress in Solid-State NMR of Low-γ Nuclei

MARK E. SMITH

Department of Physics, University of Warwick, Coventry, CV4 7AL, UK

1. Introduction 121
2. Experimental approaches 125
3. Spin-$\frac{1}{2}$ nuclei 130
   3.1. Yttrium-89 130
   3.2. Silver-107, -109 134
   3.3. Tungsten-183 137
4. Quadrupolar nuclei 138
   4.1. Nitrogen-14 138
   4.2. Magnesium-25 141
   4.3. Sulfur-33 146
   4.4. Chlorine-35, -37 148
   4.5. Potassium-39 150
   4.6. Calcium-43 154
   4.7. Titanium-47, -49 156
   4.8. Zinc-67 159
   4.9. Zirconium-91 162
   4.10. Molybdenum-95, -97 163
   4.11. Miscellaneous nuclei 168
5. Summary and conclusions 168
   References 169

1. INTRODUCTION

Most NMR spectroscopists have on some occasion examined the Periodic Table of NMR-active nuclei with ^{13}C, ^{17}O, etc., and contemplated that at first glance essentially the whole Periodic Table is potentially open to study by NMR. Solution-state NMR studies of nuclei with small magnetic moments exist, but often when papers report data concerning such nuclei the information is obtained not by simple direct excitation but indirectly using polarization transfer techniques such as INEPT and DEPT, and/or by using reverse detection methods.[1] As many of these indirect methods are not available in the

ANNUAL REPORTS ON NMR SPECTROSCOPY
VOLUME 43 ISBN 0-12-505343-6

solid state, direct detection is often the only option and consequently solid-state NMR studies of low-γ nuclei are sparse. It was recently pointed out that a general review of molybdenum NMR devoted $\ll 1\%$ to solid-state work.[2] Some more perspective on the scarcity of NMR of low-γ nuclei comes from analysis of recent annual reviews of NMR (e.g. references 3, 4), that reveals of the reported solid-state NMR studies typically <0.5% come from nuclei that have a small magnetic moment and are classified here as low-γ. The small number of solid-state NMR reports is certainly not due to a lack of potential applications. For example, in the field of the structural physics of inorganic materials there are many questions that could be answered by ^{47,49}Ti NMR, such as how the coordination of titanium changes with composition in titanium silicate and titanium aluminosilicate glasses. This review examines the background to the difficulties of studying nuclei with small magnetic moments by solid-state NMR, and details such work as has been carried out on them. The article has been aimed at researchers who want to apply NMR to understand materials and who have some NMR background, but are not necessarily NMR specialists. It would be wrong to claim that this article is completely comprehensive, but it is hoped that a significant fraction of the conventional solid-state NMR carried out on the nuclei examined has been captured. Sufficient details are given that someone wanting to observe such a nucleus for the first time will be able to find a suitable set-up compound and can estimate the experimental approach and conditions to use for the best chance of success.

First, clarification is required of what is meant by 'low-γ'. Any definition will be somewhat arbitrary, but a convenient definition taken here is one that arises from the frequency ranges of magic-angle spinning (MAS) NMR probes provided by the major manufacturers. Standard MAS NMR probes normally tune down to ^{15}N. Low-γ nuclei are therefore taken as those that resonate below ^{15}N, so that on a spectrometer equipped with a 9.4 T magnet this is below 40 MHz. This convenient working definition will be adopted in this review. The lower end is truncated at a resonant frequency of 10 MHz, since most commercial spectrometers will not operate below this frequency. The nuclei that satisfy this definition, along with some of their relevant properties, are listed in Table 1. This article also concentrates on the applications such nuclei have found in conventional solid-state NMR studies. There are always cases of applications where particular circumstances overcome the difficulties of observing such nuclei. For example often in magnetic materials the very large internal fields aid observation of low-γ nuclei with a specific case being Y_2Fe_{17}.[5] However, this is relatively unusual compared to most materials and such unusual cases will not be dealt with here.

Given the high natural abundance of some of these nuclei, they initially appear attractive. However, the small magnetic moment strongly counters any natural abundance advantage owing to a number of factors. First, at fixed field there is the fraction of nuclei that contributes to the net magnetization of the sample, which from the Boltzmann factor is proportional to γ. Then the net

Table 1. NMR properties of low-γ nuclei

Isotope	Spin	Natural abundance (A) (%)	ν_0 at 9.4 T	Relative receptivity[a]	Quadrupole moment (fm^2)[7]	Quadrupole broadening factor[b]	Sternheimer antishielding factor (γ_∞)[c]
^{57}Fe	$\frac{1}{2}$	2.19	12.952	4.2×10^{-3}			
^{89}Y	$\frac{1}{2}$	100	19.668	0.696			
^{103}Rh	$\frac{1}{2}$	100	12.689	0.180			
^{107}Ag	$\frac{1}{2}$	51.82	16.192	0.197			
^{109}Ag	$\frac{1}{2}$	48.18	18.614	0.279			
^{169}Tm	$\frac{1}{2}$	100	33.070	3.216			
^{183}W	$\frac{1}{2}$	14.40	16.647	0.061			
^{14}N	1	99.63	28.912	2.841	2.02	N.A.	−6.7
^{25}Mg	$\frac{5}{2}$	10.13	24.504	0.397	19.94	8.60	−4.1
^{33}S	$\frac{3}{2}$	0.76	30.724	0.040	−6.78	3.30	−52.2
^{35}Cl	$\frac{3}{2}$	75.53	39.236	8.091	−8.17	3.75	−42.0
^{37}Cl	$\frac{3}{2}$	24.47	32.660	1.514	−6.44	2.80	−42.0
^{39}K	$\frac{3}{2}$	93.10	18.688	1.079	6.01	4.27	−21.8
^{43}Ca	$\frac{7}{2}$	0.14	26.952	9.1×10^{-3}	−4.08	1.39×10^{-1}	−18.8
^{47}Ti	$\frac{5}{2}$	7.28	22.584	0.224	29	19.73	−9.0
^{49}Ti	$\frac{7}{2}$	5.51	22.592	0.225	24	5.74	−9.0
^{53}Cr	$\frac{3}{2}$	9.55	22.604	0.196	−15	21.9	−6.6
^{61}Ni	$\frac{3}{2}$	1.19	35.796	0.092	16.2	16.18	
^{67}Zn	$\frac{5}{2}$	4.11	25.072	0.173	15.0	4.76	−21.9
^{73}Ge	$\frac{9}{2}$	7.76	13.992	0.095	−17.3	2.62	−8.7
^{83}Kr	$\frac{9}{2}$	11.55	15.440	0.188	25.3	5.08	−85.5
^{85}Rb*	$\frac{5}{2}$	72.15	38.740	11.177	27.4	10.27	−52.8
^{87}Sr	$\frac{9}{2}$	7.02	17.396	0.164	33.5	7.91	−47.8
^{91}Zr	$\frac{5}{2}$	11.23	37.319	1.549	−20.6	6.02	−26.6
^{95}Mo	$\frac{5}{2}$	15.72	26.168	0.751	−2.2	0.98	−20[9]
^{97}Mo	$\frac{5}{2}$	9.46	26.716	0.481	25.5	12.88	−20[9]
^{99}Ru	$\frac{5}{2}$	12.72	18.456	0.213	7.9	1.80	
^{101}Ru	$\frac{5}{2}$	17.07	20.684	0.402	45.7	53.75	
^{105}Pd	$\frac{5}{2}$	22.23	18.400	0.368	66.0	125.5	
^{131}Xe*	$\frac{3}{2}$	21.18	32.980	1.350	−12.0	9.62	
^{135}Ba*	$\frac{3}{2}$	6.59	39.936	0.746	16.0	14.12	
^{177}Hf	$\frac{7}{2}$	18.50	16.168	0.278	336	1566	
^{189}Os	$\frac{3}{2}$	16.10	31.344	0.880	85.6	513.3	
^{201}Hg*	$\frac{3}{2}$	13.22	26.580	0.441	38.6	122.9	

* Not dealt with in this article as other more suitable nuclei exist.

[a] Relative receptivity: the receptivity[6] given by $\gamma^3 AI(I+1)$ relative to ^{13}C adjusted for quadrupolar nuclei by the fractional contribution of the central transition.

[b] Quadrupole broadening factor: the second-order quadrupolar broadening of the central transition which is proportional to

$$\frac{Q^2(I(I+1)-\frac{3}{4})^2}{\gamma(2I(2I-1))^2}$$

and has been normalized to ^{27}Al.

[c] Sternheimer antishielding factor is given where meaningful calculations have been carried out for ions with closed-shell structure e.g. Al^{3+}, Cl^-. Where possible given for a lattice,[8] and if not for free ions.

magnetization is proportional to this fraction multiplied by the magnetic moment, which itself is proportional to γ. Thirdly, the NMR signal is produced according to Faraday's law of electromagnetic induction by the rate of precession of this total magnetization in the NMR coil, which is also proportional to γ. Hence the intrinsic sensitivity per spin is proportional to γ^3. How strongly this factor affects sensitivity can be appreciated by considering ^{89}Y. The intrinsic nuclear sensitivity compared to ^{13}C (i.e. per magnetic nucleus) is only 7.5×10^{-3}, so that despite having natural abundance of 100%, compared to 1.1% for ^{13}C, ^{89}Y still only has a relative receptivity of 69.6% compared to ^{13}C. Often the situation is even worse than this as the relaxation needs to be taken into account. Although the relaxation strongly depends on the actual time dependence of the interactions, all other things being equal, smaller magnetic moments usually lead to less efficient relaxation for low-γ nuclei, greatly lengthening the experimental time needed to acquire an adequate signal-to-noise (S/N). There are always exceptions to this where conditions are much more favourable for observation. A good example of this is for ^{109}Ag. A high proportion of the reported solid-state NMR studies for ^{109}Ag come from silver-containing glasses in which the silver ion exhibits high ionic mobility that shortens the relaxation time, easing observation of this nucleus. Also for ^{89}Y there are a disproportionate number of reports of solid-state NMR from the high-temperture superconductors related to $YBa_2Cu_3O_7$. This is a result of the intense interest in understanding these materials, but also because the relaxation of less than a few seconds made ^{89}Y much more tractable in this system than in other materials where relaxation times of many minutes are often observed.

For nuclei with a spin $I > \frac{1}{2}$ there is the additional factor of the nuclear quadrupolar interaction which, although it is an electrical interaction, affects the NMR spectrum.[10,11] In Table 1 there is one integer spin (^{14}N) where all the transitions experience first-order broadening so that in all but the most symmetric cases extremely broad resonances will be observed, with a width proportional to ν_Q ($=e^2qQ/h$, where eQ is the nuclear quadrupole moment and eq is the maximum component of the electric field gradient). The effects this has on observation will be explored in more detail below. For non-integer spin quadrupole nuclei, the noncentral transitions experience the same first-order broadening but the central ($\frac{1}{2}$, $-\frac{1}{2}$) transition only experiences quadrupolar broadening to second order. The second-order broadening is proportional to ν_Q^2/ν_0, which means in the high-field limit ($\nu_Q \ll \nu_0$) the central transition is much narrower than the satellite transitions. The most important point for low-γ nuclei is that this broadening scales inversely proportionally with the Larmor frequency (ν_0). Hence, working at lower frequency as a result of the magnetic moment will result in a broader line compared to working at higher frequency. This adds to the problems of sensitivity. There is also the problem of detection in that, owing to a number of factors, wider lines are prone to distortions that have to be carefully compensated for.

2. EXPERIMENTAL APPROACHES

One of the key factors in making low-γ nuclei more accessible is improving the sensitivity. The most direct way is by the application of ever higher magnetic fields. The snapshot this review gives is at a time when there is beginning to be increased access to NMR spectrometers of 14.1 T and above dedicated to research on solids. Many of the nuclei in Table 1 that appeared intractable in the past in all but very special cases are certainly worth revisiting at the higher magnetic fields now available. The situation should be continuously monitored as higher magnetic fields are developed. The basic sensitivity increases as $B_0^{7/4}$ for spin-$\frac{1}{2}$ nuclei. The situation is even better for non-integer spin quadrupole nuclei because of the additional narrowing of the second-order quadrupole broadening so that the sensitivity of the experiment increases as $B_0^{11/4}$.

The most common experiment in FT NMR is the application of a single pulse followed by acquisition of the free induction decay (FID).[12] This is certainly the most direct way of performing an FT NMR experiment; but there are many potential pitfalls. Those that are particularly relevant to low-γ nuclei relate to effects that corrupt the start of the FID. Although they are numerous in origin, it is possible to divide these effects into two groups, viz. deadtime and probe ringing. Deadtime refers generally to all effects that result in the spectrometer being unable to accurately record the NMR signal. It is usual to split these effects into those from the probe[13] and those from other electronic parts of the spectrometer (e.g. filters). The probe deadtime can be readily understood: voltage associated with the nominally square pulse envelope cannot drop instantaneously to zero at its end because of the time constant of the probe circuit. This is conveniently described using the quality factor Q of the circuit. Q can be considered as the Larmor frequency/full width half maximum of the tuning curve, which also equals $\omega_0 L/R$. Then the probe deadtime is given by[14]

$$t_{\text{dead}} = \frac{Q}{\pi \nu_0} \tag{1}$$

The time t_{dead} represents the time constant for the exponential decay of the voltage induced by the transmitter pulse in the coil. It is longer for higher-Q probes and for lower resonance frequencies, hence this is a more marked problem for low-γ nuclei. Working at higher applied magnetic fields, the consequent increase in resonance frequency for a given nucleus does improve the situation. There are other electronic sources of deadtime including filters,[15,16] the preamplifier, the receiver and even the cables. These, however, usually have much higher bandwidths than the probe itself and hence the decay times are much shorter than from the probe.

Often the improvements sought in the deadtime in working at higher magnetic field are not as marked as one might expect from experience of working at a similar frequency for other nuclei at a lower magnetic field. The start of the FID can also be corrupted by ringing. Ringing is often used as an all-embracing term that describes effects that induce a voltage in the coil that is not an NMR signal. One source can be attributed to electromagnetic effects of the pulse interacting with the surroundings (e.g. the probe body) so that either mechanical and/or reradiation effects occur. An obvious source of mechanical ringing is the force exerted on the wire in the very high magnetic field as the time-varying current of the pulse is present. This can cause acousto-mechanical effects in the coil that continue for some time after the pulse is turned off and produces a short lived pseudo-FID. The overall efficiency of this process is given by[12,13]

$$E_c = \frac{k_1 B_0^2}{dV_s\left(1 + \dfrac{k_2 \rho^2 \nu_0^2}{V_s^4}\right)} \tag{2}$$

where k_1 and k_2 are constants,[13] B_0 is the applied static magnetic field, ρ is the resistivity of the metal, d is the bulk density, V_s is the acoustic wave velocity and ν_0 is the Larmor frequency. This clearly shows that at constant B_0 the situation is worse at lower frequencies so will affect low-γ nuclei more. It also shows that at constant frequency the situation is worse at higher B_0. The short-lived nature of such ringing causes a broad spectral feature that may look like a broad resonance or a baseline distortion.

These effects can be reduced by careful probe design, such as the coil orientation, and construction of the probe body. Different materials have very different ringing properties; for example, copper, silver and gold are mechanically and electrically favourable for the coil. At 16.9 MHz, taking the same diameter wire and using freestanding coils of silver, copper–silver alloy and copper–beryllium alloy produces ringing of 45, 80 and 200 μs, respectively. Anchoring the coil either on a slotted holder or by cementing/glueing it to a surface can significantly reduce the ringing compared to a freestanding coil. There is a trade-off here though, as any former will reduce the filling factor and this reduces sensitivity, which is one of the key considerations for low-γ nuclei. In static probes there is usually a choice to be made, but in virtually all magic-angle spinning probes the coil is freestanding. There are other sources of deadtime/ringing and a common one is the acoustic oscillations that can be set up in ceramic chip capacitors. These can often show strong ringing effects at particular frequencies. A lot of research has gone into reducing these effects and has been reviewed by Gerothanassis,[17] where extensive referencing of the primary literature is given.

In observing broad spectral lines, all the normal considerations[12] apply of using short enough pulses (pulse length T_p) to have sufficient bandwidth $P(\nu)$ to fully excite the lines:

$$P(\nu) = \frac{A \sin^2 \pi T_p(\nu_0 - \nu)}{(\nu_0 - \nu)^2} \tag{3}$$

This consideration is possibly more stringent for low-γ nuclei where, at least for quadrupolar nuclei, second-order line broadening effects can be much more significant. A common way to overcome deadtime/ringing problems is to form a signal with an effective time zero point outside the deadtime, i.e. an echo. There is a multiplicity of methods for forming echoes (see references 12, 18, 19 and references therein). Most methods are two-pulse sequences, e.g. the classic spin echo consisting of $90°-\tau-180°$ with refocusing at τ after the second pulse, whose effect can be explained for noninteracting spin-$\frac{1}{2}$ nuclei using a classical vector model. Hard RF-pulses are preferred for uniform excitation over broad lines. A particularly useful echo sequence proposed by Kunwar *et al.*[20] combines quadrature phase cycling with further cycling designed to cancel direct magnetization (the remaining FID) and ringing effects. The rotation produced by the second pulse in two-pulse echo experiments is not critical. In practice, the best choice is the second pulse of twice the length of the first, with the actual length being a trade-off between sensitivity and uniformity of the irradiation. Thus, for low-γ nuclei the use of short pulses that correspond to significant pulse angles, so as to produce significant sensitivity, means that a high power transmitter is necessary. There is also a trade-off in the size of coil, with smaller coils producing higher B_1 fields, and hence better lineshapes from the shorter pulses that can consequently be applied. However, there is a loss of sensitivity because of the smaller sample. In recording echoes there is an important practical consideration – applying the echo moves the effective $t = 0$ position for the FID outside the region where it is corrupted. However, in order that phasing problems do not re-emerge, the data sampling rate used should be sufficient to allow this point to be accurately defined. If T_2 is sufficiently short that an echo time can be used that allows the whole echo (both before and after the maximum) to be accurately recorded without an unacceptably large loss of intensity, there is no need to accurately define the new $t = 0$ position. Fourier transformation of the whole echo (which effectively amounts to integration between $\pm\infty$) followed by magnitude calculation removes phasing errors, producing a pure absorption lineshape with the signal-to-noise $\sqrt{2}$ larger than that obtained by transforming from the echo maximum.

Other pulse sequences have been derived to remove the baseline distortions introduced by deadtime and ringing. These are detailed and compared extensively in the article by Geronathassis.[17] The principle of most of these approaches is that signal and artefacts show differing coherence with the

pulses, so that, with a suitable combination of pulses and phase cycling, artefacts cancel. Sequences involving three pulses became popular and one of the most widely accepted approaches was the ring down elimination (RIDE) sequence.[21–23] The main problem with many of these sequences is that at relatively low pulse powers offset effects severely degrade the effectiveness of the sequence. To overcome this and the effects of RF inhomogeneity and mis-setting of the pulse angle, composite 180° pulses were shown to be much better.[22] More recently, reduction of ringing effects in one-pulse experiments have been considered. A practical solution that has been applied is to use a single pulse where the phase is modulated $\pm x$, which appears to have significant advantage in cancelling ringing.[24] Peizoelectric properties of the sample can also produce ringing effects. Often, changing the physical state of the sample, e.g. going from a single crystal or a coarse powder to a fine powder, can help considerably. Again, echo experiments are usually used and detailed calculations of echo formation to cancel out peizoelectric effects have been presented.[25]

Once lines become broader than about 200 kHz it becomes difficult to record resonances accurately using direct pulse techniques. To overcome these difficulties, several approaches have been adopted based on the philosophy that although the line is broad it can be recorded using a series of narrow-banded experiments that overcome the distortions introduced into a broad spectrum. One of these approaches is to carry out a spin-echo experiment using relatively weak RF pulses, recording only the intensity of the on-resonance magnetization and repeating the experiment at many frequencies to map out the lineshape. This approach works but is extremely time-consuming because each frequency step requires accurate retuning of the probe. Schemes that automatically retune the probe, based for example on the reflected power, would give much impetus to this approach. An alternative is to sweep the main magnetic field. There are several examples of sweeping the main magnetic field for solids dating from the earliest days of NMR, but only a limited number reported using superconducting magnets, with a recent example ^{27}Al in α-Al_2O_3.[26] Control of the field can be completely automated and integrated with the pulse programme. As with the stepped frequency experiment, relatively soft pulses are applied, and although strictly the on-resonance part of the magnetization should be used, experience shows that using the spin-echo intensity directly accurately reproduces the lineshape. This field sweep approach could be extremely useful as an alternative way of examining nuclei, especially low-γ nuclei for which narrowing techniques do not yet offer widespread opportunities for improved resolution and often the quadrupolar parameters provide the best discrimination between different phases and sites.

The most common solid-state NMR approach is magic-angle spinning (MAS). For higher-γ nuclei the tendency in recent years has been to employ ever faster spinning by using smaller diameter rotors. This is especially true for quadrupolar nuclei. As noted above, the second-order quadrupolar broadening

is usually worse for nuclei with smaller magnetic moments, so that fast spinning would seem attractive. However, the ability to narrow a wider range of lines by spinning faster is usually more than outweighed by the reduction in S/N from using a smaller sample, so that a compromise often needs to be reached. Usually a range of diameters of MAS probes is desirable, but the optimum size is probably 7–9.5 mm. The large increase in sensitivity with even larger rotors (e.g. 14 mm) is also often useful. As always, accurately setting the magic angle is very important. If the probes have restricted tuning ranges so that the nuclei usually used for setting the angle (e.g. ^{23}Na, ^{27}Al, ^{79,81}Br) cannot be observed, alternatives need to be sought. From Table 1 good candidates for setting the angle using the quadrupole satellite technique are ^{85}Rb in RbCl and ^{39}K in KBr. Alternatively, ^{14}N could be used if compounds can be found that are not too stringent regarding the accuracy with which the angle needs to be set for any spinning sidebands to be seen, and that have sufficient sensitivity for ready observation of the sidebands. Another possible candidate compound for setting the angle is $Mo(CO)_6$, as the sidebands are sensitive to angle but observation is not limited only close to the angle and it gives a reasonably strong signal. Since deadtime/ringing effects can be significant at the lower frequencies used, it is usual to acquire the MAS FID using an echo. The echo spacing is then set to an integral multiple of the period of the MAS rotation. There are of course many other solid-state NMR approaches that have been developed, especially for quadrupolar nuclei, and there is no reason in principle why these cannot be used for low-γ nuclei. Techniques[11] such as double angle rotation (DOR), dynamic angle spinning (DAS) and multiple quantum would yield useful information from low-γ nuclei, but again the main problem is one of sensitivity.

One of the advances that made solid-state NMR of dilute spin-$\frac{1}{2}$ nuclei (especially carbon) more attractive was cross-polarization (CP). One advantage of CP is the enhancement of the signal (proportional to the ratio γ_H/γ_X, where CP is from a nucleus with gyromagnetic ratio γ_H to one with a value of γ_X). There is also the advantage that the recycle time of the experiment is governed by the relaxation time of the source nucleus, which is usually shorter than that of the observed nucleus. Given that this is already a big advantage for a nucleus such as ^{13}C where the signal enhancement can be $\sim$4, there are even larger gains to be had with low-γ nuclei where, for example with ^{89}Y, this advantage could be increased to $\sim$20. As the recycle time is governed by the T_1 of the abundant spin, there is usually also a gain in being able to recycle faster, which should be more marked for nuclei with smaller magnetic moments. These big advantages can naturally only be gained in systems where there are sources of magnetization (e.g. with ^{1}H, ^{19}F, ^{31}P). There is also an important hardware consideration in that to achieve CP the Hartman–Hahn match condition ($\gamma_H B_{1H} = \gamma_X B_{1X}$) must be met. As B_1 is the RF field generated by the pulse at the respective Larmor frequencies for the two nuclei, this means that the power on the X-side has to be high for low-γ nuclei. This puts significant strain on the

probe and the preamplifier electronics. Schemes exist for reducing the power requirement on the X-side to achieve the matching condition, such as time-averaged precession and off-resonance effects. Another practical problem is that in setting up the spectrometer for CP a standard needs to be used. Weak signals can make this an extremely laborious process and Sebald has reviewed CP to less commonly observed spin-$\frac{1}{2}$ nuclei including low-γ nuclei, with suggestions for set-up compounds.[28] With modern spectrometer architecture the situation is much improved compared to a few years ago since much of the matching process can now be automated. The linearity of the amplifiers means that changes in settings can be made more predictably and that spectrometers can be set up much more reproducibly between sessions. If one is setting up on a nucleus for the first time it is often advantageous to set the CP condition approximately by measuring the output powers directly on an oscilloscope.

3. SPIN-$\frac{1}{2}$ NUCLEI

3.1. Yttrium-89

Even in diamagnetic materials ^{89}Y has quite an extensive shift range (Table 2). Several studies have reported ^{89}Y MAS NMR from Y_2O_3 that show two resonances[28–31] with a shift difference of ~40 ppm in the ratio 3 : 1, which agrees with the crystal structure that has two YO_6 environments. In Y_2O_3 T_1 for both sites has been determined to be just under 4 h.[31] To examine the effect of nearest-neighbour (nn) and next-nearest-neighbour coordination (nnn), a series of crystalline aluminates and silicates were observed.[30] Trends included the shift increasing with a greater number of nn oxygens, and increases in electronegativity of the attached group resulting in the ^{89}Y shift becoming less paramagnetic. However, it was clear that there was strong overlap from the nn and nnn effects so that detailed structural assignments based on the chemical shift alone need to be approached cautiously. There was also a wide range of linewidths in these compounds, varying from 10 to 170 Hz. The very narrow lines greatly aid observation. T_1 for $Y_3Al_5O_{12}$ was just over 1 h and the reduction compared to Y_2O_3 was attributed to the additional dipolar coupling to ^{27}Al.[31] This study also determined the chemical shift anisotropy (CSA) by using static spectra, which gave for $Y_3Al_5O_{12}$ 103 ppm, and for Y_2O_3 109 and 102 ppm for the two sites. ^{89}Y NMR data were also reported for the first time for Y_2O_2S, which had a significantly larger CSA of 161 ppm, and a longer T_1 of 6.6 h compared to Y_2O_3.[31]

^{89}Y NMR has also been reported extensively from yttrium sialon ceramics. Yttria is an important sintering aid for densifying silicon nitride. The properties of the sialon produced are determined by the nature of the grain boundary phase, which is usually a crystalline or glassy yttrium sialon. The often disordered nature of such phases can mean that broader ^{89}Y resonances are

Table 2. Summary of ^{89}Y solid-state NMR chemical shifts

Compound	δ_{iso} (ppm)*	Ref.
$Y(NO_3)_3 \cdot 6H_2O$	−55, −53.2	29, 41
$Y_2(SO_4)_3 \cdot 8H_2O$	−46, −50	29, 41
$Y(OAc)_3 \cdot 4H_2O$	47, 45	29, 41
$Y(acac)_2 \cdot 3H_2O$	27, 21.8	29, 41
Y_2O_3	314–315, 330† 270–273, 289†	28–31
$(Bi_2O_3)_{0.6}(Y_2O_3)_{0.4}$	275	34
Y_2O_2S	293†	31
$Y(OH)_3$	66	28
$YAlO_3$	214.5	30
$Y_3Al_3O_{12}$	222, 237†	30, 31
$Y_2SiBe_2O_7$	163	28
Y_2SiO_5	237, 148	30
α-$Y_2Si_2O_7$	144	30
β-$Y_2Si_2O_7$	208	30
γ-$Y_2Si_2O_7$	198	30
δ-$Y_2Si_2O_7$	122	30
$Y_2Sn_2O_7$	149	35
$Y_2Ti_2O_7$	65	35
Y_2Cl_3	762, 506	40
YCl_3	−230	40
YF_3	−112	42
$YCl_3 \cdot 6H_2O$	58	29
$YBr_3 \cdot 6H_2O$	80	42
$Y_2Si_3O_3N_4$	185–160.5	32
$Y_4Si_2O_7N_2$	202–214	32
YSi_3N_5	391, 506	33
$Y_2Si_3N_6$	394, 510	33
$Y_3Si_3N_6$	497	33
α-$YH_{0.12}$	3590	43
δ-$Y(H,D)_{1.92}$	910, 760	43
δ-$Y(H,D)_{1.98}$	920	43
δ-$YH_{1.99}$	946	44
$YH_{1.99+0.1}$	905	44
$YBa_2Cu_3O_7$	−103.2	45
Y_2BaCuO_5	−1250	45

* Shift relative to dilute aqueous YCl_3 except for † which are relative to 1.5 mol l^{-1} aqueous $Y(NO_3)_3$.

N.B. In *all* tables the values from the quoted references are given (for some the shift reference has been made consistent). Papers vary widely in the quality and accuracy of the data, which the interested reader should check.

produced that militate against ^{89}Y NMR observation. However, paramagnetic doping can greatly reduce T_1, allowing observation, with Eu^{3+} found to produce effective relaxation while not producing significant broadening of the resonance.[32] In YSiN compounds the nn effect of nitrogen produces the

expected positive shift from oxides.[32,33] $Y_2Si_3O_3N_4$ and $Y_4Si_2O_7N_2$ could be readily distinguished on the basis of the ^{89}Y NMR shift and, although the lines from the secondary phases formed in Si_3N_4 sintered with yttria were quite broad, the nature of the secondary phase was clearly determined to be one of these from the ^{89}Y NMR. This showed that the grain boundary phase formed became more yttrium-rich with increased heat treatment.[33]

One of the most useful applications of ^{89}Y NMR has been to probe atomic positions and distributions in solid solutions. For example, in $(Bi_2O_3)_{0.6}(Y_2O_3)_{0.4}$ the shift of the ^{89}Y NMR resonance at 275 ppm (very close to one of the sites in Y_2O_3) indicated that the yttrium ions prefer centrosymmetric sites created by the oxygen-vacancy pairs.[34] In $Y_{2-y}Ln_yM_2O_7$ (Ln = Ce, Pr, Nd, Sm, Eu, Yb; M = Sn, Ti) the addition of the paramagnetic ions greatly reduced the ^{89}Y T_1 and also gave rise to additional resonances.[35] These extra signals were attributed to substitutions of a Ln ion for yttrium in the nnn shell. In the pyrochlore structure these sites led to environments of the form $Y(OY)_{6-x}(OLn)_x$. The isotropic shift is different for each lanthanide but each shows an additive change with x. The exact nature of the source of this shift is unclear, probably being a combination of through-space and through-bond effects. The detection and assignment of the additional resonances means that the atomic distribution and hence the solubility in the solid solution can be determined. The sensitivity to the atomic distribution has consequences for determining rare-earth location with application to laser and phosphor materials. ^{89}Y MAS NMR has thus been applied to examine the red phosphors Eu-doped Y_2O_3[36] and Y_2O_2S[37] and Tb-doped $Y_3Al_5O_{12}$,[38] a green phosphor. In all three of these studies additional ^{89}Y resonances could be observed that were assigned to nnn substitution by a rare-earth ion. By examining the linewidths and intensity of the different resonances, correlation to the brightness of the phosphor clearly showed that optimum brightness properties were produced when the rare-earth distribution was most homogeneous. Production of $Y_3Al_5O_{12}$ by a hybrid gel route was followed by ^{89}Y MAS NMR.[39] It was shown that the yttrium environment did not change from that in the initial gel to the final *bona fide* YAG environment until after crystallization occurred.

Room-temperature ^{89}Y MAS NMR of YCl_3 and Y_2Cl_3 showed very strong deshielding in the latter compound (Table 2) due to direct Y–Y bonding giving rise to d-bonding states.[40] In CP studies various compounds were studied for their CP characteristics and $Y(NO_3)_3 \cdot 6H_2O$ was determined to be a good set-up compound even though it exhibits a broad match condition.[41] A reasonable S/N was achieved on this compound using a 7 mm rotor at 7.05 T with four pulses using a 10 s delay. From the series of hydrates of $Y(NO_3)_3$, $Y_2(SO_4)_3$, $Y(OAc)_3$ and $Y(acac)_3$, extremely narrow MAS NMR resonances (10–20 Hz) were obtained. The optimum contact time in these compounds was found to be quite long, in the range 8–30 ms. Static spectra showed CSA in the range 27–75 ppm.[41] Other CP studies of ^{89}Y have included a range of yttrium alkoxide complexes and compounds where the optimum contact time was

typically 20 ms.[42] In these compounds the number of environments was reflected in the number of ^{89}Y resonances observed, so that solid-state NMR can be used to fingerprint ligand environments and hence determine the purity of bulk samples.

Yttrium and hydrogen can form a range of compounds that have potential applications in hydrogen storage, with extensive NMR studies that have included ^{89}Y. These materials can show significant Knight shifts, which in the dihydride was determined to be 0.11%. In α-$YH_{0.18}$ no ^{89}Y NMR signal could be detected below 350 K, which was attributed to insufficient hydrogen pair ordering. At higher temperatures, averaging due to hydrogen diffusion produces a single ^{89}Y line with axial symmetry and a typical shift of 0.359%. Dihydride phases formed with deuterium showed two signals that merge at higher temperatures and can be associated with hydrogen ordering.[43] ^{1}H–^{89}Y CP was applied to δ-$YH_{1.99}$ and $YH_{1.99+0.1}$, and both showed a single peak but with very different CP characteristics that were attributed to differences in the room-temperature hydrogen motion.[44] On cooling, as the hydrogen motion is reduced, separate lines become apparent, again associated with hydrogen ordering.

Study of high-temperature superconductors related to $YBa_2Cu_3O_7$ and $YBa_2Cu_4O_8$ has extensively exploited ^{89}Y solid-state NMR. The yttrium ion resides between the CuO_2 planes that are believed to be central to the superconductivity of these materials. The NMR-determined Knight shift is the most direct way of probing at the atomic scale the temperature dependence of the spin susceptibility of these materials, reflecting both the spin and orbital character of the coupling in these highly correlated systems. The NMR measurements place significant experimental constraints on the theoretical attempts to model the electronic behaviour of these materials. In the late 1980s accurate measurements of the ^{89}Y shift were first reported and were broken down into contributions from the s and d bands. It was found that in $YBa_2Cu_3O_{7-\delta}$ changes in the shift with oxygen content were due to lowering of the density of d-states at the Fermi level. It was also realized that the static linewidth gave an estimate of the penetration depth of the magnetic field.[45–50] ^{89}Y NMR measurements showed that this shift scaled directly with the spin susceptibility and, as all three elements in the structure measured by NMR (^{17}O, ^{63}Cu, ^{89}Y) showed similar temperature dependences of their shifts, this was taken as evidence of the properties of the system being determined by a single spin fluid. There have been a number of much more complete reviews of the general application of solid-state NMR (including ^{89}Y NMR) and the theory used to probe high-temperature superconductors. A recent one is by Rigamonti *et al.*,[51] which refers extensively to the primary literature and to other previous reviews of this topic.

The structural chemistry in these compounds is very rich, with a wide range of substitutions into the different sites occurring, particularly for the plane and chain copper sites in $YBa_2(Cu_{1-x}M_x)_3O_7$.[52–55] Some elements (e.g. Fe, Co, Al

and Ga) substitute on the chain site, whereas others (e.g. Ni, Zn) go into plane sites. Substitution into the planes has little effect on the structure and properties, whereas that into the chain site causes the structure to change to tetragonal, which also affects T_c. The change of structure is neatly demonstrated by the extrapolation of all series with differing levels of doping. Those showing chain substitution extrapolate at $x = 0$ to -90 ± 2 ppm, whereas for plane substitutions this point is -103 ± 1 ppm.[53] In $YBa_2Cu_4O_8$, Zn and Ni again substitute into the CuO_2 planes, whereas Ca goes in between the planes. Intraplanar impurities lead to T_c being rapidly depressed, whereas substitution between the planes has relatively little effect.[56] The complexity of these studies and the detail with which they probe the underlying physics is highlighted by recent studies that (i) used ^{89}Y NMR data[57] to show that in $YBa_2Cu_3O_{7-\delta}$ the density of states has a peak that is pinned at the Fermi level and grows with overdoping, and (ii) used ^{89}Y T_1 measurements to indicate that the energy of the spin dynamics near q (wave vector) = 0 had to be strongly temperature dependent to be consistent with other experimental data and the one-band model of the system.[58] A recent elegant experiment used ^{89}Y on $^{16/18}O$ isotopically exchanged $YBa_2Cu_4O_8$ to examine the role of phonons in the spin and pseudo-gaps, and showed that the pseudo-gap correlations were independent of the superconducting pairing correlations.[59]

In these materials below T_c a flux lattice exists giving rise to a variation in the internal magnetic field. ^{89}Y NMR measurements provided evidence of the field distribution in this state.[60] The flux lattice motion could also be followed by the ^{89}Y resonance in slightly underdoped $YBa_2Cu_3O_7$[61] and this motion also produces an additional contribution to the T_2 of ^{89}Y. Analysing relaxation data in these systems is very complex as there can be many different sources of relaxation effects (e.g. fluctuations of the copper moments can also contribute).[62] In $YBa_2Cu_4O_8$ the magnetic field dependence of the temperature-dependent ^{89}Y T_1 showed that the activation energy of thermal depinning was proportional to the applied magnetic field.[63] These examples are meant to provide some flavour for the extensive use that has been made of ^{89}Y solid-state NMR to probe high-temperature superconductors.

3.2. Silver-107, -109

Solid-state NMR study of silver would be helpful in understanding areas from fast ion conducting glasses to organometallic complexes of biological significance. The majority of solid-state NMR work to date has used ^{109}Ag owing to its higher sensitivity. In keeping with being a heavy metal, silver shows a significant chemical shift range (~1000 ppm) making it a sensitive probe of crystallographic inequivalence. Silver is found in a range of local coordinations (typically two to four) and, given the large shift range, the more asymmetric of these are likely to exhibit significant CSA, although the number of accurate CSA

measurements for silver is extremely limited. In materials where T_1 is long and there are strong sources of magnetization, CP is advantageous. After the study of various possible CP set-up compounds, silver lactate has been suggested.[64] A characteristic of most silver CP is the long contact times typically used (10–50 ms). The signal gain in performing CP was illustrated using silver lactate, where no FID was observable under single-pulse acquisition whereas CP produced a clear signal in one scan. To date it appears that all CP has been performed using 7 mm MAS rotors with spinning speeds typically in the range 2.5–4.5 kHz. As these spinning speeds appear sufficient, there could be advantage in using larger volume CP MAS probes with 9.5–10 mm diameter.

The sensitivity of silver NMR chemical shifts is illustrated by a series of studies of silver thiolates and related compounds.[65–67] In $[(C_6H_5)_4P]_2[Ag_4(SCH_2C_6H_4CH_2S)_3] \cdot 6CH_3OH$ there are four crystallographically inequivalent AgS_3 sites, three looking very similar and the fourth on the threefold axis more distorted. The ^{109}Ag NMR spectrum shows three closely spaced peaks between 1203 and 1230 ppm and a fourth peak at 1083 ppm. The shift range of AgS_2 environments (790–890 ppm) is shifted upfield compared to AgS_3 (950–1250 ppm). Silver sites also show a significant range in their CSA with values ($\Delta\sigma$) of 570 to 2120 ppm reported from such compounds.[65] The *trans* and *gauche* forms of layered silver butanethiolate were readily distinguished, each having two inequivalent silver sites.[67] The large chemical shift characteristics of silver have also resulted in compounds that show some structural and/or atomic disorder not producing observable NMR signals.

The silver halides and related compounds have been the most-studied materials using ^{109}Ag NMR (Table 3) with several studies reporting the chemical shift of silver iodide.[68–71] Silver iodide is of central importance to silver-based fast ion conducting phases and glasses and it displays significant polytypism, with the isotropic chemical shift of the polytypes covering a range of ~100 ppm.[70] The chemical shift of the silver halides shows an inverse halogen dependence.[68] In many materials there can be significant silver ion motion, sometimes even at room temperature, which means the NMR spectra often show single peaks at a position that is a weighted average of the different environments in the structure. In the α and β polymorphs of $RbAg_4I_5$ and KAg_4I_5 a single resonance is observed.[68] In the β-phase of $RbAg_4I_5$ the decrease in site symmetry from the α phase to trigonal manifests itself as an observable CSA.[68] On further cooling to the γ-phase, the silver NMR signal is lost completely owing to a combination of T_1 lengthening and the greatly reduced motion resulting in significant linebroadening. In $Ag_xCu_{1-x}I$ solid solutions ^{109}Ag silver NMR spectra show a decreasing shift with increasing x. *Ab initio* calculations within Gaussian 94 using a double-ζ basis set related the shift change to decreases in the bond length of the AgI_4^{3-} tetrahedral units via changes in d-hole and p-electron densities.[72]

Studies of $AgI \cdot Ag_2O \cdot B_2O_3$ glasses have shown complex phase behaviour, with shift changes observed for silver depending on whether it is coordinated to

Table 3. Summary of ^{109}Ag solid-state NMR chemical shifts

Compound	δ_{iso} (ppm)*	Ref.
$Ag[CH_3CHC(OH)CO_2]$, silver lactate	345.9, 320.2, 219.7, 210.7	64
$Ag[CH_3CO_2]$, silver acetate	401.2, 382.7	64
$Ag(CH_3C_6H_4SO_3)$	44.1	64
$Ag(C_5H_7O_2)$	471.6	64
$AgN(SO_2Me)_2$	210.3	64
$AgN(SO_2Me)_2 \cdot 0.25H_2O$	182.8, 130.7, 32.5	64
$Ag_5[(S(CH_2)_3NMe_2)_3(S(CH_2)_3NMe_2H)_3](ClO_4)_2$	1228, 826	65
$[(C_6H_5)_4P]_2[Ag_4(SCH_2C_6H_4CH_2S)_3] \cdot 6MeOH$	1230, 1220, 1203, 1083	65
$AgS(CH_2)_3CH_3$ (all-*trans*)	962, 952	67
$AgS(CH_2)_3CH_3$ (all *gauche*)	1083, 1048	67
$((CH_3)_4N)_2[Ag_5(SC_6H_5)_7]$	1141, 980	65
Ag_2(1,5-pentaethiolate)	900–1300	65
$[P(C_6H_5)_3Me][AgI_3]$	675	65
$Ag_5\{\mu_2\text{-}S(CH_2)_3N(CH_3)_2\}_3$ $\{\mu^2\text{-}S(CH_2)_3NH(CH_3)_2\}_3(ClO_4)_2$	1228, 826	65
AgI	710, 728, 680	68, 69, 71
AgCl	370, 353.5, 409	68, 69
AgBr	350, 350	68, 69
AgF	−110, −125	68, 69
KAg_4I_5	810	68
$RbAg_4I_5$	790	68
$Ag_{26}I_{18}W_4O_{16}$	580	68
Ag_2MoO_4	130	71
$AgPO_3$	96	77
$Ag_4P_2O_7$	383	77
$Ag_{10}Si_4O_{13}$	320	80
$AgNO_3$	−87	79
Silver metal	−5253	79

* Relative to dilute aqueous silver nitrate.

iodide groups or borate groups.[70,73] ^{109}Ag NMR was able to follow crystallization and phase separation, and their dependence on composition.[70] T_1 measurements have been interpreted to indicate that there are two sites undergoing very different rates of motion.[73] There has been some dispute whether NMR provides unambiguous evidence for different structural sites and sites with differing mobilities. Compositions in the system $AgI \cdot xAg_2MoO_4$ show resonances from the iodide and molybdate end members and an intermediate peak at 548 ppm attributable to the glassy phase that formed.[71,74] Crystallization of glasses at $2AgI \cdot Ag_2MoO_4$ produced a powder pattern that was characteristic of an axial CSA of ~70 ppm.[71]

^{109}Ag T_1 and T_2 measurements of glasses with $x = 0.375$ and 0.50 in the system $(AgI)_x(Ag_2S \cdot GeS_2)_{1-x}$ suggest that on the NMR timescale all the silver ions are mobile.[75] In some tellurite-based AgI fast ion conducting glasses, silver NMR showed several signals that were attributed to oxyiodide and iodide

environments.[76] In these glasses the silver mobility increased with AgI content. For glasses in the system $(AgI)_x(Ag_2O)_y(P_2O_5)_{1-x-y}$ over the temperature range 50 to $-85\,^{\circ}C$, rapid narrowing of the ^{109}Ag resonance was observed. The spectra from the glasses were compared to crystalline $AgPO_3$ and $Ag_4P_2O_7$. One resonance was observed, and from accurate quantification it was clear that there is one region with the iodine effectively uniformly distributed throughout the structure. The silver is in fairly rapid motion at room temperature through the structure. Comparison of glassy and crystalline $AgPO_3$ revealed a shift difference of 90 ppm that is probably related to changes in coordination number between the two states.[77]

In Ag_9GaSe_6, ^{107}Ag and ^{109}Ag spectra and relaxation times were measured as a function of temperature and applied magnetic field.[78] Three different phases were observed. In the high-temperature cubic phase (I) T_1 was independent of applied magnetic field strength. In the fast-motion limit the ratio of relaxation times for the two silver isotopes indicated that the main relaxation mechanism was scalar coupling of the first kind via an exchange interaction. In the low-temperature phase (III) a very broad silver line ($\sim$1000 ppm) was observed that was related to CSA. ^{109}Ag NMR was also applied to follow the process of forming silver particles supported on SiO_2, η-Al_2O_3 and zeolite A.[79] Signals were detected from metallic silver, $AgNO_3$ and AgCl but not from Ag_2O nor Ag_2O_2. Initially, after drying a solution of $AgNO_3$, a resonance that approached that of bulk $AgNO_3$ was observed. After reduction, silver is formed that gives a resonance at 5252 ppm in particles that exceeded 50 nm. Smaller particles did not produce any observable resonances as surface effects broaden the resonances owing to interaction with conduction electrons. Adsorption of oxygen, chlorine and hydrogen chloride onto the surface of these silver crystallites had no effect on the silver NMR spectrum.

3.3. Tungsten-183

Tungsten has a lower receptivity than both yttrium and silver and, from the very few solid-state NMR studies that have been carried out, also shows extremely long T_1 values. Also, since it is a heavy metal, it can be anticipated that in all but the most symmetric environments CSA will spread the intensity over a very broad spectral range. In alkali tungstates and $W(CO)_6$, crystallography suggests very symmetric tungsten environments, which is reflected in very narrow MAS NMR resonances (6 Hz in the case of $W(CO)_6$) with no spinning sidebands.[81] WO_3 has two crystallographically inequivalent, equally abundant WO_6 sites and two resonances are observed (Table 4).[81] In the Keggin compound $H_3[P(W_{12}O_{40})] \cdot nH_2O$ a single resonance with a very large CSA was detected. The direct ^{183}W MAS NMR spectra reported required between 7 and 43 h to collect.

To improve both sensitivity and recycle delays when protons are present, CP can be applied.[82] Typically extremely long contact times ($\sim$100 ms) are

Table 4. Summary of ^{183}W solid-state NMR chemical shifts

Compound	δ_{iso} (ppm)*	Ref.
Li_2WO_4	−40	81
Na_2WO_4	−63	81
K_2WO_4	−18	81
Cs_2WO_4	−36	81
$CaWO_4$	29	81
$SrWO_4$	−33	81
$BaWO_4$	−78	81
WO_3	−414, −438	81
$W(CO)_6$	−3470	81
$H_3[P(W_{12}O_{40})] \cdot nH_2O$	−174	81
$(NH_4)_2WS_4$	3639.6	82
$(NH_4)_2WO_4$	−38.6, −55.8, −63.6, −80.0, −95.6, −107.4, −115.9	82
H_2WO_4	−251.1	82
$(C_5H_5)W(CO)_3Pr^i$	−3377.9, −3386.8	82

* Relative to saturated aqueous Na_2WO_4.

optimal, which puts considerable strain on the high-power amplifier at the tungsten frequency. For optimizing CP, $(NH_4)_2WS_4$ was the best compound. $(NH_4)_2WO_4$ was unusual requiring a significantly shorter optimum contact time (5–10 ms) and showed seven isotropic resonances, but there is no available crystal structure for comparison. If structural H_2O molecules were used as the source of CP, no signal could be detected. ^{183}W NMR appears to be very sensitive to structural detail as, although a signal could be readily detected from $C_5H_5W(CO)_3Pr^i$, in changing the ligand to Bu^t no CP signal could then be detected. CP is only a real advantage if $T_{1\rho}$ is favourable, but even then such experiments often required in excess of 15 h. On the basis of the limited data set collected, it is difficult to say whether it is going to be possible to distinguish WO_4 and WO_6 on the basis of the chemical shift. The difficulty of the ^{183}W solid-state NMR studies to date indicate that it is still far from routine.

4. QUADRUPOLAR NUCLEI

4.1. Nitrogen-14

^{14}N belongs to the select group of nuclei with integer spins. Quadrupolar nuclei of this group have no $(\frac{1}{2}, -\frac{1}{2})$, so that all transitions are first-order quadrupolar broadened. This means that all the intensity is spread over $\sim 2\nu_Q$ and this can be very demanding on the spectrometer, as for the satellite transitions of non-integer spins. C_Q for nitrogen has been determined in the range 0–8 MHz with typical values of 3–4 MHz.[83] The number of solid-state NMR studies of

^{14}N has been very limited even though it is 99.63% abundant. The interest in nitrogen NMR is nevertheless indicated by the number of studies that employ the spin-$\frac{1}{2}$ isotope ^{15}N, often going to the expense of enriching the sample. The importance of nitrogen in many fields of science and technology means that nitrogen NMR of solids could be widely applied. Several ingenious approaches have been developed to improve the resolution of ^{14}N NMR spectra. One of these is overtone spectroscopy which irradiates at approximately twice the Larmor frequency.[84] If the quadrupole interaction is sufficiently large that second-order quadrupole effects are significant, then the $(-1 \leftrightarrow 1)$ transition becomes weakly allowed. In powders the spectrum is still structured, which allows the interactions to be deduced, but is a factor $6\nu_0/C_Q$ times narrower. This was applied to some solids of biological interest. Consideration has also been given to improving the signal intensity of echoes for ^{14}N and the generation of double-quantum coherence in two- and three-pulse sequences.[85] In cases where ^{14}N is dipolar coupled to a spin-$\frac{1}{2}$ nucleus, the NMR interaction parameters can be deduced from the modulation of the response of the spin-$\frac{1}{2}$ nucleus. Examples of this include spin-locking[86] the ^{14}N for different periods of time and applying short pulses to the ^{14}N in the REAPDOR experiment.[87] The magnetization is transferred through quasi-adiabatic processes as MAS causes level crossing.

Other approaches for recording broad ^{14}N lines have adopted the philosophy that the spectra can be recorded piecewise, as in a frequency-stepped approach that has been applied to ^{14}N in KNO_3.[88] However, these approaches are very time inefficient as only a small fraction of the spins are excited at any particular instant. To overcome this, an approach that slowly rotates the sample ($\sim$1 rpm) has been introduced termed Rotisserie.[83] This significantly increases the sensitivity and reduces the recycle time necessary, greatly reducing the length of the experiment, and has been applied to Si_3N_4.[83] The approach has been extended to use the rotation concept to measure the modulation effect of an echo formed, which again contains information about the interaction parameters in the STEAMER experiment.[83]

In some organic phases where there is high site symmetry (and usually high motion as well), narrow resonances have been observed. For example in $((CH_3)_3NC_2H_5)ClO_4$ phase II $C_Q = 8.1$ kHz. In $((CH_3)_3NC_2H_5)NO_3$ two narrow nitrogen resonances were detected at -8 ppm for the organic nitrogen and -338.2 ppm for the nitrate relative to the accepted reference standard, nitromethane.[89] A range of teraalkylammonium and related salts have all been measured and give C_Q in the range 10–200 kHz.[90,91]

^{14}N NMR studies of single crystal have allowed C_Q to be deduced in, for example, NH_4ClO_4,[92] $NH_4Al(SO_4)_2 \cdot 12H_2O$,[93] $Ba(NO_3)_2$[94] and KNO_3.[95] By detailed analysis of the single-crystal pattern from KNO_3, elements of the chemical shift tensor could be determined, with the largest component measured as 149.6 ppm.[96] The single-crystal rotation pattern of Li_3N also shows evidence of CSA.[97] Two things emerge immediately from inspection of

the literature of ^{14}N from inorganic solids. First, there is no agreement on a suitable spectral reference. In the relatively small selection of papers, at least five different references were chosen. The other problem with nitrogen is that T_1 can be very long, with values determined of 41 s in NH_4ClO_4[92] and 1080 s in AlN.[98] For hexagonal BN a 30 minute delay was allowed between pulses.[99] Improvements in MAS probe technology, particularly in stability and control of the spinning speed, mean that MAS is possible for ^{14}N even when the quadrupole interaction is large. As the quadrupolar interaction is inhomogeneous, the wide lines will split up into a series of sharp sidebands in a crystalline sample. Ammonium halides gave sharp MAS spectra, and the chloride and bromide differ in peak position by only ~2 ppm. ^{14}N MAS NMR spectra have been reported from AlN[98] and hexagonal BN.[98,99] In hexagonal BN simulation of the sideband manifold needed both quadrupole and CSA interactions to fit with the CSA of 160 ± 20 ppm.[99,100] The spectrum from cubic BN had very many fewer sidebands, which were ascribed to the dipolar interaction. There was clear shift difference between NB_3 and NB_4 units of ~70 ppm. The ^{14}N spectrum has also been recorded from the cubic metal TiN, which shows a Knight shift (Table 5).[101] In the solid solution TiC_xN_{1-x}, as carbon was added

Table 5. Summary of solid-state NMR interaction parameters for ^{14}N

Compound	δ_{iso} (ppm)*	C_Q (MHz)	η	Ref.
Si_3N_4	N.D.	2.1	0	83
KNO_3	373.2	0.751	0.022	95
NH_4ClO_4	N.D.	0.053568	0.1288	92
ND_4ClO_4	N.D.	0.052530	0.1257	92
$N^IH_4SCN^{II}$				
I	N.D.	0.093	1	104
II	N.D.	2.28	~0.04	104
Cubic BN	−17.6	~0		100
Hexagonal BN	612	0.140 ± 0.01, 0.142	0	98, 100
AlN	N.D.	<0.01	0	98
TiN	359.5†, 338†			101
$NH_4Al(SO_4)_2 \cdot 12H_2O$	N.D.	0.196	~0	93
$(NH_4)_2SO_4$				
Site I	N.D.	0.15443	0.684	105
Site II	N.D.	0.11571	0.749	105
NH_4Cl	0	~0	~0	102
NH_4Br	2.2	N.D.	N.D.	106
Li_3N	N.D.	0.505	0	97
$Ba(NO_3)_2$	N.D.	6.998	0	94
$Pb(NO_3)_2$	350.2	N.D.	N.D.	102
NH_4IO_4	N.D.	0.013	0	107
NH_4ReO_4	N.D.	0.050	0	108

*Chemical shift relative to solid NH_4Cl except † which are reported relative to liquid ammonia. N.D., not determined or not given.

there was a change of shift that can be rationalized in terms of a change of the density of states. The static spectra became much broader in the solid solution. Although there was no discernible quadrupolar structure, it is possible that the local site symmetry is being reduced in the solid solution, producing a significant electric field gradient. The lines could consequently be much broader and hence only be partially excited.

Further ^{14}N MAS NMR studies have recently appeared using the principle that the first-order quadrupole interaction is inhomogeneous, so that provided the angle is accurately set the resonance should narrow under MAS. Procedures were described to add sidebands to enhance the S/N and to use variable spinning speeds to determine the centrebands.[102] A mixture of KNO_3, $Pb(NO_3)_2$ and NH_4Cl was taken and quantitatively deconvolved using this approach.[102] Slight deviations from the magic angle cause residual broadening in the lineshape, but if the angle is known this shape can be used to deduce the interaction.[103] NH_4Cl would appear to be a good secondary reference for solid-state NMR, as it has a narrow MAS signal and can be observed with good S/N in a single scan. It has a shift of 342.4 ppm from the primary nitrogen reference of liquid nitromethane.[103]

4.2. Magnesium-25

Magnesium is an element whose structural role is significant in many fields of science and technology. Particular applications include earth sciences in minerals and melts, in technologically important high-temperature ceramic materials, and in bio-inorganic chemistry where it is one of the most important elements in cellular biochemistry. The same type of question is posed as for other elements such as aluminium; can the NMR parameters (particularly the chemical shift) distinguish different local coordinations (e.g. MgX_4 and MgX_6)? In terms of modern MAS techniques, the first report on some simple compounds showed that cubic materials such as MgO, MgS and Mg_2Si give very narrow MAS resonances ($\leqslant$50 Hz at 8.45 T).[109] In less symmetric compounds the lines were much broader, with some showing second-order quadrupole structure from which δ_{iso} could be deduced. Some were too broad to be narrowed with MAS at 8.45 T, and it was then difficult to deduce the isotropic chemical shift. $MgCl_2$ with an unknown state of hydration gave a very different spectrum from that determined for $MgCl_2 \cdot 6H_2O$ at 77 K using a level-crossing technique.[110] For compounds in which the chemical shift could be determined, it appeared that the shift difference between MgO_6 and MgO_4 was $\sim$25 ppm.

The shift and T_1 were measured in MgO from room temperature up to 1300 °C. T_1 was long at all temperatures ($\sim$50 s) and δ_{iso} only varied from 25 to 27 ppm across the whole temperature range. The change of δ_{iso} was in the opposite direction to that expected from simple bond length versus shift

correlations, and arguments for the observed change of shift were advanced in terms of thermal vibration increasing orbital overlap.[111] In nanocrystalline MgO prepared using hydrolysis of $Mg(OCH_3)_2$, as the particle size increased from 3 to 35 nm, the linewidth decreased from 2 kHz to 450 Hz and the shift of the peak position increased from 18 to 25.3 ppm, the latter close to the position of bulk MgO.[112] In particles below 3 nm the broadening effects presumably related to disorder precluded observation of the ^{25}Mg resonance. Additions of nickel to MgO have also been followed by ^{25}Mg NMR.[113] A single-crystal study of $Mg(OH)_2$ from which C_Q and δ_{iso} were deduced found that the linewidth was a strong function of rotation angle of the crystal, which was put down to mosaic spread of the crystal.[114] Even though the Mg–O bond is quite ionic, a small CSA contribution to the linewidth of ~6 ppm could be deduced. Thermal decomposition of brucite was followed by ^{25}Mg NMR, supporting the idea that there was coherent growth of small domains on MgO that subsequently coalesced into crystallites.[115] $Mg(OH)_2$ was added as a fire retardant in ethylene–vinyl acetate copolymers. ^{25}Mg NMR was used to characterize the phases before and after combustion and showed that formation of a glassy phase was at the heart of the fire retardancy action.[116]

To find the range of NMR interaction parameters for ^{25}Mg in silicates, a study examined 18 minerals at 11.7 T using spinning at 20 kHz with single pulse excitation.[117] Linear back-prediction was applied to try to overcome the 100 μs preacquisition delay. T_1 for these minerals varied from 0.2 s (talc) to 15.9 s (MgO). Another study compared akermanite (MgO_4) to diopside (MgO_6) in ^{25}Mg-enriched specimens.[118] All this work agreed with the earlier work on the shift range, except that it suggested that the total separation between MgO_4 and MgO_6 might be slightly larger at ~40 ppm. Results for an unusual MgO_5 unit were reported from grandidierite.[119] Some very accurate single-crystal data have been reported on forsterite using dynamic nuclear polarization[120] and the quadrupole interaction was calculated using superposition analysis based on the structural distortion of the oxygen coordination tetrahedra.[121] C_Q in such silicates appears to be typically 2–3.2 MHz. For the MgO_6 units various correlations were tried between measures of the structural distortion (DI, ψ in Eq. 4) and C_Q.[117] The best correlations were those related to the bond angles:

$$DI = \frac{\sum_{i=1}^{12} |\theta_i - \theta_0|}{12\theta_0}, \qquad \psi = \sum_{i=1}^{12} |\tan(\theta_i - \theta_0)| \tag{4}$$

where θ_i is the actual bond angle and θ_0 is the bond angle for an undistorted octahedron. In minerals a key question is related to any motion of magnesium. NMR measurements up to 1400 °C on a single crystal of forsterite allowed the magnesium exchange between different sites to be deduced, and the measured

values are consistent with the estimates of hopping frequency based on diffusion.[122] High-temperature NMR work of magnesium has been extended into the melt. On melting, the shielding increases by ~4 ppm, suggesting that there is an increase in the average coordination of magnesium. It is probable that in melts magnesium prefers to take on octahedral coordination.[123] T_1 measurements suggest that the motion of magnesium is strongly coupled to the motion of the network and, as the linewidth is related to T_1, that viscosity is the fundamental limitation on observing magnesium in melts.

Thermal decomposition of magnesium-containing minerals is a technologically important process. ^{25}Mg NMR of decomposition of the carbonates magnesite[124] and dolomite[125] showed that MgO formed significantly before it was detected by X-ray diffraction (XRD). With hydrotalcite, in the initial mineral a clear second-order quadrupolar lineshape is observed and then, as heating progresses so that water loss, dehydroxylation and carbonate breakdown occur, the distinct lineshape is lost and the peak shifts progressively downfield, with MgO forming at 600 °C.[126] Heating to 1200 °C further narrows this line, but surprisingly no formation of spinel was detected. Thermal decomposition of chrysotile was shown by solid-state NMR to be more complex than previously supposed.[127] As dehydroxylation occurs, an Mg-rich amorphous phase forms that probably has Mg in octahedral coordination and that then transforms to forsterite at 670–700 °C. There is evidence that some magnesium signal is lost in such amorphous intermediate phases, presumably owing to large quadrupolar broadening that results in the signal being undetected under the conditions used. Thermal decomposition of talc was shown by ^{25}Mg to directly form orthoenstatite, with magnesium remaining in an octahedral coordination throughout.[128] Synthetic hectorite is closely related to talc and shows a similar thermal decomposition pathway.[129] As dehydroxylation begins to disrupt the phyllosilicate, layer distortion of the octahedral magnesium sites causes broadening of the NMR signal and a loss of intensity. Mixtures of magnesium hydroxide and hydrated silicic acid were ground together; one was left at room temperature for 6 months and compared to one heated to 80 °C for 2 h.[130] The extent of reaction of these two samples was very similar, with ^{25}Mg MAS NMR being one of the probe techniques showing that a poorly crystalline layer magnesium silicate formed.

MgO is used as a sintering aid to densify Si_3N_4. In studies carried out on samples with 10 wt% MgO sintered in the range 1500–1700 °C, peaks at positive shift were observed as well as a broad peak from −69 to −85 ppm. The positive peaks were close to the nitrides $MgSiN_2$ and $MgAlSiN_3$ (Table 6).[33] The negative shift peak probably corresponds to some related glassy phase containing four-coordinate magnesium. The reaction mechanism for densification was proposed to be surface SiO_2 reacting with MgO to form forsterite followed by reaction of this with Si_3N_4 to form a glassy Mg–Si–O–N phase that will not readily recrystallize. In examining the utility of solid-state ^{25}Mg NMR for characterizing biochemicals, a study was carried out on four Mg^{2+}-binding complexes

Table 6. Summary of solid-state NMR interaction parameters of ^{25}Mg

Compound	δ_{iso} (ppm)*	C_Q (MHz)	η	Ref.
MgO	26, 26.5, 25	0	0	109, 111, 117
$MgAl_2O_4$	52, 53	0	0	109, 117
MgS	−3	0	0	109
Mg_2Si	61		0	109
$MgCl_2n \cdot H_2O$	−2	N.D	N.D	109
$MgCl_2 \cdot 6H_2O$ (77 K)	N.D.	1.477	N.D.	109
$MgSO_4 \cdot 6H_2O$	0	1.6	0	109
$Mg(OH)_2$	10, 14.1, 13.5	2.9, 3.15, 3.056	0, 0, 0	109, 117, 114
$Mg_2Si_3O_8$	~0†	N.D.	N.D.	109
Mg_3N_2	~10†	N.D.	N.D.	109
$Mg_3Al_2(SiO_4)_3$, pyrope	~0†	N.D.	N.D.	109
$MgCO_3$, magnesite	4.8–8.8	2.5–2.6	0–0.3	117
$MgCa(CO_3)_2$, dolomite	−4.3	0.9	0	117
$Mg_5Al_3(OH)_{16} \cdot 1.5CO_3 \cdot 3.6H_2O$, hydrotalcite	10	4.4	0	117
$Mg_6Si_8O_{20}(OH)_4$, talc	48	2.4	0.7	117
$[Mg_{5.3}Li_{0.6}]Si_8O_{20}(OH)_4Na_{0.9} \cdot nH_2O$ hectorite	43	2.2	1.0	117
$[Al_2MgFe^{3+}](Si_{7.5}Al_{0.5})O_{20}(OH)_4(\frac{1}{2}Ca,K)_{0.7}$, montmorillonite	−4, 11	2.8, 1.5	0, 0	117
$Mg_3Si_2O_5(OH)_4$, antigorite	50	2.9	0.7	117
$K_2(Mg_{5.1}Fe_{0.3}^{2+})[Si_{5.1}Al_{2.1}Ti_{0.1}]O_{20}(OH)_4$, phlogopite	68	3.0	0.65	117
$[Mg_{2.2}Al_{1.7}Fe_{0.4}^{3+}]Si_8O_{19.6}(OH)_{1.9}(H_2O)_{4.5}Ca_{0.4}$, palygorskite	80	3.2	0.5	117

$[Mg_{7.6}Al_{0.46}]Si_{12.4}O_{30}(OH)_{1.8}(H_2O)_4 \cdot 8H_2OK_{0.2}$, sepiolite	51	2.7	0.7	117
$MgSiO_3$, enstatite	27	2.4	0.4	117
Mg_2SiO_4, forsterite	N.D.	4.996, 4.313	0.963, 0.396	120
$Ca_2MgSi_2O_7$, akermanite	49	2.8	0.25	118
$CaMgSi_2O_6$, diopside	8	20	0.95	118
$(Mg,Fe)Al_3BSiO_3$, grandidierite	55	3.8	0.6	119
Magnesium malonate $\cdot 4H_2O$	12	1.95	0.8	131
Magnesium diacetate $\cdot 4H_2O$	27	1.90	0.82	131
Tetraaqua(orotato-N,C)magnesium $2.5H_2O$	6	2.56	0.15	131
Magnesium formate $\cdot 2H_2O$				
site 1	10	1.70	1.0	131
site 2	10	1.40	0.8	
$MgTiO_3$	−15	1.88	0.10	137
$MgSiN_2$	79†, 45†, −57†	N.D.	N.D.	33
$MgAlSiN_3$	45†, −59†	N.D.	N.D.	33
Mg	1179	0.266	0	134, 135
Mg (6%Al)	1163	0.266	0	136
$Mg_{17}Al_{12}$				
(24g)	990	2.20	0.95	136
(2a)	1445	0	0	
(8c)	1705	1.2‡	~0	

* Chemical shifts referenced to aqueous $MgSO_4$, † are peak positions. ‡ is an estimate.
N.D., not determined or not given.
(24g), (2a), (8c) – different crystallographic sites.

$Mg(H_2O)_4L_2$ where L = methylmalonate, formate, acetate and orotato.[131] The MgO used in the initial synthesis was 99% ^{25}Mg-enriched. Clear quadrupole lineshapes were observed from all four, with the orotato complex providing the first solid-state ^{25}Mg NMR observation of an asymmetric centre, i.e. five oxygens and one nitrogen. Magnesium formate dihydrate has two inequivalent magnesium sites with a complex lineshape resulting from spectral overlap. Application of 3Q MAS NMR clearly resolved two sites. In some of the ^{25}Mg MAS NMR work on silicates there was a strong overlap of the different sites and 3Q MAS NMR could usefully be applied to these situations as well.

For low-γ nuclei there are often early reports of NMR from metallic specimens because of the short T_1 due to relaxation via the contact interaction with conduction electrons. There were early NMR reports of the Knight shift from elemental magnesium in powder[132] and single-crystal form.[133] With much higher magnetic fields now available, many of these early studies can usefully be revisited. A study at 9.4 T showed that there is in fact a small temperature dependence of the Knight shift, and that as the melting point was approached there was a sharp increase in the Knight shift in keeping with a first-order phase transition.[134] C_Q was determined from observation of the singularities of the satellite transitions, and showed a $T^{1.5}$ dependence.[135] Comparison of static and MAS NMR spectra showed only partial narrowing, indicating that the second-order quadrupole interaction was making a significant contribution to the linewidth. In work-hardened magnesium there was a small increase in the linewidth of the central transition but the non-central transitions were significantly smeared out owing to the distribution of electric field gradients.[136] Dilute alloys of aluminium in magnesium are increasingly used in the automotive industry since they are lightweight. In Mg–(6%)Al the ^{25}Mg NMR spectrum is very similar to that of pure magnesium except for a small change of shift and the singularities of the satellite transition again being smeared because of a distribution of interactions as aluminium substitutes into the framework. The static ^{25}Mg NMR spectrum of the intermetallic alloy $Mg_{17}Al_{12}$ was also reported.[136] Three sites with distinct Knight shifts were reported, with spectral integration giving their ratio as 1.1 : 3.6 : 12, very close to that expected from the structure of 1 : 4 : 12.

4.3. Sulfur-33

Applications of solid-state NMR of sulfur are potentially very wide ranging, including mineral processing, high technology, (e.g. semiconductors, optoelectronics) polymer processing (e.g. vulcanization) and biochemistry. Yet the number of reports of ^{33}S solid-state NMR is extremely sparse, reflecting the difficulties of observing a low-γ quadrupolar nucleus with a natural abundance of only 0.76%. Early reports on ^{33}S included the paramagnetic α-MnS[138] for which information was obtained about the transferred hyperfine field, and ferromagnetic EuS in

which the internal magnetic field at the sulfur site extrapolated to 0 K was determined to be 1.71 T.[139] The most studied ^{33}S resonance in the solid state has been that of ZnS, with at least seven reports existing in the literature.[22,140–145] A study compared the cubic and hexagonal forms of ZnS, with the latter showing what appeared to be a second-order quadrupolar powder pattern with analysis of the lineshape giving an estimate of C_Q and the CSA.[144] The cubic form gave a much more symmetric spectrum, but there was a difference in the isotropic shift between the polymorphs of only ~3 ppm.

An extensive study examined static ^{33}S NMR spectra at 11.7 T from 26 different sulfides and sulfates at natural abundance.[22] The pulse width response of all the samples indicated that only the central transition was being excited. The lineshape from hexagonal ZnS was again analysed in terms of a mixture of interactions and yielded a CSA of (23 ± 1) ppm. The sulfates tended to show broader resonances than the sulfides, with more evidence of second-order quadrupolar broadening. Most of the time distinct lineshapes could not be observed, so that linewidth was used to make an upper estimate of C_Q (or more precisely the composite interaction constant ($= \sqrt{C_Q^2(1 + \eta^2/3)}$). The sulfates clustered into a small shift range of 320–338 ppm but with a much wider variation of C_Q of 0.53–2.3 MHz. Those sulfates crystallizing in the K_2SO_4 crystal structure (except $(NH_4)_2SO_4$) all gave identical second-order quadrupolar powder patterns and there was no obvious correlation of C_Q with the counterion. The sulfides, by comparison, covered a much wider shift range of −347 to 291 ppm. The linewidths of the sulfides were much smaller, reflecting the smaller C_Q. The chemical shift trends in the sulfides could be explained by straightforward electronegativity arguments involving ionicity and bond overlap effects. The shifts of post-transition metal sulfides could be rationalized in terms of Harrison's bond orbital model, whereas for the alkali and alkali-earth sulfides a Kondo–Yamashita approach was more appropriate.[22] The temperature dependence of the shift of some of these sulfides was measured, and was in the range 0.007–0.116 ppm K^{-1}.

A more recent study has gone to even higher field (14.1 T) and applied MAS at 15–18 kHz.[145] Typical narrowing on MAS was ~10, indicating that in most cases there are a number of contributions to the static linewidth for sulfur. An interesting experiment compared a static spectrum at 4.7 T to MAS at 14.1 T using ~10 times as much sample at the lower field. Even with the much larger sample at the lower field, achieving a comparable S/N between the two experiments required 40 times longer averaging at the lower field. CaS and $NH_4Al(SO_4)_2 \cdot 12H_2O$ are good candidates as secondary solid references for ^{33}S as they have MAS linewidths of only 10 and 18 Hz, respectively. The alum is probably favoured as it has a T_1 of only 0.23 s compared to 23 s for CaS.[145] When the other broadenings were removed under MAS, four of the ten compounds showed second-order quadrupolar lineshapes. On the limited selection of compounds examined to date by solid-state NMR, the quadrupolar interactions observed do not appear to be as large as might be anticipated from

the large Sternheimer antishielding factor. It needs to be asked how representative are the parameters reported so far. Nevertheless, the data in Table 7 should encourage further study by solid-state ^{33}S NMR. It will be interesting to see what sort of spectra can be obtained from glassy materials and a number of key questions in the structural chemistry of sulfur could then be examined.

4.4. Chlorine-35, -37

The two chlorine isotopes have similar magnetic moments with Larmor frequencies differing by ~20%. Although ^{37}Cl has only 75% of the second-

Table 7. Summary of solid-state NMR interaction parameters for ^{33}S

Compound	δ_{iso} (ppm)*	C_Q (MHz)†	Ref.
ZnS, wurzite	−231, −234, −235, −229	0.43‡, N.D.	22, 144, 145, 142
ZnS, zincblende	−228, −230	N.D, N.D.	22, 144
CdS	−284	N.D.	22
Li_2S	−347	N.D.	22
Na_2S	−338	N.D.	22
MgS	−174	N.D.	22
CaS	−28.5, −28.5	N.D.	22
SrS	42.8	N.D.	22
BaS	291	N.D.	22
PbS	−297, −293, −300	N.D.	22, 22, 145
$NaSO_4$	330 (338, 333)	0.82	22, 145
$NaCa(SO_4)_2$	338	0.71	22
$Na_2Mg(SO_4)_2 \cdot 4H_2O$	321	2.2	22
$CaSO_4$	326	1.0	22
$CaSO_4 \cdot 2H_2O$	337	0.77	22
$BaSO_4$	N.D., (353, 326)	2.3	22, 145
K_2SO_4	334	1.13	22
Rb_2SO_4	329	1.01	22
Cs_2SO_4	335, (331, 326)	0.97	22, 145
Tl_2SO_4	320	1.03	22
Li_2SO_4	321	N.D.	22
$(NH_4)_2SO_4$	328, 331	0.59	22, 145
$KAl(SO_4)_2 \cdot 12H_2O$	327, (330, 325)	0.79	22, 145
$RbAl(SO_4)_2 \cdot 12H_2O$	334	0.56	22
$CsAl(SO_4)_2 \cdot 12H_2O$	331	0.53	22
$NH_4Al(SO_4)_2 \cdot 12H_2O$	333, 331	0.53	22, 145
$TlAl(SO_4)_2 \cdot 12H_2O$	332	0.56	22

* Chemical shift relative to liquid CS_2, some are peak positions not the isotropic shifts, see original references. Numbers in parentheses represent singularity positions of MAS powder patterns.
† Estimated upper limit of the quadrupole effect parameter, except ‡ which is based on lineshape analysis.
N.D., not determined or not given.

order quadrupolar broadening compared to ^{35}Cl, the greater natural abundance of ^{35}Cl results in a receptivity 5.34 times greater than that of ^{37}Cl, so that ^{35}Cl is usually favoured for NMR study. Much magnetic resonance data exists for chlorine, but the great majority of it has been nuclear quadrupole resonance (NQR) since in materials where strong covalent bonding is present C_Q values as high as 80 MHz are not uncommon.[146] The immediate implication of such high values for the quadrupole interaction is that in many cases the normal high-field limit is not reached, and attempts to carry out NMR experiments in high magnetic fields will be in the complex regime where the energy level separation is determined by both interactions and the quadrupole interaction is not a simple perturbation of the Zeeman levels.

A ^{35,37}Cl MAS NMR study at 11.7 T of the alkali and ammonium chlorides showed that they all exhibit narrow resonances spread over a shift range of ~150 ppm.[147] The equality of the shift values from the two isotopes indicated that no quadrupole effects were present. The shift values were confirmed by a second MAS study at 9.4 T.[148] KCl gave a very narrow MAS NMR signal (~20 Hz) and would make a good secondary reference. Both papers examined correlations of the observed shifts to structural parameters. As was found for the shifts of sulfur, the theory of Kondo and Yamashita rationalized well the observed shift trends. In CuCl ^{35}Cl NMR data showed that there was a 50 ppm change of shift in varying the temperature from −150 °C to the melting point just above 400 °C.[149]

A recent and extremely elegant study reported chlorine NMR results from a wide range of perchlorates.[150] MAS at 14.1 T was applied and included observation and simulation of all the transitions (i.e. including the satellite transitions). This combined approach allowed the NMR interactions to be determined accurately. The perchlorates are shifted by ~1000 ppm from the chloride region. The observed parameters were discussed in terms of the number of perchlorate sites and their site symmetry. The 13 compounds investigated covered an isotropic chemical shift range of only ~20 ppm. However, the quadrupolar parameters varied much more widely. Hydration could also be followed as there were very noticeable effects on C_Q. ^{37}Cl MAS NMR spectra were also recorded for a selection of the materials. The isotropic chemical shifts deduced from the simulations agreed with the ^{35}Cl results and the ratios of $^{35}C_Q/^{37}C_Q$ were in the range 1.23–1.28, in excellent agreement with the theoretical prediction of 1.269. The reduced second-order quadrupole broadening for ^{37}Cl may favour its application when MAS can only just narrow a resonance, but this work[150] clearly showed that its lower intrinsic sensitivity means that it is significantly more difficult to produce as good quality spectra as from ^{35}Cl.

From a detailed analysis of the rotation pattern of a single crystal of NH_4ClO_4 at room temperature, the ^{35}Cl quadrupolar and chemical shielding tensors were deduced.[92] The extreme principal components of the CSA tensor differed by 18.1 ppm. Other ^{35}Cl measurements of perchlorates included one-pulse observation of the phase changes in a range of *n*-methylammonium

perchlorates.[151] Changes of the local motions in the different phases resulted in different averaged values for C_Q, providing insight into changes in the motions. From ^{35}Cl NMR relaxation measurements in piperdinium perchlorate, C_Q was deduced and showed that in the cubic phase (I) isotropic reorientation of the perchlorate anion was occurring.[152] In pyrrolidinium perchlorate both phases I and II gave narrow chlorine resonances.[153] Double-resonance techniques were used to measure the rotator phase of $CH_3NH_3ClO_4$.[154]

In $C_4H_9NH_3Cl$ and $C_4H_9ND_3Cl$ C_Q and T_1 were measured in the rotator phase above 241 K. C_Q decreased rapidly with increasing temperature owing to increasing self-diffusion.[155] At most temperatures ^1H decoupling showed that there was strong dipolar coupling in this phase. The ^{35}Cl quadrupolar tensors have been determined precisely for both the high-temperature (>164 K) and low-temperature (<46 K) phases of $(CH_3)_3NCH_2COO \cdot CaCl_2 \cdot 2H_2O$ using single-crystal NMR studies.[156] ^{35}Cl NMR studies of cocaine hydrochloride at 7.0 T used a stepped frequency approach and were able to record an undistorted centreband lineshape despite C_Q being in excess of 5 MHz.[157]

In more complex inorganic materials, ^{35}Cl NMR has been reported from phases such as the X-ray storage phosphor BaFCl, allowing the quadrupolar parameters to be deduced (Table 8).[158] The anion dynamics, interlayer structure and phase transitions of the mixed metal layered hydroxides hydrotalcite and hydrocalunite have been investigated by ^{35}Cl solid-state NMR.[159] Such materials exhibit significant permanent anion exchange capacity, and the interlayer structure and anion dynamics are central to this role. ^{35}Cl NMR showed that the two systems investigated were very different. ^{35}Cl static NMR spectra were collected as a function of both relative humidity and temperature. From hydrocalunite a well-defined lineshape was observed for ^{35}Cl at most temperatures, whereas for hydrotalcite it was much less well defined. The phase transition for hydrotalcite occurred over a much wider range of temperature than for hydrocalunite and this was related to the degree of atomic order within the layers. Sodalite cages can be used to encapsulate metallic clusters such as $Na_{8-n-p}Ag_nCl_{2-p}$. Na_4Cl clusters give a relatively sharp peak at -122 ppm.[160] As silver is added there is at first no change except for a weak peak that corresponds to AgCl forming on the surface. Then at very high silver exchange levels a line appears at -310 ppm, attributed to Ag_4Cl clusters. The ^{35}Cl MAS NMR lineshapes, although narrow, show characteristic tails to negative shift, indicating a distribution of C_Q. When I^- was exchanged, the ^{35}Cl peak position showed some variation, indicating that the clusters are sensitive to the distribution of nearby clusters.

4.5. Potassium-39

At 93.1% natural abundance, ^{39}K appears to be quite an attractive nucleus for NMR, having a relative receptivity, considering the central transition alone,

Table 8. Summary of solid-state NMR interaction parameters for ^{35}Cl

Compound	δ_{iso} (ppm)*	C_Q (MHz)	η	Ref.
NH_4Cl	74.0	0	0	147
LiCl	5.2	0	0	148
NaCl	−46.1, −45.8, −44	0	0	147, 148
KCl	3.07, 3.9	0	0	147, 148
RbCl	44.7, 45.0	0	0	147, 148
CsCl	109.4, 109.9	0	0	147, 148
AgCl	−7	0	0	160
Trimethylammonium perchlorate	N.D.	0.318	0.6	151
Guanidinium perchlorate	N.D.	1.48	0.6	161
$LiClO_4$	988.2	1.282	0.34	150
$LiClO_4 \cdot 3H_2O$	999.9	0.695	0.00	150
$NaClO_4$	998.3	0.887	0.92	150
$NaClO_4 \cdot H_2O$	993.9	0.566	0.90	150
$KClO_4$	1003.2	0.440	0.88	150
$RbClO_4$	1003.4	0.537	0.87	150
$Mg(ClO_4)_2$	990.2	2.981	0.57	150
$Mg(ClO_4)_2 \cdot 6H_2O$				
1	1000.6	0.309	0.00	150
2	999.5	0.475	0.00	150
$Ba(ClO_4)_2$	983.6	2.256	0.58	150
$Ba(ClO_4)_2 \cdot 3H_2O$	994.6	0.383	0.00	150
$Ba(ClO_4)_2 \cdot 6H_2O$	998.4	0.328	0.00	150
$(CH_3)_4NClO_4$	1003.3	0.307	0.00	150
NH_4ClO_4	991.5	0.6949	0.755	92
$C_4H_4NH_3Cl$	N.D.	1.2	~0	154
$(CH_3)_3NCH_2COO \cdot CaCl_2 \cdot 2H_2O$				
HT	N.D.	4.871	0.882	156
LT1	N.D.	5.667	0.80	156
LT2	N.D.	4.875	0.776	156
Cocaine hydrochloride	N.D.	5.027	0.2	157
BaFCl	N.D.	2.38	0	158
$C_5H_{10}NH_2ClO_4$	~1000	1.12	0†	152
Hydrocalunite $Ca_2Al(OH)_6Cl \cdot 2H_2O$	30	2.87	~0	159

* Chemical shift from aqueous NaCl.
N.D., not determined or not given.
1, 2 – distinct sites; HT – high temperature; LT1, LT2 – distinct low temperature sites.
† Assumed value.

comparable to that of ^{13}C. Again its quadrupole nature and in particular its small magnetic moment have limited the number of solid-state NMR studies. The most extensive study to date, on 16 model potassium salts, examined static powder samples using a solid echo pulse sequence.[162] The relatively small dipolar coupling in most of these compounds meant that for the observed central transitions the powder pattern singularities were sharp. These lineshapes could be accurately simulated using only C_Q and η, indicating that

CSA contributions were very small. Most of the compounds contained single potassium sites but even for those with two inequivalent sites, there were sufficient resolved spectral features to allow accurate and unambiguous simulation.[162] For KOH NMR showed that around the antiferroelectric phase transition C_Q varied slowly, whereas η changed very rapidly, indicating the first-order nature of this change.[163] A single-crystal rotation study of KNO_3 confirmed that CSA makes only a small contribution to the lineshape.[95,96] The extreme components of the shift tensor differed by only 18 ppm. In the temperature range 295–375 K C_Q decreased by ~10%. Static NMR spectra of potassium halides at 9.4 T produced linewidths of 8.4–14.7 ppm.[148] The isotropic shifts varied by ~37 ppm through the series.

There is much geological and agronomic interest in potassium. A study showed that on the basis of the shift of the centre of gravity of the potassium NMR line it appeared that the tectosilicate orthoclase at ~205 ppm could be distinguished from phyllosilicates, where the centre of gravity was below 40 ppm.[164] An important agronomic challenge to spectroscopy is to distinguish exchangeable or available potassium from that which simply remains in the structure of minerals such as montmorillonite. There is known to be a change of availability as minerals undergo wetting and drying, with less becoming available with time. Wet montmorillonite samples showed two superimposed potassium signals. The broader line was identical to that observed in dry samples. The narrow resonance was thus attributed to exchangeable potassium that became mobile on hydration. There was a correlation between the exchangeable potassium determined by independent chemical means and the integral of the narrow potassium component.

One of the earliest studies used level crossing to generate the signal from the larger proton source. Eleven different compounds were examined, including potassium hydrogen diformate.[165] C_Q varied in the range 1.20–2.33 MHz. All of these studies indicate that potassium shows considerable promise for examining materials. This is likely to be even truer today with the much higher fields and faster spinning now available. The C_Q values observed for ^{39}K are typically 1–2 MHz in inorganic materials, so only moderate MAS is demanded. Little attention has been applied to the shift range, although the work on silicates suggests that it may be useful. Also, 3Q experiments would offer improvements in resolution and, provided that sufficient sensitivity could be generated, this would offer a good way to examine accurately the chemical shift range. Although alkali metal ions are thought to be less biochemically important than divalent metal ions, it has recently been suggested that in biological macromolecules there could well be some cases where such ions play a crucial role.[166] ^{39}K results on K · monensin revealed C_Q of ~3.2 MHz,[20] but the potassium environments in some biomolecules may have C_Q values considerably smaller than this.

One of the few MAS studies of potassium has been on the superoxide KO_2 using a 7.5 mm MAS probe spinning at 5 kHz.[167] The two polymorphs (cubic and tetragonal) show different temperature-dependent shifts and co-exist over

the temperature range 353–423 K. The source of the temperature-dependent shift is simple paramagnetism reflected in a temperature-dependent, Curie-like susceptibility. Another chemically curious range of chemicals from which ^{39}K NMR has been reported are alkalides and electrides. These are stoichiometric salts with alkali metal cations complexed by crown ethers, cryptands or hexamethylhexacyclen, and charge balanced with an alkali metal anion or a trapped electron.[168] ^{39}K powder spectra were identified from both the positive and negative ions. The cations in these systems have C_Q values at the upper end of the range detected for ^{39}K (Table 9). In some cases such as $K^+(15C5)K^-$ (15C5 = 15-crown-5 ether) only the K^- signal was observed. The loss of some signals was ascribed to very rapid relaxation broadening the resonance. The relative shifts of the lines can be explained in terms of the electron configurations of the different ions.

In KNO_2 the ^{39}K T_1 in the low-temperature plastic crystal was found to be due to NO_2^- motion.[169] KSCN undergoes an order–disorder antiferroelectric phase transition on conversion of the orthorhombic phase to a tetragonal one at 415 K. A two-dimensional ^{39}K NMR experiment that separated the homogeneous and inhomogeneous contributions to the spectrum showed the disordering process to be dynamic.[170] Mixed crystals $K_xRb_{1-x}X$ (X = Br, I) form complete solid solutions. Each series was referenced to the pure halide end member, and each well-defined compound (e.g. K_3RbI_4, $K_2Rb_2Br_4$) gave a distinct ^{39}K shift.[171] This allowed the atomic distribution in mixed crystals at other compositions to be deduced. The residual MAS linewidths were used to estimate C_Q to be in the range 0.35–0.53 MHz. ^{39}K MAS NMR was reported from $KNiF_3$ in the temperature range 180–450 K.[172] Changes of shift were correlated to the susceptibility and showed that the isotropic hyperfine interaction was nonzero. In the antiferromagnetic state a signal could still be observed just below the transition temperature, but it was rapidly broadened at lower temperatures.

Over the last few years the biggest use of solid-state ^{39}K NMR has been to examine potassium fulleride (K_3C_{60}), which shows several structural phase changes and superconducts at lower temperatures.[173–177] Signals are usually observed from the tetrahedrally and octahedrally coordinated sites, which are in the ratio of 2 : 1 expected from the structure. These can be symmetric peaks with no sign of quadrupolar structure, although slight structural distortions have been shown to give rise to an asymmetric distortion of the tetrahedral site. The tetrahedral resonance splits in $K_{3-x}C_{60}$ and has been analysed in terms of cation vacancy interaction, which can account for the temperature dependence of the distorted line.[173] Exchange between the different tetrahedral sites is thermally activated and in potassium fullerides the splitting disappears above $\sim$200 K.[175,176] The resonances all also show a very similar temperature dependence to that of the ^{13}C signal, which together with T_1 data shows that the electron density is the same as at the carbon site, indicating a uniform Pauli susceptibility. The temperature variation of the shift is dominated by the orbital contribution of the susceptibility.[176]

Table 9. Summary of solid-state NMR interaction parameters of ^{39}K

Compound	δ_{iso} (ppm)*	C_Q (MHz)	η	Ref.
KF	22.6	N.D.	N.D.	148
KCl	47.8	N.D.	N.D.	148
KBr	55.1	N.D.	N.D.	148
KI	59.3	N.D.	N.D.	148
KOH	N.D.	1.680, 1.682	0.104	162, 163
KNO_3	N.D.	1.322, 1.326	0.173	92, 162
$KHCO_3$	N.D.	1.490	0.239	162
KCO_3	N.D.	1.536, 1.546	0.860, 0.63	162
$KClO_3$	N.D.	0.978, 0.995	0.689	162
$KClO_4$	N.D.	0.738	0.274	162
K_2SO_4	N.D.	0.958, 0.864	0.043, 0.90	162
$KHSO_4$	N.D.	0.614, 1.220	0.356, ~1	162
KBF_4	N.D.	0.780	0.69	162
KNO_2	N.D.	0.056	~0	162
$KAl(SO_4)_2 \cdot 12H_2O$	N.D.	1.956	0	162
$KBrO_3$	N.D.	0.952, 0.968	0	162
KH_2AsO_4	N.D.	0.904	0	162
KH_2PO_4	N.D.	1.694, 1.680	0	162
KN_3	N.D.	0.518	0	162
KIO_4	N.D.	0.107, 0.300	0	107, 162
$KReO_4$	N.D.	1.148	0	108
$KNiF_3$	−100	N.D.	N.D.	172
K_2SiF_6	−17	N.D.	N.D.	172
K.monesin	N.D.	3.2	0.52	20
18-crown-6 ether · KNO_3	N.D.	1.80	0.37	20
$K^+(15C5)e^-$	20	1.5	N.D.	168
$K^+(C222)e^-$	58	2.72	0	168
$\underline{K}^+(C222)K^-$	−10	2.70	0	168
$\underline{K}^+(C222)Na^-$	0	2.65	0.25	168
$K^+(15C5)_2Cl^-$	−19	0.87	0.40	168
$K^+(15C5)_2I^-$	−60	1	N.D.	168
$K^+(15C5)_2\underline{K}^-$	−10.2	~0, 0.9	N.D., 0	168
$K^+(C222)\underline{K}^-$	19	N.D.	N.D.	168
K_3C_{60}	−90, −30	N.D.	N.D.	176

* Shifts measured relative to dilute aqueous KCl.
15C5 = 15-crown-5 ether; C222 = cryptand(2.2.2).
N.D., not determined or not given.
$\underline{K}$ indicates potassium to which parameters refer.

4.6. Calcium-43

Early observations of calcium in the solid state used either double resonance[178] in CaF_2 or adiabatic demagnetization at low temperature.[179] $^1H-^{43}Ca$ CP was one of the first experiments that reported more conventional NMR spectra.[180] CP used a 46 kHz spin-locking field on the protons that was matched to the central transition of the calcium. Optimum CP was achieved with a contact time of

20–30 ms, and as was noted above for CP on the spin-$\frac{1}{2}$ low-γ nuclei, this places severe RF strain on the X-nucleus side of the hardware. Calcium acetate 50% isotopically enriched was measured and two signals were observed. A narrow (24 Hz) resonance was observed close to 60 ppm and a broader more structured signal that covered the range −50 to 10 ppm. It was unclear whether the structure was from second-order quadrupole effects or from overlapping lines. As this work was carried out at only 4.7 T, working at significantly higher applied magnetic field would help in understanding this structure.

An area where ^{43}Ca NMR has been applied to try to understand local electronic structure is in the calcium-containing high-temperature ceramic superconductors.[181–184] The calcium resonance probes the spin susceptibility at the calcium site, which is usually sandwiched between CuO_2 planes. Effects of temperature and doping levels on the spin susceptibility can thus be followed. Below the superconducting transition temperature the ^{43}Ca NMR linewidth provides information about the magnetic field distribution caused by the vortex lattice.[184] In $(Bi,Pb)_2Sr_2CaCu_2O_{8+x}$ and $(Bi,Pb)_2Sr_2Ca_2Cu_3O_{10+x}$ the quadrupolar and shift parameters were deduced for the main calcium site.[183] In $(Ca_{0.5}La_{0.5})(Ba_{1.25}La_{0.75})Cu_3O_y$ ^{43}Ca MAS NMR showed a relatively symmetric line that results from the relatively high symmetry of the cations in the central plane.[182]

Examining calcium NMR in the sol-gel formation of calcium silicate, a broad symmetric peak was observed in the initial sol at ~50 ppm.[185] Immediately after gelling, the resonance was effectively too broad to observe. Then, with ageing of the gel, a peak reappeared that was broader than in the initial sol but at approximately the same peak position. The implications were that the disorder in the initial gel caused a large distribution of the NMR interaction parameters, which was reduced after ageing for 6 months. As there is effectively no change in the peak position, the calcium environment appears to remain the same throughout the whole process. ^{43}Ca MAS NMR was also reported from model compounds (CaO, $CaCO_3$, $Ca(OH)_2$) related to those of importance in cement and concrete formation.[186]

All of the more recent 'conventional' solid-state NMR observation of ^{43}Ca has been on samples with significant (>50%) isotopic enrichment. However, the relatively ionic nature of the Ca–O bond means that C_Q tends to be small and that even modest MAS rates will narrow the NMR signal. The main problem then to be overcome is the very low sensitivity (Table 1), which is largely a result of the low natural abundance of 0.14%. By using large volume rotors (>9.5 mm with 14 mm preferred), adequate S/N can be typically achieved by averaging for ~1 day. This situation should improve still further as higher magnetic fields are applied. ^{43}Ca spectra from natural-abundance samples were reported for 12 compounds that included silicates, carbonates and sulfates (Table 10).[187] A shift range of ~160 ppm was observed, but there was no resolution of the different sites at 8.45 T in samples containing multiple calcium sites.

Table 10. Summary of solid-state NMR interaction parameters of ^{43}Ca

Compound	δ_p (ppm)*	$\Delta\nu$ (Hz)†	Ref.
$Ca(CH_3COO)_2$	60, −20	24, 600	180
Ca silicate gel	50	2–3 kHz‡	185
CaO	128	20	187
$Ca_2NaH(SiO_3)_3$	45	500	187
$KFCa_4(Si_8O_{20}) \cdot 8H_2O$	7	200	187
$CaAl_2(OH)_2(Si_2O_7) \cdot H_2O$	−6	470	187
$Ca_5(PO_4)_3 \cdot (OH,F)$	−22	900	187
$Ca_2MgSi_2O_7$	−21	700	187
$Ca_6[Al(OH)_6]_2(SO_4)_3 \cdot 26H_2O$	−2	360	187
Calcite, $CaCO_3$	14[i]	250	187
Aragonite, $CaCO_3$	−34	80	187
$CaSiO_3$	−9	1400	187
$CaSO_4 \cdot 2H_2O$	−28	500	187
$CaTiO_3$	13	1000	137
$CaAl_4O_7$	45.7[i]	1300	188
$CaAl_{12}O_{19}$	−52.6	80	188

*MAS δ_p, peak position from saturated aqueous $CaCl_2$ solution.
†$\Delta\nu$, MAS linewidth, except ‡ which is the static linewidth.
[i]Isotropic chemical shift.

Aragonite and calcite, polymorphs of calcium carbonate, gave very different ^{43}Ca MAS NMR spectra. Calcite showed a characteristic second-order quadrupolar lineshape that was simulated with $\delta_{iso} = 14$ ppm, $C_Q = 1.40$ MHz and $\eta = 0$. The resonance from aragonite was much narrower, with no discernible features. The static spectrum from aragonite was ~20 times broader than under MAS, suggesting that CSA was an important contributor to the static linewidth. This was further reinforced as the static spectrum could be well simulated by CSA parameters alone. C_Q for calcite is one of the very few to have been reported. A value has also been measured for $CaAl_4O_7$, where $\delta_{iso} = 45.7$ ppm, $C_Q = 3.5$ MHz and $\eta = 0$.[188] The observed shifts from all the compounds were correlated to the mean Ca–O bond length and within each different class of compounds very similar gradients of the correlations were observed.[187] Calcium is such an important element in a number of applications (minerals, cements, bones, etc.) that as higher fields become available more NMR studies will be reported.

4.7. Titanium-47, -49

Titanium is a component of some technologically important and scientifically interesting materials; for example, there are electrical ceramics based on titanium oxide such as $BaTiO_3$ and lead zirconate titanate. The presence of

titanium in silicates dramatically changes physical properties such as thermal expansion and refractive index of glasses, and the catalytic activity of microporous materials. However, there are few solid-state Ti NMR studies published to date. The main experimental difficulty is that both isotopes have moderately large quadrupole moments (Q) in the ratio $^{49}Q/^{47}Q = 0.8275$. It is usually the second-order quadrupolar-broadened central $(\frac{1}{2}, -\frac{1}{2})$ transition that is observed where the relative broadening is $\Delta\nu^{47}/\Delta\nu^{49} \sim 3.437$. A quirk of titanium NMR is that the isotopes have extremely similar γ values; even at 14.1 T the resonance frequencies differ by only ~9 kHz so that with the width of the resonances observed most spectra will consist of completely overlapped resonances from the two isotopes. A practical point is that spectra can be referenced against the secondary standard of $SrTiO_3$. This cubic material produces sharp MAS NMR lines that are easily observed. According to Dec *et al.*[189] $SrTiO_3$ is shifted by −843 ppm against ^{49}Ti in neat, liquid $TiCl_4$, the conventional shift standard for titanium. Hence the data reported in Table 11 can be related back to the primary shift reference.

TiO_2 is an important material in its own right in many applications, such as white pigment. There are three polymorphs, anatase, rutile and brookite, all made

Table 11. Summary of solid-state NMR interaction parameters for ^{49}Ti

Compound	δ_{iso} (ppm)*	C_Q (MHz)	η	Ref.
TiO_2, anatase	−, −, −195	4.6, 4.7, 4.79	0, 0, 0	192, 191, 190
TiO_2, rutile	~0	13.9	0.19	190
TiO_2, brookite	−100	6.04	0.55	193
Ti_2O_3	1100	N.D.	0	190
$SrTiO_3$	0	0	0	
$FeTiO_3$	4500	N.D.	>0	190
$CaTiO_3$	−10.5 ± 1, N.D.	2.75, <3.7	0.70	137, 190
$CdTiO_3$ (ilmenite)	30	11.1	0.10	137
$CdTiO_3$ (perovskite)	40	4.07	0.40	137
$MgTiO_3$	−150	15.52	0.0	137
$PbTiO_3$	153	9.98	0.0	137
$BaTiO_3$	112	3.7	0.0	137
$Y_2Ti_2O_7$	−30	24.0	0	205
$LiTi_2O_4$	−300	17.6	~0	200
Ti metal	2750	9.25	0	190
TiAg	3155	~0	~0	190
Ti_3Al	3600	13.9	0.1	190
TiAl	5000	14.0	0	190
$TiAl_2$	3300	8.5	0.70	190
$TiAl_3$	27 500	14.39	0	190
TiB_2	2750	12.35	0	180
TiH_2 (cubic)	3293, 2600†	N.D.	N.D.	203, 204

* Chemical shifts quoted relative to solid $SrTiO_3$, except †.
N.D., not determined or not given.

up of TiO_6 units with the connectivity and relative orientation of these octahedral units distinguishing these polymorphs. Anatase has the most symmetric site with the smallest C_Q and, with correct excitation conditions on a static sample, allows the nested lineshapes from both isotopes to be recorded accurately.[190,191] By spinning anatase, the ^{49}Ti lineshape was clearly seen by Dec *et al.*,[189] but with the spinning speeds applied the ^{47}Ti centreband was mixed in with the sidebands from ^{49}Ti. A static powder study in which the ^{49}Ti resonance of rutile was accurately recorded[190] agreed with the parameters deduced from a single-crystal study.[192] Brookite shows shift and quadrupolar parameters intermediate to the other two polymorphs (Table 11).[190–194] A natural sample gave a much broader line than a synthetic sample, presumably owing to the natural sample containing some paramagnetic centres. For Ti_2O_3 no well-resolved lineshape could be observed from either isotope and there was a relatively large shift of 1100 ppm due to the paramagnetic shift induced by the Ti^{3+}.[190]

A recent study has reported $^{47,49}Ti$ solid-state NMR spectra from TiO_2 gels formed by hydrolysis of $Ti(OPr^i)_4$ and heated at 200–700 °C.[195] In the gel heated to 200 °C, which is still amorphous, a surprisingly narrow resonance was observed. This indicates that either the TiO_6 units are quite symmetric or that partial averaging of the quadrupolar parameters is occurring. Heating between 500 and 600 °C produces some complex lineshapes, but it was convincingly shown that these lineshapes could be decomposed into those of anatase and rutile, with the amount of rutile increasing with heat treatment. These samples only gave broad X-ray reflections, whereas the NMR lineshapes were very similar to those of the bulk crystalline materials. This implies that small but well-crystallized particles are present.

The important piezoelectric and ferroelectric properties of $BaTiO_3$ have meant that there have been several reports of the titanium NMR of this phase. Above the Curie temperature in the cubic phase, narrow $^{47,49}Ti$ resonances are observed in static NMR spectra from powders taken using a magnetic field of 7.05 T, but were lost in the tetragonal phase formed on cooling.[196] There have been three recent single-crystal rotation studies of the titanium resonances in $BaTiO_3$ at room temperature.[197–199] The static single-crystal studies of Sommer *et al.*,[197] Bastow[198] and Kanert *et al.*[199] gave values of ^{49}Ti C_Q equal to 3.65, 3.78 and 4.03 MHz, respectively. In a recent powder study three different samples of $BaTiO_3$ all gave static NMR spectra consistent with $C_Q = 3.7 \pm 0.1$ MHz.[137] Bastow[198] reported a CSA contribution of ~40 ppm to his rotation pattern. Dec *et al.* showed in a limited range of such materials that the nature of the second cation influences the $^{47,49}Ti$ NMR spectra with variations of the chemical shift, although they only reported peak positions.[189] A recent more extensive study of $ATiO_3$ perovskites and ilmenites used static and MAS spectra at 14.1 T to further examine the structural influences on the NMR interaction parameters.[137] Very clear lineshapes could in general be observed that allowed the interactions to be accurately deduced. C_Q showed a general increase with increasing shear strain, although the direct correlation was not very strong. For the perovskites

there was a reasonable linear correlation of δ_{iso} with the mean Ti–O bond length, although interestingly it was in the opposite direction to that normally observed for nuclei. The key question that has yet to be answered is that of the ability of solid-state titanium NMR to distinguish different local coordinations of titanium (i.e. TiO_4, TiO_5, TiO_6). This would allow titanium NMR to be applied to many scientifically and technologically significant problems and is an area where there is much current activity. In $FeTiO_3$ a broad line with no distinct singularities was observed. $FeTiO_3$ is paramagnetic at room temperature and the transferred hyperfine field from the Fe^{3+} produces a large positive shift.[190] $Li_{1+x}Ti_{2-x}O_4$ is a superconductor with a critical temperature of ~12 K. ^{47,49}Ti static NMR spectra were recorded in the range 160–330 K for the stoichiometric composition ($x = 0$) and as a function of composition ($x < 0.1$).[200] A negative Knight shift was observed, indicating that core polarization was probably dominant. C_Q decreased monotonically with increasing temperature.

There were early NMR reports for titanium itself using field sweeping techniques at 4 K.[201,202] Recently the NMR parameters deduced from the early work have been confirmed by FT NMR at room temperature.[190] By recording the ($\pm\frac{3}{2}$, $\pm\frac{1}{2}$) satellite transitions, C_Q was deduced, which was then used to simulate the central transition, where an axial Knight shift of 70 ± 10 ppm was necessary for accurate simulation. Titanium NMR was reported from a series of intermetallic titanium aluminides and TiAg.[190] Knight shifts in the range 5000–2750 ppm were reported along with C_Q values up to 14.4 MHz (Table 11). In $TiAl_3$, titanium showed an axial component of the Knight shift of 800 ± 50 ppm. In TiAg, the titanium has a very small electric field gradient and the observed spectrum consisted of narrow resonances from the central transition of ^{47,49}Ti split by the 6 kHz from the magnetic moment difference, superimposed on partially excited satellite transitions.

TiB_2 is a hexagonal metal. The very small Knight shift observed must be due to approximate cancellation of the positive and negative contributions to the shift.[190] The titanium Knight shift of the cubic and tetragonal phases of TiH_2 and its temperature variation has been measured.[203,204] In alloys with vanadium substitution, the Knight shift decreases as vanadium is added.[203] The solid solution $TiC_{1-x}N_x$ is a face-centred cubic structure with the lattice parameter varying closely to linearly with x.[101] The electric field gradients are expected to be small and the peak positions at 11.7 and 14.1 T showed very little change, with both isotopes clearly visible. Spectra from intermediate compositions were broader than those of the end members and the spectra showed a gradual evolution with composition.

4.8. Zinc-67

The ZnO_4 site of ZnO is axially symmetric, which is manifest in the quadrupolar lineshape with $\eta = 0$. Commercial ZnS samples are often mixtures

Table 12. Summary of solid-state NMR interaction parameters for ^{67}Zn

Compound	δ_{iso} (ppm)*	C_Q (MHz)	η	Ref.
ZnO	238, 240.1, 240	2.4, 2.4065, 2.40, 2.38	0, 0	189, 144, 206
ZnS				
cubic	378, 380.5, 381.9	~0	–, 0, 0	142, 144, 206
hexagonal	360, 365	~0, <0.5, <0.4		
ZnSe	276.3, 276	~0	–	144, 206
ZnTe	87.6	~0	–	144
$ZnSO_4 \cdot 7H_2O$	10	1.70	0.2	206
$Zn(CH_3COO)_2 \cdot 2H_2O$	0, −123†	5.3, 5.34	0.87, 0.819	206
$Zn(CH_3COO)_2$	260, 245	2.42, 2.42	0, 0.1	206, 210
$K_2[Zn(CN)_4]$	291	0		208
Zn	1776	11.983	0	209
$Cu_{1.01}Zn_{0.99}$	1879	N.D.	N.D.	209
$Zn(ClO_4)_2 \cdot 6H_2O$	−3	<0.2	N.D.	208
$Zn[ImH]_4(ClO_4)_2$	291	2.80	0.4	208
$Zn[SC(NH_2)_2]_4(NO_3)_2$	359	3.15	1.0	208
$Zn(OOCH)_2 \cdot 2H_2O$				
I	−10	6.05	0.99	212
II	0	9.52	0.39	
$Zn(OOCCH_3)_2(C_3H_4N)_2$	155	8.20	0.62	212

* Shift relative to dilute aqueous Zn^{2+}, except † shift measured relative to 1 mol l^{-1} $ZnCl_2$.
N.D., not determined or not given.
I and II are distinct sites.

of the two polymorphs, wurtzite and zincblende, and some ^{67}Zn spectra show two field-independent peaks.[189,206] A solid-state NMR analysis of the whole zinc chalcogenide range showed that in all the hexagonal forms there was a CSA contribution to the static lineshape.[144] ^{67}Zn spectra were obtained from pure samples of the two forms of ZnS. A single-crystal rotation pattern of ZnO followed the change in ν_Q in the temperature range 250–400 K.[144] A recent powder study of ZnO also determined both the quadrupole and chemical shift parameters as MAS removes CSA, leaving the spectrum determined by quadrupole effects. These quadrupole parameters can then be combined with CSA to simulate the static spectrum.[206] The CSA parameters derived agreed with the earlier single-crystal work. For ZnS the components of the CSA tensor in the hexagonal form were $\delta_{11} = 380 \pm 2$ ppm and $\delta_{22} = \delta_{33} = 358 \pm 2$ ppm.[144] ZnSe is a cubic phase and the MAS linewidth was only 16 Hz,[206] so that it would make a useful secondary reference material. Heavily doped ZnO is of technological interest since it is a transparent electrical conductor with, for example, application to advanced optical displays. Aluminium and gallium were added in the range 0.03–3 at% to form a solid solution. As gallium was added, the distinct second-order quadrupole lineshape of the ^{67}Zn spectrum was blurred through a distribution of C_Q values, although the overall linewidth

remained approximately constant.[207] The ^{67}Zn shift also changed in an approximately linear fashion with impurity concentration.

Zinc sulfate provides a ZnO_6 unit. It appears that the isotropic chemical shift ranges of the tetrahedral and octahedral coordinations are separated by ~200 ppm.[206] Analysis of all static ^{67}Zn lineshapes, except from cubic materials, requires both quadrupolar and CSA contributions. There also appears to be a direct correlation between the sizes of the CSA and quadrupole effects. MAS of $K_2[Zn(CN)_4]$ produces a high-resolution ^{67}Zn NMR spectrum with a linewidth of only 23 Hz and a T_1 of 0.77 s at 9.4 T. $^1J(^{67}Zn, ^{13}C)$ of 88 Hz could be clearly observed.[208] Recording the central and satellite transitions of zinc metal at room temperature allowed all the NMR interaction parameters to be determined, including the axial component of the Knight shift of −124 ppm.[209] The temperature dependences of K_{iso} and C_Q were determined in the range 149–432 K. Zinc acetate and its hydrate are good model compounds for determination of the interaction parameters of zinc to be expected in biochemical applications. On hydration, the zinc coordination increases from 4 to 6 as water molecules enter the structure and there is a big change in the isotropic chemical shift.[206] The octahedra are quite distorted and this is reflected in the much larger C_Q in the hydrated form. A detailed single-crystal study of ^{67}Zn in the acetate has been carried out and showed that although CSA effects are small they significantly affect the value of C_Q.[210]

Zinc is one of the most important metal centres in metalloproteins and NMR should be a good probe of the local structure of zinc-binding sites. ^{67}Zn MAS NMR spectra were recorded from zinc complexes with imidazole and thiourea, which provided ZnN_4 and ZnS_4 centres, respectively.[211] There was an approximate correlation of C_Q and the structural distortion characterized by the mean bond angle deviation. An interesting comment was that it had not been possible to record ^{67}Zn NMR spectra from unsymmetric coordination centres.[211] Further spectra from model compounds have been collected using the QCPMG approach.[212] In $Zn(OOCH)_2 \cdot 2H_2O$ there were two inequivalent zinc sites. Both are sixfold coordinate, but in one all the oxygens come from formate groups whereas in the other four come from water molecules and the other two from formate groups. The inequivalent sites differ in isotropic chemical shift by only 10 ppm, whereas their C_Q values differ by >50%. $Zn(OOCCH_3)_2(C_3H_4N_2)_2$ provides a tetrahedral coordination centre with differing nearest neighbours yet is observable. This signal from a tetrahedral site again shows a big shift from the region of octahedral resonances. By extrapolation from the S/N obtained on this compound it was suggested that on a metalloprotein 3.7 years would be necessary to achieve the same S/N.[212] It was then made clear that this is obviously the worst possible scenario and that many significant improvements are likely to bring this down to a workable timescale. ^{67}Zn solid-state NMR could see many interesting applications over the next few years.

4.9. Zirconium-91

Zirconium plays a central role in a number of recent important material developments such as high-toughness ceramics and solid oxide fuel cells. The first report of solid-state ^{91}Zr NMR appears to have been from the cubic metal $ZrZn_2$.[213] Knight shifts were also reported from the isostructural metals ZrV_2, ZrC_2 and $ZrMo_2$,[214] and also from zirconium metal at 4 K.[215] Recent high-field room-temperature measurements on zirconium metal determined C_Q and η, and compared one-pulse and stepped frequency methods of recording the resonance.[216] ^{91}Zr NMR has also been used to study amorphous Zr–Cu alloys[217] and to examine the internal field in $ZrFe_2$.[218] The cubic metals ZrCo and ZrC, and tetragonal ZrH_2 all gave relatively narrow resonances (11–16) kHz.[216] In the hydride and the carbide some minor subsidiary structure was observed in the resonances, which is probably due to structural defects. Analysis has been given of the density of states in ZrH_2 from consideration of the Knight shift and T_1.[219]

The first NMR measurement yielding C_Q on an insulating phase was from a single crystal of zircon ($ZrSiO_4$, Table 13).[220] The linewidth of the resonance showed considerable variation on rotation, which probably results from mosaic spread and also a range of field gradients arising from defects. From fitting the rotation pattern it was clear that there was a sizeable axial CSA of ~183 ppm. MAS of the cubic material $BaZrO_3$ produces a narrow NMR line.[189,221] This makes it a good candidate as a secondary solid-state NMR reference resonating at 208.1 ppm from saturated Cp_2ZrBr_2 in THF.[221] Orthorhombic $SrZrO_3$ has a more distorted local zirconium structure and a broader resonance is produced that shows some sign of second-order quadrupolar structure. The C_Q obtained for zircon means that at 9.4 T the linewidth for the central transition will be ~350 kHz. This is well beyond narrowing by any accessible MAS speed but is also beyond what can be recorded undistorted by direct pulse techniques (i.e. one-pulse, echoes, etc.). Hence, in examining the polymorphs of ZrO_2 a pointwise stepped frequency approach was used.[222] This approach is time consuming but yields undistorted lineshapes from which the quadrupolar parameters can be derived. The four zirconias covered a remarkably small isotropic chemical shift range of ~10 ppm. The polymorphs were much better discriminated on the basis of the quadrupolar parameters. This allowed deconvolution of spectra to estimate the phase composition of mixtures in transformation-toughened zirconias. To stabilize the tetragonal and cubic forms at room temperature, a second oxide (e.g. MgO, Y_2O_3) needs to be added to form a solid solution. The level of dopant is highest for the cubic phase, for which only a featureless line was observed,[222] probably as a result of the atomic disorder in the solid solution producing a range of electric field gradients.

The stepped frequency approach has been adopted in a range of more complex zirconium-containing compounds including $NaZrO_3$,[223] Na_2ZrSiO_5,[224] where the two crystallographically inequivalent zirconium sites could

Table 13. Summary of solid-state NMR interaction parameters for ^{91}Zr

Compound	δ_{iso} (ppm)*	C_Q (MHz)	η	Ref.
Zr metal (hcp)	3292	18.2	0	216
ZrCo	3377	0	–	216
ZrC	127	0	–	216
ZrH_2	2262, 2550†	~0	–	216, 219
Al_3Zr	40	7.3	0	225
m-ZrO_2	7	23.1	~0.1	222
t-ZrO_2	12	19.1	0	222
o-ZrO_2	N.D.	17	0.8	222
$BaZrO_3$	0	~0–0.05	~0	189, 221
$SrZrO_3$	−30‡, −12	N.D., 0.678	N.D., 0.6	189, 221
Ba_2ZrO_4	−29	N.D.	N.D.	221
$NaZrO_3$	~0	14.6	0.15	223
Na_2ZrSiO_3	~0	29.4	0.70	224
$CaZrO_3$	−285	1.288	0.5	226
$CuZr_2(PO_4)_3$	−374	0.318	0.9	226
$RbZr_2(PO_4)_3$	−341	1.591	0.2	226
$AgZr_2(PO_4)_3$	−375	0.637	0	226
$NaZr_2(PO_4)_3$	−359	0.848	0	226
Cs_2ZrF_6	−399	2.682	0	226
Li_2ZrF_4	−454	1.481	0	226
ZrF_4	N.D.	53.7	0.30	227

* Shift references taken from $BaZrO_3$ which is 208.1 ppm from Cp_2ZrBr_2.
† Referenced to RbCl solution and scaled from the magnetic moment of ^{85}Rb.
‡ Peak position.
N.D., not determined or not given.

not be distinguished from the ^{91}Zr NMR, and Al_3Zr.[225] In most inorganic materials it appears that the best discrimination is via C_Q. A related stepped echo approach was applied to a range of zirconium-containing phosphates and fluorides and for these materials C_Q values were much smaller, typically 1–2 MHz (Table 13).[226] ZrF_4 represented at significant challenge to record, with the static lineshape of the central transition itself extending over ~1.5 MHz.[227]

4.10. Molybdenum-95, -97

The two isotopes of molybdenum have close resonance frequencies, differing by only 2%. The higher sensitivity and significantly smaller second-order quadrupolar broadening of ^{95}Mo make it the preferred nucleus for NMR study. These factors outweigh the fact that if quadrupole relaxation is dominant, ^{97}Mo relaxes much faster. In solid anhydrous Na_2MoO_4, where relaxation of both isotopes has been determined, quadrupole relaxation does dominate T_1, with the values for ^{95}Mo and ^{97}Mo being 132 and 1.1 s,

Table 14. Summary of solid-state NMR interaction parameters for ^{95}Mo

Compound	δ_{iso} (ppm)*	C_Q (MHz)	η	Ref.
Ag_2MoO_4	82, 8	~0	N.D.	238, 239
$Ag_2Mo_2O_7$	63	N.D.	N.D.	238
Li_2MoO_4	−72	~0	N.D.	230
Na_2MoO_4	−35, 0+, −32.9	~0	N.D.	230, 229, 238
$Na_2Mo_2O_7$				
Tetrahedral	−74	N.D.	N.D.	238
Octahedral	−177	N.D.	N.D.	
α-K_2MoO_4	−24	1.5	N.D.	230
β-K_2MoO_4	12	1.3	N.D.	230
γ-K_2MoO_4	2	~0	0	230
$Na_2MoO_4 \cdot 2H_2O$	4†, 8	N.D., 1.15	N.D., 0.82	2, 230
Cs_2MoO_4	−25	~0	N.D.	230
$CsLiMoO_4$	−122	~0	N.D.	230
$CaMoO_4$	35	2.7	N.D.	230
$BaMoO_4$	−45	1.6	N.D.	230
$PbMoO_4$	108, 151	1.9, 2.05	N.D., 0.20	230
MoO_3	−150, −114‡, −30+	N.D., 3.49, 2.85	N.D., 0.99, 0.32	230, 231, 228
$H_3PMo_{12}O_{40} \cdot xH_2O$	100, (468,−29)	N.D., N.D.	N.D., N.D.	230
$Mo(CO)_6$	−1857, −1852, −1854, −1854, −1854, 1854	N.D., N.D., N.D., 0.141, 0.091, 0.0893	N.D., N.D., N.D., <0.1, 0.142, 0.151	2, 230, 231, 235–237

$[(TBA)]_4[\alpha Mo_8O_{26}]$	−30, wide peak ∼0	N.D.	N.D.	230
$(NH_4)_2Mo_2O_7$				
Tetrahedral	N.D.	2.44	0.47	231
Octahedral	N.D.	3.41	0.07	
$Al_2(MoO_4)_3$	−300†	N.D.	N.D.	231
$(NH_4)_6Mo_7O_{24} \cdot 4H_2O$	4†	(2.98, 5.76, 3.73)	(1, 0.99, 0.34)	231
$(Bu_4N)_4Mo_8O_{26}$	−9	(0.0, 6.12)	(0.34, 0.53)	231
$(Bu_4N)_2Mo_6O_{19}$	(446, −289)†	4.9	0.05	231
$(nBu_4N)_2Mo_2O_7$	−6.5	N.D.	N.D.	238
$Mo(CO)_5$(MeDBP)	−1825	1.03	0.25	2
$Mo(CO)_5(\eta'$-dppm)	−1775	1.31	0.30	2
MoS_2	-940^+	6.2	0	228
$MoSe_2$	-1000^+	5.7	0	228
Mo_2Se_4	5885^+	∼0	N.D.	228
MoSi	-2100^+	2.928	0	228
Mo_2C	900^+	6.1	0.98	228

* Shift from aqueous Na_2MoO_4 solution, except $^+$ with cubic anhydrous Na_2MoO_4 taken as zero.
† Peak position.
‡ Position of most intense singularity.
N.D., not determined or not given.

respectively.[228] Long relaxation times in common with many of the other nuclei examined in this review are often a big drawback for molybdenum. Early solid-state NMR studies of molybdenum included ^{95}Mo and ^{97}Mo of anhydrous cubic Na_2MoO_4 at 6.2 MHz (!). Both isotopes showed very similar spectra, indicating that quadrupole effects were small. Even so, the ^{97}Mo data took ~6 times longer to collect to produce a comparable S/N.[229] In moving to higher magnetic fields, a study at 19.55 MHz reported static NMR spectra from 14 inorganic molybdates.[230] Alkali molybdates generally gave $C_Q \sim 0$ MHz. The three polymorphs of K_2MoO_4 could be readily distinguished on the basis of C_Q and δ_{iso}. As the local structural distortion increased, there was clearly an increase in C_Q. It should be noted that in general this work did not take into account CSA when determining C_Q from the lineshapes and subsequent studies showed that CSA could be very large. In materials where the quadrupole interaction was small, so that the isotropic chemical shift could be more exactly determined, the ^{95}Mo resonances moved to higher shift as the Mo–O bond length decreased. A more recent MAS report of $Na_2MoO_4 \cdot 2H_2O$ showed that MAS alone was sufficient to remove the dipolar coupling to produce a well-defined second-order quadrupolar lineshape from which C_Q and η could be deduced.[2] The static spectrum then allowed the span of the CSA to be estimated as ~200 ppm.

It was unclear from early work whether on the basis of the NMR spectrum MoO_4 and MoO_6 could be directly distinguished. Spectra were subsequently obtained from a much larger range of compounds to try to determine the type of structural information that ^{95}Mo NMR could provide. Some of the materials were closer to the polyoxomolybdenum materials of interest in catalysis.[231] A combination of static and MAS measurements at 9.4 T, with MAS speeds of typically 3–4 kHz, was used, with the peak positions and linewidths for both measurements given. In several cases the spectra consisted of strongly overlapping resonances from different sites, even under MAS, so that unambiguous deconvolution at a single magnetic field is extremely difficult. The static spectra are hampered by the presence of comparable second-order quadrupole interactions and CSA effects. Hence a degree of uncertainty must remain in the simulations of spectra from materials such as $(NH_4)_2Mo_2O_7$ and $(NH_4)_6Mo_7O_{24} \cdot 4H_2O$ where two and three components, respectively, are fitted.[231] Such spectra could usefully be repeated today using the much higher magnetic fields and faster MAS available. The difficulties presented in the simulations are further illustrated by MoO_3, where comparisons between static and MAS spectra were made in two studies at 9.4 T and where there was disagreement between the NMR parameters derived from the spectra.[228,231] One of the main interests in molybdenum is as a surface species in heterogeneous catalysis. In looking at a series of samples MoO_x–Al_2O_3 with loadings in the range 3–24%, there was evidence in the spectra of several species that changed relative intensity with loading.[231]

Further work was carried out on a series of aryldiazenido-, organohydrazido- and unsubstituted polyoxomolybdates that closely mimic species playing a central role in hydrodesulfurization catalysts.[232] This later ^{95}Mo NMR data gave evidence that octahedral and tetrahedral species could be distinguished. In spectra with both species present, the tetrahedral sites appeared to give much narrower resonances than the octahedral sites. In complexes where there were inequivalent octahedral sites, the complex lines could be fitted to multiple components, often with very different quadrupole asymmetry parameters for the different sites. These NMR parameters were subsequently related to the degree of structural distortion determined from the X-ray crystallography. The effects of cobalt, caesium and potassium on molybdena-alumina catalysts were also followed by ^{95}Mo solid-state NMR techniques.[233] As many of these species are protonated, ^{1}H–^{95}Mo CP has been developed and investigated in detail for $(NH_4)_6Mo_7O_{24} \cdot 4H_2O$ and $(Bu_4N)_2Mo_2O_7$.[234] Efficient CP was achieved at 66–86% of the theoretical maximum. In adjusting the matching condition by varying B_1, structure was found and this was attributed to the different transitions being matched. The optimum contact times were 20–30 ms and the molybdenum $T_{1\rho}$ was long compared to the other relaxation processes, making it suitable for CP.

One of the most important species formed in surface interactions is $Mo(CO)_6$ and there have been at least six solid-state NMR reports.[2,230,231,235–237] The quadrupolar interaction is small, so that all transitions are readily observed (~70 kHz) in a one-pulse experiment. By considering the central and satellite transitions and using static and MAS measurements, all interaction parameters could be accurately deduced. From the static central transition the principal components of the CSA tensor were deduced as −1843, −1855 and −1865 ppm. The satellite transitions provided information on the quadrupolar parameters. The relative spatial orientation of the elements of the different tensors was discussed. In the MAS spectra, weak peaks could also be detected arising from $^{1}J(^{95}Mo, ^{13}C)$ coupling of 68 Hz.[2] $Mo(CO)_6$ would make a good solid-state NMR reference compound for molybdenum, with its narrow line that can be observed in a single scan. The spectrum is also sensitive to angle setting. The data on $Mo(CO)_6$ were improved still further in a single-crystal study using a two-axis goniometer probe.[237] This study confirmed in more detail the orientations from the powder work and greatly improved the reliability of the Euler angles of the relative tensor orientation.

The ^{95}Mo NMR spectrum was measured from a mixture of $MoSe_2$ and Mo_3Se_4, with the resonances from each being identified.[228] There was a third, broader component which was attributed to disordered material present. The large shift and relatively rapid relaxation (<1 s) of Mo_3Se_4 is caused by conduction electron effects. MoS_2 gave a static ^{95}Mo NMR lineshape that was dominated by quadrupolar effects but had a similar shift to $MoSe_2$. For $MoSi_2$ the satellite transitions allowed C_Q to be deduced, with the central transition then providing an estimate of the lower limit for K_{ax} of 17 ppm. MAS did not narrow

the spectrum from Mo_2C, indicating that quadrupolar effects dominated the lineshape. ^{95}Mo MAS NMR of a series of $(AgI)_y[(AgO)_x(MoO_3)_{1-x}]_{1-y}$ glasses showed that when $x = 0.5$ only MoO_4^{2-} groups were present, whereas when $x < 0.5$ along with these isolated tetrahedral units there were octahedral molybdate units with attached molybdate tetrahedra.[238]

4.11. Miscellaneous nuclei

So far only half the nuclei listed in Table 1 have been dealt with. If reports of solid-state NMR of these nuclei are few, then those concerning the remainder (except in unusual applications such as magnetic materials) are decidedly scant. Strontium-87 would be a useful nucleus that could be applied to a number of interesting material problems (e.g. piezo- and ferroelectrics). Cubic materials give narrow resonances (e.g. SrO, SrS) and a good standard for setting up ^{87}Sr experiments is $SrTiO_3$, which gives an MAS linewidth of ~40 Hz at 8.45 T.[240] ^{53}Cr NMR has been reported from the ferromagnets $CdCr_2S_4$ and $CuCr_2Se_4$.[241] An echo was formed by multiple-quantum effects and contained information about the magnetic hyperfine interactions. ^{61}Ni NMR was examined in the approximately equiatomic alloy $Ni_{49.6}Al_{50.4}$ at 9.4 T, giving a shift of 1220 ppm.[242] This can be compared to a value obtained on the same alloy of 1890 ppm at 1.6 T.[243] This discrepancy reflects the difficulty of the lower-field measurement, and the critical nature of the value of the magnetic moment taken to calculate the diamagnetic position.

Germanium is a nucleus very rarely studied by any form of NMR, but recently spectra were reported from single crystals of germanium with differing isotopic contents.[244] Local lattice distortions arising from isotopic disorder produced quadrupole effects in the NMR lineshape. ^{99}Ru and ^{101}Ru NMR spectra were measured in RuO_2, $SrRuO_3$, $CaRuO_3$ and Sr_2RuO_4.[245] These compounds exhibit various magnetic and superconducting properties that NMR can usefully probe. For ruthenium itself, all the transitions could be detected. From these observations it was possible to deduce that $K_{iso} = 6700$ ppm and that $C_Q = 1.93$ and 11.2 MHz for ^{99}Ru and ^{101}Ru, respectively, both with $\eta = 0$. The ratio of the C_Q values agrees exactly with the ratio of the quadrupole moments of the two isotopes. In RuO_2 only the central transition of ^{99}Ru could be detected, from which it was determined that $C_Q = 21.1$ MHz and $\eta = 0.74$.

5. SUMMARY AND CONCLUSIONS

Low-γ nuclei still represent a tiny fraction of the total solid-state NMR output each year. For the nuclei examined in detail here, most had reports of NMR measurements from the very earliest days of NMR. However, over the last decade a significant new emphasis has become apparent in some of the NMR

work on these nuclei. There were reports from conventional materials using relatively straightforward NMR techniques such as direct excitation, CP and MAS. Hence these recent measurements are certainly closer to the standard methodology of the solid-state NMR spectroscopist. The impetus behind this has been the technological advances of NMR. Most importantly, higher magnetic fields have increased sensitivity and, consequently by operating at higher frequencies, reduced difficulties such as ringing, and for non-integer-spin quadrupolar nuclei reduced second-order quadrupolar effects. After sensitivity, a common theme was the very long relaxation times that are often encountered. Although still difficult, a number of the nuclei in Table 1 can probably now be more widely studied.

The difficulty of the nuclei reviewed here varies widely, and some of those examined in this review are likely to find much wider application in the near future. Of the spin-$\frac{1}{2}$ nuclei, yttrium and silver can be classified as 'readily' observable, particularly in circumstances where their relaxation is enhanced (e.g. when paramagnetic centres have been added or there is significant motion). Of the quadrupolar nuclei some are certainly worth studying systematically at high field. Those that merit immediate further attention are ^{25}Mg, ^{39}K, ^{47,49}Ti and possibly ^{43}Ca and ^{67}Zn. The MAS work on ^{14}N[98,99,102] certainly indicates that relatively narrow resonances, albeit making up extensive sideband manifolds, could be available. It should again be emphasized that even nuclei with large quadrupole interactions can have very long relaxation times in the solid state, and this should not be underestimated in trying to observe these nuclei. The progress that solid-state NMR in general has made over the last 20 years has been astonishing. Study of some low-γ nuclei by solid-state NMR is likely to blossom over the next ten years. This review gives a snapshot of the subject's development at March 2000. It is hoped that the activity in this area is such that in ten years' time it will need significant updating.

ACKNOWLEDGEMENTS

The author thanks Dr S. Holmes for her considerable help in preparing this manuscript. The author has had many useful discussions with low-γ practitioners but would like especially to mention Dr T. J. Bastow (CSIRO, Australia), Professor R. Dupree (Warwick) and J. V. Hanna (ANSTO, Australia) for sharing their expertise and interest in this subject. The author also thanks the EPSRC for their funding of the NMR effort at Warwick.

REFERENCES

1. P. Granger, *NATO ASI Ser. C*, 1990, **322**, 63.
2. K. Eichele, R. E. Wasylishen and J. H. Nelson, 1997. *J. Phys. Chem. A*, **101**, 5463.

3. M. E. Smith, *Specialist Periodic Reports: NMR*, 1998, **27**, 222.
4. M. E. Smith, *Specialist Periodic Reports: NMR*, 1999, **28**, 232.
5. Y. D. Zhang, J. I. Budnick, D. P. Yang, G. W. Fernando, W. A. Hines and T. Manzur, *Phys. Rev. B*, 1995, **51**, 12091.
6. R. K. Harris, *NMR Spectroscopy*, Pitman, London, 1984.
7. D. R. Lide, *CRC Handbook*, 9–85, CRC Press, Boca Raton, 1996.
8. P. C. Schmidt, K. D. Sen, T. P. Das and A. Wiess, *Phys. Rev. B*, 1980, **22**, 4167.
9. W. R. Johnson, D. Kolb and K.-N. Huang, *Atomic and Nuclear Data Tables*, 1983, **28**, 333.
10. M. H. Cohen and F. Reif, *Solid State Phys*, 1957, **5**, 321.
11. M. E. Smith and E. R. H. van Eck, *Prog. NMR Spectrosc.*, 1999, **34**, 159.
12. E. Fukushima and S. B. W. Roeder, *Experimental Pulse NMR*, Addison-Wesley, Reading, MA, 1981.
13. E. Fukushima and S. B. W. Roeder, *J. Magn. Reson.*, 1979, **33**, 199.
14. J. Lowe and M. Engelsberg, *Rev. Sci. Instrum.*, 1974, **45**, 631.
15. J. Schaefer and E. O. Stejskal, *J. Magn. Reson.*, 1974, **15**, 173.
16. D. I. Hoult, C.-N. Chen, H. Eden and M. Eden, *J. Magn. Reson.*, 1983, **51**, 110.
17. I. P. Gerothanassis, *Prog. NMR Spectrosc.*, 1987, **19**, 267.
18. M. E. Smith and J. H. Strange, *Meas. Sci. Technol.*, 1996, **7**, 449.
19. P. P. Man, *Phys. Rev. B*, 1995, **52**, 9419.
20. A. C. Kunwar, G. L. Turner and E. Oldfield, *J. Magn. Reson.*, 1986, **69**, 124.
21. P. S. Belton, I. J. Cox and R. K. Harris, *J. Chem. Soc., Faraday Trans. 2*, 1985, **81**, 63.
22. H. Eckert and J. P. Yesinowski, *J. Am. Chem. Soc.*, 1986, **108**, 2140.
23. A. Benesi and P. D. Ellis, *J. Magn. Reson.*, 1988, **78**, 511.
24. S. Zhang, X. Wu and M. Mehring, *Chem. Phys. Lett.*, 1990, **168**, 227.
25. P. P. Man, *Solid State NMR*, 1992, **1**, 149.
26. I. J. F. Poplett and M. E. Smith, *Solid State NMR*, 1998, **11**, 211.
27. M. E. Smith, *Appl. Magn. Reson.*, 1993, **4**, 1.
28. A. Sebald, *NMR Basic Principles and Progress*, 1994, **31**, 92.
29. A. R. Thompson and E. Oldfield, *J. Chem. Soc., Chem. Commun.*, 1987, 27.
30. R. Dupree and M. E. Smith, *Chem. Phys. Lett.*, 1988, **148**, 41.
31. T. Harazono and T. Watanabe, *Bull. Chem. Soc. Jpn.*, 1997, **70**, 2383.
32. R. H. Meinhold and K. J. D. MacKenzie, *Solid State NMR*, 1995, **5**, 151.
33. K. J. D. MacKenzie and R. H. Meinhold, *J. Mater. Chem.*, 1994, **4**, 1595.
34. P. D. Battle, B. Montez and E. Oldfield, *J. Chem. Soc., Chem. Commun.*, 1988, 584.
35. C. P. Grey, M. E. Smith, A. K. Cheetham, C. M. Dobson and R. Dupree, *J. Am. Chem. Soc.*, 1990, **112**, 4670.
36. T. Harazono, E. Yokota, H. Uchida and T. Watanabe, *Bull. Chem. Soc. Jpn.*, 1998, **71**, 825.
37. T. Harazono, R. Adachi, N. Kijima and T. Watanabe, *Bull. Chem. Soc. Jpn.*, 1999, **72**, 2655.
38. T. Harazono, E. Yokota, H. Uchida and T. Watanabe, *Bull. Chem. Soc. Jpn.*, 1998, **71**, 2796.
39. K. J. D. MacKenzie and T. Kemmitt, *Thermochim. Acta*, 1999, **325**, 13.
40. R. K. Kremer, H. J. Mattausch, A. Simon, S. Steuernagel and M. E. Smith, *J. Solid State Chem.*, 1992, **96**, 237.
41. L. H. Merwin and A. Sebald, *J. Magn. Reson.*, 1990, **88**, 167.
42. J. Wu, T. J. Boyle, J. L. Shreeve, J. W. Ziller and W. J. Evans, *Inorg. Chem.*, 1993, **32**, 1130.
43. R. G. Barnes, D. R. Torgeson, T. J. M. Bastow, G. W. West, E. F. W. Seymour and M. E. Smith, *Z. Phys. Chem. Neue Folge*, 1989, **164**, S867.
44. X. Helluy, J. Kummerlen, A. Sebald and O. J. Zogal, *Solid State NMR*, 1999, **14**, 225.
45. G. Balakrishnan, R. Dupree, I. Farnan, D. McKPaul and M. E. Smith, *J. Phys. C.*, 1988, **21**, L847.
46. J. T. Markert, T. W. Noh, S. E. Russek and R. M. Cotts, *Solid State Commun.*, 1987, **63**, 847.
47. H. Alloul, P. Mendels, H. Casalta, J. F. Marucco and J. Arabski, *Phys. Rev. Lett.*, 1991, **67**, 3140.
48. H. Alloul, P. Mendels, G. Collin and P. Monod, *Phys. Rev. Lett.*, 1988, **61**, 746.

49. T. Ohno, K. Mizuno, T. Kanashiro and H. Alloul, *Physica C*, 1991, **185**, 1067.
50. T. Ohno, H. Alloul, P. Mendels, G. Collin and J. F. Marucco, *J. Magn. Magn. Mater.*, 1990, **90–91**, 657.
51. A. Rigamonti, F. Borsa and P. Carretta, *Rep. Prog. Phys.*, 1998, **61**, 1367.
52. G. Balakrishnan, L. W. J. Caves, R. Dupree, D. McKPaul and M. E. Smith, *Physica C*, 1989, **161**, 9.
53. R. Dupree, A. Gencten and D. McKPaul, *Physica C*, 1992, **193**, 81.
54. T. M. Riseman, H. Alloul, A. V. Mahajan, P. Mendels, N. Blanchard, G. Collin and J. F. Marucco, *Physica C*, 1994, **235**, 1593.
55. D. P. Tunstall and W. J. Webster, *Superconductor Sci. Techn.*, 1991, **4**, S406.
56. G. V. M. Williams and J. L. Tallon, *Phys. Rev. B*, 1998, **57**, 10984.
57. G. V. M. Williams, J. L. Tallon, R. Michalak and R. Dupree, *Phys. Rev. B*, 1998, **57**, 8696.
58. T. Auler, M. Horvatic, J. A. Gillet, C. Berthier, Y. Berthier, P. Carretta, Y. Kitaoka, P. Segransan and J. Y. Henry, *Physica C*, 1999, **313**, 255.
59. G. V. M. Williams, J. L. Tallon, J. W. Quilty, H. J. Trodahl and N. E. Flower, *Phys. Rev. Lett.*, 1998, **80**, 377.
60. H. B. Brom and H. Alloul, *Physica C*, 1991, **185**, 1789.
61. P. Carretta and M. Costi, *Phys. Rev. Lett.*, 1992, **68**, 1236.
62. J. Suh, D. R. Torgeson and F. Borsa, *Phys. Rev. Lett.*, 1993, **71**, 3001.
63. F. Borsa, P. Carretta, M. Costi, K. Nehrke, A. Rigamonti and F. Tabak, *Nuovo Cimento D*, 1997, **19**, 1199.
64. L. H. Merwin and A. Sebald, *J. Magn. Reson.*, 1992, **97**, 628.
65. H. G. Fijolek, T. A. Oriskovich, A. J. Benesi, P. Gonzalez-Duarte and M. J. Natan, *Inorg. Chem.*, 1996, **35**, 797.
66. H. G. Fijolek, J. R. Grohal, J. L. Sample and M. J. Natan, *Inorg. Chem.*, 1997, **36**, 622.
67. H. G. Fijolek, P. Gonzalez-Duarte, S. H. Park, S. L. Suib and M. J. Natan, *Inorg. Chem.*, 1997, **36**, 5299.
68. H. Looser and D. Brinkmann, *J. Magn. Reson.*, 1985, **64**, 76.
69. K. D. Becker and E. von Goldammer, *Chem. Phys.*, 1990, **48**, 193.
70. M. Villa, G. Chiodelli, A. Magistris and G. Licheri, *J. Chem. Phys.*, 1986, **85**, 2392
71. P. Mustarelli, C. Tomasi, E. Quartarone, A. Magistris, M. Cutroni and A. Mandanici, *Phys. Rev. B*, 1998, **58**, 9054.
72. T. Ida, K. Endo, M. Suhara, M. Kenmotsu, K. Honda, S. Kitagawa and H. Kawabe, *Bull. Chem. Soc. Jpn.*, 1999, **72**, 2061.
73. S. H. Chung, K. R. Jeffrey, J. R. Stevens and L. Borjesson, *Phys. Rev. B*, 1990, **41**, 6154.
74. P. Mustarelli, C. Tomasi, A. Magistris and M. Cutroni, *J. Non-Cryst. Solids*, 1998, **232–234**, 532.
75. J. Roos, D. Brinkmann, M. Mali, A. Pradel and M. Ribes, *Solid State Ionics*, 1988, **28–30**, 710.
76. J. Sanz, P. Herrero, R. Rojas, J. M. Rojas, S. Rossignol, J. M. Reau and B. Tanguy, *Solid State Ionics*, 1995, **82**, 129.
77. K. K. Olsen and J. W. Zwanziger, *Solid State NMR*, 1995, **5**, 123.
78. M. Tansho, H. Wada, M. Ishii and Y. Onoda, *Solid State Ionics*, 1996, **86–88**, 155.
79. J. K. Plischke, A. J. Benesi and M. A. Vannice, *J. Phys. Chem.*, 1992, **96**, 3799.
80. M. Jansen, *Angew. Chem. Int Ed.*, 1987, **99**, 1098.
81. C. T. G. Knight, G. L. Turner, R. J. Kirkpatrick and E. Oldfield, *J. Am. Chem. Soc.*, 1986, **108**, 7426.
82. L. H. Merwin and A. Sebald, *Solid State NMR*, 1992, **1**, 45.
83. J. P. Yesinowski and E. A. Hill, *Solid State NMR Spectroscopy of Inorganic Materials*, ACS Symposium Series 717, 358, 1999.
84. R. Tycko and S. J. Opella, *J. Chem. Phys.*, 1987, **86**, 1761.
85. E. E. Ylinen, A. Kaikkonen and M. Punkkinen, *Solid State NMR*, 1997, **10**, 25.

86. C. P. Grey, A. P. A. M. Eijkelenboom and W. S. Veeman, *Solid State NMR*, 1995, **4**, 113.
87. Y. Ba, H.-M. Kao, C. P. Grey, L. Chopin and T. Gullion, *J. Magn. Reson.*, 1998, **133**, 104.
88. E. A. Hill and J. P. Yesinowski, *J. Am. Chem. Soc.*, 1996, **118**, 6798.
89. H. Ono, S. Ishimaru, R. Ikeda and H. Ishida, *Bull. Chem. Soc. Jpn.*, 1997, **70**, 2963.
90. T. K. Pratum and M. P. Klein, *J. Magn. Reson.*, 1983, **53**, 473.
91. T. K. Pratum and M. P. Klein, *J. Magn. Reson.*, 1983, **55**, 421.
92. T. J. Bastow and S. N. Stuart, *J. Phys.: Condensed Matter*, 1989, **1**, 4649.
93. W. C. Bailey and H. S. Story, *J. Chem. Phys.*, 1974, **60**, 1952.
94. N. Weiden and A. Weiss, *18th AMPERE Congress*, p. 257, 1974.
95. T. J. Bastow and S. N. Stuart, *Z. Naturforsch. A*, 1990, **45**, 459.
96. T. J. Bastow and S. N. Stuart, *Chem. Phys. Lett.*, 1991, **180**, 305.
97. K. Differt and R. Messer, *J. Phys. C*, 1980, **13**, 717.
98. T. J. Bastow, D. Massiot and J. P. Coutures, *Solid State NMR*, 1998, **10**, 241.
99. G. Jeschke, W. Hoffbauer and M. Jansen, *Solid State NMR*, 1998, **12**, 1.
100. G. Jeschke and M. Jansen, *Angew. Chem. Int. Ed.*, 1998, **37**, 1282.
101. K. J. D. MacKenzie, R. H. Meinhold, D. G. McGavin, J. A. Ripmeester and I. Moudrakovski, *Solid State NMR*, 1995, **4**, 193.
102. K. Ermolaev and B. M. Fung, *J. Chem. Phys.*, 1999, **110**, 7977.
103. A. K. Khitrin and B. M. Fung, *J. Chem. Phys.*, 1999, **111**, 8963.
104. L. S. Batchelder and J. L. Ragle, *J. Magn. Reson.*, 1980, **37**, 469.
105. R. Blinc, J. Seliger, V. Zager, T. Apih, J. Dolinsek, H. Warharek, A. Fuith and W. Schranz, *Phys. Rev. B*, 1990, **42**, 8125.
106. M. E. Smith (unpublished results).
107. S. L. Segel, *J. Chem. Phys.*, 1981, **75**, 4746.
108. S. L. Segel, *J. Chem. Phys.*, 1978, **68**, 330.
109. R. Dupree and M. E. Smith, *J. Chem. Soc., Chem. Commun.*, 1988, 1483.
110. Y. Hiyama, P. M. Woyciesjes, T. L. Brown and D. A. Torchia, *J. Magn. Reson.*, 1987, **72**, 1.
111. P. S. Fiske, J. F. Stebbins and I. Farnan, *Phys. Chem. Minerals*, 1994, **20**, 587.
112. A. V. Chadwick, I. J. F. Poplett, D. T. S. Maitland and M. E. Smith, *Chem. Mater.*, 1998, **10**, 864.
113. M. A. Fedotov and G. F. Gerasimova, *React Kinet. Catal. Lett.*, 1983, **22**, 1977.
114. T. J. Bastow, *Solid State Commun.*, 1991, **77**, 547.
115. K. J. D. MacKenzie and R. H. Meinhold, *Thermochim. Acta*, 1993, **230**, 339.
116. N. Pecoul, S. Bourbigot and B. Revel, *Macromol. Symp.*, 1997, **119**, 309.
117. K. J. D. MacKenzie and R. H. Meinhold, *Am. Miner.*, 1994, **79**, 250.
118. P. S. Fiske and J. F. Stebbins, *Am. Miner.*, 1994, **79**, 848.
119. K. J. D. MacKenzie and R. H. Meinhold, *Am. Miner.*, 1997, **82**, 479.
120. B. Derighetti, S. Hafner, H. Marxer and H. Rager, *Phys. Lett.*, 1978, **66A**, 150.
121. K. P. Such and G. Lehmann, *Chem. Phys. Lett.*, 1988, **143**, 463.
122. J. F. Stebbins, *Am. Miner.*, 1996, **81**, 1315.
123. A. M. George and J. F. Stebbins, *Am. Miner.*, 1998, **83**, 1022.
124. K. J. D. MacKenzie and R. H. Meinhold, *J. Mater. Sci. Lett.*, 1993, **12**, 1696.
125. K. J. D. MacKenzie and R. H. Meinhold, *Thermochim. Acta*, 1993, **230**, 331.
126. K. J. D. MacKenzie, R. H. Meinhold, B. L. Sherriff and Z. Xu, *J. Mater. Chem.*, 1993, **3**, 1263.
127. K. J. D. MacKenzie and R. H. Meinhold, *Am. Mineral.*, 1994, **79**, 43.
128. K. J. D. MacKenzie and R. H. Meinhold, *Thermochim. Acta*, 1994, **244**, 195.
129. K. J. D. MacKenzie and R. H. Meinhold, *Thermochim. Acta*, 1994, **232**, 85.
130. J. Temuujin, K. Okada and K. J. D. MacKenzie, *J. Am. Ceram. Soc.*, 1998, **81**, 754.
131. S. Sham and G. Wu, *Inorg. Chem.*, 2000, **39**, 4.
132. E. M. Dickson and E. F. W. Seymour, *J. Phys. C*, 1970, **3**, 666.
133. P. D. Dougan, S. N. Sharma and D. L. Williams, *Can. J. Phys.*, 1969, **47**, 1047.

134. T. J. Bastow and S. Celotto, *Solid State Commun.*, 1999, **110**, 271.
135. T. J. Bastow, *J. Phys.: Condensed Matter*, 1991, **3**, 753.
136. T. J. Bastow and M. E. Smith, *J. Phys.: Condensed Matter*, 1995, **7**, 4929.
137. D. Padro, A. P. Howes, M. E. Smith and R. Dupree, *Solid State NMR*, 2000, **15**, 231.
138. K. Lee, *Phys. Rev.*, 1968, **172**, 284.
139. H. Suzuki, T. Komaru, T. Hihara and Y. Koi, *J. Phys. Soc. Jpn.*, 1971, **30**, 288.
140. H. L. Retcofsky and R. A. Friedel, *J. Am. Chem. Soc.*, 1972, **94**, 6579.
141. C. Karr and H. D. Schultz, *Spectrosc. Lett.*, 1968, **1**, 205.
142. M. Haller, W. E. Hertler, O. Lutz and A. Nolle, *Solid State Commun.*, 1980, **33**, 1051.
143. O. Lutz, *NATO ASI Ser. C*, 1983, **103**, 389.
144. T. J. Bastow and S. N. Stuart, *Phys. Stat. Sol.*, 1988, **145**, 719.
145. W. A. Daunch and P. L. Rinaldi, *J. Magn. Reson. A*, 1996, **123**, 219.
146. E. A. C. Lucken, *Nuclear Quadrupole Coupling Constants*, Academic Press, London, 1969.
147. T. L. Weeding and W. S. Veeman, *J. Chem. Soc., Chem. Commun.*, 1989, 946.
148. S. Hayashi and K. Hayamizu, *Bull. Chem. Soc. Jpn.*, 1990, **63**, 913.
149. K. D. Becker, *J. Chem. Phys.*, 1978, **68**, 3785.
150. J. Skibsted and H. J. Jakobsen, *Inorg. Chem.*, 1999, **38**, 1806.
151. S. Jurga, G. S. Harbison, B. Blumich, H. W. Spiess, F. Fujara and A. Olinger, *Ber. Bunsenges. Phys. Chem. Chem. Phys.*, 1986, **90**, 1153.
152. H. Ono, S. Ishimaru, R. Ikeda and H. Ishida, *Chem. Phys. Lett.*, 1997, **275**, 485.
153. H. Ono, S. Ishimaru, R. Ikeda and H. Ishida, *Bull. Chem. Soc. Jpn.*, 1999, **72**, 2049.
154. S. Jurga, J. Seliger, R. Blinc and H. W. Spiess, *Phys. Lett. A*, 1986, **116**, 295.
155. M. Hattori, Y. Onoda, E. Tomoki, M. E. Smith, H. Masakazu, H. Ohki and R. Ikeda, *Z. Naturforsch.*, 1994, **49a**, 291.
156. K.-P. Holzer, U. Hacker, J. Petersson, D. Michel and S. Kluthe, *Solid State Commun.*, 1995, **94**, 275.
157. J. P. Yesinowski, M. L. Buess, A. N. Garroway, M. Ziegeweid and A. Pines, *Anal. Chem.*, 1995, **67**, 2256.
158. T. J. Bastow, S. N. Stuart, W. G. McDugle, R. S. Eachus and J. M. Spaeth, *J. Phys.: Condensed Matter*, 1994, **6**, 8633.
159. R. J. Kirkpatrick, P. Yu, X. Hou and Y. Kim, *Am. Mineral.*, 1999, **84**, 1186.
160. R. Jelinek, A. Stein and G. A. Ozin, *J. Am. Chem. Soc.*, 1993, **115**, 2390.
161. Y. Furukawa and R. Ikeda, *Ber. Bunsenges. Phys. Chem. Chem. Phys.*, 1993, **97**, 1143.
162. T. J. Bastow, *J. Chem. Soc., Faraday Trans.*, 1991, **87**, 2453 (and references therein).
163. T. J. Bastow, S. L. Segel and K. R. Jeffrey, *Solid State Commun.*, 1991, **78**, 565.
164. J-F. Lambert, R. Prost and M. E. Smith, *Clays and Clay Minerals*, 1992, **40**, 253.
165. I. J. F. Poplett and J. A. S. Smith, *J. Chem. Soc., Faraday Trans. 2*, 1981, **77**, 1155.
166. G. Wu, *Biochem. Cell Biol.*, 1998, **76**, 429.
167. T. R. Krawietz, D. K. Murray and J. F. Haw, *J. Phys. Chem. A*, 1998, **102**, 8779.
168. J. Kim, J. L. Eglin, A. S. Ellaboudy, L. E. H. McMills, S. Huang and J. L. Dye, *J. Phys. Chem.*, 1996, **100**, 2885.
169. M. Kenmotsu, H. Honda, H. Ohki, R. Ikeda, T. Erata, A. Tasaki and Y. Furukawa, *Z. Naturforsch. A*, 1994, **49**, 247.
170. R. Blinc, J. Dolinsek, J. Apih, W. Schranz, A. Fuith and H. Warharek, *Solid State Commun.*, 1995, **93**, 609.
171. K. Endo, M. Kenmotsu, J. Frye, K. Honda, S. Kitagawa and K. Deguchi, *J. Phys. Chem. Solids*, 1996, **57**, 1609.
172. D. Markgrabe and G. Engelhardt, *Chem. Phys. Lett.*, 1999, **300**, 701.
173. M. Apostol, *J. Phys. Chem.*, 1996, **100**, 3175.
174. S. Sasaki, A. Matsuda and C. W. Chu, *Physica C*, 1998, **302**, 319.
175. M. Apostol, C. Goze, F. Rachdi, M. Mehring and J. E. Fischer, *Solid State Commun.*, 1996, **98**, 253.

176. H. Alloul, K. Holczer, Y. Yoshinari and O. Klein, *Physica C*, 1994, **235–240**, 2509.
177. Y. Yoshinari, H. Alloul, V. Brouet, G. Kriza, K. Holczer and L. Forro, *Phys. Rev. B*, 1996, **54**, 6155.
178. D. A. McArthur, E. L. Hahn and R. E. Walstedt, *Phys. Rev.*, 1969, **188**, 609.
179. J. F. Jacquinot, W. T. Wenckebach, M. Goldman and A. Abragam, *Phys. Rev. Lett.*, 1974, **32**, 1096.
180. R. G. Bryant, S. Ganapathy and S. D. Kennedy, *J. Magn. Reson.* 1987, **72**, 379.
181. A. Trokiner, L. Lenoc, K. Mikhalev, A. Yakubovskii, H. Lutgemeier, I. Heinmaa, A. Gippius, S. Verkhovskii, D. Goldschmidt and Y. Eckstein, *Physica C*, 1994, **226**, 43.
182. A. Trokiner, L. L. Noc, A. Yakubovskii, K. N. Mykhalyov and S. V. Verkhovskii, *J. Chim. Phys. Phys. Chim. Biol.*, 1994, **91**, 862.
183. A. Trokiner, L. Lenoc, A. Yakubovskii, K. N. Mykhalyov and S. V. Verkhovskii, *Z. Naturforsch. A*, 1994, **49**, 373.
184. P. V. Bellot, A. Trokiner, Y. Zhdanov and A. Yakubovskii, *J. Chim. Phys. Phys. Chim. Biol.*, 1998, **95**, 280.
185. P. Nieto, R. Dron, R. Thouvenot, H. Zanni and F. Brivot, *C. R. Acad. Paris II*, 1995, **320**, 485.
186. H. Zanni, R. Rassem-Bertolo, S. Masso, L. Fernandez, P. Nieto and B. Bresson, *Magn. Reson. Imaging*, 1996, **14**, 827.
187. R. Dupree, A. P. Howes and S. C. Kohn, *Chem. Phys. Lett.*, 1997, **276**, 399.
188. K. J. D. MacKenzie and M. E. Smith (unpublished results).
189. S. F. Dec, M. F. Davis, G. E. Maciel, C. E. Bronnimann, J. J. Fitzgerald and S. Han, *Inorg. Chem.*, 1993, **32**, 955.
190. T. J. Bastow, M. A. Gibson and C. T. Forwood, *Solid State NMR*, 1998, **12**, 201.
191. A. Labouriau and W. L. Earl, *Chem. Phys. Lett.*, 1997, **270**, 278.
192. O. Kanert and H. Kolem, *J. Phys. C*, 1988, **21**, 3909.
193. T. J. Bastow, G. Doran and H. J. Whitfield, *Chem. Mater.*, 2000, **12**, 436.
194. T. J. Bastow, *Z. Naturforsch. A*, 2000, **55**, 291.
195. T. J. Bastow and H. J. Whitfield, *Chem. Mater.*, 1999, **11**, 3518.
196. C. E. Forbes, W. B. Harwood, N. E. Cipollini and J. F. Lynch, *J. Chem. Soc., Chem. Commun.*, 1987, 433.
197. R. Sommer, M. Maglione and J. J. van der Klink, *Ferroelectrics*, 1990, **107**, 307.
198. T. J. Bastow, *J. Phys.: Condensed Matter*, 1989, **1**, 4985.
199. O. Kanert, H. Schulz and J. Albers, *Solid State Commun.*, 1994, **91**, 465.
200. D. P. Tunstall, J. R. M. Todd, S. Arumugam, G. Dai, M. Dalton and P. P. Edwards, *Phys. Rev. B*, 1994, **50**, 16541.
201. A. Narath, *Phys. Rev.*, 1967, **162**, 320.
202. H. Ebert, J. Abart and J. Voitlander, *J. Phys. F*, 1986, **16**, 1287.
203. B. Nowak, O. J. Zogal and K. Niedzwiedz, *J. Alloys Compounds*, 1992, **189**, 141.
204. R. C. Frisch and R. A. Forman, *J. Chem. Phys.*, 1968, **48**, 5187.
205. D. Padro, R. Dupree, A. Howes and M. E. Smith (unpublished results).
206. G. Wu, *Chem. Phys. Lett.*, 1998, **298**, 375.
207. N. Roberts, R.-P. Wang, A. W. Sleight and W. W. Warren. *Phys. Rev. B*, 1998, **57**, 5734.
208. G. Wu, S. Kroeker and R. E. Wasylishen, *Inorg. Chem.*, 1995, **34**, 1595.
209. T. J. Bastow, *J Phys: Condensed Matter*, 1996, **8**, 11309.
210. T. Vosegaard, U. Andersen and H. J. Jakobsen, *J. Am. Chem. Soc.*, 1999, **121**, 1970.
211. S. Sham and G. Wu, *Can. J. Chem.*, 1999, **77**, 1782.
212. F. H. Larsen, A. S. Lipton, H. J. Jakobsen, N. C. Nielsen and P. D. Ellis, *J. Am. Chem. Soc.*, 1999, **121**, 3783.
213. T. Yamada and M. Asanuma, *Phys. Rev. Lett.*, 1965, **15**, 695.
214. D. R. Torgeson and R. G. Barnes, *Bull. Am. Phys. Soc.*, 1967, **12**, 313.
215. T. Hioki, M. Kontani and Y. Masuda, *J. Phys. Soc. Jpn.*, 1975, **39**, 958.

216. T. J. Bastow, M. E. Smith and S. N. Stuart, *Chem. Phys. Lett.*, 1992, **191**, 125.
217. J. Abart, W. Socher and J. Voitlander, *Z. Naturforsch. A*, 1982, **37**, 1030.
218. T. Dumelow and P. C. Riedi, *Hyperfine Interactions*, 1987, **34**, 407.
219. O. J. Zogal, B. Nowak and K. Niedzwiedz, *Solid State Commun.*, 1991, **80**, 601.
220. T. J. Bastow, *J. Phys.: Condensed Matter*, 1990, **2**, 6327.
221. J. S. Hartman, F. P. Koffyberg and J. A. Ripmeester, *J. Magn. Reson.*, 1991, **91**, 400.
222. T. J. Bastow and M. E. Smith, *Solid State NMR*, 1992, **1**, 165.
223. T. J. Bastow, M. E. Hobday, M. E. Smith and H. J. Whitfield, *Solid State NMR*, 1994, **3**, 49.
224. T. J. Bastow, M. E. Hobday, M. E. Smith and H. J. Whitfield, *Solid State NMR*, 1996, **5**, 293.
225. T. J. Bastow, C. T. Forwood, M. A. Gibson and M. E. Smith, *Phys. Rev. B*, 1998, **58**, 2988.
226. P. Hartmann and G. Scheler, *Z. Naturforsch.*, 1995, **50a**, 90.
227. T. J. Bastow, *Z. Naturforsch.*, 1994, **49a**, 320.
228. T. J. Bastow, *Solid State NMR*, 1998, **12**, 191.
229. G. F. Lynch and S. L. Segel, *Can. J. Phys.*, 1972, **50**, 567.
230. V. M. Mastikhin, O. B. Lapina and R. I. Maximovskaya, *Chem. Phys. Lett.*, 1988, **148**, 413.
231. J. C. Edwards, R. D. Adams and P. D. Ellis, *J. Am. Chem. Soc.*, 1990, **112**, 8349.
232. J. C. Edwards, J. Zubieta, S. N. Shaikh, Q. Chen, S. Bank and P. D. Ellis, *Inorg. Chem.*, 1990, **29**, 3381.
233. J. C. Edwards and P. D. Ellis, *Langmuir*, 1991, **7**, 2117
234. J. C. Edwards and P. D. Ellis, *Magn. Reson. Chem.*, 1990, **28**, S59.
235. A. Nolle, *Z. Phys. A*, 1977, **280**, 231.
236. W. M. Shirley, *Z. Phys. Chem.*, 1987, **152**, 41.
237. T. Vosegaard, J. Skibsted and H. J. Jakobsen, *J. Phys. Chem. A*, 1999, **103**, 9144.
238. N. Machida and H. Eckert, *Solid State Ionics*, 1998, **107**, 255.
239. W. D. Kautt, H. Kruger, O. Lutz, H. Maier and A. Nolle, *Z. Naturforsch. A*, 1976, **31**, 351.
240. V. Anuradhu, MPhil. Thesis, University of Warwick (unpublished), 1990.
241. G. N. Abelyashev, V. N. Berzhanskij, N. A. Sergeev and Y. V. Fedotov, *Phys. Lett. A*, 1988, **133**, 263.
242. T. J. Bastow, M. E. Smith and G. W. West, *J. Phys.: Condensed Matter*, 1997, **9**, 6085.
243. L. E. Drain and G. W. West, *Phil. Mag.*, 1965, **11**, 1061.
244. S. V. Verkhovskii, B. Z. Malkin, A. Trokiner, A. Yakubovskii, E. Haller, A. Ananyev, A. Gerashenko, Y. Piskunov, S. Saikin, A. Tikhomirov and V. Ozhogin, *Z. Naturforsch. A Phys. Sci.*, 2000, **55**, 105.
245. H. Mukuda, K. Ishida, Y. Kitaoka, K. Asayama, R. Kanno and M. Takano, *Phys. Rev. B*, 1999, **60**, 12279.

Index

Page numbers in *italics* refer to figures and tables

Absorption signal in the time domain, 64
N-Acetylaspartate (NAA), 95–6, *97*, *99*
^{107}Ag, 134–7
^{109}Ag, 124, 134–7
  solid-state NMR chemical shifts, *136*
AgCl, 137
Ag_4Cl, 150
$Ag_xCu_{1-x}I$, 135
Ag_9GaSe_6, 137
$(AgI)_x(Ag_2O)_y(P_2O_5)_{1-x-y}$, 137
$(AgI)_x(Ag_2S{-}GeS_2)_{1-x}$, 136
$(AgI)_y[(AgO)_x(MoO_3)_{1-x}]_{1-y}$, 168
$2AgI{-}Ag_2MoO_4$, 136
$AgI{-}Ag_2O{-}B_2O_3$, 135
$AgI{-}xAg_2MoO_4$, 136
$AgNO_3$, 137
Ag_2O_2, 137
$Ag_4P_2O_7$, 137
$AgPO_3$, 137
^{27}Al, 128
AlN, 140
α-Al_2O_3, 128
α-relaxation process, 17, 46
Angular frequency tensor, 73

Bacteriorhodopsin, 30
BaFCl, 150
$Ba(NO_3)_2$, 139
Basis functions, 99
$BaTiO_3$, 156, 158
Bayesian probability theory, 114
β-relaxation process, 46
$(Bi_2O_3)_{0.6}(Y_2O_3)_{0.4}$, 132
Biological materials, solid-state NMR techniques, 47–51
$(Bi,Pb)_2Sr_2Ca_2Cu_2O_{8+x}$, 155
$(Bi,Pb)_2Sr_2Ca_2Cu_3O_{10+x}$, 155
Blending, 46
Bloch equations, 65
BN, 140
Bombyx mori, 50
Brownian motional narrowing, 79–81
$(Bu_4N)_2Mo_2O_7$, 167

^{13}C, 124
^{13}C chemical shift anisotropy, 17
  powder pattern, *9*
^{13}C exchange NMR, 35
^{13}C FID, 19
^{13}C NMR, 13, 48, 53
^{13}C powder patterns, 8
^{13}C shielding tensor, 11
^{13}C spin pairs, 17
^{13}C spins, 19
^{13}C transverse magnetization, *18*, 24
^{13}C two-dimensional MAS exchange spectrum, 34
$^{13}C{-}^{13}C$ dipolar coupling, 17, *17*
$^{13}C{-}^{1}H$ dipolar coupling, 8, 17, 20
$^{13}C{-}^{1}H$ internuclear vector, 20
$^{13}C{-}^{2}H$ correlation experiment, pulse sequence, *25*
$^{13}C{-}^{2}H$ dipolar recoupling, 25
^{13}CO intercalated in C_{60}, 9–10
^{13}CO molecule, *10*, 11
C_{60} molecules, 9–11
^{43}Ca, 154–6
  solid-state NMR interaction parameters, *156*
Carbohydrates, 49
Carbonyl ligands, 54
$CaRuO_3$, 168
$CdCr_2S_4$, 168
$C{-}^{2}H$ bond, 8
Characteristic frequency, 32–3
$C_5H_5W(CO)_3Pr^i$, 138
Chemical shielding tensor, 73
Chemical shift anisotropy, 34
  ^{2}H powder lineshapes, 22–3
  lineshapes, 9–16
  recoupling, 16
$((CH_3)_3NC_2H_5)ClO_4$, 139
$(CH_3)_3NCH_2COO{-}CaCl_2{-}2H_2O$, 150
$C_4H_9ND_3Cl$, 150
$C_4H_9NH_3Cl$, 150
Cholesterol[25, 26, 27-^{13}C], 92, *92*
Choline, 95, *99*
$[(C_6H_5)_4P]_2[Ag_4(SCH_2C_6H_4CH_2S)_3]{-}6CH_3OH$, 135
^{35}Cl, 148–50
  solid-state NMR interaction parameters, *151*
^{37}Cl, 148–50
CO molecules, 11, 12
Co—C bond, 50
CODEX NMR (centreband only detection of exchange) experiment, 43–5
Coefficients of rational function approximation, *89*
Combined magic-angle spinning and multiple pulse sequences (CRAMPS), 19

Complex error function, 84
Continuous wave (CW) NMR lineshape, 63
Cope rearrangement, *14*
Correlation function, 27
Cp_2ZrBr_2, 162
$Cr(\eta^6$-arene$)(CO)_3$ complexes, 54
Cramér–Rao lower bound, 93–4
Creatine, 96, *99*
Cross-linking, 46–7
Cross-polarization (CP), 129
Cross-relaxation rate constants, 31
$CuCr_2Se_4$, 168
Curing, 46
Cyanobullvalene, *14*
  molecular structure, *13*

Damping factors, 105
DANTE pulse sequence, 54
DEPT, 121
Deuterium, 82
Dianin inclusion compounds, 52
Dimethyldibenzotetraaza[14]annulene, 30, *31*
Dimethylsulfone (DMS), 16, *23*, 30, 37, 43–5
Dimyristoylphosphatidylcholine (DMPC), 47, 92, *92*
Dimyristoylphosphatidylglycerol (DMPG), 47
Dioxane, 46–7
Dipalmitoylphosphatidylcholine (DPPC), 47–8
Dipolar coupling lineshapes, 16–20
Dipolar filter techniques, 45
Dipolar shift ^{13}C spectrum, *9*
Discrete Fourier transform (DFT), 114
DNA dodecamer, 49, *50*
DNA oligomers, 49
Double angle rotation (DOR), 129
Double-quantum ^2H experiment, pulse sequence, *24*
Double-quantum coherence, 19
Double-quantum spectra, 19
Dynamic angle spinning (DAS), 129
Dynamic heterogeneity in polymer systems, 46

Effective chemical shift anisotropy, 16
Eight-pulse experiment for three-dimensional ^2H exchange experiments, 37
Energy level splitting, *77*
$E(SiMe_3)_4$, 34
  molecular structure, *35*
Euler angles, 73
Exchange experiments, 32–45
  improving resolution, 40–5
  role of, 32
  solid state, 33
Exchange narrowing, NMR lineshapes due to, 70–3

^{19}F spinning sideband patterns, 13
$(F_3PNPh)_2$, molecular structure, *12*
Faraday's law of electromagnetic induction, 124
$FeTiO_3$, 159
Fischer information matrix, 93
Five-pulse sequence for ^2H exchange spectra, *36*
Fluorobullvalene, molecular structure, *13*
Four-dimensional exchange NMR, 37–8
Fourier transform (FT), 63, 70, 94, 101, 106
Fourier transform (FT) NMR, 125
Free induction decay (FID), 5, 14, *18*, *22*, 32, 35, 41, 42, 44, 63, *71*, *88*, 102, 109, 110, 125, 126, 127
Frequency domain
  Lorentzian lineshape function, 65
  methods, 64
  nonlinear least-squares fitting, 97–8
  time domain, *67*
Full width at half maximum height (FWHM), 65–6, 68, 69, 80, 81, 98

Gauss–Lorentz product curve, 84
Gaussian line broadening, 22
Gaussian lineshape, 66–70, *90*
Gaussian noise, 94
Gyromagnetic moment, 86

^1H decoupling, 8
^1H lineshape, 18
^1H magnetization, *18*
^1H NMR spectrum, *99*
^1H spectrum, 19
^1H spins, 19
^1H wideline spectra, 19
^1H—^{13}C dipolar coupling, 8, 18, 20
^1H—^{13}C internuclear vector, 20
^1H—^1H cross-relaxation rates, *32*
^1H—^1H dipolar coupling, 8, 17, 19, 30–1
  lineshapes, 18
^2H exchange experiments, 35
^2H exchange spectra, five-pulse sequence for, *36*
^2H labelling, 23
^2H lineshape analysis, 20, 21
^2H MAS NMR spectroscopy, 21
^2H MAS spectra, *7*
^2H NMR, 20–5, 48
^2H NMR lineshape studies, 51
^2H NMR spectra, *7*, 22, *23*
^2H powder lineshapes, 21
  chemical shift anisotropy, 22–3
^2H powder pattern lineshapes, resolution, 23
^2H quadrupole coupling, 17
^2H quadrupole coupling tensor, 8
^2H quadrupole echo FID, 22–3
^2H relaxation studies, 28

^{2}H spectral lineshapes, 28
^{2}H spinning sideband patterns, 24
Hamiltonian operator, 26
Hankel–Lanczos singular value decomposition (HLSVD), 100, 105, 108
Hankel singular value decomposition (HSVD), 101, 104–6, *107*, *108*
Hankel structure of X, 105
Hartman—Hahn match condition, 129
Hexabenzocoronene, molecular structure, *20*
High-density polyethylene, 17
High-resolution two-dimensional exchange experiments, 34
Higher-dimensional exchange spectra, 36–40
Host–guest compounds, 51–3
$H_3[P(W_{12}O_{40}]$—nH_2O, 137
HTLS, 107
Hybrid lineshapes, 89, *90*
Hydrogen bonding, 50

INEPT, 121
Intensity function, 74
In vivo localized NMR spectroscopy, 64

^{39}K, 129, 150–3
  solid-state NMR interaction parameters, *154*
KAg_4I_5, 135
KBr, 129
$K_{3-x}C_{60}$, 153
KCl, 149
K_2MoO_4, 166
$KNiF_3$, 153
Knight shift, 159
KNO_2, 153
KNO_3, 139, 152
KO_2, 152
Kondo–Yamashita approach, 147
Kramers–Kronig relations, 63
Kubo–Tomita curve, 84
$K_2[Zn(CN)_4]$, 161

Lanczos algorithm, 105–7
Larmor frequency, 27–8, 30, 124–6, 129, 139, 148
Lead zirconate titanate, 156
Legendre polynomial, 73, 76, 84
Levenberg–Marquardt method, 94–8, 114
Li_3N, 139
Line-broadening mechanisms, 63
Linear prediction and related techniques, 100–8
Linear prediction equation, 101
Linear prediction singular value decomposition (LPSVD), 100–4, *106*, 107, *107*, 112
Linear time domain analysis, 106
Lineshape analysis, 2
  powder, 3–25
  powder pattern, 4–9
Lineshape fitting procedures, 59–120
  comparison, *113*
  criteria for good fit, 93–4
Lineshape function, 74
Lineshapes, comparison, 81–4
Longitudinal relaxation, 26–8
Lorentzian lineshapes, 63–6
Lorentzian resonances, 72
Low-γ nuclei
  NMR properties, *123*
  solid-state NMR, 121–75
    experimental approaches, 125–30

Magic-angle spinning (MAS), 4, 12, 19, 24, 25, 128, 129, 140
  FID, 129
  ^{2}H NMR, 21
  lineshape analysis, 13
  NMR probes, 122
Magnetic field inhomogeneity, 63, 64
Magnetic resonance spectroscopy (MRS), 64–6, 88, 94, 98, 114
Magnetic site exchange, 70
Magnitude spectra, 64
Markov models, 4, 5, *6*, 21
Markov process, 5
Maximum-entropy method (MEM), 109–11, *110*
Maximum-entropy reconstruction (MaxEnt), 109–11
Metal–ligand bonding, 54
Methionine (Met), 48–9
Methyl-deuterated bisphenol-A polycarbonate, 29
^{25}Mg, 141–6
  solid-state NMR interaction parameters, *144–5*
$Mg_{17}Al_{12}$, 146
$MgAlSiN_3$, 143
$MgCl_2$, 141
$MgCl_2$—$6H_2O$, 141
MgO, 141, 142, 143
MgO_4, 141, 142
MgO_5, 142
MgO_6, 141, 142
$Mg(OCH_3)_2$, 142
MgS, 141
Mg_2Si, 141
$MgSiN_2$, 143
α-MnS, 146
^{95}Mo, 163–8
  solid-state NMR interaction parameters, *164–5*
^{97}Mo, 163–8
$Mo(CO)_6$, 129, 167

Molecular dynamics, polyelectrolytes, 46
Molecular motion
  potential governing, *6*
  solid-state NMR, 1–58
Moment expansions, 85–8
Moments of various lineshapes, *68*
MoO_3, 166
MoO_4, 166
MoO_6, 166
MoO_x—Al_2O_3, 166
$MoSe_2$, 167
Mo_3Se_4, 167
$MoSi_2$, 167
Motional frequencies, 28
Multidimensional NMR spectra, 4

^{14}N, 129, 138–41
  solid-state NMR interaction parameters, *140*
  spin—lattice relaxation, 22
$Na_{8-n-p}Ag_nCl_{2-p}$, 150
Na_2MoO_4, 166
$NaZrO_3$, 162
Na_2ZrSiO, 162
NB_3, 140
NB_4, 140
$NH_4Al(SO_4)_2$—$12H_2O$, 139, 147
NH_4Cl, 141
NH_4ClO_4, 139, 140, 149
$(NH_4)_2Mo_2O_7$, 166
$(NH_4)_6Mo_7O_{24}$—$4H_2O$, 166, 167
$(NH_4)_2SO_4$, 147
$(NH_4)_2WO_4$, 138
$Ni_{49.6}Al_{50.4}$, 168
p-Nitroaniline-*N*,*N*-d_2, 22
NMR lineshapes, 65–85, *72*
  approximations, 84–93
  due to exchange narrowing, 70–3
  see also Lineshapes
NMR timescale, 18
NOESY experiment, 31, *32*
Nonlinear least-squares fitting
  frequency domain, 97–8
  time domain, 94–7
Normalized Lorentzian lineshape function, 65
Nuclear Overhauser effect (NOE), 30
Nuclear quadrupole resonance (NQR), 149
Nuclear spin interaction anisotropy, 2
Nuclear spin interaction tensor, 27
Nutation frequencies, 28

ODESSA, 43, 49
One-dimensional CODEX (centreband only detection of exchange) for spin-$\frac{1}{2}$ nuclei, pulse sequence for, *44*
One-dimensional dipolar-shift experiment, *9*
One-dimensional ODESSA (one-dimensional exchange spectroscopy by sideband alternation) experiment, 43, 49
Organometallic compounds, molecular dynamics, 53–4

^{31}P NMR, 47–8
^{31}P spectrum, *106*
^{31}P spinning sideband patterns, 13
^{31}P—^{19}F scalar coupling, 13
Pake doublet or Pake pattern, 79
$Pb(NO_3)_2$, 141
Periodic Table, 121
Phenyl ring rotation, 16
Polarization transfer techniques, 121
Poly(butadiene), *83*
Polyelectrolytes, molecular dynamics, 46
Polyglycine, 49
Polymers
  dynamic heterogeneity in, 46
  dynamics, 46
  solid-state NMR techniques, 45–7
Polystyrene, 47
Powder lineshape, 73–4, *75*
  analysis, 3–25
Powder patterns
  lineshape analysis, 4–9
  resolving, 3–4
Power spectra, 64
Principal axis frame, 8, 27
Prior knowledge, 64, 104
Probe deadtime, 125
Prony's method, 101
Provotorov theory, 63
Pulse sequences, 127–8
  see also specific pulse sequences

Quadrupolar broadening, 30
Quadrupolar Carr–Purcell–Meiboom–Gill (QCPMG) pulse sequence, 21, *22*, *23*, 161
Quadrupolar interaction, *77*, *78*, *80*
Quadrupolar lineshape, 75–9
  analysis, 20–5
Quadrupolar nuclei, 138–41
Quadrupole coupling, 34
Quality factor Q, 125
Quantum mechanics, golden rule, 26

Rational function expansions, 88–93
^{85}Rb, 129
$RbAg_4I_5$, 135
RbCl, 129
REAPDOR experiment, 139
Rectangular lineshape, 69–70
Reduced four-dimensional exchange experiment, *39*, *40*
Reference deconvolution technique, 64
Relaxation data, 28
α-relaxation process, 17, 46
β-relaxation process, 46

Relaxation time measurements, 25–32
Resonance frequency, 42
Retinal, 29, 30
6-*s-trans*-Retinoic acid, 29, *29*
Ring down elimination (RIDE) sequence, 128
Rotating frame relaxation processes, 28
^{99}Ru, 168
^{101}Ru, 168
$Ru(C_5H_5)_2$, *9*
RuO_2, 168

^{33}S, 146–8
  solid-state NMR interaction parameters, *148*
Samia cynthia ricini, 50
Scaled chemical shift anisotropy, 16
Selective inversion, 30
^{29}Si exchange NMR, 35
Sialon, 130
Signal–noise ratio (SNR), 64, 65, 92, *93*, 95, *96*, *97*, 104, 107, 112, 116, 124, 127, 129
Silicon nitride, 130
Si_3N_4, 132
Singular value decomposition (SVD), 100–2, *103*, 104–6, 108, 112
Smoluchowski model, 5, 6
Solid–solid phase transformations, 2
Solid-state heteronuclear multiple-quantum correlation (HMQC) experiment, 25
Solid-state NMR
  biological materials, 47–51
  low-γ nuclei, 121–75
    experimental approaches, 125–30
  molecular motion, 1–58
Solution-state NMR studies, 121
Spatial heterogeneity of polymer dynamics, 39
Spectral density, 27, 31
Spin-$\frac{1}{2}$ nuclei, 19, 70, 127, 130–8
  improving resolution, 43
Spin-1 nucleus, *78*
Spin–lattice relaxation measurements, 45
Spinning speed, 31
^{87}Sr, 168
$SrRuO_3$, 168
Sr_2RuO_4, 168
$SrTiO_3$, 157, 168
State-space methods, 100, 101, 104–6
Static quadrupolar coupling constant, 76
STEAMER experiment, 139
Sternheimer antishielding factor, 148
Streptomyces subtilisin inhibitor (SSI), 48
Super-Lorentzian lineshape, 81, *82*
Symmetric lineshapes, 89
Synthetic rubber SBR 1500 (poly(styrene-co-butadiene)), 31

Taylor series expansion, 85
Three-dimensional ^{2}H exchange experiments, eight-pulse experiment for, 37
Three-dimensional ^{2}H exchange spectra, 37
Three-dimensional difference correlation (3D-DICO) spectroscopy, 37, 38, *38*
Three-dimensional exchange pulse sequence, *36*
Three-dimensional exchange spectroscopy, 37
Three-dimensional NOESY spectroscopy, 32
Three-dimensional variable-angle correlation spectroscopy (VACSY) exchange experiment, 14–16, 41, 46
^{47}Ti NMR, 122, 156–9
^{49}Ti NMR, 122, 156–9
^{49}Ti solid-state NMR interaction parameters, *157*
TiAg, 159
$TiAl_3$, 159
TiB_2, 159
$TiC_{1-x}N_x$, 159
$TiCl_4$, 157
TiC_xN_{1-x}, 140
Time domain
  frequency domain, *67*
  methods, 64
  nonlinear least-squares fitting, 94–7
  signal model, 105
TiN, 140
TiO_2, 157
TiO_6, 158
$Ti(OPr^i)_4$, 158
Total anisotropy, 73
Total least-squares (TLS) method, 104, 106
Transverse magnetization, 32
Transverse relaxation, 28
Transverse relaxation time, 66
Two-dimensional ^{13}C exchange spectra, 39
Two-dimensional exchange pulse sequence, *33*
Two-dimensional MAS ^{13}C exchange NMR spectra, *14*
Two-dimensional NOESY experiment, 31
  pulse sequence, *32*
Two-dimensional NOESY spectra, 31
Two-dimensional VACSY experiment, 14–16, *41*, 46
Two-dimensional wideline ^{1}H spectroscopy (WISE), 45
Tyrosine ethyl ester, *15*

VACSY exchange experiment, 14–16, *41*, 46
Variable-angle correlation spectroscopy (VACSY), 14–16, 41, 46
VARPRO, 98–100
Voigt function, 81, 84–5, *86*, 97–8
Voigt lineshape, *66*, 68–9, 88, 114
  approximations, 84–5
Voigt parameter, 69

^{183}W, 137–8
  solid-state NMR chemical shifts, *138*
$[W(\eta^5—C_5Me_5)Me_4][PF_6]$, 53–4, *54*
$W(CO)_6$, 137
WISE (wideline spectroscopy) technique, 18
WO_3, 137
WO_4, 138
WO_6, 138

^{89}Y, 124, 130–4
solid-state NMR chemical shifts, *131*
$Y(acac)_3$, 132
$Y_3Al_5O_{12}$, 130, 132
$YBa_2(Cu_{1-x}M_x)_3O_7$, 133
$YBa_2Cu_3O_7$, 133, 134
$YBa_2Cu_4O_8$, 133, 134
YCl_3, 132
Y_2Cl_3, 132
Y_2Fe_{17}, 122
α-$YH_{0.18}$, 133
$YH_{1.99+0.1}$, 133
δ-$YH_{1.99}$, 133
$Y_{2-x}Ln_xM_2O_7$, 132
$Y(NO_3)_3$, 132
Y_2O_2S, 130, 132
Y_2O_3, 130, 132
$Y(OAc)_3$, 132
YSiN, 131
$Y_2Si_3O_3N_4$, 132
$Y_4Si_2O_7N_2$, 132
$Y_2(SO_4)_3$, 132
Yttria, 130

Zeeman interaction, 26, *77*, *78*
Zeeman order relaxation, 28
Zeeman–quadrupolar Hamiltonian, 76
Zeeman spin levels, 27
Zeolites, 51–2
^{67}Zn, 159–61
  solid-state NMR interaction parameters, *160*
ZnO, 159, 160
ZnN_4, 161
ZnO_4, 159
ZnO_6, 161
$Zn(OOCCH_3)_2(C_3H_4N_2)_2$, 161
$Zn(OOCH)_2ú2H_2O$, 161
ZnS, 147, 159
ZnS_4, 161
ZnSe, 160
^{91}Zr, 162–3
  solid-state NMR interaction parameters, *163*
ZrC, 162
ZrC_2, 162
ZrH_2, 162
$ZrMo_2$, 162
ZrO_2, 162
$ZrSiO_4$, 162
$ZrZn_2$, 162